Imperial College
London

Random Matrix Modelling of Polarised Light Scattering In Disordered Media

Niall Francis Byrnes

Imperial College London
Department of Physics

Thesis submitted in partial fulfilment of the requirements
for the degree of Doctor of Philosophy
and the Diploma of Imperial College

July 26, 2023

Statement of originality

I hereby declare that this thesis and the work contained within are entirely a product of my own original work. I have used no other sources except as noted by citations.

Copyright declaration

Abstract

The polarisation properties of light are often used as a means of information transfer, as well as in assessing the structural and compositional properties of materials. In many practical situations, however, the propagation of polarised light is impeded by random scattering, which tends to scramble the information content of the underlying fields. Theoretical study of the random scattering of light is an old, complex field of research, in which approximate, numerical methods are often favoured over exact mathematical analysis. Random matrix theory, in which systems are modelled using random scattering matrices, has uncovered universal properties of wide classes of random media, most notably in the field of quantum scattering. Despite also finding success in optics, a random matrix theory of polarised light has yet to be pursued.

In this thesis we apply the notion of random matrices to develop statistical techniques for modelling the random scattering of polarised light. We present a full derivation of the symmetries of the vectorial scattering and transfer matrices that describe dielectric scattering media, including the scattering of evanescent wave components. We then consider the circular ensembles as a simple random matrix model and explore its implications for the scattering of polarised light. Moving beyond elementary models, a rigorous, statistical theory of the scattering matrix for discrete random media is presented, and exact mathematical results are derived in certain special cases. A numerical simulation method for studying scattering matrices describing random media of arbitrary thickness is then developed and validated against known physical phenomena. Finally, the techniques developed within this thesis are applied to the problem of the recovery of polarisation information within light that has propagated through a random medium.

To my loving family.

Acknowledgements

This thesis, though strictly written by me, is in reality the collective result of a community of people who have provided me with invaluable support, both intellectual and emotional, during my time in London. It would therefore be remiss of me not to express a few words of gratitude to those who have helped me on my journey.

Above all, I would like to thank my supervisor Matthew Foreman, whose scrupulous scientific guidance I have found greatly edifying and formative over the last few years. Though I initially faced the prospect of returning to university with considerable trepidation, Matthew has always been welcoming, kind and empathetic towards the struggles I've faced, particularly at some of my lower moments during the pandemic. I would also like to thank Riccardo Sapienza for his consistent support at several important milestones of my studies, as well as for his inspiring, charismatic demeanour.

I am indebted to all of the members of the Photonics group in Blackett Laboratory, who helped foster a productive and friendly working environment. Most notably, I would like to thank Cheryl, Yuchen and Joel, who graciously initiated me into their office and brought me along on their lunch time expeditions, for which the topic of conversation was always a pleasant surprise. My repatriation into the world of academia would have been far more difficult and dull were it not for all of your kindness. More recently, I would like to thank Stefanos, who possesses unparalleled charm and who has exerted an immensely positive influence on me, with the possible exception of certain Friday night shenanigans in the pub.

I have had the honour of encountering a great number of fascinating characters in London, both in my attempts to maintain my Mandarin abilities and otherwise. Lest I forget someone of importance, I would like to extend a collective thank you to all I have crossed paths with during our fleeting time together in this vibrant city. Your energy, positivity, and love and affection has helped me remain sane, and has reminded me to always cherish the present moment.

Finally, I would like to thank my family for their unending and unconditional love and support throughout my life.

Contents

List of Figures

List of Tables

List of Symbols

a	Particle size or radius
$\mathbf{a}$	Vector components of right-propagating/decaying wave
	Object field
$\mathbf{A}$	Amplitude matrix
$\mathcal{A}$	Scattering plane amplitude matrix element
$\mathbf{b}$	Vector components of left-propagating/decaying wave
	Image field
$\mathbf{B}$	Near field amplitude matrix
$\mathcal{B}$	Band of strong correlations
c	Cosine (associated with plane wave wavevector)
$\mathbf{c}$	Vector of wave components
C	Regular correlation function
$\widehat{C}$	Pseudo correlation function
$\mathbf{C}$	Cholesky decomposition
	Correlation matrix
D	Diattenuation
DoP	Degree of polarisation
e	'Evanescent'
$\mathbf{e}$	Spherical polar basis vector
$\mathbf{E}$	Complex electric field
$\mathcal{E}$	Real electric field
${}_2F_1$	Hypergeometric function
g	Anisotropy parameter
	Pair distribution function
$\mathfrak{g}$	Differential transfer matrix Lie algebra
G	Scalar Green's function
$\mathbf{G}$	Vector Green's function
$\mathcal{G}$	Transfer matrix group

h	Spherical Hankel function of the first kind
H	Heaviside step function
$\mathbf{H}$	Complex magnetic field
	Hamiltonian
$\mathcal{H}$	Real magnetic field
	Correlation function
I	Intensity
$\mathbf{I}$	Vector components of waves propagating/decaying towards the medium
$\mathbb{I}$	Identity matrix
Im	Imaginary part
j	Spherical Bessel function of the first kind
$\mathbf{J}$	Jones vector
	Exchange matrix
k	Wavenumber
Δk	Transverse wavevector lattice spacing
$\mathbf{k}$	Wavevector
K_e	Set of evanescent wave transverse wavevectors
K_p	Set of propagating wave transverse wavevectors
l or l_s	Scattering mean free path
l_a	Absorption mean free path
l_p	Length scale associated with phase evolution
l_t	Transport mean free path
L	Scattering medium thickness
$\mathbf{L}$	Vector components of waves on the left side of the medium
m	Relative refractive index
$\mathbf{M}$	Transfer matrix
	Mueller matrix
	Electromagnetic multipole field
n	Particle number density
	Refractive index
N	Number (used in various contexts)
$\mathbf{N}$	Electromagnetic multipole field

$\mathbf{O}$	Vector components of waves propagating/decaying away form the medium
$\mathbb{O}$	Zero matrix
p	Scattering phase function
	'Propagating'
	Probability density function
$\mathbf{p}$	Dipole moment
P	'Pseudo'
	Associated Legendre polynomial
$\mathbf{P}$	Poynting vector
r	Magnitude of position vector (distance)
$\mathbf{r}$	Position vector
	Reflection matrix
$\mathbf{r}'$	Reflection matrix for right side of medium
R	Spherical radius
	Retardance
	'Regular'
$\mathbf{R}$	Vector components of waves on the right side of the medium
	Rotation matrix
$^{\mathrm{R}}$	Reciprocal operator
Re	Real part
Rg	Regularised (multipole fields)
s	Singular value
	Normalised Stokes parameter
	Secant (associated with plane wave wavevector)
S	Stokes parameter
$\mathbf{S}$	Scattering matrix
	Stokes vector
$\mathcal{S}_a$	Support of object field
t	Time
$\mathbf{t}$	Transmission matrix
$\mathbf{t}'$	Right to left transmission matrix
T	T matrix

$\mathbf{T}$	Jones matrix
$^{\mathrm{T}}$	Transpose operator
$\hat{\mathbf{u}}$	Unit direction vector
$\mathbf{U}$	Unitary matrix
V	Integration volume
∂V	Integration volume boundary
$\mathbf{V}$	Unitary matrix
w	Integration weight
W	Power flow through surface
$\mathbf{W}$	Weight matrix
Y	Scalar spherical harmonic
$\mathbf{Y}$	Vector spherical harmonic
x	Sphere size parameter
$\mathcal{Z}$	Z transform
α	Parameter denoting different blocks of scattering matrix
$\boldsymbol{\alpha}$	Top left block of transfer matrix
$\boldsymbol{\beta}$	Top right block of transfer matrix
γ	Factor related to z component of wavevector. See Eq. (3.7).
$\boldsymbol{\gamma}$	Bottom left block of transfer matrix
Γ	Parameter appearing in universal correlation matrix
Γ_e	Set of evanescent transverse wavevectors
Γ_p	Set of propagating transverse wavevectors
δ	Parameter appearing in universal correlation matrix
$\boldsymbol{\delta}$	Bottom right block of transfer matrix
ϵ	Permittivity
$\boldsymbol{\epsilon}$	Differential transfer matrix
$\boldsymbol{\eta}$	Matrix appearing in transfer matrix reciprocity constraint
$\boldsymbol{\kappa}$	Transverse wavevector
λ	Wavelength
Λ	Multipole field
	Propagation matrix
μ	Permeability

	Absorption/Scattering coefficient
Π	Multipole field
ρ	Reflection eigenvalue
$\boldsymbol{\rho}$	Transverse position vector
	Matrix appearing in scattering matrix polar decomposition
	'Depolarisation' parameter
σ	Scattering cross section
$\boldsymbol{\sigma}$	Matrices appearing in scattering matrix symmetries
	Pauli matrix
$\boldsymbol{\Sigma}$	Generalised Pauli matrix
	Matrix containing singular values
	Covariance matrix
τ	Transmission eigenvalue
$\boldsymbol{\tau}$	Matrix appearing in scattering matrix polar decomposition
θ	Scattering angle
	Eigenvalue of retarder matrix
ω	Optical frequency
$\boldsymbol{\omega}$	Matrix appearing in scattering matrix reciprocity constraint
Ω	Integration surface
	Domain of physically allowed transverse wavevectors
$\boldsymbol{\Omega}$	Matrix appearing in transfer matrix energy conservation constraint

Chapter 1

Introduction

1.1 Motivation and aims

Scattering encompasses a wide range of physical phenomena in which the motion of a particle or wave is made to deviate from a straight trajectory. This thesis specifically concerns the scattering of polarised light, primarily in the context of classical physics where light is viewed as an electromagnetic wave. Fundamentally, scattering occurs due to the heterogeneity of a system [1], which is caused by the presence of localised collections of matter. Even if electrically neutral overall, virtually all matter is composed of charged particles, which, when illuminated by light, are set into oscillatory motion by the force imparted upon them by light's constituent electric field. These oscillating charges produce additional, scattered electromagnetic waves that, in general, propagate in all directions. The combination of the incident and scattered waves results in a total electromagnetic field that can be markedly different to that which would exist if the matter were not present. Given the abundance of matter in the world around us, scattering is the rule rather than the exception, as virtually all light that we perceive or interact with undergoes scattering of some kind during its existence.

Light is routinely used as a means of transferring information [2]. In optical communications, for example, information is encoded into the various degrees of freedom

available in the electric and magnetic fields. In other situations, light is used as a tool with which information can be garnered about a particular system. Imaging, for example, involves collecting and processing light that emerges from some object of interest so that its physical form can be better appreciated or analysed for other purposes. Scattering is, by and large, detrimental to these goals. Regardless of the situation, light must travel from a source to a receiver through some intermediary environment. The signal measured at the receiver is therefore a function of both the source signal and the intermediary environment. If this environment is strongly scattering, the information content in the received signal may be scrambled and bear little resemblance to that which originally emerged from the source [3]. Scattering therefore causes information loss, the complete recovery of which remains an unsolved problem that continues to be the subject of a vast amount of research.

Determining the form of the scattered field for a given incident wave and scattering medium is a notoriously difficult and broad problem. Throughout nature, scattering media vary dramatically in terms of scale, structure and complexity. The physical properties of scatterers, such as shape, size, orientation and spatial position, can follow complex, random distributions that vary between different types of environments. Knowledge of these distributions may be difficult or impossible to ascertain experimentally, depending on the complexity of the system. In addition, most scattering media in reality are dynamic, experiencing random temporal fluctuations. In colloidal suspensions, for example, particles undergo Brownian motion, causing the spatial structure of the medium to change randomly in time [4]. As a result, it may be of little value to be able to compute the scattered field for a given, static arrangement of scatterers, as such a solution may only be accurate at a fixed moment in time. Moreover, even if the scattering medium is in fact static, a solution specific to a particular system may be of no use when a new scattering medium possessing a totally different microscopic configuration of scatterers is encountered. As such, statistical methods that aim to uncover universal features common to large classes of scattering media are considered of greatest value.

There exists a profusion of ideas and techniques for modelling and simulating scattering in random media. Typically, the validity of a given method tends to be restricted to a certain class of scattering media that satisfies various constraining

assumptions. Among these tools, the scattering matrix approach has proven to be particularly fruitful, owing to its wide domain of applicability, the facility with which it can be measured experimentally, and the level of control it permits for manipulating waves after it has been determined [5]. In the scattering matrix formalism, waves on either side of a scattering medium are decomposed into linear combinations of basis states. The elements of the scattering matrix describe the coupling between these states, accounting for changes in amplitude, phase, and polarisation state in the most general case. The scattering matrix can be measured experimentally in complete ignorance of the microscopic state of the scattering medium and, in conjunction with wavefront shaping technology, can be used to manipulate the scattered field in stunning ways. For example, while the intensity of a beam of light generally decays as it propagates through a random medium due to random scattering, it is possible to construct tailored states of light that have extraordinary transmissive properties by exploiting complex interferences within the medium. Such states, it can be shown, correspond to eigenvectors of certain matrices that can be computed straightforwardly from the scattering matrix. It is also possible to design wavefronts that are tightly focused by the scattering medium to spots tighter than that achievable by more traditional diffraction-limited optics [6].

Applying the machinery of statistics to the scattering matrix formalism leads naturally to random matrix theory, in which the elements of the scattering matrix are modelled as random variables. In early works, random matrix theorists explored simple probability distributions over broad sets of matrices constrained only to be such that they accord with fundamental physical principles, such as energy conservation, reciprocity and time reversal symmetry [7]. The statistics of quantities derived from the scattering matrix can be related to various physical phenomena and the non-specific nature of such models means that theoretical results are applicable to large classes of scattering media. Universal conductance fluctuations for example, which in optics manifests as system-independent, infinite-range speckle correlations, can be explained in terms of the statistical properties of the singular values of the transmission matrix: a block of the scattering matrix [8]. The success of random matrix theory has been celebrated in physics due to the simplicity of the theory and the universality of its predictions. The lack of specificity inherent

in random matrix theories, however, results in their failing to account for a large number of non-universal scattering phenomena that depend on the precise nature of the scattering medium's constituent particles. The depolarisation of light, for example, which can be cast in terms of second-order moments of the scattering matrix elements, depends intricately on scattering anisotropy, which is known to be related to the size of the scatterers [9]. Traditional random matrix models, despite their success, have therefore seen only limited application in optical scattering, and virtually no steps have been taken towards developing a random matrix model for the scattering of polarised light.

The absence of polarisation in random matrix models is understandable considering the history of the field. Traditional applications of random matrix theory in physics concerned quantum scattering in electronic systems [10], for which the vectorial nature of light has no obvious analogue. In optics, however, the polarisation state of light is a fundamental property that is frequently exploited in a myriad of technologies and applications, such as astronomical magnetic field measurements [11], thin film analysis [12], multiplexed data storage [13], biomedical imaging [14], and determining the orientation of molecules [15]. The omission of polarisation in theoretical models hence precludes the possibility of further enhancing the performance of such techniques, and of advancing new ones through greater overall understanding. The aim of this thesis is thus to make headway towards developing random matrix techniques that are able to model the scattering of polarised light in random media. In particular, we will seek to generalise results from classical random matrix theory so as to incorporate the polarisation state of light. In addition, we will present a novel simulation technique for generating random scattering matrices able to describe random media with tailored scattering properties. Finally, we will apply our technique to examine the question of to what degree polarimetric information is transmitted through random scattering media. It is hoped that the methods and ideas developed in this thesis will pave the way for future research that will improve our overall understanding of the random scattering of polarised light.

1.2 Thesis structure

In Chapter 2, we shall specify more concretely the type of scattering media with which this thesis is concerned. We will then give a brief introduction to key concepts from scattering theory that will be important throughout the thesis. In the second half of Chapter 2, we will review a selection of existing methods for simulating random scattering in complex media, giving commentary on each method's relative merits and shortcomings. The purpose of this section will be to establish the playing field against which the random matrix approach, which will discussed in more depth in later chapters, can be compared.

In Chapter 3, we will introduce the scattering and transfer matrices within a rigorous mathematical formalism. We shall proceed to derive the constraints satisfied by these matrices due to energy conservation, reciprocity and time reversal symmetry. These constraints will allow us to establish an appropriate random matrix theory in subsequent chapters. Finally, we will briefly discuss the differential transfer matrix and discuss its algebraic properties.

In Chapter 4 we will introduce basic ideas from random matrix theory and apply them to scattering matrices satisfying the constraints derived in Chapter 3. This approach is conceptually simple and will be sufficient to derive interesting statistical behaviour of polarimetric quantities, including retardance and diattenuation. The results of this chapter will later serve as limiting statistical distributions for more general models.

In Chapter 5 we will introduce a more general statistical theory of the scattering matrix associated with a discrete, random scattering medium. Using this approach, we will derive the mean, covariance, and pseudo-covariance of the scattering matrix elements and give physical interpretations of these results. While our results will primarily apply to far field scattering, some discussion will be given regarding extending the results to incorporate near field modes. The results of this chapter will also serve as the basis for our simulation method.

In Chapter 6 we will introduce and expound our simulation method for generating random scattering matrices describing random media of arbitrary thickness. We will present validatory numerical results that demonstrate the method's ability

to accurately model realistic scattering media. We will then present a numerical analysis of the computation speed, precision and accuracy of the method.

In Chapter 7 we will apply the framework and simulation method developed throughout the thesis to tackle the toy problem of reconstructing a hidden incident field with a non-uniform polarisation structure. We will give an introductory presentation of a procedure able to achieve this, with numerical data serving as a proof of principle.

In Chapter 8 we summarise the key findings of the thesis and discuss possible avenues for future work.

Chapter 2

Background

The goal of this thesis is to explore and develop random matrix techniques for modelling the scattering of polarised light in random media. Without clarification as to what types of scattering media are amenable to this approach, however, this problem is exceptionally broad and not well defined. In this chapter we therefore begin by specifying the type of scattering and scattering environments that are relevant to the work within this thesis. The discussion in this chapter will be largely qualitative, and a more rigorous mathematical presentation of the problem will be delayed until Chapter 3, where the scattering matrix formalism will be introduced in greater detail.

After elucidating the type of scattering media under consideration, we will give a brief overview of some fundamental concepts from scattering theory that will support discussions in later chapters. Particular focus will be placed on the polarisation properties of light and the effects that scattering has upon them. In the second half of this chapter, we will review a variety of existing methods for simulating scattering in random scattering media, comparing the performances of different approaches and their respective domains of applicability. Theoretical modelling of random scattering is, of course, an old subject and new techniques are only valuable if they offer advantages over other available methods. The aim of this review will thus be to assess the limits of extant methods and to motivate a random matrix approach.

This chapter will assume basic familiarity with concepts from polarisation optics,

such as Stokes parameters and the Poincaré sphere. An introduction to these topics can be found in many classic textbooks [12, 16, 17, 18]. Alternatively, a brief review of the concepts most pertinent to this thesis is given in Appendix. A.

2.1 Scattering of polarised light

As stated in the introduction, scattering is not a single process, but rather an umbrella term for a large number of different phenomena. When viewed at the right length scale, even reflection and refraction at a planar boundary can be understood as aggregate scattering effects [19]. Another important class of light-matter interactions distinct from scattering fall into the category of absorption, which is the transformation of electromagnetic energy into other non-radiative forms, such as thermal energy [1]. In general, there exists a plethora of terms for categorising the full range of different types of interactions between light and matter, and this thesis makes no pretence of being exhaustive in scope.

We will restrict our study to volumetric, elastic scattering by conglomerations of small particles that form linear, dielectric, random media. Moving forwards, this combination of properties defines what shall be meant by a complex scattering medium. By volumetric, we refer to scattering that occurs within the interior of a scattering medium, rather than at its boundaries. We shall therefore not consider, for example, scattering from rough surfaces [20]. We note, however, that surface effects can be incorporated into our theory, and some discussion of how this might be achieved will be given in Chapter 3. The restriction of elastic scattering entails neglecting absorption, inelastic scattering such as Raman and Brouillon scattering [21], and other resonant effects involving frequency changes, such as fluorescence [22]. As shall be seen in Chapter 3, changes in energy complicates affairs as energy conservation simplifies the algebraic structure of the scattering matrix. In addition, changes in frequency between the incident and scattered fields requires the use of a polychromatic scattering matrix, which is more complicated than the monochromatic case. The notion of a small particle in this work can be understood as a inhomogeneity in the spatial permittivity and permeability functions. There is no particular limit on the size of these inhomogeneities, but we shall suppose that they

are localised to scales roughly up the order of several wavelengths. Linearity of the scattering medium is necessary for matrix methods to be applicable, but naturally excludes non-linear optical effects, such as second harmonic generation [23]. Finally, the stipulation that the scattering medium is dielectric forgoes consideration of potential excitation of surface plasmon polaritons that can occur at metal-dielectric boundaries [24]. All of the effects we have excluded are of course interesting and important, and their exclusion inevitably limits the applicability of our work. Nevertheless, we are still left with a domain of investigation that is rich in physics and, despite an immense amount of research, is far from being fully understood.

The type of models that will be most prominently explored in this thesis can be described as mesoscopic, in contrast to microscopic and macroscopic. These terms refer to scale, both of the systems under consideration and of the theory being used. Although there is no sharp delineation between these terms, it is possible to compare extreme examples. Consider for example scattering by a cloud. A microscopic scattering theory may concern the scattering of light by individual raindrops through consideration of the interaction of light with its constituent water molecules. A macroscopic theory, on the other hand, may attempt to assess the optical properties of the cloud as a whole, such as its albedo, by considering its bulk chemical composition [25]. Mesoscopic scattering theory, which occupies an intermediate length scale, can be thought of bridging these two extremes. In a mesoscopic theory, one may consider transport of light through the cloud at the level of inter-particle scattering sequences. Physics at this scale contains a variety of interesting effects, which have important consequences for the cloud's macroscopic optical properties.

Most scattering media encountered in nature, such as fog, interstellar dust, and biological tissue, consist of a large number of randomly positioned particles [26]. The complexity of such systems necessitates mathematical descriptions able to account for multiple scattering events, where the scattered field from one particle can scatter again from other particles. Before exploring these, however, it will be useful to begin by examining the scattering of polarised light by a single, isolated particle, which is a much simpler problem that will nevertheless provide valuable insight in preparation for more complex systems.

2.1.1 Scattering by an isolated particle

Since polarisation is a geometric property of light, it is not surprising that its transformation upon scattering depends heavily on the geometry of the scatterer in relation to the polarisation state of the incident field. Given a particle of arbitrary shape illuminated by an arbitrary incident field, little can be said in general about the exact form of the scattered field as a function of space and time. Nonetheless, several key concepts can be introduced that allow for rather general comparisons of different types of scatterers.

2.1.1.1 General considerations

Suppose that an isolated particle located at the origin of a homogeneous background medium is illuminated by a monochromatic, time harmonic plane wave. Let $\mathbf{E}_i$ denote the complex envelope of the incident field[1] and suppose that

$$\mathbf{E}_i(\mathbf{r}) = \mathbf{E}_0 \exp(i\mathbf{k}_i \cdot \mathbf{r}), \tag{2.1}$$

where $\mathbf{k}_i$ denotes the incident wavevector, $\mathbf{r}$ is a position vector and $\mathbf{E}_0$ describes the polarisation state of the wave. The incident field will give rise to a scattered field $\mathbf{E}_s$, such that the total field $\mathbf{E}$ at any point in space is given by the sum of the incident and scattered fields, i.e. $\mathbf{E} = \mathbf{E}_i + \mathbf{E}_s$. In discussing the form of the scattered field throughout space, it is useful to define the near and far field regions of the scatterer as being points for which $kr \leq 1$ and $kr \gg 1$ respectively, where $k = |\mathbf{k}_i|$ and $r = |\mathbf{r}|$. While there is no sharp delineation between these two regions, in what follows we will only consider points for which the far field condition holds. Near field scattering will be considered briefly in Chapter 5.

In the far field of the scatterer, it is known that the scattered field can be well approximated by a spherical wave [1]. Far away from the scatterer, the polarisation state of the scattered field does not vary in the radial direction, but only over the surface of a large sphere centred on the scatterer, each point of which represents a different scattering direction. The relationship between $\mathbf{E}_s$ in a particular direction

[1] Throughout this thesis, it will be assumed that expressions such as 'field', 'polarisation state', 'polarisation vector' and so on refer exclusively to the electric field and not the magnetic field.

$\hat{\mathbf{u}}$, where a hat denotes that the vector has unit length, and $\mathbf{E}_i$ can be described by a matrix $\mathbf{A}(\hat{\mathbf{u}}, \hat{\mathbf{k}}_i)$, which we shall refer to as the amplitude matrix. The vector $\hat{\mathbf{k}}_i$ describes the direction of the incident field. In general, $\mathbf{A}$ is a complex function of both of these directions. For particles exhibiting certain types of symmetry, however, such as spheres, it can be shown that $\mathbf{A}$ depends only on the angle between these two directions [27]. This angle, $\theta = \arccos(\hat{\mathbf{u}} \cdot \hat{\mathbf{k}}_i)$, is called the scattering angle.

In general, there is no simple mathematical expression for the amplitude matrix. Certain mathematical constraints for the amplitude matrix do exist however when the scatterer it describes is invariant with respect to certain geometric transformations, such as reflections and rotations [1, 27, 28]. A more general symmetry known as reciprocity holds largely in disregard of the shape of the scatterer. Specifically, reciprocity is a relationship between $\mathbf{A}(\hat{\mathbf{u}}, \hat{\mathbf{u}}')$ and $\mathbf{A}(-\hat{\mathbf{u}}', -\hat{\mathbf{u}})$, where $\hat{\mathbf{u}}$ and $\hat{\mathbf{u}}'$ are arbitrary direction vectors. Reciprocity can thus be thought of as a relationship between amplitude matrices that are connected by inverting and negating the incident and scattering directions. In particular, in Cartesian coordiantes, reciprocity manifests as the constraint

$$\mathbf{A}(\hat{\mathbf{u}}, \hat{\mathbf{u}}') = \mathbf{A}(-\hat{\mathbf{u}}', -\hat{\mathbf{u}})^{\mathrm{T}}, \tag{2.2}$$

where the superscript $^{\mathrm{T}}$ denotes the matrix transpose. Reciprocity is not universal, but holds for a large class of scatterers, requiring only that the permeability, permittivity and conductivity tensors are symmetric [29]. Examples of non-reciprocal scatterers typically involve magneto-optic or non-linear effects [30, 31, 32], which shall not be considered in this thesis.

It is useful to describe the relative power flow of the scattered field in different scattering directions. This can be formalised by considering a small, ideal power detector positioned at different points on a spherical surface located in the far field of the scatterer. The amount of power received by the detector as a function of scattering direction gives rise to a function called the differential cross section $\mathrm{d}\sigma/\mathrm{d}\Omega$ [1]. Integrating this function over the entire spherical surface yields the scattering cross section σ, which measures the total power carried away from the particle by the scattered field. It is common to normalise the differential cross section by σ,

which yields the so-called scattering phase function p. In a quantum picture, the phase function can be interpreted as the probability density for a photon to scatter from its incident direction into a small solid angle centred on a particular scattering direction [33]. Another useful quantity is the anisotropy parameter g, defined by $g = \langle \cos(\theta) \rangle$ where the angle brackets $\langle \cdot \rangle$ denote an angular average with respect to the scattering phase function, i.e.

$$g = \int p(\hat{\mathbf{u}}, \hat{\mathbf{k}}_i)(\hat{\mathbf{u}} \cdot \hat{\mathbf{k}}_i) \mathrm{d}\hat{\mathbf{u}}, \tag{2.3}$$

where the integral is taken over the unit sphere. Due to the normalisation of p, the anisotropy parameter is bounded in the interval $-1 \leq g \leq 1$ and its value gives a quantitative description of how much light is scattered 'forwards' versus 'backwards'. Here, forwards and backwards can be understood as meaning scattering into the two half-spaces delineated by a plane perpendicular to the incident direction that passes through the centre of the particle. For example, $g = 1$ when all light is scattered forwards, $g = -1$ when all light is scattered backwards and $g = 0$ when there is an equal amount of scattering in both directions.

2.1.1.2 Scattering regimes

For all but the simplest of particle geometries, such as spheres or infinitely long cylinders, mathematical expressions for the amplitude matrix are often left in terms of infinite series of intractable integrals [34]. One major simplification, however, known as Rayleigh scattering, is possible in the limiting case of particles much smaller than the wavelength of the incident light.

Suppose that the size of a particle can be reasonably described by a number a, where a has the dimension of length. For a spherical particle, for example, a may be the radius. In the limit $ka \ll 1$, the particle, regardless of its shape, behaves like an electric dipole, producing a scattered field proportional to $\hat{\mathbf{r}} \times \hat{\mathbf{r}} \times \mathbf{p}$, where $\mathbf{p}$ is the induced dipole moment of an ideal electric dipole located at the centre of the particle [28]. Note that throughout this thesis, triple vector products shall always be understood in the sense that $\mathbf{a} \times \mathbf{b} \times \mathbf{c} = \mathbf{a} \times (\mathbf{b} \times \mathbf{c})$. In the case that the particle's polarisability is isotropic and the incident polarisation state is linear, the

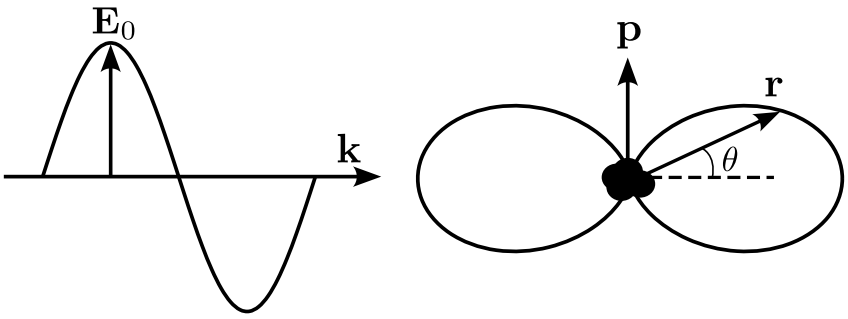

Figure 2.1: In-plane Rayleigh scattering profile for an incident plane wave with wavevector $\mathbf{k}_i$ and linear polarisation state $\mathbf{E}_0$. The vector $\mathbf{p}$ shows the induced dipole moment, assumed to be parallel to the incident field. On the right side of the figure, θ denotes the scattering angle and the length of the vector $\mathbf{r}$ from the particle to the figure eight curve represents the relative probability of scattering in that direction.

vector $\mathbf{p}$ aligns with $\mathbf{E}_0$ and the angular profile of the phase function assumes a characteristic toroidal shape, a cross section of which is shown in Figure 2.1. By symmetry, it is evident that $g = 0$, which leads to the commonly encountered claim that Rayleigh scattering is isotropic. This, however, is not true in the sense that Rayleigh scattering has a uniform phase function. Although Rayleigh scatterers have no effective size, symmetry is broken by the orientation of $\mathbf{p}$. More specifically, as can be seen in Figure 2.1, no light is scattered in the direction of $\mathbf{p}$ when the incident field is linearly polarised. In general, it is obvious from the definition of g that isotropic scattering implies $g = 0$, but the converse is not true.

Rayleigh scattering, rather than being a wishful idealisation, is relatively common in nature. Most notably, it is the process by which visible light scatters from gas molecules in the atmosphere, which gives skylight a characteristic polarisation pattern [35]. Rayleigh scattering is also the mechanism by which light tends to scatter from small molecules and nanoparticles, which are often the subject of imaging, tracking and sizing experiments [36, 37].

The small size constraint for Rayleigh scattering can be relaxed to some extent when the refractive index of the particle is close to that of its background medium, leading to what is known as Rayleigh-Gans scattering [1]. To make this more precise, it is useful to define the relative refractive index $m = n_p/n_b$, where n_p and n_b are the refractive indices of the particle and background medium respectively. Similar general characteristics to Rayleigh scattering are observed when both $|m - 1| \ll 1$ and $ka|m - 1| \ll 1$. Notably, the latter of these constraints allows for a to be

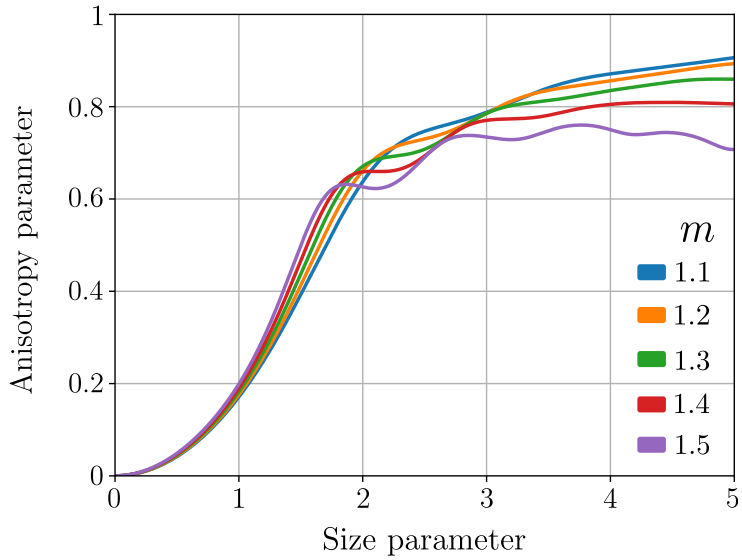

Figure 2.2: Anisotropy parameter g for spheres as a function of dimensionless size parameter x for different values of relative refractive index m.

larger than previously stipulated for Rayleigh scattering [38]. Examples of particles satisfying these constraints include nanoparticles [39], snowflakes [40] and disk-like particles found in the ocean [41].

Collectively, Rayleigh and Rayleigh-Gans scattering is one of the only instances for which the scattering phase function can be expressed in terms of simple trigonometric functions. In all other cases, the phase function has no simple form, and must be evaluated numerically from a more complex theory. The phase function can often be approximated, however, using for example the Henyey-Greenstein phase function, which is a simple mathematical function that only requires the specification of g, which can be estimated or obtained by some other means, such as from experimental data. [42]. While this function accords with realistic phase functions relatively well for isotropic scatterers, discrepancies between it and more accurate models have been shown to increase for large values of g [43].

Moving beyond the small particle limit, the shape of the particle cannot be neglected. Scattering by an isotropic sphere of arbitrary radius and uniform refractive index is famous for being one of the few problems that is exactly solvable analytically. The solution is known as Mie theory, the mathematical details of which are well documented in numerous classical texts and shall not be repeated here [1, 28, 34, 44]. For our purposes, it is sufficient to note that, for a fixed refractive

index, the anisotropy parameter tends to increase with particle radius. In other words, as the radius of the sphere increases, there is a larger power flow in the forward direction. This is demonstrated in Figure 2.2, which shows the anisotropy parameter as a function of the dimensionless size parameter $x = ka$, where a is the particle radius, for different values of m. The relationship between x and g is mostly monotonic in the range of values shown, although small oscillations can be seen when $m \sim 1.5$. Large values of m are relatively uncommon in nature. In biological tissue, for example, scatterers tend to have mean refractive indices at around $n_p \sim 1.4$ [45]. Taking water as the background medium ($n_b \sim 1.33$) puts the relative refractive index in the range $m < 1.1$. As a final remark, we note that when $ka \gg 1$, Mie theory converges to geometrical optics [46], which is a relatively simple theory that can be applied to large particles of irregular shape [47]. Particles of this size, however, shall not be considered in this thesis.

2.1.2 Scattering by a complex medium

The scattering of polarised light in complex media of the type described at the beginning of this chapter is markedly different to scattering by a single particle. As mentioned previously, the key difference between an isolated particle and a collection of particles is that in the latter case the scattered field from one particle can interact with other particles, yielding additional scattered fields. Assuming that the incident field is coherent, such as light from a laser, multiple scattered fields propagate through the medium along different tortuous paths, accruing random, uncorrelated phases. After finally emerging from the medium, these fields interfere, resulting in a complex interference pattern of bright and dark spots, known as speckle [48, 49]. In dynamic media, random motion of the constituent scatterers causes the relative phases of different contributions to the total field to change in time, causing fluctuations in the scattered intensity distribution. Numerical analysis of these fluctuations, such as measuring the speckle intensity autocorrelation function, can reveal information about the diffusion properties of the scatterers, which can be used to deduce particle size or mass [50, 51]. Even for a static medium, speckle fluctuations occur if an incident beam is scanned across different spatial regions of the scattering medium.

The polarisation state of a field emerging from a dynamic scattering medium is a random function of space and time [52]. If one observes the path traced by the tip of the scattered electric field vector over a sufficiently long measurement time t_m, it will not be elliptical, but instead more erratic. One can imagine, however, some time scale t_p, determined by the rate of motion of the scatterers in the medium, such that for $t_m < t_p$ the scatterers will have moved so little that the electric field vector can be said to have traced an approximately fixed ellipse. In reality, for any practical measurement time, the field vector will have traced many cycles of this ellipse [12]. Roughly speaking then, over a long duration t_m, separated into N segments of duration t_p, i.e. $t_m = Nt_p$, the electric field will transition between approximately N different elliptical polarisation states. Considering the limiting distribution of these polarisation states as $N \to \infty$, it is possible to assign a number to the scattered field, known as the degree of polarisation DoP, which can be thought of as the degree to which any particular polarisation state is 'preferred' over the entire distribution of states, i.e. if it occurs more commonly than any others. The degree of polarisation, by definition, is confined to the interval $0 \leq \text{DoP} \leq 1$. When $\text{DoP} = 0$, no particular polarisation state is preferred over any other and the field is said to be unpolarised. When $\text{DoP} = 1$, on the other hand, the distribution consists of only a single polarisation state and is said to be fully polarised. For any other value of DoP, the field is said to be partially polarised. Distributions of polarisation states can be conveniently visualised as probability distributions over the surface of the Poincaré sphere. It is interesting to note that, at least in principle, $\text{DoP} = 0$ does not imply a spherical uniform distribution. For example, a bimodal distribution of left and right handed circular polarisation states satisfies $\text{DoP} = 0$ by symmetry, but is clearly non-uniform. The existence of different types of unpolarised fields have been pointed out in the literature, such as in Ref. [53].

Given a fully polarised incident field, which by definition satisfies $\text{DoP} = 1$, the production of a scattered field for which $\text{DoP} < 1$ is known as depolarisation. More generally, if the incident field is partially polarised, such as that from a thermal source with non-zero spectral bandwidth [49], depolarisation refers to any reduction in the degree of polarisation in the resulting scattered field. Practically speaking, the degree of polarisation can be determined experimentally by measuring the time-

averaged Stokes parameters of the scattered field, which does not require explicit determination of the aforementioned distribution of polarisation states [12].

When fully polarised light impinges upon a static medium, the scattered field at any given point in space will be fully polarised. Different points in space, however, will tend to have different polarisation states. In this case, it is possible to determine a degree of polarisation by averaging the scattered Stokes vector over different spatial positions or far field scattering direction. Alternatively, one may determine a degree of polarisation by averaging Stokes vectors over a collection of speckle patterns associated with different realisations of the scattering medium, perhaps arising from a beam illuminating different regions of the medium. In any case, it is clear that the degree of polarisation is a potentially ambiguous quantity that depends on what exactly is being measured. In some cases, however, it may be assumed, or in fact demonstrable, that the degree of polarisation is independent of the type of average performed. For example, in a dynamic medium it may be the case that the particles move through a considerable proportion of all possible microstates so that a temporal average is effectively equivalent to averaging over a corresponding ensemble of static media that have similar macroscopic properties. This property is known as ergodicity and its validity has strong experimental justification [54].

Complex media are frequently described using several different length scales. The simplest of these are the scattering and absorption mean free paths l_s and l_a, which, in a photonic picture, are the average length scales over which a photon propagates before it is scattered or absorbed [17]. In the weak scattering limit $kl_s \ll 1$, the scattering mean free path can be related to the mean scattering cross section σ and number density n of the constituent scatterers by $l_s = (n\sigma)^{-1}$. This expression fails for dense scattering media and alternative formulas must be used [55]. In the absence of absorption, the scattering mean free path is also the length scale over which the intensity I of the unscattered component of the field transmitted through a random medium decays, as described by the Beer-Lambert law

$$I \sim e^{-L/l_s}, \tag{2.4}$$

where L is the length of the medium in the direction of the incident field. As

the medium thickness increases, there is a greater amount of scattering, and more light is thus scattered from the incident field into the scattered field, resulting in a decrease in I. We note that this law takes numerous alternative forms, depending on the properties of the scattering medium [33, 56]. More complex behaviour can also occur in the presence of absorption. For example, in systems for which the absorption length is comparable to the inter-particle spacing, absorption can suppress multiple scattering [57].

In addition to l_a and l_s, there exist other length scales that are useful in characterising scattering media. Neglecting absorption, the transport mean free path, given by $l_t = l_s/(1-g)$, is often interpreted as the length scale over which the incident wave 'forgets' its initial propagation direction. Alternatively, by expanding $1/(1-g)$ as a geometric series, it can be seen that the transport mean free path is the distance travelled by a photon that moves along of an infinite number of steps of length l_s, where after each step its wavevector turns through the mean scattering angle [58]. For isotropic scatterers, $l_s = l_t$. For anisotropic scatterers, however, l_t can be many times larger than l_s, with $l_t/l_s \to \infty$ as $g \to 1$.

Once the thickness of a scattering medium exceeds the transport mean free path, many of the finer details associated with the individual scatterers, such as the single particle phase function, lose significance, and the medium as a whole tends to scatter isotropically. This allows one to study the transport properties of random media using relatively simple diffusion models [59]. An important exception to this, however, is the coherent backscattering effect, whereby even in the limit $L \gg l_t$, a strong peak in scattered intensity can be observed in the direction opposite to the incident field's wavevector relative to the mean background intensity in other directions [55, 60, 61, 62]. This peak arises due to the constructive interference of photons that propagate along time-reversed paths through a scattering medium and is robust to statistical averaging. Coherent backscattering, fundamentally an interference phenomenon, is a precursor to the more stark effect of Anderson localisation, in which the transmission of light through a random medium is halted entirely under certain conditions [63]. Anderson localisation, however, will not be considered in this thesis.

It is also possible to define length scales over which light is depolarised. It

turns out, however, that, in addition to depending on the properties of the scattering medium, the rate of depolarisation shows a pronounced dependence on the incident polarisation state. This effect was first observed in diffusing-wave spectroscopy experiments that examined light backscattered from suspensions of latex spheres in water [64]. In particular, time-averaged intensity autocorrelation functions of backscattered speckle patterns were measured for incident linear and circular polarisation states, from which correlation decay times were calculated. The key observation was that for spheres with size $ka \geq 1$, incident circularly polarised light exhibited a notably long decay time when measured with a polarisation analyser selecting the helicity-preserving channel, indicating that circularly polarised light tends to preserve its polarisation state. This effect, known as the polarisation memory effect, can be explained by scattering anisotropy [65].

For large particles, $g \approx 1$ and a large contribution of the backscattered field comes from light that propagates along long paths, undergoing a large number of small angle scattering events. The helicity of circularly polarised light is highly robust to small angle scattering and circularly polarised light thus tends to preserve its polarisation state [66]. Unlike circularly polarised light, the scattering of linearly polarised light is more sensitive to the exact direction in which light is scattered. A parallel transport argument shows that backscattered light tends to contain equal contributions of light polarised parallel and perpendicular to the incident polarisation state, showing that linearly polarised light depolarises more easily than circularly polarised light [65]. For small particles, for which $g \approx 0$, the backscattered field consists largely of contributions arising from relatively short scattering sequences involving large angle scattering events close to the surface of the medium. These large angle scattering events cause helicity to flip, resulting in quicker depolarisation for incident circularly polarised light than in the case of large particles. More sophisticated diagrammatic calculations show that, in this regime, linearly polarised light depolarises less quickly than circularly polarised light, with a depolarisation length exactly twice that for circularly polarised light [9].

The rate at which light depolarises has been widely studied theoretically [67, 68, 69, 70, 71] and experimentally [45, 72, 73, 74, 75], for both pulsed [76] and continuous wave illumination [77]. A full review is beyond the scope of this thesis,

but it is worth noting that in addition to particle size, depolarisation rates are also affected by particle concentration [78, 79, 80], polydispersion [81, 82, 83] and other polarisation phenomena, such as birefringence [84] and dichroism [85]. Besides being an academic curiosity, depolarisation characteristics of disordered media have been exploited in a variety of technologies. For example, polarisation can be used as a gating mechanism, allowing for depth-resolved imaging [86]. Difference imaging techniques, in which images produced with orthogonal polarisation analysers are combined in suitable ways, also allow for the discrimination of photons that penetrate shallowly or deeply into scattering media by, for example, rejecting photons that do not possess the desired helicity [14, 87, 88, 89].

Although depolarisation generally limits the transfer of polarimetric information through scattering media, the intricate relationship between depolarisation rates and medium parameters has motivated the use of depolarisation as a signal for determining scattering medium properties. For example, consideration of depolarisation can be used to infer scatterer size, which has been used to discriminate healthy and cancerous tissue [90, 91, 92]. Polarisation patterns in skylight, which are primarily caused by Rayleigh scattering in the atmosphere, can also be used for navigation [93]. Multiple scattering corrections to the theory unpinning these methods can help improve accuracy [94, 95], as well as describe scattering by other objects in the atmosphere, such as clouds [96].

2.2 Numerical modelling of scattering media

Multiple scattering is notoriously difficult to model mathematically. It is therefore often necessary to resort to numerical simulations to gain more concrete understanding. In this section we shall give a brief review of some of the more popular simulation methods and discuss some of their advantages and disadvantages. In Chapter 6 we shall introduce a novel simulation method based on random matrix techniques. It is thus hoped that the discussion in this section will help motivate our technique and allow us to better compare it to those that already exist.

Simulation methods tend to differ in the degree to which they make assumptions or approximations. We shall attempt to present the methods approximately in

decreasing order of mathematical rigour, or, alternatively, in increasing order of number of assumptions. Of course, such a categorisation is ultimately somewhat arbitrary.

Before examining simulation methods in detail, a couple of generic comments can be made. Generally speaking, a larger number of approximations tends to result in a method being quicker to run and less demanding in computer resources. Naturally, the primary drawback of approximations is that they result in poorer accuracy and limit the applicability of the method to special types of scattering media for which the approximations are reasonably valid. It is also worth bearing in mind that, besides physical considerations, there may be more practical reasons that determine which method is most appropriate for a given user. Methods based on more fundamental physics require a greater degree of expertise to properly appreciate and make use of, and may therefore be less suitable for practitioners working in other scientific disciplines who lack the time or resources to become competent users. In addition, the popularity of a simulation method may simply be determined by the availability of a free, robust code online.

2.2.1 Exact simulation methods

We shall begin by considering 'exact methods' for simulating the scattering of polarised light in complex systems. Of course a simulation, by definition, is never truly an exact replica of reality. By 'exact' we therefore mean methods that can be rigorously justified from first principles and that can be clearly traced back to fundamental physical theory with minimal assumptions. These methods stand in contrast to more heuristic approaches that shall be discussed in Section 2.2.2.

In classical physics, the scattering of light is a problem in electromagnetism, which is described by Maxwell's equations [97]. The most obvious way to find the scattered field for a particular system is thus to solve Maxwell's equations. Numerical solvers of Maxwell's equations largely belong to one of two types: those that solve the differential Maxwell equations or associated wave equations, and those that solve the integral counterparts of Maxwell's equations [26]. With these methods, statistical analysis of random systems can be viewed as a two step process. First, a probabilistic model is chosen for the structure of the scattering medium. This

may involve, for example, the statistical distributions of the physical properties of the scatterers as well as their positions. Using this model, different realisations of the scattering medium can be randomly generated. For each of these realisations, one can solve numerically for the scattered field at some set of relevant observation points. Averaging results over many realisations then provides a statistical description of scattering by the random medium ensemble.

2.2.1.1 Differential equations

Differential equation techniques can be applied both in the time and frequency domains using the finite difference and finite element methods [98]. In the finite difference time domain method, Maxwell's curl equations are discretised in space and time and all derivatives appearing in the equations are approximated by finite differences [99]. In the frequency domain, it is instead common to apply the finite element method to the Helmholtz equation discretised in space [100]. While finite difference techniques typically involve regular spatial lattices, finite element methods discretise space using sophisticated mesh structures, which can more accurately handle irregular geometries at the expense of increased complexity. Finite difference frequency domain [101], finite element time domain [102] and various hybrid techniques [103, 104] have also been proposed, which combine the merits of the different approaches. In any case, discretisation converts a system of differential equations into a system of algebraic equations, which can then be solved by matrix algebra techniques. While finite difference and finite element methods are conceptually similar, the exact numerical procedures involved in calculating solutions are quite different.

Both finite difference and finite element methods face practical challenges with regard to the geometry of the computational domains, which must be truncated to finite sizes. In particular, care must be taken in both methods to ensure that the fields behave physically at the domain boundaries. In time domain simulations, one must specify appropriate boundary conditions to avoid, for example, spurious boundary reflections of outgoing transient waves. This can be accomplished using the perfectly matched layer technique, which establishes an absorbing boundary to the computational domain [105]. In the frequency domain, in which one solves for

steady state solutions, one must also ensure that the solution satisfies the radiation condition at infinity. One way to achieve this is to use a spherical computational domain and match the field components at the boundary with spherical vector wave functions existing outside the domain, for which the radiation condition is automatically satisfied [106]. Alternative boundary conditions, such as Floquet boundary conditions, can also be used for periodic systems [107].

Another issue with the finite difference method lies in the choice of discretisation. While rectangular spatial grids are generally the easiest to implement, they may not conform optimally to the shape of the scatterers. For example, in a rectangular grid a curved surface of a particle would be represented by a discrete step function, which would introduce inaccuracies. This problem can be ameliorated either by implementing a non-rectangular grid that better matches the geometry of the scatterer [108], or by preserving the rectangular grid, but using the Maxwell-Garnet rule to compute averaged values of the permittivity function to be used at grid points [109].

Despite the aforementioned issues, the finite difference and element methods are are highly flexible, being applicable to scattering by an assortment of arbitrarily shaped particles. The primary drawback of the methods are computational speed and system scale: computation time tends to scale with the volume of the system [110], rendering the methods relatively unsuitable for macroscopic media. Both methods also require that the computational domain extends beyond the system of particles of interest, requiring additional computation that is avoided in alternative methods [111]. In addition, as previously mentioned, in order to obtain statistical averages, simulations must be repeated for different microscopic realisations of the scattering medium, which further increases total computation time. Simulations must also be repeated when other initial conditions are altered, such as the shape or polarisation state of the incident field.

2.2.1.2 The volume integral equation

Rather than solving the Maxwell or Helmholtz equations directly, an alternative approach is to consider the volume integral equation, which can be derived from the Helmholtz equation by introducing the free-space dyadic Green's function. This

equation is given by [26]

$$\mathbf{E}(\mathbf{r}) = \mathbf{E}_i(\mathbf{r}) + k^2 \int [m^2(\mathbf{r}) - 1]\mathbf{G}(\mathbf{r}, \mathbf{r}')\mathbf{E}(\mathbf{r}')\mathrm{d}\mathbf{r}', \tag{2.5}$$

where $\mathbf{E}_i$ and $\mathbf{E}$ are the incident and total electric fields respectively, k is the wavenumber in the background medium, m is the ratio of the refractive index of the scatterer to the background medium, $\mathbf{G}$ is the aforementioned Green's function and the domain of integration is the region occupied by the scatterer. Finding $\mathbf{E}$ is tantamount to resolving the integral in Eq. (2.5), which can be handled in several ways.

The simplest approach to solving the volume-integral equation is the method of moments, which approximates the integral as a sum of simpler integrals over smaller spatial regions whose union comprises the original domain of integration [112]. One of the simplest implementations of this idea is to use a cubical spatial discretisation and to assume that each volume element has an approximately constant permittivity function [113]. Other cubature geometries involving tetrahedral and hexahedral elements, have also been considered [114, 115]. The discretisation scheme allows one to transform the original volume integral equation into a system of linear equations for the total electric field at different points in space, which can then be solved by standard procedures, such as Gaussian elimination or the conjugate gradient method [116]. A variety of more sophisticated numerical techniques, such as the fast Fourier transform method [117], the multilevel fast multipole algorithm [118], and the multi-scale compressed block decomposition method [119] have also been developed to push the capabilities of the method to larger, more complex systems [120].

An alternative approach to solving the volume integral is the discrete dipole approximation, also known as the coupled dipole method [121, 122]. As with the method of moments, the discrete dipole approximation also involves discretising space, commonly into a cubical lattice [123]. Provided that each lattice element is sufficiently small, each element can be modelled as an electric dipole, which scatters in response to both the incident field and the scattered dipole fields from all other elements [111]. Within this framework, it is again possible to reduce the volume

integral equation to a system of linear equations, this time for the fields exciting each dipole. The discrete dipole approximation is thus conceptually similar to the method of moments, and similar Fourier-based numerical optimisations can be used for improved performance [124].

One important aspect of the discrete dipole approximation is to relate the polarisability of each volume element to its electric permittivity. Originally this was achieved using the Clausius-Mossotti relation [125]. This relation, however, is only exact in the limit $kd \to 0$, where d is the lattice spacing, and radiative corrections have thus been proposed [126]. In addition, for large structures consisting of an arrangement of smaller subdivisions, the permittivity of individual elements can be found from the bulk optical properties of the larger structure using effective medium theories, such as the Maxwell-Garnett relation [127].

The discrete dipole approximation method has proven to be immensely popular, in part thanks to the fact that robust implementations of the method are freely available online [128]. As with the method of moments, fast Fourier methods can be used for regular lattices, which offer substantial speed improvements. In addition, for periodic scattering systems, one can use tailored Greens functions that better handle the boundary conditions and for which efficient computational methods have been developed [129, 130].

Since volume integral methods are inherently based on Greens function techniques, solutions automatically satisfy the radiation condition, although some care is needed in handling integral singularities [131]. Compared to time-domain methods, which require tracking the evolution of transient fields, volume integral methods also generally require a smaller spatial computational domain. Computational accuracy, however, improves slowly with the number of lattice cells used, limiting the applicability of volume based methods to macroscopic systems [111]. Volume integral methods also suffer from the problem that, like differential equation techniques, simulations must be repeated when initial conditions are altered, which limits their utility for statistical studies.

Another class of approaches to solving the volume integral equation makes use of the fact that solutions to the Helmholtz equation can be represented as an angular spectrum of plane waves, which is especially useful for modelling scattering in

periodic planar media [132]. An infinite plane periodic medium can be thought of as being made up of many small, repeating unit cells. The set of plane waves whose wavevectors lie on points within the corresponding reciprocal lattice automatically satisfy the appropriate periodic boundary conditions and can thus be used as a complete basis for the scattered field [133]. Ultimately, within such a framework, the volume integral equation can be recast within this Fourier basis and solved using similar discretisation procedures [134]. In order to better model realistic scattering media, which in general are not periodic, one can increase the size of the unit cell by using a larger number of plane wave components in Fourier space. Naturally, this comes at the cost of an larger amount of required memory and computing time. While Fourier methods do well at modelling media of larger scales, they also suffer from the problem of requiring repeated runs to collect sufficient data for statistical averaging [135].

2.2.1.3 T-matrix

The methods discussed so far all involve computing the scattered field for a given set of initial or boundary conditions. In contrast, the T-matrix method involves the computation of a matrix that allows the user to quickly compute the field scattered by a system for any arbitrary incident field [136]. Mathematical details of the T-matrix will be given later in Section 5.4 in the context of near-field scattering. The discussion in this section will thus be qualitative.

Within the T-matrix formalism, the incident and scattered fields are expressed as infinite sums of vector spherical functions. For practical purposes, these sums must be truncated at some finite cut-off, where a greater number of remaining terms generally results in better accuracy. If the coefficients of each vector spherical function are collated into vectors, then the T-matrix relates the vectors corresponding to the incident and scattered fields. Importantly, the T-matrix is independent of the structure of the incident and scattered fields and only depends on the properties of the scatterers. As such, it only needs to be calculated once and can then be reused at will for different incident fields.

Computation of the T-matrix can be performed in several ways. For individual scatterers, the standard procedure uses the extended boundary condition method,

in which the elements of the T-matrix can be related to integrals that must be numerically evaluated over the surface of the particle [137]. Computation of such integrals is simpler for symmetric particles, particularly solids of revolution [138], although the method has been used for more general particle shapes such as non-rotationally symmetric ellipsoids [139]. Using modified vector spherical functions, the T-matrix method has also been generalised to other particle morphologies, such as multilayered scatterers [140], chiral particles [141] and general anisotropic particles [142]. The T-matrix for a multi-particle group can also be calculated using the superposition T-matrix method, which exploits a translation addition theorem of the underlying spherical vector functions [143]. The superposition method, however, requires that the T-matrices of the individual scatterers are already known, which may not always be the case in reality. The superposition method requires solving a large system of linear equations, which, for a large number of particles, becomes intractable. Iterative methods are thus frequently used for large particle groups [144].

The T-matrix method generally performs very well and has shown to be several orders of magnitude faster than volume-integral methods for computations involving non-spherical particle clusters with fixed orientation [145]. Moreover, the T-matrix framework allows for some degree of analytic averaging of particle properties, such as orientation, minimising the need to repeat simulations with different initial conditions [146, 147]. The primary issue with the standard implementation of the T-matrix method is that, along with scaling issues for large media, the method is numerically unstable for certain types of pathological particles, such as prolate or oblate spheroids with large aspect ratios or particles with extreme refractive indices [136].

2.2.2 Approximate simulation methods

In this section we will examine several methods that have a more phenomenological flavour. The techniques to be presented in this section, while inspired by physical principles, may not be immediately, or at all, derivable from Maxwell's equations. As such, they do not involve the direct computation of the scattered fields for a specified set of initial or boundary conditions. In some cases, such as in radiative

transfer theory, the quantity that is calculated is not even a fundamental physical quantity, but rather one that is heuristically motivated. Despite all this, approximate methods tend to be relatively simple and less computationally demanding than exact methods. Additionally, in some cases, statistical quantities can be calculated directly, removing the need for repeat simulations. Finally, it is worth remembering that the quality of any particular model lies ultimately in its accordance with reality, and approximate methods have been successful in this regard.

2.2.2.1 Random phasor sums

One of the simplest ways of modelling multiple scattering of coherent fields has its origin in the common physical explanation of speckle. Since speckle is produced by the interference of many partial scattered fields that have random amplitudes and phases, a scattered field can be modelled as a sum of a large number of complex phasor expressions, i.e. [48]

$$\mathbf{E}_s = \sum_{n=1}^{N} a_n e^{i\theta_n}, \tag{2.6}$$

where a_n and θ_n are some random collection of amplitudes and phases. In such a sum, as more terms are added, the partial sum can be visualised as performing a random walk in the complex plane. The statistical properties of such sums are well understood and have been presented in several classic works [48, 49]. For complex phasors whose phases are distributed uniformly from zero to 2π, as the number of terms in the sum tends to infinity, a central limit argument shows that the sum behaves as a circular, complex Gaussian variable, whose amplitude is described by a Rayleigh distribution. Although primitive, this approach assumes virtually nothing about the properties of the scattering medium and Gaussian statistics in speckle patterns are observed almost universally [148, 149, 150].

Vectorial extensions to the random phasor sum approach, which are able to determine polarisation statistics, have also been considered [73, 151]. In addition, Gaussian statistics for the scattered electric field has a number of important consequences for the statistics of various polarimetric quantities. Beginning from this assumption, the statistics of Stokes parameters and associated quantities, such as the

degree of polarisation and elliptical polarisation parameters have been extensively analysed mathematically [152, 153, 154, 155, 156]

Briefly, it is worth mentioning that under certain conditions speckle statistics deviate from being Gaussian. This typically occurs for weak scattering media, where the number of scatterers is relatively small [148, 157]. Mathematically, a small number of scatterers means that only a small number of complex phasor terms will be present in the sum, and the conditions for the central limit theorem are therefore violated. In other circumstances, speckle statistics may be Gaussian, but non-circular. Statistics of this sort can be constructed artificially [158], and occur naturally in the scattering from rough surfaces [159, 160].

2.2.2.2 Radiative transfer theory

One of the most well known theories for modelling multiple scattering media is radiative transfer, which has its origins in astrophysics [161]. At its inception, the goal of radiative transfer was to derive a Boltzmann equation that could describe the transport of light through scattering media on the basis of energy conservation [162]. The radiative transfer equation takes numerous forms depending on the assumptions made in its derivation. One form of the equation is given by [33]

$$\frac{\partial I(\mathbf{r},\mathbf{u})}{\partial z} = -(\mu_a + \mu_s) I(\mathbf{r},\mathbf{u}) + \frac{\mu_s}{4\pi} \int I(\mathbf{r},\mathbf{u}') p(\mathbf{u},\mathbf{u}') \mathrm{d}\mathbf{u}', \tag{2.7}$$

where z is a coordinate through the scattering medium, $\mu_s = 1/l_s$ and $\mu_a = 1/l_a$ are so-called scattering coefficients, $\mathbf{u}$ and $\mathbf{u}'$ are direction vectors, p is the scattering phase function for the scatterers that make up the scattering medium and the integral is taken over the unit sphere. $I(\mathbf{r},\mathbf{u})$, known as the specific intensity, is a somewhat convoluted quantity that, at a position $\mathbf{r}$, describes the flow of optical power in a small frequency interval through an elementary area oriented in the direction given by $\mathbf{u}$ [163]. In terms of energy balance, the first term on the right hand side of Eq. (2.7) represents losses due to absorption and scattering away from the direction $\mathbf{u}$, while the second term accounts for light that is scattered back into direction $\mathbf{u}$ from other directions. Radiative transfer theory began as a scalar theory, but a vectorial generalisation was subsequently developed in which I is replaced by

a set of analogous Stokes parameters and the phase function p is replaced by a single scattering Mueller matrix, thus accounting for changes in polarisation state [164].

Solutions of the radiative transfer equation are statistically averaged quantities, and, unlike previous methods, there is thus no need for repeated simulations. In fact, a full microscopic description of the scattering medium is not at all required. Assuming that a scattering medium has no absorption or gain, the only adjustable parameter in the radiative transfer equation is the single particle phase function p, or single particle Mueller matrix in the vectorial case [27]. In the scalar case, the phase function is often approximated using the previously discussed Henyey-Greenstein function or other multi-parameter generalisations [165, 166]. Radiative transfer is therefore conceptually simple: given input parameters that describe rudimentary single scattering properties of the particles, the theory describes multiple scattering of a large collection of such particles. Radiative transfer theory can also be used to attempt to solve inverse problems, namely the determination of the parameters of a scattering medium based on measurements of the scattered fields [167].

Because of its relative conceptual simplicity and accessibility, radiative transfer theory has been used widely throughout science, in fields such as astronomy [168], geophysics [169], biology [170] and communications [171]. Despite its simplicity, however, the radiative transfer equation is difficult to solve directly. Analytic solutions have only been found for several simple cases, such as plane parallel media and isotropic scattering [163]. One method of simplifying the radiative transfer equation is the diffusion approximation, in which the diffuse intensity is assumed to be quasi-isotropic [172]. This assumption allows one to derive a diffusion equation for the diffuse intensity, which is comparatively easier to solve. The diffusion approximation has been shown to agree well with experimental results for weakly absorbing particles satisfying $g \ll 1$, but can perform poorly in other circumstances [173, 174].

In the general case, the radiative transfer equation must be solved numerically, which can be achieved using a variety of methods. The discrete ordinates method, for example, involves discretising both space and the angular domain specifying the direction in which radiation can flow [175, 176, 177]. Another method, known as the adding-doubling method, is particularly powerful for parallel planar media [178]. This method simplifies calculations for media that can be formed by composing many

planar slabs by using knowledge of the scattering properties of the individual slabs. Other methods, to name a few, involve the use of spherical harmonic functions [179], the Galerkin technique [180], the eigenfunctions method [181], and the F_N and P_N methods [182, 183]. Analysis of the radiative transfer equation can also be simplified by exploiting symmetries of the scattering matrix [184].

In terms of scattering regimes, application of radiative transfer is limited, as its most common implementations are only able to model random assortments of sparsely distributed, uncorrelated scatterers, hence neglecting near field effects. Generalisations, however, appropriate for dense particular media have been developed [185]. Radiative transfer does not directly simulate diffraction and assumes no correlation between different components of multiply scattered fields, meaning it is unable to reproduce interference effects, such as speckle [163]. It is noteworthy that, despite originating as a heuristic model, the radiative transfer equation has since been derived from the ladder approximation in rigorous multiple scattering theory, solidifying its position as respectable physical theory [164]. The ladder approximation, however, fails to account for the coherent backscattering peak, which emerges from 'crossed' scattering diagrams in multiple scattering theory [186].

2.2.2.3 Monte Carlo simulations

Among the many numerical methods that exist for solving the radiative transfer equation, the Monte Carlo method [187] is notably popular and has seen widespread use in a variety of different fields, such as wireless communications [188], biology [189] and remote sensing [190]. Unlike other methods, the Monte Carlo approach is not a standard differential equation solver, but instead a simulation framework based on a physical interpretation of radiative transfer theory.

In the standard Monte Carlo method, a 'photon' is injected into a scattering medium that occupies some spatial domain. The photon is modelled as a ray that propagates through the medium in a fixed direction. After travelling some random distance, typically sampled using a negative exponential distribution [191], a scattering event is said to occur. When scattering occurs, the propagation direction of the photon is updated, becoming a new direction that is randomly sampled in accordance with the phase function of the scatterers in the medium. The photon

then continues to propagate in its new direction and the process is repeated. The process terminates when the photon exits the confines of the scattering medium and the outgoing propagation direction is recorded. This entire sequence is iterated for a large number of photons, which then yields a distribution of scattered photon directions.

It is straightforward to incorporate additional effects, such as absorption [192] and polarisation [193] into the Monte Carlo method. Absorption can be introduced by attaching a weight to each photon that is incrementally decreased upon each scattering event in relation to the particle albedo [194]. If this weight reaches zero before the photon exits the medium, the photon is rejected. Otherwise, once the photon leaves the medium, its residual weight is used to scale its contribution to the overall intensity distribution of the scattered field. Polarisation can be introduced into the Monte Carlo method by introducing a local coordinate system that follows the photon and which is rotated after each scattering event [85]. Tracking and transformation of this coordinate system can be achieved using several methods, such as the use of meridian and scattering planes [195], Euler angles [196] and quaternions [197]. In polarisation implementations, the Stokes vector of the photon is tracked as it propagates and, after each scattering event, is updated using a single particle Mueller matrix, from which the phase function can also be derived [198]. Alternatively, for fully polarised fields, one can instead track the field components and use the amplitude matrix to update the polarisation state and propagation direction [199]. This approach enables the tracking of phase and is able to simulate polarised speckle. Generalisations to the Monte Carlo approach have also allowed for studies of birefringent media using effective Mueller matrices at scattering events that also incorporate properties of the background medium [84].

While flexible, the Monte Carlo procedure is slow as it requires a large number of photons for statistical results to have sufficiently converged. Simulations must also be repeated if the initial distribution of photon directions or polarisation states are altered. Several techniques exist, however, to increase performance. For example, a condensed Monte Carlo procedure allows for the simulation of different albedos based on results for a single albedo [200]. In addition, there exist hybrid techniques that combine the merits of the Monte Carlo method and diffusion theory for increased

speed [201].

2.3 Conclusion

In this chapter we have attempted to motivate the need for methods of simulating the random scattering of polarised light. As has been discussed, the transformation of the polarisation of state in random media is a complex process, and analytic theories quickly become intractable for all but the simplest of systems, necessitating numerical techniques. Numerical simulations have enjoyed great success at providing insight into the many intricacies of random scattering and have proven to be indispensable tools for theoretical study. As is evident, however, no single method is optimal for all possible problems, and the number of ideas that have been proposed over the years is a reflection of the vast diversity and complexity of scattering media found throughout the natural world. It is of course healthy that such a broad range of tools exist, so that as new problems are encountered and old ones are re-examined there is an ever-expanding pool of resources with which they can be analysed, and from which inspiration can be drawn.

In comparing the various methods in this chapter, the rigorous techniques closely tied to Maxwell's equations have shown to be most accurate and flexible, as they make minimal assumptions and allow the user to specify arbitrary scattering media. Within this class of methods, it is interesting to highlight the conceptual difference between the T-matrix approach and the others. As noted, the T-matrix is re-usable and in some sense gives a mathematical representation of the scattering medium itself, rather than just the scattered field for a fixed set of initial conditions. The T-matrix may therefore contain additional information pertaining to the random scattering medium that is not immediately transparent in expressions for the scattered field. For example, as was briefly introduced in Chapter 1, speckle patterns exhibit a variety of correlations, which may manifest as statistical correlations between different elements of the T-matrix for different combinations of incident and scattered field components. One prominent example of this is the memory effect, which will be described in more detail in Chapter 5. The scattering matrix method that will be pursued in this thesis shares this nature with the T-matrix. Unlike the

T-matrix method, however, which is ideally suited for individual particles, or multi-particle conglomerates, our scattering matrix approach will enable the modelling of macroscopic scattering media of arbitrary thickness without unreasonable scaling in computation time with system size.

Having established the landscape of extant simulation methods, for the remainder of this thesis we will focus our attention on the scattering and transfer matrix formalisms. In the next chapter we will give a formal, rigorous introduction to these matrices and derive their mathematical properties.

Chapter 3

Scattering and transfer matrices

Having explored a variety of theoretical techniques for modelling random scattering in Chapter 2, we now turn our attention to the scattering and transfer matrices, the study and use of which will comprise the remainder of this thesis. We shall begin by giving a brief and general introduction to the scattering and transfer matrix formalisms, and describe some of their applications in different areas of physics. We shall then define more concretely the scattering medium we wish to study and apply a rigorous scattering formalism to it. Specifically, we shall consider a scattering medium with slab geometry that has finite thickness and is infinite in its transverse dimensions. This choice of system precludes the analysis of systems with closed geometries, but is general enough to be applicable to a wide range of realistic scattering media.

We shall describe the incident and scattered fields using an angular spectrum of plane waves, which is a natural choice of mode decomposition for several reasons. First, an angular spectrum allows us to frame the theory in terms of the scattering of plane waves, for which there is extensive literature to draw upon. Secondly, an angular spectrum allows for the easy separation of propagating and evanescent plane wave components. Traditionally, the scattering matrix formalism has only been applied to far field scattering, which, in an angular spectrum decomposition, corresponds to a simple truncation of the set of transverse wavevectors. Advances in near field optical technologies, however, such as scanning near field optical mi-

croscopy, necessitate the development of theories able to account for the scattering of evanescent plane wave components [202]. In this chapter, we shall therefore provide a general scattering matrix theory able to incorporate both types of plane wave components.

Once the scattering problem and matrix formalisms have been clearly established, we shall proceed to derive the set of mathematical constraints satisfied by the scattering and transfer matrices due to energy conservation, reciprocity and time reversal symmetry. These constraints place limits on the set of physically allowable scattering and transfer matrices, and can hence serve as useful guides in determining whether a given system satisfies the corresponding physical laws. Conversely, matrix constraints can guide theoretical models of scattering media, and can simplify theoretical calculations by, for example, reducing the number of degrees of freedom available within the matrices. These constraints will be invaluable in Chapters 4 and 6, where they will be applied in a random matrix theory of polarisation statistics as well as in numerical simulations of random scattering media.

The conclusions of this chapter are novel and were recently presented in the literature in Ref. [203].

3.1 Introduction

The scattering and transfer matrix formalisms are useful mathematical frameworks for describing scattering systems. It should be stressed at the outset that scattering and transfer matrices fundamentally contain the same information about the scattering medium they describe and should therefore not be thought of as two independent formalisms. Rather, it is the case that, due to their different mathematical properties, one may be simpler to implement than the other, depending on the nature of the problem under investigation. For convenience, we may at times exclusively refer to the scattering matrix. It should be remembered however that at such instances an analogous comment can also be made about the transfer matrix.

The core concept of the scattering matrix formalism is relatively simple. The scattering medium under investigation is treated as a black box, about which, in principle, nothing may be known. A collection of state vectors are defined, which

describe all possible channels or modes for waves that impinge upon and depart from the scattering medium. In optics, the components of these vectors can contain information about, for example, the relative amplitudes, phases and polarisation states of waves in different modes. The scattering matrix describes the transformation between these states. Conceptually, the scattering matrix does not give a direct description of a scattering medium. Instead, it allows one to answer the question of how a particular state will scatter, which in many cases may be what is ultimately desired. As discussed in Chapter 2, analysis of the scattered field can, however, also reveal information about the scattering medium indirectly. Practically, a scattering matrix can be determined through sequential measurements of the scattered field for a series of known incident states [5]. Once it has been found, the scattering matrix then enables the determination of the scattered field for any arbitrary incident state.

Historically, the scattering matrix has been extensively used in quantum physics, where it is also referred to as the S-matrix [204]. It has recently however become a popular tool in optics, where it has found use in a variety of applications, including wavefront shaping [205], imaging [206], focusing light [207], particle cooling [208], data encryption [209], communications [210], and lasing [211]. The entire scattering matrix describes how waves incident upon different sides of a scattering medium are transmitted and reflected by the medium. For practical reasons, it is difficult to arrange an experimental setup that can measure all of these components simultaneously. In a single experiment, it is thus more common to measure isolated sections of the scattering matrix, such as the transmission or reflection matrices, which describes how waves incident upon one side of a scattering medium are transmitted and reflected respectively.

Many optical scattering experiments involve illuminating complex scattering media with open geometries, where the scattered field is not confined to a specific region of space and where there is no natural set of modes. In such cases, the transmission and reflection matrices are typically measured by designing incident fields using a spatial light modulator [5, 212]. The states that describe the incident field are determined by the configuration of an array of pixels on the surface of the modulator, which controls the relative phases of waves emanating from different spatial positions. The states describing the detected field may be, for example, the electric

field measured at different spatial positions, such as at different pixels on a camera. While in the simplest case the incident and scattered fields may be described by their spatial intensity distributions, more sophisticated experimental setups involving interferometry also allow for phase detection [213] as well as the control and measurement of polarisation states [214, 215]. We note that a spatial basis of modes can be related to an angular spectrum via the Fourier transform [216], which can be applied to the scattering matrix numerically, or performed experimentally by measuring the scattered field in the Fourier plane of a collecting lens.

From a theoretical perspective, it is worth noting that experiments involving open geometries typically fail to capture the full set of degrees of freedom of the incident and scattered fields. The finite size of detection optics, for example, may fail to capture waves that scatter at large angles with respect to the optical axis. An experimental scattering matrix should therefore be thought of as a sub-matrix of a theoretical scattering matrix that fully describes the complete set of components of the fields [217]. In other contexts, however, a complete scattering matrix may be determinable if the geometry of the system restricts the number of modes to a reasonable, finite value. Scattering matrices have also been widely employed for structures with closed geometries, such as cavities [211], optical fibres [218], photonic crystals [219], as well as for axial propagation of light along layered media, such as fibre Bragg gratings [220] and superlattices [221].

3.2 Continuous scattering and transfer matrices

We shall now set up the theoretical problem to be studied in this chapter and introduce the scattering and transfer matrices more rigorously.

3.2.1 Definitions

Consider the problem depicted in Figure 3.1. A dielectric scattering medium is situated within the region $-L/2 \leq z \leq L/2$, which we denote by $\mathcal{R}^s$. We denote by $\mathcal{R}^-$ and $\mathcal{R}^+$ the regions $L^- < z < -L/2$ and $L/2 < z < L^+$ surrounding the scattering medium, which are assumed to be dielectric with constant background permittivity ϵ_b, assumed for simplicity to be the same on both sides of the scattering

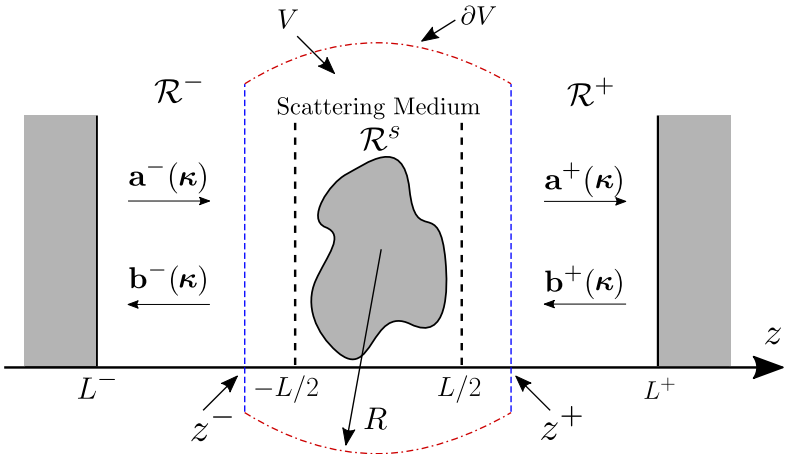

Figure 3.1: Geometry of the scattering problem. The integrating surface ∂V used in deriving the energy conservation and reciprocity constraints is also depicted. Dashed lines denote the planar sections of ∂V and dot-dashed curves denote the spherical section of radius R.

medium. Although the shape of the scattering medium is arbitrary, confining it to a slab-shaped region of space facilitates the introduction of angular spectrum decompositions for the incident and scattered fields, which shall be introduced shortly in this section. All incident field sources are contained in the regions $z < L^-$ and $z > L^+$. We assume that the scattering medium is linear and all fields are monochromatic with angular frequency ω. The domain $L^- < z < L^+$ can be described by a spatially inhomogeneous, complex-valued permittivity function $\epsilon = \epsilon(\mathbf{r}, \omega)$, where $\mathbf{r} = (x, y, z)^{\mathrm{T}}$ is the position vector. Note that in general ϵ is a 3×3 matrix. We also assume that both the scattering and background media are non-magnetic and have magnetic permeabilities equal to the vacuum permeability μ_0.

We denote by $\mathbf{E}(\mathbf{r})$ and $\mathbf{H}(\mathbf{r})$ the complex representations of of the total real electric $\mathcal{E}$ and magnetic $\mathcal{H}$ fields, with a suppressed time factor of $\exp(-i\omega t)$. The real electric field, for example, is given by $\mathcal{E}(\mathbf{r}, t) = \mathrm{Re}[\mathbf{E}(\mathbf{r})e^{-i\omega t}]$, where Re denotes the real part of a complex quantity. The frequency-domain Maxwell equations for

the entire region $L^- < z < L^+$ are given by [27]

$$\nabla \cdot \mathbf{E}(\mathbf{r}) = 0, \tag{3.1}$$

$$\nabla \cdot \mathbf{H}(\mathbf{r}) = 0, \tag{3.2}$$

$$\nabla \times \mathbf{E}(\mathbf{r}) = i\omega\mu_0 \mathbf{H}(\mathbf{r}), \tag{3.3}$$

$$\nabla \times \mathbf{H}(\mathbf{r}) = -i\omega\epsilon(\mathbf{r}, \omega)\mathbf{E}(\mathbf{r}). \tag{3.4}$$

Taking the curl of Eq. (3.3) and using Eq. (3.4), the vector wave equation for the electric field can be shown to be

$$\nabla \times \nabla \times \mathbf{E}(\mathbf{r}) - \omega^2\mu_0\epsilon(\mathbf{r}, \omega)\mathbf{E}(\mathbf{r}) = \mathbf{0}. \tag{3.5}$$

We remind the reader that triple cross products should be understood in the sense $\mathbf{a} \times \mathbf{b} \times \mathbf{c} = \mathbf{a} \times (\mathbf{b} \times \mathbf{c})$. In $\mathcal{R}^-$ and $\mathcal{R}^+$, the permittivity function is given by the background permittivity and we have $\omega^2\mu_0\epsilon(\mathbf{r}, \omega) = \omega^2\mu_0\epsilon_b = k^2 = n_b^2 k_0^2 = n_b^2(2\pi/\lambda_0)^2$, where k and k_0 are the wavenumbers in the background medium and vacuum respectively, λ_0 is the wavelength of light in vacuum, $n_b = \sqrt{\epsilon_b/\epsilon_0}$ is the background refractive index and ϵ_0 is the vacuum permittivity. In these regions we may write the electric field as a spectrum of plane wave components [19]

$$\mathbf{E}^{\pm}(\mathbf{r}) = \int \left[\mathbf{a}^{\pm}(\boldsymbol{\kappa})e^{i\gamma z} + \mathbf{b}^{\pm}(\boldsymbol{\kappa})e^{-i\gamma z}\right] e^{i\boldsymbol{\kappa}\cdot\boldsymbol{\rho}} \mathrm{d}\boldsymbol{\kappa}, \tag{3.6}$$

where the plus or minus superscript is chosen to accord with the superscript of the region under consideration and $\mathrm{d}\boldsymbol{\kappa} = \mathrm{d}k_x \mathrm{d}k_y$, where k_x and k_y are the x and y components of the transverse wavevector $\boldsymbol{\kappa} = (k_x, k_y)^{\mathrm{T}}$, and $\boldsymbol{\rho} = (x, y)^{\mathrm{T}}$ is the transverse position vector. For each plane wave component, $\gamma = \gamma(\boldsymbol{\kappa})$ is given by

$$\gamma(\boldsymbol{\kappa}) = \begin{cases} \sqrt{k^2 - |\boldsymbol{\kappa}|^2}, & \text{if } |\boldsymbol{\kappa}|^2 \leq k^2, \\ i\sqrt{|\boldsymbol{\kappa}|^2 - k^2}, & \text{if } |\boldsymbol{\kappa}|^2 > k^2. \end{cases} \tag{3.7}$$

Though we shall frequently drop its dependence on $\boldsymbol{\kappa}$, it should be remembered that γ is a function of $\boldsymbol{\kappa}$.

Through inspection of Eq. (3.6), it can be seen that $\mathbf{a}^{\pm}(\boldsymbol{\kappa})$ is a vector that

characterises the polarisation state of the plane wave with wavevector $(k_x, k_y, \gamma)^{\mathrm{T}}$. Similarly, $\mathbf{b}^{\pm}(\boldsymbol{\kappa})$ characterises the polarisation state of the plane wave component with wavevector $(k_x, k_y, -\gamma)^{\mathrm{T}}$. When working with angular spectra, it is sufficient to keep track of only the transverse wavevector $\boldsymbol{\kappa}$, as the z component of the full wavevector can be always be calculated from Eq. (3.7) and by consideration of the direction of the wave. Since at times we will need to refer to full three component wavevectors, it will be useful to define the symbols $\mathbf{k}$ and $\widetilde{\mathbf{k}}$, which should also be thought of as functions of $\boldsymbol{\kappa}$. We define these as

$$\mathbf{k} = (k_x, k_y, \gamma)^{\mathrm{T}}, \tag{3.8}$$

$$\widetilde{\mathbf{k}} = (k_x, k_y, -\gamma)^{\mathrm{T}}. \tag{3.9}$$

Clearly, $\mathbf{k}$ and $\widetilde{\mathbf{k}}$ can be thought of as right propagating and left propagating wavevectors respectively. The domain of integration of the integral in Eq. (3.6) and, unless specified otherwise, all integrals that follow in this chapter, is assumed to be $\mathbb{R}^2$, i.e. the infinite two-dimensional real plane. In light of Eq. (3.3), the corresponding angular spectrum representation of the magnetic field can be obtained by taking the curl of Eq. (3.6), which yields

$$\mathbf{H}^{\pm}(\mathbf{r}) = \frac{1}{\omega\mu_0} \int \left[\mathbf{k} \times \mathbf{a}^{\pm}(\boldsymbol{\kappa}) e^{i\gamma z} + \widetilde{\mathbf{k}} \times \mathbf{b}^{\pm}(\boldsymbol{\kappa}) e^{-i\gamma z}\right] e^{i\boldsymbol{\kappa}\cdot\boldsymbol{\rho}} \mathrm{d}\boldsymbol{\kappa}. \tag{3.10}$$

Inspecting Eq. (3.7), it is clear that when $|\boldsymbol{\kappa}|^2 \leq k^2$, γ is a real quantity and the plane wave components in the integrand are thus homogeneous, or propagating. In particular, it is clear that the plane wave components associated with $\mathbf{a}^{\pm}(\boldsymbol{\kappa})$ propagate in the positive z direction and those associated with $\mathbf{b}^{\pm}(\boldsymbol{\kappa})$ propagate in the negative z direction. When $|\boldsymbol{\kappa}|^2 > k^2$, on the other hand, γ is an imaginary quantity and the plane waves are thus inhomogeneous, or evanescent. In this case, the amplitude of plane wave components associated with $\mathbf{a}^{\pm}(\boldsymbol{\kappa})$ decay in the positive z direction and the amplitude of those associated with $\mathbf{b}^{\pm}(\boldsymbol{\kappa})$ decay in the negative z direction. For convenience, we define the sets Γ_p and Γ_e, where $\Gamma_p = \{\boldsymbol{\kappa} : |\boldsymbol{\kappa}|^2 \leq k^2\}$ is the set of all transverse wavevectors corresponding to propagating plane waves and $\Gamma_e = \{\boldsymbol{\kappa} : |\boldsymbol{\kappa}|^2 > k^2\}$ is the set of all transverse wavevectors corresponding to evanescent plane waves.

As the scattering medium is assumed to be linear, the vector coefficients of plane wave components travelling (or decaying in the case of evanescent waves) towards and away from the scattering medium can be related using the scattering matrix. Specifically, if we define the column vectors

$$\mathbf{I}(\boldsymbol{\kappa}) = [\mathbf{a}^-(\boldsymbol{\kappa}), \mathbf{b}^+(\boldsymbol{\kappa})]^{\mathrm{T}}, \tag{3.11}$$

$$\mathbf{O}(\boldsymbol{\kappa}) = [\mathbf{b}^-(\boldsymbol{\kappa}), \mathbf{a}^+(\boldsymbol{\kappa})]^{\mathrm{T}}, \tag{3.12}$$

which contain coefficients of plane wave components that are incident upon and outgoing from $\mathcal{R}^s$ respectively, the continuous scattering matrix $\mathbf{S}$ is defined to be the matrix that satisfies

$$\mathbf{O}(\boldsymbol{\kappa}) = \int \mathbf{S}(\boldsymbol{\kappa}, \boldsymbol{\kappa}')\mathbf{I}(\boldsymbol{\kappa}')\mathrm{d}\boldsymbol{\kappa}'. \tag{3.13}$$

In the admittedly somewhat awkward vector notation in Eqs. (3.11) and (3.12), both vectors within the square brackets should be imagined as being flattened to give a one dimensional row vector containing all six of the interior vectors' scalar components. The transpose operator on the outside of the square brackets then converts this row vector into a six component column vector.

As is evident from Eq. (3.13), $\mathbf{S}$ is a function of the incident and outgoing transverse wavevectors. For a given pair of transverse wavevectors $\boldsymbol{\kappa}$ and $\boldsymbol{\kappa}'$, the scattering matrix $\mathbf{S}(\boldsymbol{\kappa}, \boldsymbol{\kappa}')$ is a 6×6 matrix of complex entries, which can be conveniently written as a 2×2 block matrix in the form

$$\mathbf{S}(\boldsymbol{\kappa}, \boldsymbol{\kappa}') = \begin{pmatrix} \mathbf{r}(\boldsymbol{\kappa}, \boldsymbol{\kappa}') & \mathbf{t}'(\boldsymbol{\kappa}, \boldsymbol{\kappa}') \\ \mathbf{t}(\boldsymbol{\kappa}, \boldsymbol{\kappa}') & \mathbf{r}'(\boldsymbol{\kappa}, \boldsymbol{\kappa}') \end{pmatrix}, \tag{3.14}$$

where $\mathbf{r}, \mathbf{r}', \mathbf{t}$ and $\mathbf{t}'$ are 3×3 matrix generalisations of transmission and reflection coefficients.

An alternative description of the scattering problem is possible using the transfer matrix $\mathbf{M}$, which relates the amplitudes of plane waves on the left and right hand

side of the medium. Letting

$$\mathbf{L}(\boldsymbol{\kappa}) = [\mathbf{a}^{-}(\boldsymbol{\kappa}), \mathbf{b}^{-}(\boldsymbol{\kappa})]^{\mathrm{T}}, \tag{3.15}$$

$$\mathbf{R}(\boldsymbol{\kappa}) = [\mathbf{a}^{+}(\boldsymbol{\kappa}), \mathbf{b}^{+}(\boldsymbol{\kappa})]^{\mathrm{T}}, \tag{3.16}$$

the continuous transfer matrix $\mathbf{M}$ is defined to be the matrix that satisfies

$$\mathbf{R}(\boldsymbol{\kappa}) = \int \mathbf{M}(\boldsymbol{\kappa}, \boldsymbol{\kappa}')\mathbf{L}(\boldsymbol{\kappa}')\mathrm{d}\boldsymbol{\kappa}'. \tag{3.17}$$

As with the scattering matrix, it is useful to write the transfer matrix as a 2×2 block matrix in the form

$$\mathbf{M}(\boldsymbol{\kappa}, \boldsymbol{\kappa}') = \begin{pmatrix} \boldsymbol{\alpha}(\boldsymbol{\kappa}, \boldsymbol{\kappa}') & \boldsymbol{\beta}(\boldsymbol{\kappa}, \boldsymbol{\kappa}') \\ \boldsymbol{\gamma}(\boldsymbol{\kappa}, \boldsymbol{\kappa}') & \boldsymbol{\delta}(\boldsymbol{\kappa}, \boldsymbol{\kappa}') \end{pmatrix}. \tag{3.18}$$

Unlike the scattering matrix, however, the sub-matrices $\boldsymbol{\alpha}, \boldsymbol{\beta}, \boldsymbol{\gamma}$ and $\boldsymbol{\delta}$, do not have obvious physical interpretations.

3.2.2 Energy conservation

In this section we shall consider the constraints placed upon the scattering and transfer matrices by energy conservation. We shall proceed by outlining the derivation of the constraints for the scattering matrix and then presenting the final result for the transfer matrix without its corresponding derivation. Ultimately, the differences between the two derivations are purely algebraic, and there is little additional insight to be gained by working through both derivations. To expand upon a point made earlier in this chapter, while the scattering matrix is more physically intuitive, the transfer matrix, as shall be seen in Chapter 6, can be more convenient for numerical calculations. It is thus worthwhile to examine the constraints imposed upon both matrices, and both shall be given in this chapter.

In classical electromagnetism, the energy carried by an electromagnetic wave is described by the Poynting vector, which we denote by $\mathbf{P}(\mathbf{r}, t)$. At optical frequencies, the Poynting vector is a rapidly oscillating function of time that most instruments are incapable of following. It is thus more common to use the time averaged Ponyting

vector $\langle \mathbf{P}(\mathbf{r}) \rangle$, where the time interval used in the averaging is assumed to be large compared to $1/\omega$ [1].

For time harmonic fields, the Poynting vector is given by [1]

$$\langle \mathbf{P}(\mathbf{r}) \rangle = \frac{1}{2} \mathrm{Re}[\mathbf{E}(\mathbf{r}) \times \mathbf{H}^*(\mathbf{r})]. \tag{3.19}$$

This can be calculated using the angular spectra given in Eqs. (3.6) and (3.10) for the electric and magnetic fields, although care is necessary in handling the complex conjugate of $\mathbf{H}$ due to the presence of evanescent waves, which change the nature of the exponential terms appearing in Eq. (3.10). We find that

$$\begin{aligned}
\langle \mathbf{P}^{\pm}(\mathbf{r}) \rangle = \frac{1}{2\omega\mu_0} \mathrm{Re} \Bigg[& \int\!\!\int_{\boldsymbol{\kappa} \in \Gamma_p} \Big(\mathbf{a}^{\pm}(\boldsymbol{\kappa}') \times \mathbf{k} \times \mathbf{a}^{\pm *}(\boldsymbol{\kappa}) e^{i(\gamma' - \gamma)z} \\
& + \mathbf{a}^{\pm}(\boldsymbol{\kappa}') \times \widetilde{\mathbf{k}} \times \mathbf{b}^{\pm *}(\boldsymbol{\kappa}) e^{i(\gamma' + \gamma)z} \\
& + \mathbf{b}^{\pm}(\boldsymbol{\kappa}') \times \mathbf{k} \times \mathbf{a}^{\pm *}(\boldsymbol{\kappa}) e^{-i(\gamma + \gamma')z} \\
& + \mathbf{b}^{\pm}(\boldsymbol{\kappa}') \times \widetilde{\mathbf{k}} \times \mathbf{b}^{\pm *}(\boldsymbol{\kappa}) e^{i(\gamma - \gamma')z} \Big) e^{i(\boldsymbol{\kappa}' - \boldsymbol{\kappa}) \cdot \boldsymbol{\rho}} \mathrm{d}\boldsymbol{\kappa} \mathrm{d}\boldsymbol{\kappa}' \\
+ & \int\!\!\int_{\boldsymbol{\kappa} \in \Gamma_e} \Big(\mathbf{a}^{\pm}(\boldsymbol{\kappa}') \times \widetilde{\mathbf{k}} \times \mathbf{a}^{\pm *}(\boldsymbol{\kappa}) e^{i(\gamma' + \gamma)z} \\
& + \mathbf{a}^{\pm}(\boldsymbol{\kappa}') \times \mathbf{k} \times \mathbf{b}^{\pm *}(\boldsymbol{\kappa}) e^{i(\gamma' - \gamma)z} \\
& + \mathbf{b}^{\pm}(\boldsymbol{\kappa}') \times \widetilde{\mathbf{k}} \times \mathbf{a}^{\pm *}(\boldsymbol{\kappa}) e^{i(\gamma - \gamma')z} \\
& + \mathbf{b}^{\pm}(\boldsymbol{\kappa}') \times \mathbf{k} \times \mathbf{b}^{\pm *}(\boldsymbol{\kappa}) e^{-i(\gamma + \gamma')z} \Big) e^{i(\boldsymbol{\kappa}' - \boldsymbol{\kappa}) \cdot \boldsymbol{\rho}} \mathrm{d}\boldsymbol{\kappa} \mathrm{d}\boldsymbol{\kappa}' \Bigg].
\end{aligned} \tag{3.20}$$

We point out that for both terms in Eq. (3.20) the integration domain for $\boldsymbol{\kappa}$ is restricted. The transverse wavevector $\boldsymbol{\kappa}'$, however, is free to vary over all of $\mathbb{R}^2$.

In order to discuss the flow of energy into and out of the scattering medium, it is necessary to choose a surface over which the Poynting vector can be integrated. Generally speaking, the average net rate W at which electromagnetic energy flows out of any closed surface Ω is given by [19]

$$W = \int_{\Omega} \langle \mathbf{P} \rangle \cdot \hat{\mathbf{n}} \, \mathrm{d}A, \tag{3.21}$$

where $\hat{\mathbf{n}}$ is the outward unit normal vector to the surface and $\mathrm{d}A$ is the infinitesimal

area element. If energy is not absorbed within the volume enclosed by the surface, then $W = 0$ by energy conservation and the integral in Eq. (3.21) must vanish.

Suppose now that Ω is taken to be the surface ∂V shown in Figure 3.1 bounding the volume V. The volume V is the intersection of a slab $z^- < z < z^+$, where $z^- \in \mathcal{R}^-$ and $z^+ \in \mathcal{R}^+$, and a spherical volume of radius R centred at the origin whose interior contains the scattering medium. The surface ∂V therefore consists of several parts: two planar sections at the fixed z coordinates $z = z^-$ and $z = z^+$, and a spherical section of radius R in between the two planar sections. We suppose that the scattering medium is of finite size characterised by length scale a and that $R \gg a$, so that the surface of the sphere lies far from the scattering medium. On the spherical section of ∂V, the electric and magnetic fields can be expressed as superpositions of incoming and outgoing spherical waves [27], i.e.

$$\mathbf{E}(\mathbf{r}) = \mathbf{E}^{in}(\hat{\mathbf{r}})\frac{e^{-ikR}}{R} + \mathbf{E}^{out}(\hat{\mathbf{r}})\frac{e^{ikR}}{R}, \tag{3.22}$$

$$\mathbf{H}(\mathbf{r}) = \mathbf{H}^{in}(\hat{\mathbf{r}})\frac{e^{-ikR}}{R} + \mathbf{H}^{out}(\hat{\mathbf{r}})\frac{e^{ikR}}{R}, \tag{3.23}$$

where $\mathbf{E}^{in}, \mathbf{E}^{out}, \mathbf{H}^{in}$ and $\mathbf{H}^{out}$ are all independent of R. It is thus straightforward by inspecting Eqs. (3.22) and (3.23) to see that the the amplitude of the Poynting vector in the far field decays as $\sim 1/R^2$. The surface area of the spherical section of ∂V, however, is equal to πLR, which grows linearly in R. Therefore, the integral of the Poynting vector over the spherical section of ∂V decays as $\sim 1/R$, which means the energy flow becomes negligible in the limit $R \to \infty$. In Eq. (3.21), it is thus only necessary to integrate over the planar sections of ∂R, which expand to infinite planes as $R \to \infty$. The total energy flow can thus be written as

$$W = W^+ + W^- = \int_{z=z^+} \langle \mathbf{P}^+(\mathbf{r}) \rangle \cdot \hat{\mathbf{z}} \, \mathrm{d}\boldsymbol{\rho} - \int_{z=z^-} \langle \mathbf{P}^-(\mathbf{r}) \rangle \cdot \hat{\mathbf{z}} \, \mathrm{d}\boldsymbol{\rho}, \tag{3.24}$$

where $\mathrm{d}\boldsymbol{\rho} = \mathrm{d}x\mathrm{d}y$ and the second term obtains a negative sign due to the orientation of $\hat{\mathbf{n}}$.

Since, in deriving Eq. (3.24), we take the limit $R \to \infty$, the preceding argument that allowed us to neglect contributions on the spherical caps of ∂V can be applied to arbitrarily large scattering media. We note that in reality, particularly as any

realistic illumination beam will be finite in transverse extent, a scattering medium that is 'practically infinite' is one for which the transverse extent is far greater than the lateral thickness L.

For simplicity, consider the first integral in Eq. (3.24) over the plane $z = z^+$ and, for ease of notation, let us temporarily drop superscripts so that $\mathbf{S} = \mathbf{S}^+$, $\mathbf{a} = \mathbf{a}^+$ and $\mathbf{b} = \mathbf{b}^+$. We wish to insert the expression for $\langle \mathbf{P} \rangle$ as given by Eq. (3.20) into this integral. Inspecting the form of Eq. (3.20), we see that the only dependence of $\langle \mathbf{S} \rangle$ on $\boldsymbol{\rho}$ is in the term $e^{i(\boldsymbol{\kappa}' - \boldsymbol{\kappa})\cdot\boldsymbol{\rho}}$. This can be integrated over the plane using the identity [222]

$$\int_{\mathbb{R}^2} e^{i(\boldsymbol{\kappa}' - \boldsymbol{\kappa})\cdot\boldsymbol{\rho}} \mathrm{d}\boldsymbol{\rho} = (2\pi)^2 \delta(\boldsymbol{\kappa}' - \boldsymbol{\kappa}), \tag{3.25}$$

where δ is the Dirac delta function and $\delta(\boldsymbol{\kappa}' - \boldsymbol{\kappa}) = \delta(k'_x - k_x)\delta(k'_y - k_y)$. The integral over $\boldsymbol{\kappa}'$ in Eq. (3.20) is eliminated by this delta function, which enforces the identity $\boldsymbol{\kappa}' = \boldsymbol{\kappa}$, from which it also follows that $\gamma' = \gamma$. We thus find, dropping now in our notation the dependence of $\mathbf{a}$ and $\mathbf{b}$ on $\boldsymbol{\kappa}$, that

$$\begin{aligned} W^+ = \frac{(2\pi)^2}{2\omega\mu_0} \mathrm{Re}\Bigg[& \int_{\Gamma_p} \Big(\mathbf{a} \times \mathbf{k} \times \mathbf{a}^* + \mathbf{b} \times \widetilde{\mathbf{k}} \times \mathbf{b}^* \\ & \qquad + \mathbf{a} \times \widetilde{\mathbf{k}} \times \mathbf{b}^* e^{2i\gamma z} + \mathbf{b} \times \mathbf{k} \times \mathbf{a}^* e^{-2i\gamma z} \Big) \cdot \hat{\mathbf{z}} \, \mathrm{d}\boldsymbol{\kappa} \\ + & \int_{\Gamma_e} \Big(\mathbf{a} \times \mathbf{k} \times \mathbf{b}^* + \mathbf{b} \times \widetilde{\mathbf{k}} \times \mathbf{a}^* \\ & \qquad + \mathbf{a} \times \widetilde{\mathbf{k}} \times \mathbf{a}^* e^{2i\gamma z} + \mathbf{b} \times \mathbf{k} \times \mathbf{b}^* e^{-2i\gamma z} \Big) \cdot \hat{\mathbf{z}} \, \mathrm{d}\boldsymbol{\kappa} \Bigg]. \end{aligned} \tag{3.26}$$

Consider the term $\mathbf{a} \times \mathbf{k} \times \mathbf{a}^*$ contained within the first integral of Eq. (3.26). This can be simplified using the identity [223]

$$\mathbf{a} \times \mathbf{b} \times \mathbf{c} = (\mathbf{a} \cdot \mathbf{c})\mathbf{b} - (\mathbf{a} \cdot \mathbf{b})\mathbf{c}, \tag{3.27}$$

which holds for any three vectors $\mathbf{a}$, $\mathbf{b}$ and $\mathbf{c}$. Using the fact that $\mathbf{a} \cdot \mathbf{k} = 0$, which follows straightforwardly from Eq. (3.1) and taking the divergence of Eq. (3.6), it is easy to show that

$$(\mathbf{a} \times \mathbf{k} \times \mathbf{a}^*) \cdot \hat{\mathbf{z}} = \Big(|\mathbf{a}|^2 \mathbf{k} - (\mathbf{a} \cdot \mathbf{k})\mathbf{a} \Big) \cdot \hat{\mathbf{z}} = |\mathbf{a}|^2 \gamma \tag{3.28}$$

is a real quantity. Similarly, we have $\mathbf{b} \cdot \widetilde{\mathbf{k}} = 0$, from which it follows that

$$(\mathbf{b} \times \widetilde{\mathbf{k}} \times \mathbf{b}^*) \cdot \hat{\mathbf{z}} = -|\mathbf{b}|^2 \gamma \tag{3.29}$$

is also a real quantity. In addition, it can also be shown that, for the first integral in Eq. (3.26)

$$\left(\mathbf{a} \times \widetilde{\mathbf{k}} \times \mathbf{b}^* e^{2i\gamma z} + \mathbf{b} \times \mathbf{k} \times \mathbf{a}^* e^{-2i\gamma z}\right) \cdot \hat{\mathbf{z}} = 2i\gamma \mathrm{Im}[(2a_z b_z^* - \mathbf{a} \cdot \mathbf{b}^*) e^{2i\gamma z}], \tag{3.30}$$

which, importantly, is an imaginary quantity. Note that Im denotes the imaginary part of a complex quantity. In deriving Eq. (3.30), it is necessary to make use of the fact that $\mathbf{a} \cdot \widetilde{\mathbf{k}} = -2a_z\gamma$ and $\mathbf{b} \cdot \mathbf{k} = 2b_z\gamma$, which also follow from the aforementioned divergence property. Thus, after taking the real part in Eq. (3.26), the integrand of first integral reduces to simply $\gamma(|\mathbf{a}|^2 - |\mathbf{b}|^2)$. Similar calculations can be performed for the second integral over evanescent components, ultimately leading to the result

$$W^+ = \frac{(2\pi)^2}{2\omega\mu_0} \left[\int_{\Gamma_p} \gamma(|\mathbf{a}|^2 - |\mathbf{b}|^2) \mathrm{d}\boldsymbol{\kappa} + \int_{\Gamma_e} \gamma(\mathbf{a} \cdot \mathbf{b}^* - \mathbf{a}^* \cdot \mathbf{b}) \mathrm{d}\boldsymbol{\kappa} \right]. \tag{3.31}$$

Returning to Eq. (3.24), we are now in a position to enforce energy conservation. If no energy is absorbed within the volume V, then $W = 0$. Using the result of Eq. (3.31) and reintroducing the appropriate superscripts, we find that energy conservation is equivalent to the condition

$$\begin{aligned} &\int_{\Gamma_p} \gamma \Big[|\mathbf{a}^-|^2 - |\mathbf{a}^+|^2 - (|\mathbf{b}^-|^2 - |\mathbf{b}^+|^2) \Big] \mathrm{d}\boldsymbol{\kappa} \\ &\quad + \int_{\Gamma_e} \gamma \Big[\mathbf{a}^- \cdot \mathbf{b}^{-*} - \mathbf{a}^+ \cdot \mathbf{b}^{+*} - (\mathbf{a}^{-*} \cdot \mathbf{b}^- - \mathbf{a}^{+*} \cdot \mathbf{b}^+) \Big] \mathrm{d}\boldsymbol{\kappa} = 0. \end{aligned} \tag{3.32}$$

An expression of energy conservation in terms of the scattering matrix can be obtained by recasting Eq. (3.32) in terms of $\mathbf{I}$ and $\mathbf{O}$ as defined in Eqs. (3.11) and (3.12). Doing so yields the equivalent equation

$$\int_{\Gamma_p} \gamma \Big[|\mathbf{I}(\boldsymbol{\kappa})|^2 - |\mathbf{O}(\boldsymbol{\kappa})|^2 \Big] \mathrm{d}\boldsymbol{\kappa} + \int_{\Gamma_e} \gamma \Big[\mathbf{I}(\boldsymbol{\kappa}) \cdot \mathbf{O}^*(\boldsymbol{\kappa}) - \mathbf{I}^*(\boldsymbol{\kappa}) \cdot \mathbf{O}(\boldsymbol{\kappa}) \Big] \mathrm{d}\boldsymbol{\kappa} = 0. \tag{3.33}$$

It's worth pointing out that Eq. (3.33) already has a simple physical interpretation.

In the absence of evanescent waves, only the first integral is relevant. This integral can be interpreted as being the difference between the total power flux into and out of the scattering medium in the z direction. For plane waves that graze the planar boundaries, for example, for which $\gamma \approx 0$, very little electromagnetic energy is transported in the z direction and their contribution to the integral is relatively small. Of course, if energy is conserved, then the power flux into and out of the medium are equal.

We now introduce the scattering matrix using Eq. (3.13). Moreover, we make use of the trivial fact that

$$\mathbf{I}(\boldsymbol{\kappa}) = \int \mathbf{I}(\boldsymbol{\kappa}')\delta(\boldsymbol{\kappa} - \boldsymbol{\kappa}')\mathrm{d}\boldsymbol{\kappa}', \tag{3.34}$$

which is the sifting property of the Dirac delta function. We shall at this point switch to matrix notation so that, for example $|\mathbf{I}(\boldsymbol{\kappa})|^2 = \mathbf{I}^\dagger(\boldsymbol{\kappa})\mathbf{I}(\boldsymbol{\kappa})$, $\mathbf{I}(\boldsymbol{\kappa}) \cdot \mathbf{O}^*(\boldsymbol{\kappa}) = \mathbf{O}^\dagger(\boldsymbol{\kappa})\mathbf{I}(\boldsymbol{\kappa})$ and so on, where $\dagger$ is the conjugate transpose. In addition, we define $\mathbf{I} = \mathbf{I}(\boldsymbol{\kappa})$, $\mathbf{I}' = \mathbf{I}(\boldsymbol{\kappa}')$, $\mathbf{I}'' = \mathbf{I}(\boldsymbol{\kappa}'')$ and similarly for $\mathbf{O}$, $\mathbf{O}'$, and $\mathbf{O}''$. Analysing each term of Eq. (3.33) individually, we find that

$$\int_{\Gamma_p} \gamma\, \mathbf{I}^\dagger \mathbf{I}\, \mathrm{d}\boldsymbol{\kappa} = \int\int\int_{\boldsymbol{\kappa}\in\Gamma_p} \gamma \mathbf{I}'^\dagger \Big[\mathbb{I}_6 \delta(\boldsymbol{\kappa} - \boldsymbol{\kappa}')\delta(\boldsymbol{\kappa} - \boldsymbol{\kappa}'')\Big] \mathbf{I}''^\dagger \mathrm{d}\boldsymbol{\kappa}\mathrm{d}\boldsymbol{\kappa}'\mathrm{d}\boldsymbol{\kappa}'', \tag{3.35}$$

$$\int_{\Gamma_p} \gamma\, \mathbf{O}^\dagger \mathbf{O}\, \mathrm{d}\boldsymbol{\kappa} = \int\int\int_{\boldsymbol{\kappa}\in\Gamma_p} \gamma \mathbf{I}'^\dagger \Big[\mathbf{S}^\dagger(\boldsymbol{\kappa}, \boldsymbol{\kappa}')\mathbf{S}(\boldsymbol{\kappa}, \boldsymbol{\kappa}'')\Big] \mathbf{I}''^\dagger \mathrm{d}\boldsymbol{\kappa}\mathrm{d}\boldsymbol{\kappa}'\mathrm{d}\boldsymbol{\kappa}'', \tag{3.36}$$

$$\int_{\Gamma_e} \gamma\, \mathbf{I}^\dagger \mathbf{O}\, \mathrm{d}\boldsymbol{\kappa} = \int\int\int_{\boldsymbol{\kappa}\in\Gamma_e} \gamma \mathbf{I}'^\dagger \Big[\delta(\boldsymbol{\kappa} - \boldsymbol{\kappa}')\mathbf{S}(\boldsymbol{\kappa}, \boldsymbol{\kappa}'')\Big] \mathbf{I}''^\dagger \mathrm{d}\boldsymbol{\kappa}\mathrm{d}\boldsymbol{\kappa}'\mathrm{d}\boldsymbol{\kappa}'', \tag{3.37}$$

$$\int_{\Gamma_e} \gamma\, \mathbf{O}^\dagger \mathbf{I}\, \mathrm{d}\boldsymbol{\kappa} = \int\int\int_{\boldsymbol{\kappa}\in\Gamma_e} \gamma \mathbf{I}'^\dagger \Big[\mathbf{S}^\dagger(\boldsymbol{\kappa}, \boldsymbol{\kappa}')\delta(\boldsymbol{\kappa} - \boldsymbol{\kappa}'')\Big] \mathbf{I}''^\dagger \mathrm{d}\boldsymbol{\kappa}\mathrm{d}\boldsymbol{\kappa}'\mathrm{d}\boldsymbol{\kappa}'', \tag{3.38}$$

where $\mathbb{I}_n$ denotes the $n \times n$ identity matrix. Eqs. (3.35)-(3.38) combine to give

$$\begin{aligned}
&\int\int \mathbf{I}'^\dagger \left[\int_{\Gamma_p} \gamma \mathbf{S}^\dagger(\boldsymbol{\kappa}, \boldsymbol{\kappa}')\mathbf{S}(\boldsymbol{\kappa}, \boldsymbol{\kappa}'')\mathrm{d}\boldsymbol{\kappa}\right] \mathbf{I}''\mathrm{d}\boldsymbol{\kappa}'\mathrm{d}\boldsymbol{\kappa}' \\
&\quad = \int\int \mathbf{I}'^\dagger \left[\int_{\Gamma_p} \gamma \mathbb{I}_6 \delta(\boldsymbol{\kappa} - \boldsymbol{\kappa}')\delta(\boldsymbol{\kappa} - \boldsymbol{\kappa}'')\mathrm{d}\boldsymbol{\kappa}\right. \\
&\qquad \left. + \int_{\Gamma_e} \gamma \Big(\mathbf{S}^\dagger(\boldsymbol{\kappa}, \boldsymbol{\kappa}')\delta(\boldsymbol{\kappa} - \boldsymbol{\kappa}'') - \mathbf{S}(\boldsymbol{\kappa}, \boldsymbol{\kappa}'')\delta(\boldsymbol{\kappa} - \boldsymbol{\kappa}')\Big)\mathrm{d}\boldsymbol{\kappa}\right] \mathbf{I}''\mathrm{d}\boldsymbol{\kappa}'\mathrm{d}\boldsymbol{\kappa}''.
\end{aligned} \tag{3.39}$$

In order for Eq. (3.39) to hold for all possible incident fields $\mathbf{I}'$ and $\mathbf{I}''$, it must be the case that the terms inside square brackets on either side of the equation are equal[1]. On the right hand side of the equation, the integrals over $\boldsymbol{\kappa}$ can be evaluated using the delta functions. Whether or not the delta functions evaluate to zero, however, depends on the relationship between $\boldsymbol{\kappa}$, $\boldsymbol{\kappa}'$ and $\boldsymbol{\kappa}''$. In total there are four cases, which are summarised in the final result

$$\int_{\Gamma_p} \gamma \mathbf{S}^\dagger(\boldsymbol{\kappa}, \boldsymbol{\kappa}') \mathbf{S}(\boldsymbol{\kappa}, \boldsymbol{\kappa}'') \, \mathrm{d}\boldsymbol{\kappa} = \begin{cases} \gamma' \delta(\boldsymbol{\kappa}' - \boldsymbol{\kappa}'') \mathbb{I}_6 & \text{if } \boldsymbol{\kappa}' \in \Gamma_p,\ \boldsymbol{\kappa}'' \in \Gamma_p, \\ \gamma'' \mathbf{S}^\dagger(\boldsymbol{\kappa}'', \boldsymbol{\kappa}') & \text{if } \boldsymbol{\kappa}' \in \Gamma_p,\ \boldsymbol{\kappa}'' \in \Gamma_e, \\ -\gamma' \mathbf{S}(\boldsymbol{\kappa}', \boldsymbol{\kappa}'') & \text{if } \boldsymbol{\kappa}' \in \Gamma_e,\ \boldsymbol{\kappa}'' \in \Gamma_p, \\ \gamma'' \mathbf{S}^\dagger(\boldsymbol{\kappa}'', \boldsymbol{\kappa}') - \gamma' \mathbf{S}(\boldsymbol{\kappa}', \boldsymbol{\kappa}'') & \text{if } \boldsymbol{\kappa}' \in \Gamma_e,\ \boldsymbol{\kappa}'' \in \Gamma_e. \end{cases} \tag{3.40}$$

Eq. (3.40), which collectively have been referred to as extended-unitarity relations [224], is the most general form of conservation of energy and includes both evanescent wave components and polarisation.

The transfer matrix can also be shown to obey a similar set of equations to Eq. (3.40). Returning to Eq. (3.32), we can use Eqs. (3.15) and (3.16) to write the integrands in the alternate form

$$\begin{aligned} \int_{\Gamma_p} \gamma \Big[\mathbf{L}^\dagger(\boldsymbol{\kappa}) \boldsymbol{\Sigma}_3^z \mathbf{L}(\boldsymbol{\kappa}) - \mathbf{R}^\dagger(\boldsymbol{\kappa}) \boldsymbol{\Sigma}_3^z \mathbf{R}(\boldsymbol{\kappa}) \Big] \, \mathrm{d}\boldsymbol{\kappa} \\ - \int_{\Gamma_e} i\gamma [\mathbf{L}^\dagger(\boldsymbol{\kappa}) \boldsymbol{\Sigma}_3^y \mathbf{L}(\boldsymbol{\kappa}) - \mathbf{R}^\dagger(\boldsymbol{\kappa}) \boldsymbol{\Sigma}_3^y \mathbf{R}(\boldsymbol{\kappa})] \, \mathrm{d}\boldsymbol{\kappa} = 0, \end{aligned} \tag{3.41}$$

where

$$\boldsymbol{\Sigma}_n^z = \begin{pmatrix} 1 & 0 \\ 0 & -1 \end{pmatrix} \otimes \mathbb{I}_n = \begin{pmatrix} \mathbb{I}_n & \mathbb{O}_n \\ \mathbb{O}_n & -\mathbb{I}_n \end{pmatrix}, \tag{3.42}$$

$$\boldsymbol{\Sigma}_n^y = i \begin{pmatrix} 0 & -1 \\ 1 & 0 \end{pmatrix} \otimes \mathbb{I}_n = i \begin{pmatrix} \mathbb{O}_n & -\mathbb{I}_n \\ \mathbb{I}_n & \mathbb{O}_n \end{pmatrix}, \tag{3.43}$$

are generalised Pauli matrices, $\otimes$ denotes the Kronecker product and $\mathbb{O}_n$ denotes

[1] This can be made more rigorous using an argument akin to the proof of the fundamental lemma of the calculus of variations.

the $n \times n$ zero matrix. Similarly to before, we can introduce the transfer matrix into Eq. (3.41) using Eq. (3.17). Performing a similar analysis to that used for the scattering matrix ultimately leads to the result

$$\begin{aligned}\int_{\Gamma_p} \gamma \mathbf{M}^\dagger(\boldsymbol{\kappa}, \boldsymbol{\kappa}'') \boldsymbol{\Sigma}_3^z \mathbf{M}(\boldsymbol{\kappa}, \boldsymbol{\kappa}') \, \mathrm{d}\boldsymbol{\kappa} - \int_{\Gamma_e} i\gamma \mathbf{M}^\dagger(\boldsymbol{\kappa}, \boldsymbol{\kappa}'') \boldsymbol{\Sigma}_3^y \mathbf{M}(\boldsymbol{\kappa}, \boldsymbol{\kappa}') \, \mathrm{d}\boldsymbol{\kappa} \\ = \begin{cases} \gamma' \delta(\boldsymbol{\kappa}' - \boldsymbol{\kappa}'') \boldsymbol{\Sigma}_3^z & \text{if } \boldsymbol{\kappa}' \in \Gamma_p, \, \boldsymbol{\kappa}'' \in \Gamma_p, \\ -i\gamma' \delta(\boldsymbol{\kappa}' - \boldsymbol{\kappa}'') \boldsymbol{\Sigma}_3^y & \text{if } \boldsymbol{\kappa}' \in \Gamma_e, \, \boldsymbol{\kappa}'' \in \Gamma_e, \\ \mathbb{O}_6 & \text{otherwise.} \end{cases}\end{aligned} \tag{3.44}$$

Eq. (3.44) is equivalent to Eq. (3.40) and expresses conservation of energy in terms of the transfer matrix.

3.2.3 Reciprocity

Reciprocity, as previously discussed in Chapter 2, is a type of symmetry related to the interchange of incoming and outgoing plane wave directions. In this section we shall explore its implications for the scattering and transfer matrices.

Consider again the volume V shown in Figure 3.1 and its bounding surface ∂V. Let $\mathbf{E}_1$ and $\mathbf{E}_2$ be two arbitrary fields that satisfy Maxwell's equations, i.e. Eqs. (3.1)-(3.4). Applying the vector analogue of Green's second identity to these two fields over the volume V gives [225]

$$\begin{aligned}\int_V \Big(\mathbf{E}_1 \cdot \nabla \times \nabla \times \mathbf{E}_2 - \mathbf{E}_2 \cdot \nabla \times \nabla \times \mathbf{E}_1 \Big) \, \mathrm{d}V \\ = \int_{\partial V} \Big(\mathbf{E}_2 \times \nabla \times \mathbf{E}_1 - \mathbf{E}_1 \times \nabla \times \mathbf{E}_2 \Big) \cdot \hat{\mathbf{n}} \, \mathrm{d}A,\end{aligned} \tag{3.45}$$

where $\mathrm{d}V$ is an infinitesimal volume element. It follows simply from the wave equation Eq. (3.5) that

$$\mathbf{E}_1 \cdot \nabla \times \nabla \times \mathbf{E}_2 - \mathbf{E}_2 \cdot \nabla \times \nabla \times \mathbf{E}_1 = \omega^2 \mu_0 \mathbf{E}_1^{\mathrm{T}} \Big(\epsilon(\mathbf{r}, \omega) - \epsilon^{\mathrm{T}}(\mathbf{r}, \omega) \Big) \mathbf{E}_2. \tag{3.46}$$

Therefore, in the case that ϵ is a symmetric matrix, i.e. $\epsilon(\mathbf{r}, \omega) = \epsilon^{\mathrm{T}}(\mathbf{r}, \omega)$, it follows that the integral over V in Eq. (3.45) is equal to zero. This can be taken to be the

case for the types of scattering media considered in this thesis [19].

As before, the integral over the boundary ∂V can be separated into several parts. Consider first the integral over the spherical section of ∂V. This contribution to the integral can be neglected using essentially the same argument as that used in Section 3.2.2. Assuming that R is large enough so that ∂V is in the far field of the scattering medium, we may express $\mathbf{E}_1$ and $\mathbf{E}_2$ as superpositions of incoming and outgoing spherical waves. Since $\nabla \times \mathbf{E}_i$ is, by Eq. (3.3), essentially equal to the corresponding magnetic field, it follows that the amplitude of $\mathbf{E}_j \times \nabla \times \mathbf{E}_i$ also scales as $\sim 1/R^2$ for large R. Therefore, the integral over the spherical section of ∂V scales as $\sim 1/R$, which is negligible in the limit $R \to \infty$. Overall, we find that the integral on the right hand side of Eq. (3.45) over the infinite planes is equal to zero. Expressing $\mathbf{E}_1$ and $\mathbf{E}_2$ as angular spectra, we find

$$\begin{aligned}\mathbf{E}_2 \times \nabla \times \mathbf{E}_1 = i \int\int \Big[& \mathbf{a}_2(\boldsymbol{\kappa}') \times \mathbf{k} \times \mathbf{a}_1(\boldsymbol{\kappa}) e^{i(\gamma+\gamma')z} \\ & + \mathbf{a}_2(\boldsymbol{\kappa}') \times \widetilde{\mathbf{k}} \times \mathbf{b}_1(\boldsymbol{\kappa}) e^{i(\gamma+\gamma')z} \\ & + \mathbf{b}_2(\boldsymbol{\kappa}') \times \mathbf{k} \times \mathbf{a}_1(\boldsymbol{\kappa}) e^{i(\gamma+\gamma')z} \\ & + \mathbf{b}_2(\boldsymbol{\kappa}') \times \widetilde{\mathbf{k}} \times \mathbf{b}_1(\boldsymbol{\kappa}) e^{i(\gamma+\gamma')z} \Big] e^{i(\boldsymbol{\kappa}+\boldsymbol{\kappa}')\cdot\boldsymbol{\rho}} \mathrm{d}\boldsymbol{\kappa} \mathrm{d}\boldsymbol{\kappa}',\end{aligned} \tag{3.47}$$

where we have again omitted for brevity the superscripts that denote the region in which the field is being described. As before, in integrating over the planes, the $e^{i(\boldsymbol{\kappa}+\boldsymbol{\kappa}')\cdot\boldsymbol{\rho}}$ term turns into a delta function, which reduces Eq. (3.47) to a single integral over $\boldsymbol{\kappa}$ while enforcing the constraint $\boldsymbol{\kappa}' = -\boldsymbol{\kappa}$, from which it follows that

$\gamma' = \gamma$. Hence,

$$\begin{aligned}
&\int_{\mathbb{R}^2} (\mathbf{E}_2 \times \nabla \times \mathbf{E}_1 - \mathbf{E}_1 \times \nabla \times \mathbf{E}_2) \cdot \hat{\mathbf{z}} \, \mathrm{d}A \\
&\quad = i \int \Big[e^{2i\gamma z} \Big(\mathbf{a}_2(-\boldsymbol{\kappa}) \times \mathbf{k} \times \mathbf{a}_1(\boldsymbol{\kappa}) - \mathbf{a}_1(-\boldsymbol{\kappa}) \times \mathbf{k} \times \mathbf{a}_2(\boldsymbol{\kappa}) \Big) \\
&\qquad + e^{-2i\gamma z} \Big(\mathbf{b}_2(-\boldsymbol{\kappa}) \times \widetilde{\mathbf{k}} \times \mathbf{b}_1(\boldsymbol{\kappa}) - \mathbf{b}_1(-\boldsymbol{\kappa}) \times \widetilde{\mathbf{k}} \times \mathbf{b}_2(\boldsymbol{\kappa}) \Big) \\
&\qquad\quad + \mathbf{a}_2(-\boldsymbol{\kappa}) \times \widetilde{\mathbf{k}} \times \mathbf{b}_1(\boldsymbol{\kappa}) - \mathbf{a}_1(-\boldsymbol{\kappa}) \times \widetilde{\mathbf{k}} \times \mathbf{b}_2(\boldsymbol{\kappa}) \\
&\qquad\quad + \mathbf{b}_2(-\boldsymbol{\kappa}) \times \mathbf{k} \times \mathbf{a}_1(\boldsymbol{\kappa}) - \mathbf{b}_1(-\boldsymbol{\kappa}) \times \mathbf{k} \times \mathbf{a}_2(\boldsymbol{\kappa}) \Big] \cdot \hat{\mathbf{z}} \, \mathrm{d}\boldsymbol{\kappa}.
\end{aligned} \tag{3.48}$$

After a bit of algebra, we find that

$$\begin{aligned}
&e^{2i\gamma z} \Big(\mathbf{a}_2(-\boldsymbol{\kappa}) \times \mathbf{k} \times \mathbf{a}_1(\boldsymbol{\kappa}) - \mathbf{a}_1(-\boldsymbol{\kappa}) \times \mathbf{k} \times \mathbf{a}_2(\boldsymbol{\kappa}) \Big) \cdot \hat{\mathbf{z}} \\
&\quad = e^{2i\gamma z} \Big(\mathbf{a}_1(\boldsymbol{\kappa}) \cdot \mathbf{a}_2(-\boldsymbol{\kappa}) - \mathbf{a}_2(\boldsymbol{\kappa}) \cdot \mathbf{a}_1(-\boldsymbol{\kappa}) + 2a_z(-\boldsymbol{\kappa}) - 2a_z(\boldsymbol{\kappa}) \Big),
\end{aligned} \tag{3.49}$$

which is an odd function of $\boldsymbol{\kappa}$ and thus does not contribute to the integral. An analogous argument applies to the term in Eq. (3.48) containing the $e^{-2i\gamma z}$ factor. Simplifying the remaining two terms leads to the equation $I_{z^-} = I_{z^+}$, where

$$\begin{aligned}
I_{z^\pm} = \int \gamma [&\mathbf{a}_1^\pm(\boldsymbol{\kappa}) \cdot \mathbf{b}_2^\pm(-\boldsymbol{\kappa}) + \mathbf{a}_1^\pm(-\boldsymbol{\kappa}) \cdot \mathbf{b}_2^\pm(\boldsymbol{\kappa}) \\
&- \mathbf{a}_2^\pm(\boldsymbol{\kappa}) \cdot \mathbf{b}_1^\pm(-\boldsymbol{\kappa}) - \mathbf{a}_2^\pm(-\boldsymbol{\kappa}) \cdot \mathbf{b}_1^\pm(\boldsymbol{\kappa})] \mathrm{d}\boldsymbol{\kappa}.
\end{aligned} \tag{3.50}$$

In terms of $\mathbf{I}$ and $\mathbf{O}$, the equation $I_{z^-} = I_{z^+}$ becomes

$$\int \gamma [\mathbf{I}_1(\boldsymbol{\kappa}) \cdot \mathbf{O}_2(-\boldsymbol{\kappa}) - \mathbf{I}_2(\boldsymbol{\kappa}) \cdot \mathbf{O}_1(-\boldsymbol{\kappa})] \mathrm{d}\boldsymbol{\kappa} = 0. \tag{3.51}$$

Expressing $\mathbf{O}$ in terms of the scattering matrix, Eq. (3.51) becomes

$$\int \int \gamma \Big[\mathbf{I}_1^{\mathrm{T}} \mathbf{S}(-\boldsymbol{\kappa}, \boldsymbol{\kappa}') \mathbf{I}_2' - \mathbf{I}_1'^{\mathrm{T}} \mathbf{S}^{\mathrm{T}}(-\boldsymbol{\kappa}, \boldsymbol{\kappa}') \mathbf{I}_2 \Big] \mathrm{d}\boldsymbol{\kappa} \mathrm{d}\boldsymbol{\kappa}' = 0. \tag{3.52}$$

Finally, we make the change of variables[2] $\boldsymbol{\kappa} \leftrightarrow \boldsymbol{\kappa}'$ on the second term in the integral

[2] This is possible as $\boldsymbol{\kappa}$ and $\boldsymbol{\kappa}'$ are dummy variables from the point of view of the integral.

in Eq. (3.52), giving

$$\int\int \mathbf{I}_1^{\mathrm{T}}\Big[\gamma\mathbf{S}(-\boldsymbol{\kappa},\boldsymbol{\kappa}') - \gamma'\mathbf{S}^{\mathrm{T}}(-\boldsymbol{\kappa}',\boldsymbol{\kappa})\Big]\mathbf{I}_2'\mathrm{d}\boldsymbol{\kappa}\mathrm{d}\boldsymbol{\kappa}' = 0. \tag{3.53}$$

Since Eq. (3.53) must hold for all $\mathbf{I}_1$ and $\mathbf{I}_2$, it follows after a slight relabelling of the variables that

$$\gamma\mathbf{S}(\boldsymbol{\kappa},\boldsymbol{\kappa}') = \gamma'\mathbf{S}^{\mathrm{T}}(-\boldsymbol{\kappa}',-\boldsymbol{\kappa}), \tag{3.54}$$

which is the reciprocity theorem for the scattering matrix. Reciprocity relations for the constituent transmission and reflection matrices can be obtained by considering the block form of the scattering matrix as shown in Eq. (3.14). Comparing blocks on either side of Eq. (3.54), we obtain

$$\gamma\mathbf{r}(\boldsymbol{\kappa},\boldsymbol{\kappa}') = \gamma'\mathbf{r}^{\mathrm{T}}(-\boldsymbol{\kappa}',-\boldsymbol{\kappa}), \tag{3.55}$$

$$\gamma\mathbf{r}'(\boldsymbol{\kappa},\boldsymbol{\kappa}') = \gamma'\mathbf{r}'^{\mathrm{T}}(-\boldsymbol{\kappa}',-\boldsymbol{\kappa}), \tag{3.56}$$

$$\gamma\mathbf{t}(\boldsymbol{\kappa}',\boldsymbol{\kappa}') = \gamma'\mathbf{t}'^{\mathrm{T}}(-\boldsymbol{\kappa}',-\boldsymbol{\kappa}). \tag{3.57}$$

These equations are consistent with those previously reported for a radiating point dipole source [226], but apply to fields with arbitrary incident angular spectra.

To derive the corresponding reciprocity constraint for the transfer matrix, we instead write Eq. (3.51) in terms of $\mathbf{L}$ and $\mathbf{R}$, which gives

$$\int \gamma[\mathbf{L}_1^{\mathrm{T}}(\boldsymbol{\kappa})\boldsymbol{\Sigma}_3^y\mathbf{L}_2(-\boldsymbol{\kappa}) - \mathbf{R}_1^{\mathrm{T}}(\boldsymbol{\kappa})\boldsymbol{\Sigma}_3^y\mathbf{R}_2(-\boldsymbol{\kappa})]\mathrm{d}\boldsymbol{\kappa} = 0. \tag{3.58}$$

Now, introducing the transfer matrix using Eq. (3.17), and, making use of the trivial fact that

$$\mathbf{L}(\boldsymbol{\kappa}) = \int \mathbf{L}(\boldsymbol{\kappa}')\delta(\boldsymbol{\kappa}-\boldsymbol{\kappa}')\mathrm{d}\boldsymbol{\kappa}'. \tag{3.59}$$

we find that Eq. (3.58) becomes

$$\int\int \mathbf{L}_1'^{\mathrm{T}}\left[\gamma'\delta(\boldsymbol{\kappa}'+\boldsymbol{\kappa}'')\boldsymbol{\Sigma}_3^y - \int \gamma\mathbf{M}^{\mathrm{T}}(\boldsymbol{\kappa},\boldsymbol{\kappa}')\boldsymbol{\Sigma}_3^y\mathbf{M}(-\boldsymbol{\kappa},\boldsymbol{\kappa}'')\mathrm{d}\boldsymbol{\kappa}\right]\mathbf{L}_2''\mathrm{d}\boldsymbol{\kappa}'\mathrm{d}\boldsymbol{\kappa}'' = 0. \tag{3.60}$$

Finally, since Eq. (3.60) must hold for all $\mathbf{L}_1$ and $\mathbf{L}_2$, it follows that

$$\int \gamma\mathbf{M}^{\mathrm{T}}(\boldsymbol{\kappa},\boldsymbol{\kappa}')\boldsymbol{\Sigma}_3^y\mathbf{M}(-\boldsymbol{\kappa},\boldsymbol{\kappa}'')\mathrm{d}\boldsymbol{\kappa} = \gamma'\delta(\boldsymbol{\kappa}'+\boldsymbol{\kappa}'')\boldsymbol{\Sigma}_3^y, \tag{3.61}$$

which is the reciprocity relation for the transfer matrix.

3.2.4 Time reversal symmetry

In this section we consider time reversal symmetry, which describes an invariance of the scattering and transfer matrices under the transformation $t \to -t$. To begin, let $\mathcal{E}_1(\mathbf{r},t)$ be an arbitrary, real valued electric field. Since $\mathcal{E}_1$ is real, $\mathcal{E}_1 = \mathcal{E}_1^*$. In terms of its Fourier transform $\mathbf{E}_1$, we have

$$\mathcal{E}_1(\mathbf{r},t) = \int_{-\infty}^{\infty}\mathbf{E}_1(\mathbf{r},\omega)e^{-i\omega t}\mathrm{d}\omega = \int_{-\infty}^{\infty}\mathbf{E}_1^*(\mathbf{r},\omega)e^{i\omega t}\mathrm{d}\omega = \int_{-\infty}^{\infty}\mathbf{E}_1^*(\mathbf{r},-\omega)e^{-i\omega t}\mathrm{d}\omega. \tag{3.62}$$

where the final integral follows from the penultimate one by making the change of variables $\omega \to -\omega$. Comparing the leftmost and rightmost integrals, it's clear that $\mathbf{E}_1(\mathbf{r},\omega) = \mathbf{E}_1^*(\mathbf{r},-\omega)$. Manipulating the Fourier integral for the time reversed field $\mathcal{E}_2(\mathbf{r},t) = \mathcal{E}_1(\mathbf{r},-t)$ leads to

$$\mathcal{E}_1(\mathbf{r},-t) = \int_{-\infty}^{\infty}\mathbf{E}_1(\mathbf{r},\omega)e^{i\omega t}\mathrm{d}\omega = \int_{-\infty}^{\infty}\mathbf{E}_1(\mathbf{r},-\omega)e^{-i\omega t}\mathrm{d}\omega = \int_{-\infty}^{\infty}\mathbf{E}_1^*(\mathbf{r},\omega)e^{-i\omega t}\mathrm{d}\omega. \tag{3.63}$$

In Eq. (3.63), the second integral follows from the first by again making the change of variables $\omega \to -\omega$. Comparing the first integral of Eq. (3.62) with the final one of Eq. (3.63), we can conclude that the frequency spectrum of the time reversed field is the complex conjugate of the frequency spectrum of the original field, i.e.

$\mathbf{E}_2(\mathbf{r},\omega) = \mathbf{E}_1^*(\mathbf{r},\omega)$. Suppose now that the fields are again time harmonic with frequency ω. Using the same variables as in Eq. (3.6), the angular spectrum of the complex representation of the time reversed field is given by

$$\begin{aligned}\mathbf{E}_2^{\pm}(\mathbf{r}) &= \int \left[\mathbf{a}_2^{\pm *}(\boldsymbol{\kappa})e^{-i\gamma^* z} + \mathbf{b}_2^{\pm *}(\boldsymbol{\kappa})e^{i\gamma^* z}\right] e^{-i\boldsymbol{\kappa}\cdot\boldsymbol{\rho}}\mathrm{d}\boldsymbol{\kappa} \\ &= \int \left[\mathbf{a}_2^{\pm *}(-\boldsymbol{\kappa})e^{-i\gamma^* z} + \mathbf{b}_2^{\pm *}(-\boldsymbol{\kappa})e^{i\gamma^* z}\right] e^{i\boldsymbol{\kappa}\cdot\boldsymbol{\rho}}\mathrm{d}\boldsymbol{\kappa},\end{aligned} \tag{3.64}$$

where the second line follows from the first by the change of variables $\boldsymbol{\kappa} \to -\boldsymbol{\kappa}$. Comparing Eqs. (3.6) and (3.64), it can be seen that the effect of time reversal is to make the transformation

$$\mathbf{a}^{\pm}(\boldsymbol{\kappa})e^{i\gamma z} + \mathbf{b}^{\pm}(\boldsymbol{\kappa})e^{-i\gamma z} \to \mathbf{a}^{\pm *}(-\boldsymbol{\kappa})e^{-i\gamma^* z} + \mathbf{b}^{\pm *}(-\boldsymbol{\kappa})e^{i\gamma^* z} \tag{3.65}$$

in the angular spectrum. Therefore, if the subscript 1 denotes the original field, we have

$$\mathbf{a}_2^{\pm}(\boldsymbol{\kappa})e^{i\gamma z} + \mathbf{b}_2^{\pm}(\boldsymbol{\kappa})e^{-i\gamma z} = \mathbf{a}_1^{\pm *}(-\boldsymbol{\kappa})e^{-i\gamma^* z} + \mathbf{b}_1^{\pm *}(-\boldsymbol{\kappa})e^{i\gamma^* z}. \tag{3.66}$$

Suppose now that $\boldsymbol{\kappa} \in \Gamma_p$. Since γ is real, $\gamma = \gamma^*$ and the complex conjugates within the exponentials in Eq. (3.66) can be ignored. Since the equality must hold for all values of z, we may equate the coefficients of the complex exponentials, giving

$$\mathbf{a}_2^{\pm}(\boldsymbol{\kappa}) = \mathbf{b}_1^{\pm *}(-\boldsymbol{\kappa}), \tag{3.67}$$

$$\mathbf{b}_2^{\pm}(\boldsymbol{\kappa}) = \mathbf{a}_1^{\pm *}(-\boldsymbol{\kappa}). \tag{3.68}$$

If, on the other hand, $\boldsymbol{\kappa} \in \Gamma_e$, then $\gamma = i|\gamma|$ is imaginary and we have $i\gamma = -|\gamma|$ and $i\gamma^* = |\gamma|$. Eq. (3.66) hence becomes

$$\mathbf{a}_2^{\pm}(\boldsymbol{\kappa})e^{-|\gamma| z} + \mathbf{b}_2^{\pm}(\boldsymbol{\kappa})e^{|\gamma| z} = \mathbf{a}_1^{\pm *}(-\boldsymbol{\kappa})e^{-|\gamma| z} + \mathbf{b}_1^{\pm *}(-\boldsymbol{\kappa})e^{|\gamma| z}. \tag{3.69}$$

Equating terms on either side leads to the equations

$$\mathbf{a}_2^{\pm}(\boldsymbol{\kappa}) = \mathbf{a}_1^{\pm *}(-\boldsymbol{\kappa}), \tag{3.70}$$

$$\mathbf{b}_2^{\pm}(\boldsymbol{\kappa}) = \mathbf{b}_1^{\pm *}(-\boldsymbol{\kappa}). \tag{3.71}$$

In terms of the scattering matrix, a system is time reversal invariant if both $\mathbf{E}_1$ and $\mathbf{E}_2$ satisfy Eq. (3.13) for the same scattering matrix $\mathbf{S}$. We therefore have

$$\mathbf{O}_2(\boldsymbol{\kappa}) = \int \mathbf{S}(\boldsymbol{\kappa}, \boldsymbol{\kappa}')\mathbf{I}_2(\boldsymbol{\kappa}')\mathrm{d}\boldsymbol{\kappa}, \tag{3.72}$$

where $\mathbf{I}_2$ and $\mathbf{O}_2$ contain the components for the time reversed field. Suppose first that $\boldsymbol{\kappa} \in \Gamma_p$. Using the above results, Eq. (3.72) becomes

$$\mathbf{I}_1^*(-\boldsymbol{\kappa}) = \int_{\Gamma_p} \mathbf{S}(\boldsymbol{\kappa}, \boldsymbol{\kappa}')\mathbf{O}_1^*(-\boldsymbol{\kappa}')\mathrm{d}\boldsymbol{\kappa}' + \int_{\Gamma_e} \mathbf{S}(\boldsymbol{\kappa}, \boldsymbol{\kappa}')\mathbf{I}_1^*(-\boldsymbol{\kappa}')\mathrm{d}\boldsymbol{\kappa}'. \tag{3.73}$$

Using again the definition of the scattering matrix, Eq. (3.73) can be put in the form

$$\begin{aligned}\int \Big[\delta(\boldsymbol{\kappa}'' + \boldsymbol{\kappa}')\mathbb{I}_6\Big]\mathbf{I}_1^*(\boldsymbol{\kappa}'')\mathrm{d}\boldsymbol{\kappa}'' = &\int \Big[\int_{\Gamma_p} \mathbf{S}(\boldsymbol{\kappa}, \boldsymbol{\kappa}')\mathbf{S}^*(-\boldsymbol{\kappa}', \boldsymbol{\kappa}'')\mathrm{d}\boldsymbol{\kappa}'\Big]\mathbf{I}_1^*(\boldsymbol{\kappa}'')\mathrm{d}\boldsymbol{\kappa}'' \\ &+ \int \Big[\int_{\Gamma_e} \mathbf{S}(\boldsymbol{\kappa}, \boldsymbol{\kappa}')\delta(\boldsymbol{\kappa}'' + \boldsymbol{\kappa}')\mathrm{d}\boldsymbol{\kappa}'\Big]\mathbf{I}_1^*(\boldsymbol{\kappa}'')\mathrm{d}\boldsymbol{\kappa}''.\end{aligned} \tag{3.74}$$

Since Eq. (3.74) must hold for all $\mathbf{I}_1$, terms within the square brackets can be equated. As before, however, different cases must be considered. For example, if $\boldsymbol{\kappa}'' \in \Gamma_p$ then the final term of Eq. (3.74) vanishes, as the argument of the delta function cannot be zero, since $\boldsymbol{\kappa}' \in \Gamma_e$ as dictated by the domain of integration. Analysis of all possible cases, including when $\boldsymbol{\kappa} \in \Gamma_e$, leads to the final result

$$\int_{\Gamma_p} \mathbf{S}(\boldsymbol{\kappa}', \boldsymbol{\kappa})\mathbf{S}^*(-\boldsymbol{\kappa}, \boldsymbol{\kappa}'')\,\mathrm{d}\boldsymbol{\kappa} = \begin{cases} \delta(\boldsymbol{\kappa}' + \boldsymbol{\kappa}'')\mathbb{I}_6 & \text{if } \boldsymbol{\kappa}' \in \Gamma_p,\ \boldsymbol{\kappa}'' \in \Gamma_p, \\ -\mathbf{S}(\boldsymbol{\kappa}', -\boldsymbol{\kappa}'') & \text{if } \boldsymbol{\kappa}' \in \Gamma_p,\ \boldsymbol{\kappa}'' \in \Gamma_e, \\ \mathbf{S}^*(-\boldsymbol{\kappa}', \boldsymbol{\kappa}'') & \text{if } \boldsymbol{\kappa}' \in \Gamma_e,\ \boldsymbol{\kappa}'' \in \Gamma_p, \\ -\mathbf{S}(\boldsymbol{\kappa}', -\boldsymbol{\kappa}'') + \mathbf{S}^*(-\boldsymbol{\kappa}', \boldsymbol{\kappa}'') & \text{if } \boldsymbol{\kappa}' \in \Gamma_e,\ \boldsymbol{\kappa}'' \in \Gamma_e, \end{cases} \tag{3.75}$$

which is an expression of time reversal symmetry for the scattering matrix.

A completely analogous argument can be made instead for the transfer matrix. If the system is time reversal invariant, then both $\mathbf{E}_1$ and $\mathbf{E}_2$ satisfy Eq. (3.17) for the same scattering matrix $\mathbf{M}$. The final result is that

$$\mathbf{M}(\boldsymbol{\kappa}', \boldsymbol{\kappa}'') = \begin{cases} \boldsymbol{\Sigma}_3^x \mathbf{M}^*(-\boldsymbol{\kappa}', -\boldsymbol{\kappa}'') \boldsymbol{\Sigma}_3^x & \text{if } \boldsymbol{\kappa}' \in \Gamma_p,\ \boldsymbol{\kappa}'' \in \Gamma_p, \\ \boldsymbol{\Sigma}_3^x \mathbf{M}^*(-\boldsymbol{\kappa}', -\boldsymbol{\kappa}'') & \text{if } \boldsymbol{\kappa}' \in \Gamma_p,\ \boldsymbol{\kappa}'' \in \Gamma_e, \\ \mathbf{M}^*(-\boldsymbol{\kappa}', -\boldsymbol{\kappa}'') \boldsymbol{\Sigma}_3^x & \text{if } \boldsymbol{\kappa}' \in \Gamma_e,\ \boldsymbol{\kappa}'' \in \Gamma_p, \\ \mathbf{M}^*(-\boldsymbol{\kappa}', -\boldsymbol{\kappa}'') & \text{if } \boldsymbol{\kappa}' \in \Gamma_e,\ \boldsymbol{\kappa}'' \in \Gamma_e, \end{cases} \tag{3.76}$$

where

$$\boldsymbol{\Sigma}_n^x = \begin{pmatrix} 0 & 1 \\ 1 & 0 \end{pmatrix} \otimes \mathbb{I}_n = \begin{pmatrix} \mathbb{O}_n & \mathbb{I}_n \\ \mathbb{I}_n & \mathbb{O}_n \end{pmatrix}. \tag{3.77}$$

Eq. (3.76) is therefore the time reversal symmetry constraint for the transfer matrix.

To conclude this section, we note that reciprocity and time reversal symmetry, despite some confusion in the literature, are distinct concepts. An absorbing scattering medium, for example, may satisfy reciprocity, but is not time reversal invariant [3]. Nevertheless, in the case that energy conservation holds, it can be shown, in accordance with Ref. [224], that time reversal symmetry and reciprocity are equivalent. It is not hard to see, for example, by minimal algebraic manipulation, that Eqs. (3.40) and (3.54), (energy conservation and reciprocity for the scattering matrix), imply Eq. (3.75), (time reversal symmetry for the scattering matrix). Similarly, it is relatively transparent that Eqs. (3.44) and (3.76) (energy conservation and time reversal symmetry for the transfer matrix) imply Eq. (3.61) (reciprocity for the transfer matrix).

Although reciprocity and time reversal symmetry are equivalent for energy conserving systems, there is still value in having derived both results. In Section 3.3.3, we shall see that choosing the correct condition as a starting point simplifies the derivation of the corresponding symmetry for the discrete scattering and transfer matrices, which shall be defined in the next section.

3.3 Discrete scattering and transfer matrices

The scattering and transfer matrices we have considered so far are mathematical functions defined for all pairs of conceivable transverse wavevectors $\boldsymbol{\kappa}$ and $\boldsymbol{\kappa}'$, which form an uncountably infinite continuous spectrum. In both experiments and numerical simulations, however, fields cannot be resolved with infinite precision and must be described using some finite set of modes [227]. Beyond merely being a practical limitation, the number of independent modes a system can support in reality must be finite due to the wave nature of light and is often constrained by the geometry of the scattering system. This is particularly relevant for waveguides, such as optical fibres, where the number of modes is determined by the radius and refractive index of the fibre [228]. Even for waves in open geometries, however, diffraction places a lower limit on the resolution to which a field can be discretely sampled [216]. When an incident beam passes through a slab-shaped scattering medium, two transmitted wavevectors will be independent provided that their angular separation exceeds the size of the transmitted speckle angular intensity correlation function. The number of independent modes can thus be related to the mean speckle size. For an incident beam with finite cross sectional area A, the number of modes transmitted through the medium N is on the order $N \sim 2A/\lambda^2$, which is necessarily finite in any realistic scenario [229]. The finitude of the number of modes of an optical system is also related to the finite space-bandwidth product a system, which is a dimensionless quantity that can be thought of its information throughput [230].

In order to move to a discrete description of the scattered fields, it is necessary to reduce the continuous spectrum of plane waves into a discrete collection of plane wave components. There is no unique way of doing this, and the way in which the discretisation is performed may depend on the nature of the system being modelled. In this section, however, we shall assume that a discretisation has already been agreed upon and consider general properties that hold irrespective of the exact discretisation scheme used. The question of which discretisation scheme is most useful in practice shall be given more discussion in Chapter 6. Given a discrete set of plane wave components, we will be able to define the discrete scattering and transfer matrices. These matrices will be more practical for numerical modelling and

will allow us to develop a theory that has a closer connection to scattering matrices measurable in experiments. For these matrices, we shall derive the corresponding constraints that are imposed by the conditions explored in the previous section, namely energy conservation, reciprocity and time reversal symmetry.

3.3.1 Definitions

Consider a finite set of plane waves with distinct transverse wavevectors. We first define two sets, K_p and K_e, containing transverse wavevectors corresponding to propagating and evanescent waves respectively. Specifically, we form K_p by choosing N_p transverse wavevectors $\boldsymbol{\kappa}_i^p$ corresponding to propagating waves together with their additive inverses $-\boldsymbol{\kappa}_i^p$ and the two-component zero vector $\mathbf{0} = (0,0)^{\mathrm{T}}$, which corresponds to the wavevector $(0,0,k)^{\mathrm{T}}$. The inclusion of modes in inverse pairs, as shall be demonstrated, is necessary to fully explore the effects of reciprocity and time reversal symmetry. Similarly, we construct K_e by taking N_e transverse wavevectors $\boldsymbol{\kappa}_i^e$ corresponding to evanescent waves and their additive inverses $-\boldsymbol{\kappa}_i^e$. Thus, we have

$$K_p = \{-\boldsymbol{\kappa}_{N_p}^p, \ldots, -\boldsymbol{\kappa}_2^p, -\boldsymbol{\kappa}_1^p, \mathbf{0}, \boldsymbol{\kappa}_1^p, \boldsymbol{\kappa}_2^p, \ldots, \boldsymbol{\kappa}_{N_p}^p\}, \tag{3.78}$$

$$K_e = \{-\boldsymbol{\kappa}_{N_e}^e, \ldots, -\boldsymbol{\kappa}_2^e, -\boldsymbol{\kappa}_1^e, \boldsymbol{\kappa}_1^e, \boldsymbol{\kappa}_2^e, \ldots, \boldsymbol{\kappa}_{N_e}^e\}, \tag{3.79}$$

which contain $2N_p + 1$ and $2N_e$ elements respectively. The set of all wavevectors K is the union of these sets, i.e. $K = K_p \cup K_e$. A sample of several modes is shown in Figure 3.2. We emphasise again that while in Figure 3.2 we have, for simplicity, distributed modes at points on a rectangular lattice in k-space, this choice is arbitrary and other geometries, such as for example a hexagonal lattice, may have practical advantages [231]. Note also that although k-space is theoretically unbounded, there is a practical upper limit to the size of $|\boldsymbol{\kappa}_i^e|$. This is because a larger $|\boldsymbol{\kappa}_i^e|$ corresponds to an evanescent wave with a greater decay rate in the z direction. When $|\boldsymbol{\kappa}_i^e|$ is sufficiently large, its corresponding wave amplitude, even at positions very close to the scattering medium, will have decayed to the point of being practically unmeasurable.

Since $\mathbf{a}(\boldsymbol{\kappa}) \cdot \mathbf{k} = \mathbf{b}(\boldsymbol{\kappa}) \cdot \widetilde{\mathbf{k}} = 0$, the vector amplitude associated with each plane

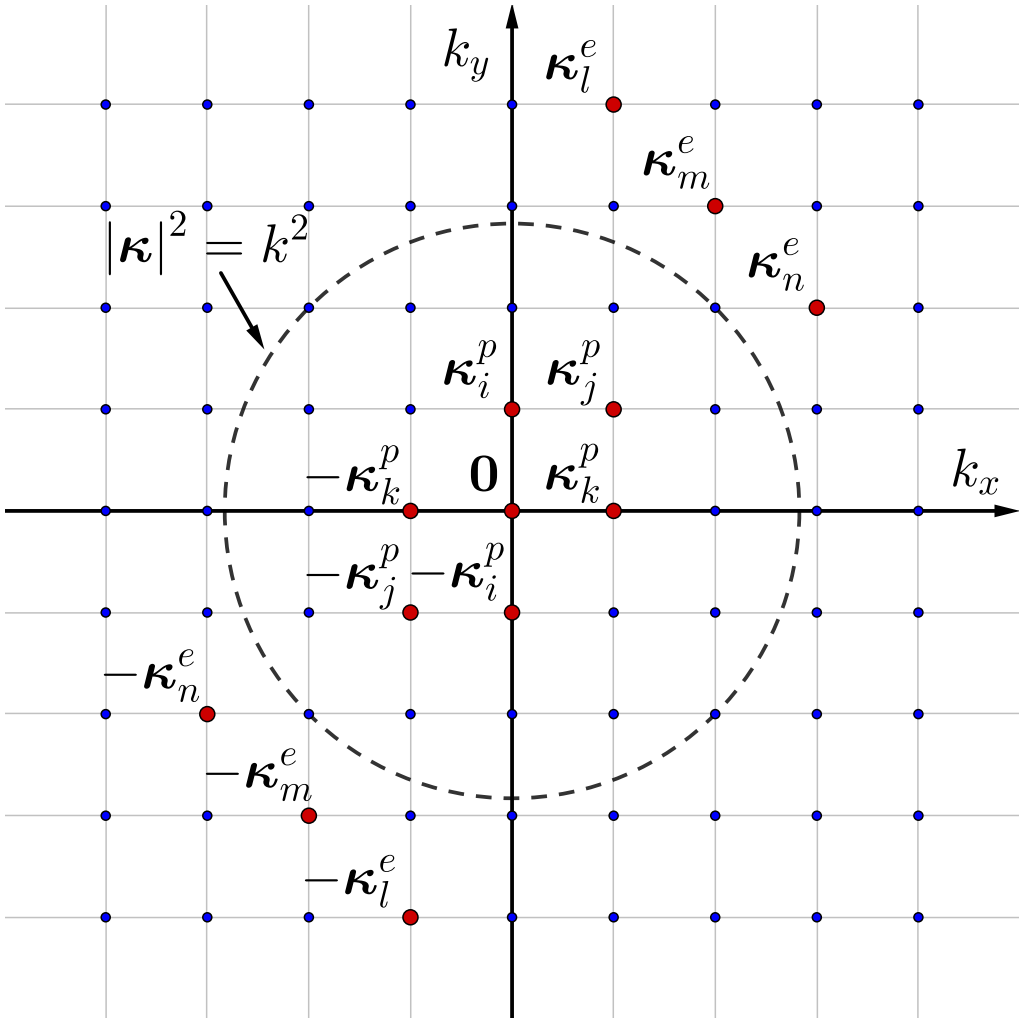

Figure 3.2: Transverse wavevector modes distributed on a rectangular lattice in k-space. The dashed circle $|\boldsymbol{\kappa}|^2 = k^2$ defines the boundary between propagating and evanescent modes. A selection of modes and their additive inverses have been highlighted in red.

wave component has only two degrees of freedom. For propagating plane wave components this constraint means that the electric field is constrained to vibrate perpendicular to the wavevector. Therefore, in order to remove extraneous information and simplify the ensuing mathematics, it will be useful to introduce the

vectors

$$\hat{\mathbf{e}}_k(\boldsymbol{\kappa},\gamma) = \frac{\mathbf{k}}{k} = \frac{1}{k}\begin{pmatrix} k_x \\ k_y \\ \gamma \end{pmatrix}, \tag{3.80}$$

$$\hat{\mathbf{e}}_\phi(\boldsymbol{\kappa},\gamma) = \frac{(\hat{\mathbf{z}}\times\hat{\mathbf{e}}_k)}{|\hat{\mathbf{z}}\times\hat{\mathbf{e}}_k|} = \frac{1}{|\boldsymbol{\kappa}|}\begin{pmatrix} -k_y \\ k_x \\ 0 \end{pmatrix}, \tag{3.81}$$

$$\hat{\mathbf{e}}_\theta(\boldsymbol{\kappa},\gamma) = \frac{(\hat{\mathbf{e}}_\phi\times\hat{\mathbf{e}}_k)}{|\hat{\mathbf{e}}_\phi\times\hat{\mathbf{e}}_k|} = \frac{1}{k|\boldsymbol{\kappa}|}\begin{pmatrix} k_x\gamma \\ k_y\gamma \\ -k_x^2-k_y^2 \end{pmatrix}, \tag{3.82}$$

which will allow us to separate the transverse and longitudinal electric field components. In Eqs. (3.80)-(3.82), we note that we have written γ as a second parameter of each basis vector. To be clear, the magnitude of γ is given by the magnitude of that defined by Eq. (3.7), but we allow for the possibility of its sign being negated, which is necessary in order to describe left-propagating plane wave components. In this case, we shall write, for example, $\hat{\mathbf{e}}_\theta(\boldsymbol{\kappa},-\gamma)$. We also note that for the special cases $\hat{\mathbf{e}}_k = \pm\hat{\mathbf{z}}$, $\hat{\mathbf{e}}_\phi$ in Eq. (3.81) is undefined. In these cases we define $\hat{\mathbf{e}}_\phi = \pm\mathbf{y}$, where the sign agrees with that of $\hat{\mathbf{e}}_k$. This choice will turn out to yield the correct reciprocity relations.

Note that when $\boldsymbol{\kappa}\in\Gamma_p$, γ is real and the vectors $\hat{\mathbf{e}}_k, \hat{\mathbf{e}}_\phi$ and $\hat{\mathbf{e}}_\theta$ are the standard unit basis vectors in spherical polar coordinates. When $\boldsymbol{\kappa}\in\Gamma_e$, however, $\hat{\mathbf{e}}_k$ and $\hat{\mathbf{e}}_\theta$ become complex. The vectors $\hat{\mathbf{e}}_\phi$ and $\hat{\mathbf{e}}_\theta$ are also classically referred to as s and p modes in polarisation theory [19]. Since we reserve the letter p for 'propagating', however, the labels ϕ and θ shall be used instead.

By the definitions of the basis vectors, it follows that

$$\hat{\mathbf{e}}_\phi(\boldsymbol{\kappa},\gamma)\cdot\mathbf{k} = \hat{\mathbf{e}}_\theta(\boldsymbol{\kappa},\gamma)\cdot\mathbf{k} = 0, \tag{3.83}$$

$$\hat{\mathbf{e}}_\phi(\boldsymbol{\kappa},-\gamma)\cdot\widetilde{\mathbf{k}} = \hat{\mathbf{e}}_\theta(\boldsymbol{\kappa},-\gamma)\cdot\widetilde{\mathbf{k}} = 0. \tag{3.84}$$

This means that we may express $\mathbf{a}^\pm(\boldsymbol{\kappa})$ and $\mathbf{b}^\pm(\boldsymbol{\kappa})$ in terms of their θ and ϕ com-

ponents. Explicitly, we have

$$\mathbf{a}^{\pm}(\boldsymbol{\kappa}) = a_{\theta}^{\pm}(\boldsymbol{\kappa})\hat{\mathbf{e}}_{\theta}(\boldsymbol{\kappa},\gamma) + a_{\phi}^{\pm}(\boldsymbol{\kappa})\hat{\mathbf{e}}_{\phi}(\boldsymbol{\kappa},\gamma), \tag{3.85}$$

$$\mathbf{b}^{\pm}(\boldsymbol{\kappa}) = b_{\theta}^{\pm}(\boldsymbol{\kappa})\hat{\mathbf{e}}_{\theta}(\boldsymbol{\kappa},-\gamma) + b_{\phi}^{\pm}(\boldsymbol{\kappa})\hat{\mathbf{e}}_{\phi}(\boldsymbol{\kappa},-\gamma). \tag{3.86}$$

It is now possible to reduce the 3×3 blocks of the continuous scattering and transfer matrices $\mathbf{r}, \mathbf{r}', \mathbf{t}, \mathbf{t}', \boldsymbol{\alpha}, \boldsymbol{\beta}, \boldsymbol{\gamma}$ and $\boldsymbol{\delta}$ to 2×2 matrices that couple the θ and ϕ components of $\mathbf{a}^{\pm}(\boldsymbol{\kappa})$ and $\mathbf{b}^{\pm}(\boldsymbol{\kappa})$. Moving forward, transverse wavevectors should be thought of as being selected from the previously defined set K, and subscripts shall be given to them to reflect their discrete nature. As an example, consider $\mathbf{r}(\boldsymbol{\kappa}_j, \boldsymbol{\kappa}_i)$, where $\boldsymbol{\kappa}_i, \boldsymbol{\kappa}_j \in K_p$. This matrix describes the reflection at the left side of the medium of the right-propagating incident plane wave with wavevector $(\boldsymbol{\kappa}_i, \gamma_i)^{\mathrm{T}}$ and vector amplitude $\mathbf{a}^{-}(\boldsymbol{\kappa}_i)$ to the left-propagating plane wave with wavevector $(\boldsymbol{\kappa}_j, -\gamma_j)^{\mathrm{T}}$ and vector amplitude $\mathbf{b}^{-}(\boldsymbol{\kappa}_j)$. We define the 2×2 reduced reflection matrix for the pair of modes $\boldsymbol{\kappa}_i$ and $\boldsymbol{\kappa}_j$ as the matrix $\mathbf{r}_{(j,i)}$, where

$$\boldsymbol{r}_{(j,i)} = \begin{pmatrix} r_{(j,i)\theta\theta} & r_{(j,i)\theta\phi} \\ r_{(j,i)\phi\theta} & r_{(j,i)\phi\phi} \end{pmatrix} \tag{3.87}$$

and

$$r_{(j,i)mn} = \hat{\mathbf{e}}_m^{\mathrm{T}}(\boldsymbol{\kappa}_j, -\gamma_j)\mathbf{r}(\boldsymbol{\kappa}_j, \boldsymbol{\kappa}_i)\hat{\mathbf{e}}_n(\boldsymbol{\kappa}_i, \gamma_i), \tag{3.88}$$

where m and n may be chosen to be either θ or ϕ. We allow for negative numbers and zero in the subscript of a reduced matrix, where a negative index corresponds to a transverse wavevector appearing in K with a minus sign. For example, $\mathbf{r}_{(-1,0)}$ denotes the reduced reflection matrix derived from $\mathbf{r}(-\boldsymbol{\kappa}_1, \boldsymbol{\kappa}_0)$. Note that

$$\hat{\mathbf{e}}_k^{\mathrm{T}}(\boldsymbol{\kappa}_j, -\gamma_j)\mathbf{r}(\boldsymbol{\kappa}_j, \boldsymbol{\kappa}_i) = \mathbf{0}^{\mathrm{T}} \tag{3.89}$$

for all $\boldsymbol{\kappa}_j$ and $\boldsymbol{\kappa}_i$, but, since $\mathbf{a}^{-}(\boldsymbol{\kappa}_i)$ has no k component, $\mathbf{r}(\boldsymbol{\kappa}_j, \boldsymbol{\kappa}_i)\hat{\mathbf{e}}_k(\boldsymbol{\kappa}_i, \gamma_i)$ is unde-

fined. We therefore assign

$$\mathbf{r}(\boldsymbol{\kappa}_j, \boldsymbol{\kappa}_i)\hat{\mathbf{e}}_k(\boldsymbol{\kappa}_i, \gamma_i) = \mathbf{0}, \tag{3.90}$$

which justifies the construction of the reduced reflection matrix as only the four components in Eq. (3.87) are unconstrained. The other seven blocks of $\mathbf{S}$ and $\mathbf{M}$ can be handled similarly. The components of these blocks, after consideration of the propagation directions of the incident and scattered wavevectors, can be shown to be given by

$$r_{(j,i)mn} = \hat{\mathbf{e}}_m^{\mathrm{T}}(\boldsymbol{\kappa}_j, -\gamma_j)\mathbf{r}(\boldsymbol{\kappa}_j, \boldsymbol{\kappa}_i)\hat{\mathbf{e}}_n(\boldsymbol{\kappa}_i, \gamma_i), \tag{3.91}$$

$$r'_{(j,i)mn} = \hat{\mathbf{e}}_m^{\mathrm{T}}(\boldsymbol{\kappa}_j, \gamma_j)\mathbf{r}'(\boldsymbol{\kappa}_j, \boldsymbol{\kappa}_i)\hat{\mathbf{e}}_n(\boldsymbol{\kappa}_i, -\gamma_i), \tag{3.92}$$

$$t_{(j,i)mn} = \hat{\mathbf{e}}_m^{\mathrm{T}}(\boldsymbol{\kappa}_j, \gamma_j)\mathbf{t}(\boldsymbol{\kappa}_j, \boldsymbol{\kappa}_i)\hat{\mathbf{e}}_n(\boldsymbol{\kappa}_i, \gamma_i), \tag{3.93}$$

$$t'_{(j,i)mn} = \hat{\mathbf{e}}_m^{\mathrm{T}}(\boldsymbol{\kappa}_j, -\gamma_j)\mathbf{t}'(\boldsymbol{\kappa}_j, \boldsymbol{\kappa}_i)\hat{\mathbf{e}}_n(\boldsymbol{\kappa}_i, -\gamma_i), \tag{3.94}$$

$$\alpha_{(j,i)mn} = \hat{\mathbf{e}}_m^{\mathrm{T}}(\boldsymbol{\kappa}_j, \gamma_j)\boldsymbol{\alpha}(\boldsymbol{\kappa}_j, \boldsymbol{\kappa}_i)\hat{\mathbf{e}}_n(\boldsymbol{\kappa}_i, \gamma_i), \tag{3.95}$$

$$\beta_{(j,i)mn} = \hat{\mathbf{e}}_m^{\mathrm{T}}(\boldsymbol{\kappa}_j, \gamma_j)\boldsymbol{\beta}(\boldsymbol{\kappa}_j, \boldsymbol{\kappa}_i)\hat{\mathbf{e}}_n(\boldsymbol{\kappa}_i, -\gamma_i), \tag{3.96}$$

$$\gamma_{(j,i)mn} = \hat{\mathbf{e}}_m^{\mathrm{T}}(\boldsymbol{\kappa}_j, -\gamma_j)\boldsymbol{\gamma}(\boldsymbol{\kappa}_j, \boldsymbol{\kappa}_i)\hat{\mathbf{e}}_n(\boldsymbol{\kappa}_i, \gamma_i), \tag{3.97}$$

$$\delta_{(j,i)mn} = \hat{\mathbf{e}}_m^{\mathrm{T}}(\boldsymbol{\kappa}_j, -\gamma_j)\boldsymbol{\delta}(\boldsymbol{\kappa}_j, \boldsymbol{\kappa}_i)\hat{\mathbf{e}}_n(\boldsymbol{\kappa}_i, -\gamma_i). \tag{3.98}$$

We can now construct the discrete scattering matrix for our finite set of modes by discretizing Eq. (3.13). To achieve this, we employ a cubature scheme over k-space with nodes given by the transverse wavevectors within the set K. For each node, we define the associated weight w_i, so that integrals of functions of $\boldsymbol{\kappa}$ can be approximated by

$$\int f(\boldsymbol{\kappa})\mathrm{d}\boldsymbol{\kappa} \approx \sum_i f(\boldsymbol{\kappa}_i)w_i. \tag{3.99}$$

If, for example, a rectangular partitioning is used, then $w_i = \Delta k_x \Delta k_y$, where Δk_x and Δk_y describe the mode spacings in the x and y directions in k-space. Naturally, increasing the number of wavevectors in K will improve the accuracy of the approximation, albeit at the cost of an increase in computational complexity. With such a

cubature scheme, Eq. (3.13) becomes

$$\begin{pmatrix} b_\theta^-(\boldsymbol{\kappa}_j) \\ b_\phi^-(\boldsymbol{\kappa}_j) \\ a_\theta^+(\boldsymbol{\kappa}_j) \\ a_\phi^+(\boldsymbol{\kappa}_j) \end{pmatrix} = \sum_{\boldsymbol{\kappa}_i \in K} \begin{pmatrix} r_{(j,i)\theta\theta} & r_{(j,i)\theta\phi} & t'_{(j,i)\theta\theta} & t'_{(j,i)\theta\phi} \\ r_{(j,i)\phi\theta} & r_{(j,i)\phi\phi} & t'_{(j,i)\phi\theta} & t'_{(j,i)\phi\phi} \\ t_{(j,i)\theta\theta} & t_{(j,i)\theta\phi} & r'_{(j,i)\theta\theta} & r'_{(j,i)\theta\phi} \\ t_{(j,i)\theta\theta} & t_{(j,i)\theta\phi} & r'_{(j,i)\theta\theta} & r'_{(j,i)\theta\phi} \end{pmatrix} \begin{pmatrix} a_\theta^-(\boldsymbol{\kappa}_i) \\ a_\phi^-(\boldsymbol{\kappa}_i) \\ b_\theta^+(\boldsymbol{\kappa}_i) \\ b_\phi^+(\boldsymbol{\kappa}_i) \end{pmatrix} w_i, \tag{3.100}$$

where $\boldsymbol{\kappa}_i$ in the sum ranges over all wavevectors in K. By now letting $\boldsymbol{\kappa}_j$ vary over the set K, we obtain a system of equations, each of which have the same form as Eq. (3.100), which can be combined into a single matrix equation. To facilitate this, we first introduce the notation

$$\mathbf{u}_q^\pm = (u_\theta^\pm(-\boldsymbol{\kappa}_{N_q}^q), u_\phi^\pm(-\boldsymbol{\kappa}_{N_q}^q), \ldots, u_\theta^\pm(\boldsymbol{\kappa}_{N_q}^q), u_\phi^\pm(\boldsymbol{\kappa}_{N_q}^q)), \tag{3.101}$$

where $\mathbf{u}$ stands for either $\mathbf{a}$ or $\mathbf{b}$ and q stands for either p or e. Regardless of the choice of q, we order the transverse wavevectors within $\mathbf{u}$ from left to right in the same way as they are presented in Eqs. (3.78) and (3.79). Using the notation in Eq. (3.101), we define the four vectors

$$\mathbf{c}_i = (\mathbf{a}_p^-, \mathbf{b}_p^+, \mathbf{a}_e^-, \mathbf{b}_e^+)^{\mathrm{T}}, \tag{3.102}$$

$$\mathbf{c}_o = (\mathbf{b}_p^-, \mathbf{a}_p^+, \mathbf{b}_e^-, \mathbf{a}_e^+)^{\mathrm{T}}, \tag{3.103}$$

$$\mathbf{c}_l = (\mathbf{a}_p^-, \mathbf{b}_p^-, \mathbf{a}_e^-, \mathbf{b}_e^-)^{\mathrm{T}}, \tag{3.104}$$

$$\mathbf{c}_r = (\mathbf{a}_p^+, \mathbf{b}_p^+, \mathbf{a}_e^+, \mathbf{b}_e^+)^{\mathrm{T}}, \tag{3.105}$$

which contain all complex amplitudes of the plane wave components in the angular spectra. In addition, we define the weight matrix

$$\mathbf{W} = \begin{pmatrix} \mathbf{W}_p & \mathbf{O} \\ \mathbf{O} & \mathbf{W}_e \end{pmatrix}, \tag{3.106}$$

where

$$\mathbf{W}_p = \mathbb{I}_2 \otimes \mathrm{diag}(w^p_{-N_p}, \ldots, w^p_0, \ldots, w^p_{N_p}) \otimes \mathbb{I}_2, \tag{3.107}$$

$$\mathbf{W}_e = \mathbb{I}_2 \otimes \mathrm{diag}(w^e_{-N_e}, \ldots, w^e_{N_e}) \otimes \mathbb{I}_2, \tag{3.108}$$

and w^p and w^e are weights associated with propagating and evanescent plane wave components respectively. We may now define the discrete scattering matrix $\mathbf{S}$ as the matrix satisfying

$$\mathbf{c}_o = \mathbf{S}\mathbf{W}\mathbf{c}_i. \tag{3.109}$$

Note that the effect of the weight matrix is to correctly distribute the weights among the elements of $\mathbf{c}_i$ in accordance with Eq. (3.100).

Given our ordering of the modes, the matrix $\mathbf{S}$ can be written in the block form

$$\mathbf{S} = \begin{pmatrix} \mathbf{S}_{pp} & \mathbf{S}_{pe} \\ \mathbf{S}_{ep} & \mathbf{S}_{ee} \end{pmatrix} = \begin{pmatrix} \mathbf{r}_{pp} & \mathbf{t}'_{pp} & \mathbf{r}_{pe} & \mathbf{t}'_{pe} \\ \mathbf{t}_{pp} & \mathbf{r}'_{pp} & \mathbf{t}_{pe} & \mathbf{r}'_{pe} \\ \mathbf{r}_{ep} & \mathbf{t}'_{ep} & \mathbf{r}_{ee} & \mathbf{t}'_{ee} \\ \mathbf{t}_{ep} & \mathbf{r}'_{ep} & \mathbf{t}_{ee} & \mathbf{r}'_{ee} \end{pmatrix}, \tag{3.110}$$

where

$$\mathbf{S}_{ab} = \begin{pmatrix} \mathbf{r}_{ab} & \mathbf{t}'_{ab} \\ \mathbf{t}_{ab} & \mathbf{r}'_{ab} \end{pmatrix} \tag{3.111}$$

and a and b are to be chosen from p or e. For each sub-matrix, the right subscript denotes the type of incident mode (i.e. propagating or evanescent) and the left subscript denotes the type of outgoing mode. For example, $\mathbf{r}_{pe}$ describes the reflection at the left hand side of the system of incoming evanescent modes to outgoing propagating modes. It is formed by concatenating 2×2 reduced reflection matrices of the form in Eq. (3.87). All other sub-matrices of $\mathbf{S}$ can be understood in an analogous manner. Similarly, the discrete transfer matrix $\mathbf{M}$ is defined to be the matrix that

satisfies

$$\mathbf{c}_r = \mathbf{M}\mathbf{W}\mathbf{c}_l. \tag{3.112}$$

This matrix can also be partitioned in an analogous way to the discrete scattering matrix. Explicitly,

$$\mathbf{M} = \begin{pmatrix} \mathbf{M}_{pp} & \mathbf{M}_{pe} \\ \mathbf{M}_{ep} & \mathbf{M}_{ee} \end{pmatrix} = \begin{pmatrix} \boldsymbol{\alpha}_{pp} & \boldsymbol{\beta}_{pp} & \boldsymbol{\alpha}_{pe} & \boldsymbol{\beta}_{pe} \\ \boldsymbol{\gamma}_{pp} & \boldsymbol{\delta}_{pp} & \boldsymbol{\gamma}_{pe} & \boldsymbol{\delta}_{pe} \\ \boldsymbol{\alpha}_{ep} & \boldsymbol{\beta}_{ep} & \boldsymbol{\alpha}_{ee} & \boldsymbol{\beta}_{ee} \\ \boldsymbol{\gamma}_{ep} & \boldsymbol{\delta}_{ep} & \boldsymbol{\gamma}_{ee} & \boldsymbol{\delta}_{ee} \end{pmatrix}. \tag{3.113}$$

To give an example of the precise structure of these matrices, let us consider $\mathbf{t}_{pp}$, which we shall momentarily refer to as just $\mathbf{t}$. The indices i and j, which label the 2×2 blocks $\mathbf{t}_{(j,i)}$ span from $-N_p$ to N_p, meaning there are a total of $(2N_p+1)^2$ 2×2 blocks within $\mathbf{t}$. The overall structure of $\mathbf{t}$ is given by

$$\mathbf{t} = \begin{array}{c} \begin{matrix} -\boldsymbol{\kappa}_{N_k} & \cdots & -\boldsymbol{\kappa}_1 & \mathbf{0} & \boldsymbol{\kappa}_1 & \cdots & \boldsymbol{\kappa}_{N_k} \end{matrix} \\ \begin{pmatrix} \mathbf{t}_{(-N_k,-N_k)} & \cdots & \mathbf{t}_{(-N_k,-1)} & \mathbf{t}_{(-N_k,0)} & \mathbf{t}_{(-N_k,1)} & \cdots & \mathbf{t}_{(-N_k,N_k)} \\ \vdots & \ddots & \vdots & \vdots & \vdots & \ddots & \vdots \\ \mathbf{t}_{(-1,-N_k)} & \cdots & \mathbf{t}_{(-1,-1)} & \mathbf{t}_{(-1,0)} & \mathbf{t}_{(-1,1)} & \cdots & \mathbf{t}_{(-1,N_k)} \\ \mathbf{t}_{(0,-N_k)} & \cdots & \mathbf{t}_{(0,-1)} & \mathbf{t}_{(0,0)} & \mathbf{t}_{(0,1)} & \cdots & \mathbf{t}_{(0,N_k)} \\ \mathbf{t}_{(1,-N_k)} & \cdots & \mathbf{t}_{(1,-1)} & \mathbf{t}_{(1,0)} & \mathbf{t}_{(1,1)} & \cdots & \mathbf{t}_{(1,N_k)} \\ \vdots & \ddots & \vdots & \vdots & \vdots & \ddots & \vdots \\ \mathbf{t}_{(N_k,-N_k)} & \cdots & \mathbf{t}_{(N_k,-1)} & \mathbf{t}_{(N_k,0)} & \mathbf{t}_{(N_k,1)} & \cdots & \mathbf{t}_{(N_k,N_k)} \end{pmatrix} \end{array} \begin{matrix} -\boldsymbol{\kappa}_{N_k} \\ \vdots \\ -\boldsymbol{\kappa}_1 \\ \mathbf{0} \\ \boldsymbol{\kappa}_1 \\ \vdots \\ \boldsymbol{\kappa}_{N_k} \end{matrix}. \tag{3.114}$$

The vectors displayed above and to the right of the matrix indicate the incident and outgoing modes respectively. For example, the block $\mathbf{t}_{(3,-2)}$ describes transmission through the medium from mode $-\boldsymbol{\kappa}_2$ to mode $\boldsymbol{\kappa}_3$, i.e. from the incident right-propagating plane wave with wavevector $\mathbf{k}_{-2} = (-k_{2x}, -k_{2y}, \gamma_2)^{\mathrm{T}}$ to that with wavevector $\mathbf{k}_3 = (k_{3x}, k_{3y}, \gamma_3)^{\mathrm{T}}$.

In order to simplify the matrix constraints that will be derived in the following sections, it will be useful to define normalised scattering and transfer matrices. If

we let $\mathbf{A}$ denote any of the matrices $\mathbf{r}, \mathbf{t}, \mathbf{t}', \mathbf{r}', \boldsymbol{\alpha}, \boldsymbol{\beta}, \boldsymbol{\gamma}$ or $\boldsymbol{\delta}$, we define

$$\bar{\mathbf{A}}_{(j,i)} = \mathbf{A}_{(j,i)} \sqrt{\frac{|\gamma_j|}{|\gamma_i|} w_i w_j}. \tag{3.115}$$

All 2×2 blocks within $\mathbf{S}$ and $\mathbf{M}$ can then be replaced by their normalised counterparts to give the normalised scattering and transfer matrices $\bar{\mathbf{S}}$ and $\bar{\mathbf{M}}$. To understand the physics of this normalisation, suppose that the incident field illuminates the scattering medium on the left hand side. In the incident plane wave spectrum, normalisation of the scattering matrix is equivalent to the redefinition $e^{i\mathbf{k}_i \cdot \mathbf{r}} \rightarrow e^{i\mathbf{k}_i \cdot \mathbf{r}} \sqrt{w_i} / \sqrt{|\gamma_i|}$. For plane wave components propagating away from the scattering medium in either reflection or transmission, the normalisation is equivalent to the angular spectra redefinition $e^{i\mathbf{k}_j \cdot \mathbf{r}} \rightarrow e^{i\mathbf{k}_j \cdot \mathbf{r}} / (\sqrt{|\gamma_j|} \sqrt{w_j})$. The inclusion of the γ terms in these transformations mean that each plane wave delivers an equal energy flux per unit cross-sectional area perpendicular to the z direction. Note that the asymmetry between the transformations for the incident and outgoing spectra is related to the fact that the coefficeints of the outgoing plane wave components are given by the integral relation in Eq. (3.13) and that, within the normalised framework, all matrices are dimensionless.

To end this section, we note that it is possible to convert between the discrete scattering and transfer matrices. Consdering the definitions of the matrices, it can be shown that [232]

$$\mathbf{r} = -\boldsymbol{\delta}^{-1} \boldsymbol{\gamma}, \tag{3.116}$$

$$\mathbf{r}' = \boldsymbol{\beta} \boldsymbol{\delta}^{-1}, \tag{3.117}$$

$$\mathbf{t} = \boldsymbol{\alpha} - \boldsymbol{\beta} \boldsymbol{\delta}^{-1} \boldsymbol{\gamma}, \tag{3.118}$$

$$\mathbf{t}' = \boldsymbol{\delta}^{-1}, \tag{3.119}$$

$$\boldsymbol{\alpha} = \mathbf{t} - \mathbf{r}' (\mathbf{t}')^{-1} \mathbf{r}, \tag{3.120}$$

$$\boldsymbol{\beta} = \mathbf{r}' (\mathbf{t}')^{-1}, \tag{3.121}$$

$$\boldsymbol{\gamma} = -(\mathbf{t}')^{-1} \mathbf{r}, \tag{3.122}$$

$$\boldsymbol{\delta} = (\mathbf{t}')^{-1}, \tag{3.123}$$

where, for example,

$$\mathbf{r} = \begin{pmatrix} \mathbf{r}_{pp} & \mathbf{r}_{pe} \\ \mathbf{r}_{ep} & \mathbf{r}_{ee} \end{pmatrix} \tag{3.124}$$

and the other matrices are defined analogously. These equations also hold for the normalised scattering and transfer matrices.

3.3.2 Energy conservation

In this section we shall derive the constraints imposed upon $\bar{\mathbf{S}}$ and $\bar{\mathbf{M}}$ by energy conservation. We begin by discretizing the conservation of energy equation for the continuous scattering matrix, namely Eq. (3.40). As before, we employ a cubature scheme as defined by Eq. (3.99) so that integrals can be approximated by sums. The Dirac delta function $\delta(\boldsymbol{\kappa}' - \boldsymbol{\kappa}'')$, whose integral is by definition unity, can be replaced by the normalised Kronecker delta δ_{ij}/w_i. Note there is some freedom in how one picks the denominator of the normalised Kronecker delta. Instead of w_i, w_j and $\sqrt{w_i w_j}$ would serve equally well, as the Kronecker delta forces the equality of w_i and w_j in any case. We shall return to this point in Chapter 6. Rewriting $\boldsymbol{\kappa}, \boldsymbol{\kappa}'$ and $\boldsymbol{\kappa}''$ as $\boldsymbol{\kappa}_l, \boldsymbol{\kappa}_i$ and $\boldsymbol{\kappa}_j$ respectively, we obtain

$$\sum_{\boldsymbol{\kappa}_l \in K_p} \gamma_l \mathbf{S}^\dagger(\boldsymbol{\kappa}_l, \boldsymbol{\kappa}_i)\mathbf{S}(\boldsymbol{\kappa}_l, \boldsymbol{\kappa}_j) w_l = \begin{cases} \gamma_i \delta_{ij} \mathbb{I}_6 / w_i & \text{if } \boldsymbol{\kappa}_i \in K_p,\ \boldsymbol{\kappa}_j \in K_p, \\ \gamma_j \mathbf{S}^\dagger(\boldsymbol{\kappa}_j, \boldsymbol{\kappa}_i) & \text{if } \boldsymbol{\kappa}_i \in K_p,\ \boldsymbol{\kappa}_j \in K_e, \\ -\gamma_i \mathbf{S}(\boldsymbol{\kappa}_i, \boldsymbol{\kappa}_j) & \text{if } \boldsymbol{\kappa}_i \in K_e,\ \boldsymbol{\kappa}_j \in K_p, \\ \gamma_j \mathbf{S}^\dagger(\boldsymbol{\kappa}_j, \boldsymbol{\kappa}_i) - \gamma_i \mathbf{S}(\boldsymbol{\kappa}_i, \boldsymbol{\kappa}_j) & \text{if } \boldsymbol{\kappa}_i \in K_e,\ \boldsymbol{\kappa}_j \in K_e. \end{cases} \tag{3.125}$$

We now multiply both sides of Eq. (3.125) by $\sqrt{w_i w_j / |\gamma_i \gamma_j|}$. First, note that, since γ_l by definition corresponds to a propagating wavevector, we have $\gamma_l = |\gamma_l|$ and the left hand side becomes

$$\sum_{\boldsymbol{\kappa}_l \in K_p} \sqrt{\frac{|\gamma_l|}{|\gamma_i|} w_l w_i} \mathbf{S}^\dagger(\boldsymbol{\kappa}_l, \boldsymbol{\kappa}_i) \sqrt{\frac{|\gamma_l|}{|\gamma_j|} w_l w_j} \mathbf{S}(\boldsymbol{\kappa}_l, \boldsymbol{\kappa}_j) = \sum_{\boldsymbol{\kappa}_l \in K_p} \bar{\mathbf{S}}^\dagger(\boldsymbol{\kappa}_l, \boldsymbol{\kappa}_i) \bar{\mathbf{S}}(\boldsymbol{\kappa}_l, \boldsymbol{\kappa}_j). \tag{3.126}$$

In the case that $\boldsymbol{\kappa}_i, \boldsymbol{\kappa}_j \in K_p$, all weights and γ terms on the right hand side cancel due to the Kronecker delta, and we are left with $\delta_{ij}\mathbb{I}_6$. For the other three cases, note that γ terms that correspond to evanescent plane wave components satisfy $\gamma = i|\gamma|$. Eq. (3.125) thus becomes

$$\sum_{\boldsymbol{\kappa}_l \in K_p} \bar{\mathbf{S}}^{\dagger}(\boldsymbol{\kappa}_l, \boldsymbol{\kappa}_i)\bar{\mathbf{S}}(\boldsymbol{\kappa}_l, \boldsymbol{\kappa}_j) = \begin{cases} \delta_{ij}\mathbb{I}_6 & \text{if } \boldsymbol{\kappa}_i \in K_p,\ \boldsymbol{\kappa}_j \in K_p, \\ i\bar{\mathbf{S}}^{\dagger}(\boldsymbol{\kappa}_j, \boldsymbol{\kappa}_i) & \text{if } \boldsymbol{\kappa}_i \in K_p,\ \boldsymbol{\kappa}_j \in K_e, \\ -i\bar{\mathbf{S}}(\boldsymbol{\kappa}_i, \boldsymbol{\kappa}_j) & \text{if } \boldsymbol{\kappa}_i \in K_e,\ \boldsymbol{\kappa}_j \in K_p, \\ i\bar{\mathbf{S}}^{\dagger}(\boldsymbol{\kappa}_j, \boldsymbol{\kappa}_i) - i\bar{\mathbf{S}}(\boldsymbol{\kappa}_i, \boldsymbol{\kappa}_j) & \text{if } \boldsymbol{\kappa}_i \in K_e,\ \boldsymbol{\kappa}_j \in K_e. \end{cases} \tag{3.127}$$

We can consider each of the four cases in Eq. (3.127) separately. In each case, we may form four matrix equations by equating different blocks of the scattering matrices. Analysing the full set of possible equations consists of a lot of repetitive and unenlightening algebra. We shall therefore only present a single example here. Suppose $\boldsymbol{\kappa}_i, \boldsymbol{\kappa}_j \in K_p$ so that we may consider the first case of Eq. (3.127). Equating the top-left blocks of the matrices on either side, we obtain

$$\sum_{\boldsymbol{\kappa}_l \in K_p} \left[\bar{\mathbf{r}}^{\dagger}(\boldsymbol{\kappa}_l, \boldsymbol{\kappa}_i)\bar{\mathbf{r}}(\boldsymbol{\kappa}_l, \boldsymbol{\kappa}_j) + \bar{\mathbf{t}}^{\dagger}(\boldsymbol{\kappa}_l, \boldsymbol{\kappa}_i)\bar{\mathbf{t}}(\boldsymbol{\kappa}_l, \boldsymbol{\kappa}_j)\right] = \delta_{ij}\mathbb{I}_3. \tag{3.128}$$

Equations involving the reduced matrices can be extracted by pre-multiplying and post-multiplying both sides by different combinations of the basis vectors $\mathbf{e}_\theta$ and $\mathbf{e}_\phi$. First, note that since $\mathbf{e}_k(\boldsymbol{\kappa}, \pm\gamma), \mathbf{e}_\theta(\boldsymbol{\kappa}, \pm\gamma)$ and $\mathbf{e}_\phi(\boldsymbol{\kappa}, \pm\gamma)$ form an orthonormal basis of $\mathbb{C}^3$, we have [233]

$$\mathbf{e}_k\mathbf{e}_k^{\mathrm{T}} + \mathbf{e}_\theta\mathbf{e}_\theta^{\mathrm{T}} + \mathbf{e}_\phi\mathbf{e}_\phi^{\mathrm{T}} = \mathbb{I}_3. \tag{3.129}$$

This means that multiplying any matrix by the combination of vectors on the left hand side of Eq. (3.129) leaves the matrix unchanged. Inserting this combination of vectors in between the matrix products in Eq. (3.128), pre-multiplying the equation

by $\mathbf{e}_\theta^{\mathrm{T}}(\boldsymbol{\kappa}_i, \gamma_i)$ and post-multiplying the equation by $\mathbf{e}_\theta(\boldsymbol{\kappa}_j, \gamma_j)$ yields

$$\mathbf{e}_\theta^{\mathrm{T}} \sum_{\boldsymbol{\kappa}_l \in K_p} \Big[\bar{\mathbf{r}}^\dagger(\boldsymbol{\kappa}_l, \boldsymbol{\kappa}_i) \big[\mathbf{e}_\theta \mathbf{e}_\theta^{\mathrm{T}} + \mathbf{e}_\phi \mathbf{e}_\phi^{\mathrm{T}}\big] \bar{\mathbf{r}}(\boldsymbol{\kappa}_l, \boldsymbol{\kappa}_j) + \bar{\mathbf{t}}^\dagger(\boldsymbol{\kappa}_l, \boldsymbol{\kappa}_i) \big[\mathbf{e}_\theta \mathbf{e}_\theta^{\mathrm{T}} + \mathbf{e}_\phi \mathbf{e}_\phi^{\mathrm{T}}\big] \bar{\mathbf{t}}(\boldsymbol{\kappa}_l, \boldsymbol{\kappa}_j) \Big] \mathbf{e}_\theta = \delta_{ij}. \tag{3.130}$$

It is important to remember that the basis vectors inserted between the reflection and transmission matrices in Eq. (3.130) are not the same. Those between the transmission matrices are of the form $\mathbf{e}_\theta(\boldsymbol{\kappa}, \gamma)$, while those between the reflection matrices are of the form $\mathbf{e}_\theta(\boldsymbol{\kappa}, -\gamma)$, since reflected waves propagate to the left. Note also that all terms involving either $\mathbf{e}_k$ or $\mathbf{e}_k^{\mathrm{T}}$ vanish, as discussed in Section 3.3.1. The left hand side of Eq. (3.130) consists of eight bilinear forms, each of which can be simplified separately. For example, the first part of the first term in the sum in Eq. (3.130) can be shown to be

$$\mathbf{e}_\theta^{\mathrm{T}}(\boldsymbol{\kappa}_i, \gamma_i) \bar{\mathbf{r}}^\dagger(\boldsymbol{\kappa}_l, \boldsymbol{\kappa}_i) \mathbf{e}_\theta(\boldsymbol{\kappa}_l, -\gamma_l) = \bar{r}^*_{(l,i)\theta\theta}, \tag{3.131}$$

by making use the fact that $\mathbf{e}_\theta^\dagger = \mathbf{e}_\theta^{\mathrm{T}}$ for propagating waves. Simplifying all terms in Eq. (3.130) in a similar way gives

$$\sum_{\boldsymbol{\kappa}_l \in K_p} \Big[\bar{r}^*_{(l,i)\theta\theta} \bar{r}_{(l,j)\theta\theta} + \bar{r}^*_{(l,i)\phi\theta} \bar{r}_{(l,j)\phi\theta} + \bar{t}^*_{(l,i)\theta\theta} \bar{t}_{(l,j)\theta\theta} + \bar{t}^*_{(l,i)\phi\theta} \bar{t}_{(l,j)\phi\theta} \Big] = \delta_{ij} \tag{3.132}$$

Considering Eq. (3.132), it can be seen that the left hand side is the inner product of two columns of $\bar{\mathbf{S}}$. Therefore, the equation effectively states that the inner product of a column with itself is unity, while the product of a column with another column is zero. A similar analysis can be applied to all other blocks of $\bar{\mathbf{S}}$ and incident and outgoing polarisation states, resulting in a large system of equations that is ultimately equivalent to the single matrix equation

$$\bar{\mathbf{S}}_{pp}^\dagger \bar{\mathbf{S}}_{pp} = \mathbb{I}_{8N_p+4}. \tag{3.133}$$

Eq. (3.133) is the classic result that a scattering matrix for a system that conserves

energy and only contains propagating modes is unitary.

It is interesting to consider what happens to Eq. (3.133) if energy conservation is relaxed. To gain physical intuition, it is helpful to consider the so-called polar decomposition of the scattering matrix, which is given by [7]

$$\bar{\mathbf{S}}_{pp} = \begin{pmatrix} \mathbf{U} & \mathbb{O} \\ \mathbb{O} & \mathbf{V} \end{pmatrix} \begin{pmatrix} -\sqrt{\boldsymbol{\rho}} & \sqrt{\boldsymbol{\tau}} \\ \sqrt{\boldsymbol{\tau}} & \sqrt{\boldsymbol{\rho}} \end{pmatrix} \begin{pmatrix} \mathbf{U}' & \mathbb{O} \\ \mathbb{O} & \mathbf{V}' \end{pmatrix}, \tag{3.134}$$

where $\boldsymbol{\tau}$ and $\boldsymbol{\rho}$ are diagonal matrices containing the eigenvalues of $\mathbf{t}^\dagger\mathbf{t}$ and $\mathbf{r}^\dagger\mathbf{r}$ respectively and $\mathbf{U}$, $\mathbf{U}'$, $\mathbf{V}$ and $\mathbf{V}'$ are unitary matrices. Essentially, Eq. (3.134) comes from taking the singular value decomposition of each block of $\bar{\mathbf{S}}_{pp}$ and separating out the different matrix factors. In the case that energy is conserved, it follows from unitarity that $\boldsymbol{\rho} + \boldsymbol{\tau} = \mathbb{I}$. Physically, this constraint enforces the fact that, if, for example, the scattering medium is illuminated by a plane wave incident upon the left face of the medium, then the difference in energy carried by the incident and transmitted fields must be accounted for by the reflected field. In the extreme case that no light is reflected by the scattering medium, we have $\boldsymbol{\tau} = \mathbb{I}$ and the transmission matrix becomes unitary.

Suppose now that the scattering medium absorbs light. Intuitively, one would expect that the total energy carried by the transmitted and reflected fields would be less than that carried by the incident field, the difference being accounted for by absorption. In this case we would have $\boldsymbol{\rho}+\boldsymbol{\tau} \prec \mathbb{I}$, where the notation $\mathbf{A} \prec \mathbf{B}$ means that $\mathbf{A} - \mathbf{B}$ is negative definite. Since $\boldsymbol{\rho}$ and $\boldsymbol{\tau}$ are diagonal matrices, however, this simply means that each element of $\boldsymbol{\rho} + \boldsymbol{\tau}$ is less than unity. Similar considerations carry over to the entire scattering matrix. For an absorbing medium we would expect the scattering matrix to be 'sub-unitary', i.e. $\bar{\mathbf{S}}_{pp}^\dagger \bar{\mathbf{S}}_{pp} \prec \mathbb{I}$. If, on the other hand, there were gain within the medium, we may instead expect that the scattering matrix is 'super-unitary', i.e. $\bar{\mathbf{S}}_{pp}^\dagger \bar{\mathbf{S}}_{pp} \succ \mathbb{I}$, which means that $\bar{\mathbf{S}}_{pp}^\dagger \bar{\mathbf{S}}_{pp} - \mathbb{I}$ is positive definite. For completion, if there were a combination of absorption and gain so that some modes were absorbed and others received gain, we may expect a distribution of eigenvalues of $\bar{\mathbf{S}}_{pp}^\dagger \bar{\mathbf{S}}_{pp}$ where some exceed one and others are less than one, so that all that could be said is that $\bar{\mathbf{S}}_{pp}^\dagger \bar{\mathbf{S}}_{pp} \neq \mathbb{I}$.

The other three cases for $\boldsymbol{\kappa}_i$ and $\boldsymbol{\kappa}_j$ in Eq. (3.127) can be treated similarly. After

more algebra, we obtain the equations

$$\bar{\mathbf{S}}_{pp}^{\dagger}\bar{\mathbf{S}}_{pe} = i\bar{\mathbf{S}}_{ep}^{\dagger}, \tag{3.135}$$

$$\bar{\mathbf{S}}_{pe}^{\dagger}\bar{\mathbf{S}}_{pe} = i(\bar{\mathbf{S}}_{ee}^{\dagger} - \bar{\mathbf{S}}_{ee}). \tag{3.136}$$

Introducing now the matrices $\mathbb{I}_p = \mathrm{diag}(\mathbb{I}_{8N_p+4}, \mathbb{O}_{8N_e})$ and $\mathbb{I}_e = \mathrm{diag}(\mathbb{O}_{8N_p+4}, \mathbb{I}_{8N_e})$, Eqs. (3.133)-(3.136) can be combined into the single equation

$$\bar{\mathbf{S}}^{\dagger}\mathbb{I}_p\bar{\mathbf{S}} = \mathbb{I}_p + i(\bar{\mathbf{S}}^{\dagger}\mathbb{I}_e - \mathbb{I}_e\bar{\mathbf{S}}), \tag{3.137}$$

which is the most general form of energy conservation for the scattering matrix. Our result is consistent with Ref. [234], in which energy conservation is examined in the context of a generalised optical theorem.

Consideration of Eq. (3.136) reveals some of the peculiarities of evanescent waves. Suppose for example that the field incident upon the scattering medium consists of a single evanescent component that decays towards the medium and is polarised parallel to one of the basis states (e.g. $\mathbf{e}_\phi$). Examining the on-diagonal elements of the matrices on either side of Eq. (3.136), it can be seen that the total energy radiated away from the medium by propagating waves is intimately tied to the reflected evanescent wave whose transverse wavevector is equal to that of the incident wave, but which decays away from the medium (in particular, the imaginary part of its scattering amplitude). If, due to scattering, there are any outgoing propagating waves, then this reflected evanescent wave must also be present. Conversely, if this reflected evanescent wave is not present, then there cannot be any outgoing propagating waves, neither in reflection nor transmission.

Deriving the energy conservation constraint for the discrete transfer matrix involves essentially the same type of mathematical steps as were performed for the scattering matrix. By discretising Eq. (3.44) and converting to normalised matrices,

one can obtain

$$\sum_{\boldsymbol{\kappa}_l \in K_p} \bar{\mathbf{M}}^\dagger(\boldsymbol{\kappa}_l, \boldsymbol{\kappa}_i)\boldsymbol{\Sigma}_3^z \bar{\mathbf{M}}(\boldsymbol{\kappa}_l, \boldsymbol{\kappa}_j) + \sum_{\boldsymbol{\kappa}_l \in K_e} \bar{\mathbf{M}}^\dagger(\boldsymbol{\kappa}_l, \boldsymbol{\kappa}_i)\boldsymbol{\Sigma}_3^y \bar{\mathbf{M}}(\boldsymbol{\kappa}_l, \boldsymbol{\kappa}_j) = \begin{cases} \delta_{ij}\boldsymbol{\Sigma}_3^z & \text{if } \boldsymbol{\kappa}_i \in K_p,\ \boldsymbol{\kappa}_j \in K_p, \\ \delta_{ij}\boldsymbol{\Sigma}_3^y & \text{if } \boldsymbol{\kappa}_i \in K_e,\ \boldsymbol{\kappa}_j \in K_e, \\ \mathbb{O}_6 & \text{otherwise,} \end{cases} \tag{3.138}$$

which, after a case analysis, leads to the set of equations

$$\bar{\mathbf{M}}_{pp}^\dagger \boldsymbol{\Sigma}_{4N_p+2}^z \bar{\mathbf{M}}_{pp} + \bar{\mathbf{M}}_{ep}^\dagger \boldsymbol{\Sigma}_{4N_e}^y \bar{\mathbf{M}}_{ep} = \boldsymbol{\Sigma}_{4N_p+2}^z, \tag{3.139}$$

$$\bar{\mathbf{M}}_{pp}^\dagger \boldsymbol{\Sigma}_{4N_p+2}^z \bar{\mathbf{M}}_{pe} + \bar{\mathbf{M}}_{ep}^\dagger \boldsymbol{\Sigma}_{4N_e}^y \bar{\mathbf{M}}_{ee} = \mathbb{O}, \tag{3.140}$$

$$\bar{\mathbf{M}}_{pe}^\dagger \boldsymbol{\Sigma}_{4N_p+2}^z \bar{\mathbf{M}}_{pe} + \bar{\mathbf{M}}_{ee}^\dagger \boldsymbol{\Sigma}_{4N_e}^y \bar{\mathbf{M}}_{ee} = \boldsymbol{\Sigma}_{4N_e}^y, \tag{3.141}$$

where the zero matrix in Eq. (3.140) is of size $(4N_p + 2) \times 4N_e$. Eqs. (3.139)-(3.141) can be combined into the single equation

$$\bar{\mathbf{M}}^\dagger \boldsymbol{\Omega} \bar{\mathbf{M}} = \boldsymbol{\Omega}, \tag{3.142}$$

where $\boldsymbol{\Omega} = \text{diag}(\boldsymbol{\Sigma}_{4N_p+2}^z, \boldsymbol{\Sigma}_{4N_e}^y)$. Eq. (3.142) therefore represents conservation of energy for the discrete transfer matrix.

3.3.3 Reciprocity and time reversal symmetry

As discussed previously, when energy is conserved, reciprocity and time reversal symmetry are equivalent. Taking this to be the case, in this section we shall henceforth refer to both conditions as 'reciprocity' for simplicity. We begin by deriving the reciprocity constraint for the discrete scattering matrix. Note that for the continuous scattering matrix reciprocity (Eq. (3.54)) is a considerably simpler constraint than time reversal symmetry (Eq. (3.75)), particularly as it does not involve an integral.

Once again, making the replacements $\boldsymbol{\kappa} \to \boldsymbol{\kappa}_j$, $\boldsymbol{\kappa}' \to \boldsymbol{\kappa}_i$ and multiplying Eq.

(3.54) by $\sqrt{w_i w_j/(|\gamma_i||\gamma_j|)}$ yields

$$\bar{\mathbf{S}}(\boldsymbol{\kappa}_j, \boldsymbol{\kappa}_i) = \begin{cases} \bar{\mathbf{S}}^{\mathrm{T}}(-\boldsymbol{\kappa}_i, -\boldsymbol{\kappa}_j) & \text{if } \boldsymbol{\kappa}_i, \boldsymbol{\kappa}_j \in K_p \text{ or } \boldsymbol{\kappa}_i, \boldsymbol{\kappa}_j \in K_e \\ i\bar{\mathbf{S}}^{\mathrm{T}}(-\boldsymbol{\kappa}_i, -\boldsymbol{\kappa}_j) & \text{otherwise} \end{cases} \tag{3.143}$$

Let us consider first the case where $\boldsymbol{\kappa}_i, \boldsymbol{\kappa}_j \in K_p$. As in the previous section, we again equate different blocks of Eq. (3.143) separately. Comparing top-left blocks, we have

$$\bar{\mathbf{r}}(\boldsymbol{\kappa}_j, \boldsymbol{\kappa}_i) = \bar{\mathbf{r}}(-\boldsymbol{\kappa}_i, -\boldsymbol{\kappa}_j). \tag{3.144}$$

If we pre-multiply Eq. (3.144) by $\mathbf{e}_\theta^{\mathrm{T}}(\boldsymbol{\kappa}_j, -\gamma_j)$ and post-multiply by $\mathbf{e}_\theta(\boldsymbol{\kappa}_i, \gamma_i)$, the left hand side becomes $r_{(j,i)\theta\theta}$ and the right hand side, after a bit of manipulation, becomes $r_{(-i,-j)\theta\theta}$. Repeating this for all four combinations of $\mathbf{e}_\theta$ and $\mathbf{e}_\phi$, we obtain

$$\bar{r}_{(j,i)\theta\theta} = \bar{r}_{(-i,-j)\theta\theta}, , \tag{3.145}$$

$$\bar{r}_{(j,i)\theta\phi} = -\bar{r}_{(-i,-j)\phi\theta}, \tag{3.146}$$

$$\bar{r}_{(j,i)\phi\theta} = -\bar{r}_{(-i,-j)\theta\phi}, \tag{3.147}$$

$$\bar{r}_{(j,i)\phi\phi} = \bar{r}_{(-i,-j)\phi\phi}. \tag{3.148}$$

Eqs. (3.145)-(3.148) are equivalent to the single matrix relation

$$\bar{\mathbf{r}}_{(j,i)} = \bar{\mathbf{r}}^{\mathrm{R}}_{(-i,-j)}, \tag{3.149}$$

where we have introduced the reciprocal operator R, which we define such that if $[\mathbf{A}]_{mn}$ is the (m, n) element of the matrix $\mathbf{A}$, then

$$[\mathbf{A}^{\mathrm{R}}]_{mn} = [\mathbf{A}]_{nm}(-1)^{m+n}. \tag{3.150}$$

This particular symmetry of the reflection matrix is a well-known result in scattering theory and is sometimes referred to as the backscattering theorem [28]. The operator R has also been discussed previously in the context of Jones matrices for stacks of plane parallel plates [235].

By now carefully considering the structure of the matrix $\bar{\mathbf{r}}_{pp}$, it follows from Eq. (3.149) that

$$\bar{\mathbf{r}}_{pp} = \boldsymbol{\sigma}_p \bar{\mathbf{r}}^{\mathrm{R}}_{pp} \boldsymbol{\sigma}_p. \tag{3.151}$$

Letting

$$\mathbf{J}_n = \begin{pmatrix} 0 & & 1 \\ & \iddots & \\ 1 & & 0 \end{pmatrix} \tag{3.152}$$

be the $n \times n$ exchange matrix, i.e. the matrix with n ones on its anti-diagonal and zeroes elsewhere, $\boldsymbol{\sigma}_p$ is defined as

$$\boldsymbol{\sigma}_p = \mathbf{J}_{2N_p+1} \otimes \mathbb{I}_2 = \begin{pmatrix} \mathbb{O} & & \mathbb{I}_2 \\ & \iddots & \\ \mathbb{I}_2 & & \mathbb{O} \end{pmatrix}, \tag{3.153}$$

which contains $2N_p + 1$ copies of the 2×2 identity matrix on its anti-diagonal. The effect of multiplying a matrix on either side by $\boldsymbol{\sigma}_p$ is to reflect the positions of all 2×2 sub-matrices horizontally and vertically about the central rows and columns of the matrix, but to leave the sub-matrices themselves unchanged. This is necessary so that Eq. (3.151) correctly equates sub-matrices of $\bar{\mathbf{r}}_{pp}$ that are related by an inversion of transverse wavevectors. We point out that this particular form of Eq. (3.151) is, to some extent, an artefact of the way in which the modes are ordered in K_p. Of course, given some different ordering, a different transformation would be required to achieve the equivalent of matching inverse wavevector pairs. In any case, different versions of these equations will always be related by unitary transformations, and the basic forms of the equations will remain unchanged. Considering the other sub-matrices of $\bar{\mathbf{S}}$, we find

$$\bar{\mathbf{t}}_{pp} = \boldsymbol{\sigma}_p \bar{\mathbf{t}}'^{\mathrm{R}}_{pp} \boldsymbol{\sigma}_p, \tag{3.154}$$

$$\bar{\mathbf{r}}'_{pp} = \boldsymbol{\sigma}_p \bar{\mathbf{r}}'^{\mathrm{R}}_{pp} \boldsymbol{\sigma}_p, \tag{3.155}$$

which can be combined into the single equation

$$\bar{\mathbf{S}}_{pp} = \boldsymbol{\sigma}_{pp}\bar{\mathbf{S}}^{\mathrm{R}}_{pp}\boldsymbol{\sigma}_{pp}, \tag{3.156}$$

where $\boldsymbol{\sigma}_{pp} = \mathbb{I}_2 \otimes \boldsymbol{\sigma}_p = \mathbb{I}_2 \otimes \mathbf{J}_{2N_p+1} \otimes \mathbb{I}_2$. If we similarly introduce $\boldsymbol{\sigma}_{ee} = \mathbb{I}_2 \otimes \mathbf{J}_{2N_e} \otimes \mathbb{I}_2$, we can further derive

$$\bar{\mathbf{S}}_{pe} = \boldsymbol{\sigma}_{pp} i\bar{\mathbf{S}}^{\mathrm{R}}_{ep}\boldsymbol{\sigma}_{ee}, \tag{3.157}$$

$$\bar{\mathbf{S}}_{ee} = \boldsymbol{\sigma}_{ee}\bar{\mathbf{S}}^{\mathrm{R}}_{ee}\boldsymbol{\sigma}_{ee}. \tag{3.158}$$

Finally, Eqs. (3.156)-(3.158) can be combined into the single equation

$$\bar{\mathbf{S}} = \boldsymbol{\omega}'^{*}\bar{\mathbf{S}}^{\mathrm{R}}\boldsymbol{\omega}', \tag{3.159}$$

$$\boldsymbol{\omega}' = \begin{pmatrix} \mathbb{I}_2 \otimes \mathbf{J}_{2N_p+1} \otimes \mathbb{I}_2 & \mathbb{O} \\ \mathbb{O} & i\mathbb{I}_2 \otimes \mathbf{J}_{2N_e} \otimes \mathbb{I}_2 \end{pmatrix}. \tag{3.160}$$

Eq. (3.159) thus expresses reciprocity for the scattering matrix.

It is worth pointing out that the effect of the reciprocal operator R can also be achieved using a combination of the matrix transpose and multiplication by a fixed matrix that intersperses negative signs in appropriate positions within the scattering matrix. In particular, it can be shown for a general matrix $\mathbf{A}$ that

$$\mathbf{A}^{\mathrm{R}} = \mathbf{K}\mathbf{A}^{\mathrm{T}}\mathbf{K}, \tag{3.161}$$

$$\mathbf{K} = \mathbb{I} \otimes \boldsymbol{\Sigma}^z_1, \tag{3.162}$$

where the size of $\mathbb{I}$ is half that of the matrix $\mathbf{A}$. With this in mind, Eq. (3.159) can be written in the alternate form

$$\bar{\mathbf{S}} = \boldsymbol{\omega}^{*}\bar{\mathbf{S}}^{\mathrm{T}}\boldsymbol{\omega}, \tag{3.163}$$

$$\boldsymbol{\omega} = \begin{pmatrix} \mathbb{I}_2 \otimes \mathbf{J}_{2N_p+1} \otimes \boldsymbol{\Sigma}^z_1 & \mathbb{O} \\ \mathbb{O} & i\mathbb{I}_2 \otimes \mathbf{J}_{2N_e} \otimes \boldsymbol{\Sigma}^z_1 \end{pmatrix}. \tag{3.164}$$

Reciprocity for the transfer matrix can be derived mostly simply by beginning

with time reversal invariance for the continuous transfer matrix (Eq. (3.76)), which is notably simpler than the reciprocity constraint (Eq. (3.61)). Once again, we perform similar steps to those taken in the scattering matrix derivation, eventually arriving at the equations

$$\bar{\mathbf{M}}_{pp} = \boldsymbol{\sigma}^x_{pp}\bar{\mathbf{M}}^{\dagger\mathrm{R}}_{pp}\boldsymbol{\sigma}^x_{pp}, \tag{3.165}$$

$$\bar{\mathbf{M}}_{pe} = \boldsymbol{\sigma}^x_{pp}\bar{\mathbf{M}}^{\dagger\mathrm{R}}_{pe}\boldsymbol{\sigma}_{ee}, \tag{3.166}$$

$$\bar{\mathbf{M}}_{ep} = \boldsymbol{\sigma}_{ee}\bar{\mathbf{M}}^{\dagger\mathrm{R}}_{ep}\boldsymbol{\sigma}^x_{pp}, \tag{3.167}$$

$$\bar{\mathbf{M}}_{ee} = \boldsymbol{\sigma}_{ee}\bar{\mathbf{M}}^{\dagger\mathrm{R}}_{pp}\boldsymbol{\sigma}_{ee}, \tag{3.168}$$

where

$$\boldsymbol{\sigma}^x_{pp} = \boldsymbol{\Sigma}^x_{4N_p+2}\boldsymbol{\sigma}_{pp} = (\boldsymbol{\Sigma}^x_1 \otimes \mathbf{I}_{4N_p+2})(\mathbb{I}_2 \otimes \mathbf{J}_{2N_p+1} \otimes \mathbb{I}_2) = \boldsymbol{\Sigma}^x_1 \otimes \mathbf{J}_{2N_p+1} \otimes \mathbb{I}_2. \tag{3.169}$$

The final equality in Eq. (3.169) follows from the identity

$$(\mathbf{A} \otimes \mathbf{B})(\mathbf{C} \otimes \mathbf{D}) = (\mathbf{AC}) \otimes (\mathbf{BD}). \tag{3.170}$$

Eqs. (3.165)-(3.168) can be combined into the single equation

$$\bar{\mathbf{M}} = \boldsymbol{\eta}'\bar{\mathbf{M}}^{\dagger\mathrm{R}}\boldsymbol{\eta}', \tag{3.171}$$

$$\boldsymbol{\eta}' = \begin{pmatrix} \boldsymbol{\Sigma}^x_1 \otimes \mathbf{J}_{2N_p+1} \otimes \mathbb{I}_2 & \mathbb{O} \\ \mathbb{O} & \mathbb{I}_2 \otimes \mathbf{J}_{2N_e} \otimes \mathbb{I}_2 \end{pmatrix}. \tag{3.172}$$

Eq. (3.171) hence embodies reciprocity for the discrete transfer matrix. In light of the previous discussion regarding the reciprocal operator, Eq. (3.171) can be written in the alternate form

$$\bar{\mathbf{M}} = \boldsymbol{\eta}\bar{\mathbf{M}}^*\boldsymbol{\eta}, \tag{3.173}$$

$$\boldsymbol{\eta} = \begin{pmatrix} \boldsymbol{\Sigma}^x_1 \otimes \mathbf{J}_{2N_p+1} \otimes \boldsymbol{\Sigma}^z_1 & \mathbb{O} \\ \mathbb{O} & \mathbb{I}_2 \otimes \mathbf{J}_{2N_e} \otimes \boldsymbol{\Sigma}^z_1 \end{pmatrix}. \tag{3.174}$$

3.3.4 Comparison with scalar equations

In this section we briefly compare the derived constraints with those that are more commonly found in the literature, which are pertinent for the scattering of scalar waves. In particular, we shall demonstrate that the more commonly presented equations follow from the general results derived here as special cases. From Refs. [3, 7, 236, 237] and others we see that, for a system that conserves energy and and is reciprocal/time reversal invariant, the matrices $\bar{\mathbf{S}}$ and $\bar{\mathbf{M}}$ obey the equations

$$\bar{\mathbf{S}}\bar{\mathbf{S}}^{\dagger} = \mathbb{I}, \tag{3.175}$$

$$\bar{\mathbf{S}}^{\mathrm{T}} = \bar{\mathbf{S}}, \tag{3.176}$$

$$\bar{\mathbf{M}}^{\dagger}\boldsymbol{\Sigma}^{z}\bar{\mathbf{M}} = \boldsymbol{\Sigma}^{z}, \tag{3.177}$$

$$\boldsymbol{\Sigma}^{x}\bar{\mathbf{M}}\boldsymbol{\Sigma}^{x} = \bar{\mathbf{M}}^{*}, \tag{3.178}$$

where $\mathbb{I}, \boldsymbol{\Sigma}^{x}$ and $\boldsymbol{\Sigma}^{z}$ are of the appropriate size. It is interesting to contrast these equations with those derived in this chapter for $\bar{\mathbf{S}}_{pp}$ and $\bar{\mathbf{M}}_{pp}$, which are given by (dropping subscripts for brevity)

$$\bar{\mathbf{S}}\bar{\mathbf{S}}^{\dagger} = \mathbb{I}, \tag{3.179}$$

$$[\mathbb{I}\otimes\mathbf{J}\otimes\boldsymbol{\Sigma}^{z}]\bar{\mathbf{S}}^{\mathrm{T}}[\mathbb{I}\otimes\mathbf{J}\otimes\boldsymbol{\Sigma}^{z}] = \bar{\mathbf{S}}, \tag{3.180}$$

$$\bar{\mathbf{M}}^{\dagger}\boldsymbol{\Sigma}^{z}\bar{\mathbf{M}} = \boldsymbol{\Sigma}^{z}, \tag{3.181}$$

$$[\boldsymbol{\Sigma}^{x}\otimes\mathbf{J}\otimes\boldsymbol{\Sigma}^{z}]\bar{\mathbf{M}}[\boldsymbol{\Sigma}^{x}\otimes\mathbf{J}\otimes\boldsymbol{\Sigma}^{z}] = \bar{\mathbf{M}}^{*}. \tag{3.182}$$

Though the conservation of energy constraints are equivalent, there are obvious differences between the reciprocity constraints, which is a result of the intricate block structure of our matrices.

Eqs. (3.175)-(3.178) are valid for scalar waves. A scalar wave formalism is appropriate when there is no change in polarisation state induced by the scattering medium. For this to be the case within the formalism outlined in this chapter, it is necessary for the off-diagonal elements of each 2×2 sub-matrix within $\bar{\mathbf{S}}$ and $\bar{\mathbf{M}}$ to be zero. In this case, the $\boldsymbol{\Sigma}_{1}^{z}$ terms appearing at the end of the Kronecker products in Eqs. (3.180) and (3.182) no longer play a role and can be discarded. Of course,

this would mean that the sizes of the scattering and transfer matrices would halve.

Eqs. (3.175)-(3.178) are valid in situations for which each mode has a wavevector with a unique z component. In other words, there are no two modes whose wavevectors have the same z components, but different transverse components. What is especially relevant for the comparison being made here is that such models make no distinction between the two modes with wavevectors $(\boldsymbol{\kappa}, \gamma)^{\mathrm{T}}$ and $(-\boldsymbol{\kappa}, \gamma)^{\mathrm{T}}$. If this were enforced within the formalism presented in this chapter, all transverse wavevectors in the sets defined in Eqs. (3.78) and (3.79) containing a minus sign would become extraneous and could be removed. Moreover, the use of the exchange matrices $\mathbf{J}$ in Eqs. (3.180) and (3.182) to correctly associate sub-matrices of $\bar{\mathbf{S}}$ and $\bar{\mathbf{M}}$ that describe scattering between modes with inverse transverse wavevectors would no longer be necessary and, after removing degenerate transverse wavevectors from K, the exchange matrices appearing in Eqs. (3.164) and (3.174) would be replaced by identity matrices of the appropriate size.

Overall, the factors multiplying $\bar{\mathbf{S}}^{\mathrm{T}}$ in Eq. (3.180) would reduce to identity matrices, thus recovering Eq. (3.176). Similarly, the factors multiplying $\bar{\mathbf{M}}^{\mathrm{T}}$ in Eq. (3.182) would reduce to $\boldsymbol{\Sigma}^{x}$, and the equation would hence coincide with Eq. (3.178). Thus, we see that the equations commonly seen in the literature are special cases of the more general results presented here.

3.4 Algebraic properties of transfer matrices

In this section we shall examine in more detail some of the mathematical consequences of these constraints imposed upon the transfer matrix. In particular, we shall show that the transfer matrices form a matrix Lie group and derive the algebraic properties of its corresponding Lie algebra. These algebraic properties will allow for a novel matrix parametrisation that will be important in Chapter 6, where it will be used to randomly generate transfer matrices for numerical simulations of random scattering media.

3.4.1 Group structure

We shall now demonstrate that the transfer matrices, under the constraints of energy conservation and reciprocity, form a matrix Lie group, which can be achieved by showing that the transfer matrices are a closed subgroup of the general linear group, i.e. the set of invertible matrices [238]. We note that, by the form of Eqs. (3.142) and (3.171), there are clear parallels between our transfer matrices and so-called 'pseudounitary' group $SU(N,N)$, which is isomorphic to the symplectic group [236]. The constant matrices appearing in our equations, however, are different to those in the classical group definitions.

Suppose that the set of transfer matrices satisfying Eqs. (3.142) and (3.171) is denoted by $\mathcal{G}$. For convenience, these equations are $\bar{\mathbf{M}}^\dagger\boldsymbol{\Omega}\bar{\mathbf{M}} = \boldsymbol{\Omega}$ and $\bar{\mathbf{M}} = \boldsymbol{\eta}\bar{\mathbf{M}}^*\boldsymbol{\eta}$, which we shall temporarily refer to as (1) and (2) respectively. First, using the fact that $\boldsymbol{\eta}^2 = \mathbb{I}$, it is trivial to see that both equations are satisfied by $\bar{\mathbf{M}} = \mathbb{I}$ and hence $\mathbb{I} \in \mathcal{G}$. Physically, the identity matrix describes a medium that causes no change in amplitude, phase or polarisation state, such as would be the case if no scatterers were present, or if the slab had zero thickness. Taking determinants of both equations yields $|\det(\bar{\mathbf{M}})|^2 = 1$ and $\det(\bar{\mathbf{M}}) = \det(\bar{\mathbf{M}})^*$, from which it follows that $\det(\bar{\mathbf{M}}) = \pm 1$. In fact, more sophisticated algebraic arguments [239] show that $\det(\bar{\mathbf{M}}) = 1$, although in any case it is clear that $\det(\bar{\mathbf{M}}) \neq 0$ and thus $\bar{\mathbf{M}}$ is invertible. Now, starting from (1), pre-multiplication by $(\bar{\mathbf{M}}^\dagger)^{-1}$ and post-multiplication by $\bar{\mathbf{M}}^{-1}$ yields $\boldsymbol{\Omega} = (\bar{\mathbf{M}}^\dagger)^{-1}\boldsymbol{\Omega}\bar{\mathbf{M}}^{-1} = (\bar{\mathbf{M}}^{-1})^\dagger\boldsymbol{\Omega}\bar{\mathbf{M}}^{-1}$, showing that $\bar{\mathbf{M}}^{-1}$ satisfies (1). A similar argument shows that $\bar{\mathbf{M}}^{-1}$ satisfies (2) and hence $\bar{\mathbf{M}}^{-1} \in \mathcal{G}$.

It remains to show that $\mathcal{G}$ is closed under matrix multiplication. Let $\bar{\mathbf{M}}_1$ and $\bar{\mathbf{M}}_2$ be any two matrices satisfying (1). Then

$$(\bar{\mathbf{M}}_1\bar{\mathbf{M}}_2)^\dagger\boldsymbol{\Omega}\bar{\mathbf{M}}_1\bar{\mathbf{M}}_2 = \bar{\mathbf{M}}_2^\dagger(\bar{\mathbf{M}}_1^\dagger\boldsymbol{\Omega}\bar{\mathbf{M}}_1)\bar{\mathbf{M}}_2 = \bar{\mathbf{M}}_2^\dagger\boldsymbol{\Omega}\bar{\mathbf{M}}_2 = \boldsymbol{\Omega}, \tag{3.183}$$

and thus the product $\bar{\mathbf{M}}_1\bar{\mathbf{M}}_2$ satisfies (1). Similarly, if $\bar{\mathbf{M}}_1$ and $\bar{\mathbf{M}}_2$ satisfy (2), then

$$\boldsymbol{\eta}\bar{\mathbf{M}}_1^*\bar{\mathbf{M}}_2^*\boldsymbol{\eta} = \boldsymbol{\eta}\bar{\mathbf{M}}_1^*\boldsymbol{\eta}\boldsymbol{\eta}\bar{\mathbf{M}}_2^*\boldsymbol{\eta} = \bar{\mathbf{M}}_1\bar{\mathbf{M}}_2, \tag{3.184}$$

which shows that $\bar{\mathbf{M}}_1\bar{\mathbf{M}}_2$ satisfies (2). Thus we see that $\mathcal{G}$ is closed under multiplication, which, combined with the previous properties, shows that $\mathcal{G}$ is indeed a closed subgroup of the general linear group and is hence a matrix Lie group.

We finish this section by noting that, when considering only propagating waves, energy conservation alone restricts the set of scattering matrices to be the unitary group. Reciprocity, however, which requires scattering matrices to be symmetric, destroys this group structure with respect to standard matrix multiplication. This can be seen by noting that the set of symmetric, unitary matrices is not closed under multiplication, since

$$(\mathbf{S}_1\mathbf{S}_2)^{\mathrm{T}} = \mathbf{S}_2^{\mathrm{T}}\mathbf{S}_1^{\mathrm{T}} = \mathbf{S}_2\mathbf{S}_1 \neq \mathbf{S}_1\mathbf{S}_2. \tag{3.185}$$

One can, however, define a composition operator for scattering matrices, such as that which appears later in Eq. (6.23), with respect to which the scattering matrices are a closed set.

3.4.2 Differential transfer matrix

Associated with the group of transfer matrices $\mathcal{G}$ is the corresponding Lie algebra $\mathfrak{g}$. For our purposes, this can be thought of as the set of matrices whose matrix exponentials yield transfer matrices. Thus, if $\boldsymbol{\epsilon} \in \mathfrak{g}$, then $\exp(\boldsymbol{\epsilon}) \in \mathcal{G}$, where the matrix exponential is defined as

$$\exp(\mathbf{A}) = \sum_{n=0}^{\infty} \frac{1}{n!}\mathbf{A}^n = \mathbb{I} + \mathbf{A} + \frac{1}{2}\mathbf{A}^2 + \dots. \tag{3.186}$$

Suppose that the matrix $\mathbf{A}$ is in some sense close to the zero matrix. More formally, we may have that $||\mathbf{A}|| \ll \delta$ for some matrix norm, where $\delta \ll 1$ is some small quantity. Then, since $||\mathbf{A}^n|| \leq ||\mathbf{A}||^n \leq \delta^n$, which becomes vanishing small for large n, large powers of $\mathbf{A}$ become increasingly negligible and the series can be truncated to give

$$\bar{\mathbf{M}} = \exp(\boldsymbol{\epsilon}) \approx \mathbb{I} + \boldsymbol{\epsilon}. \tag{3.187}$$

In this limit, the matrix $\boldsymbol{\epsilon}$ can thus be thought of as a small perturbation of the transfer matrix from the identity matrix. Physically, $\boldsymbol{\epsilon}$ thus describes the effect of a weak scattering medium, such as a thin slab containing weakly scattering particles. Elements of Lie algebras are sometimes referred to as infinitesimal generators. We shall however refer to $\boldsymbol{\epsilon}$ as a 'differential transfer matrix', in accordance with the differential Jones and Mueller matrices in the polarisation literature [240].

The differential transfer matrices have their own set of constraints enforced by the energy conservation, reciprocity and time reversal symmetry. Fortunately, these can be derived rather readily from the symmetries of the transfer matrix. Writing $\bar{\mathbf{M}} = \exp(\boldsymbol{\epsilon})$, energy conservation becomes

$$\boldsymbol{\Omega}\exp(\boldsymbol{\epsilon})\boldsymbol{\Omega} = [\exp(\boldsymbol{\epsilon})]^{-1}. \tag{3.188}$$

Now, using the facts that $\boldsymbol{\Omega} = \boldsymbol{\Omega}^{-1}$, $\boldsymbol{\Omega}\exp(\boldsymbol{\epsilon})\boldsymbol{\Omega} = \exp(\boldsymbol{\Omega}\boldsymbol{\epsilon}\boldsymbol{\Omega})$ and $[\exp(\boldsymbol{\epsilon})]^{-1} = \exp(-\boldsymbol{\epsilon})$ [238], Eq. (3.188) becomes

$$-\boldsymbol{\epsilon}^{\dagger} = \boldsymbol{\Omega}\boldsymbol{\epsilon}\boldsymbol{\Omega}. \tag{3.189}$$

Similar calculations show that $\boldsymbol{\epsilon}$ also satisfies the same reciprocity relation as the transfer matrix, i.e.

$$\boldsymbol{\epsilon} = \boldsymbol{\eta}\boldsymbol{\epsilon}^{*}\boldsymbol{\eta}. \tag{3.190}$$

Suppose now that $\boldsymbol{\epsilon}$ has block structure

$$\boldsymbol{\epsilon} = \begin{pmatrix} \boldsymbol{\epsilon}^{pp} & \boldsymbol{\epsilon}^{pe} \\ \boldsymbol{\epsilon}^{ep} & \boldsymbol{\epsilon}^{ee} \end{pmatrix} = \begin{pmatrix} \boldsymbol{\epsilon}_{\alpha}^{pp} & \boldsymbol{\epsilon}_{\beta}^{pp} & \boldsymbol{\epsilon}_{\alpha}^{pe} & \boldsymbol{\epsilon}_{\beta}^{pe} \\ \boldsymbol{\epsilon}_{\gamma}^{pp} & \boldsymbol{\epsilon}_{\delta}^{pp} & \boldsymbol{\epsilon}_{\gamma}^{pe} & \boldsymbol{\epsilon}_{\delta}^{pe} \\ \boldsymbol{\epsilon}_{\alpha}^{ep} & \boldsymbol{\epsilon}_{\beta}^{ep} & \boldsymbol{\epsilon}_{\alpha}^{ee} & \boldsymbol{\epsilon}_{\beta}^{ee} \\ \boldsymbol{\epsilon}_{\gamma}^{ep} & \boldsymbol{\epsilon}_{\delta}^{ep} & \boldsymbol{\epsilon}_{\gamma}^{ee} & \boldsymbol{\epsilon}_{\delta}^{ee} \end{pmatrix}, \tag{3.191}$$

where, as before p and e refer to propagating and evanescent waves. Expanding Eqs. (3.189) and (3.190) into their block forms and equating different blocks, we

find after some algebra that the blocks of $\boldsymbol{\epsilon}$ can be written as

$$\boldsymbol{\epsilon}^{pp} = \begin{pmatrix} \boldsymbol{\epsilon}_\alpha^{pp} & \boldsymbol{\epsilon}_\beta^{pp} \\ \boldsymbol{\epsilon}_\beta^{pp\dagger} & (\mathbf{J}^p \otimes \boldsymbol{\Sigma}_1^z)\boldsymbol{\epsilon}_\alpha^{pp*}(\mathbf{J}^p \otimes \boldsymbol{\Sigma}_1^z) \end{pmatrix}, \tag{3.192}$$

$$\boldsymbol{\epsilon}^{pe} = \begin{pmatrix} \boldsymbol{\epsilon}_\alpha^{pe} & \boldsymbol{\epsilon}_\beta^{pe} \\ (\mathbf{J}^p \otimes \boldsymbol{\Sigma}_1^z)\boldsymbol{\epsilon}_\alpha^{pe*}(\mathbf{J}^e \otimes \boldsymbol{\Sigma}_1^z) & (\mathbf{J}^p \otimes \boldsymbol{\Sigma}_1^z)\boldsymbol{\epsilon}_\beta^{pe*}(\mathbf{J}^e \otimes \boldsymbol{\Sigma}_1^z) \end{pmatrix}, \tag{3.193}$$

$$\boldsymbol{\epsilon}^{ep} = \begin{pmatrix} i\boldsymbol{\epsilon}_\beta^{pe\dagger} & -i(\mathbf{J}^e \otimes \boldsymbol{\Sigma}_1^z)\boldsymbol{\epsilon}_\beta^{pe\mathrm{T}}(\mathbf{J}^p \otimes \boldsymbol{\Sigma}_1^z) \\ -i\boldsymbol{\epsilon}_\alpha^{pe\dagger} & i(\mathbf{J}^e \otimes \boldsymbol{\Sigma}_1^z)\boldsymbol{\epsilon}_\alpha^{pe\mathrm{T}}(\mathbf{J}^p \otimes \boldsymbol{\Sigma}_1^z) \end{pmatrix}, \tag{3.194}$$

$$\boldsymbol{\epsilon}^{ee} = \begin{pmatrix} \boldsymbol{\epsilon}_\alpha^{ee} & \boldsymbol{\epsilon}_\beta^{ee} \\ \boldsymbol{\epsilon}_\gamma^{ee} & -\boldsymbol{\epsilon}_\alpha^{ee\dagger} \end{pmatrix}, \tag{3.195}$$

where $\mathbf{J}^p = \mathbf{J}_{2N_p+1}$ and $\mathbf{J}^e = \mathbf{J}_{2N_e}$. We see that only 7 of the 16 sub-blocks, namely $\boldsymbol{\epsilon}_\alpha^{pp}, \boldsymbol{\epsilon}_\beta^{pp}, \boldsymbol{\epsilon}_\alpha^{pe}, \boldsymbol{\epsilon}_\beta^{pe}, \boldsymbol{\epsilon}_\alpha^{ee}, \boldsymbol{\epsilon}_\beta^{ee}$ and $\boldsymbol{\epsilon}_\gamma^{ee}$ are independent. Furthermore, these sub-blocks satisfy the equations

$$\boldsymbol{\epsilon}_\alpha^{pp\dagger} = -\boldsymbol{\epsilon}_\alpha^{pp}, \tag{3.196}$$

$$\boldsymbol{\epsilon}_\beta^{pp} = (\mathbf{J}^p \otimes \boldsymbol{\Sigma}_1^z)\boldsymbol{\epsilon}_\beta^{pp\mathrm{T}}(\mathbf{J}^p \otimes \boldsymbol{\Sigma}_1^z), \tag{3.197}$$

$$\boldsymbol{\epsilon}_\beta^{ee\dagger} = \boldsymbol{\epsilon}_\beta^{ee}, \tag{3.198}$$

$$\boldsymbol{\epsilon}_\gamma^{ee\dagger} = \boldsymbol{\epsilon}_\gamma^{ee}, \tag{3.199}$$

$$\boldsymbol{\epsilon}_\alpha^{ee} = (\mathbf{J}^e \otimes \boldsymbol{\Sigma}_1^z)\boldsymbol{\epsilon}_\alpha^{ee*}(\mathbf{J}^e \otimes \boldsymbol{\Sigma}_1^z), \tag{3.200}$$

$$\boldsymbol{\epsilon}_\beta^{ee} = (\mathbf{J}^e \otimes \boldsymbol{\Sigma}_1^z)\boldsymbol{\epsilon}_\beta^{ee*}(\mathbf{J}^e \otimes \boldsymbol{\Sigma}_1^z), \tag{3.201}$$

$$\boldsymbol{\epsilon}_\gamma^{ee} = (\mathbf{J}^e \otimes \boldsymbol{\Sigma}_1^z)\boldsymbol{\epsilon}_\gamma^{ee*}(\mathbf{J}^e \otimes \boldsymbol{\Sigma}_1^z). \tag{3.202}$$

The differential transfer matrix gives a convenient parametrisation of the scattering and transfer matrices. By choosing elements of $\boldsymbol{\epsilon}$ that satisfy the symmetry constraints, one can generate a transfer and scattering matrix satisfying their corresponding symmetry constraints by taking the matrix exponential. This may be useful, as parametrisations that satisfy the symmetries of the scattering and transfer matrices are relatively difficult to construct. Unitary of $\bar{\mathbf{S}}_{pp}$, for example, consists of a large system of quadratic equations, from which it is difficult to extract a set of independent elements from which the rest of the matrix elements can be found.

The Lie algebra $\mathfrak{g}$, however, is a vector space, and a matrix $\boldsymbol{\epsilon}$ is therefore easy to construct by choosing a basis over this space. For example, inspecting Eq. (3.196) it can be seen that $\boldsymbol{\epsilon}_{\alpha}^{pp}$ is skew-Hermitian, which is an easy condition to fulfil by specifying elements either above or below (and on) the main diagonal. The other blocks of $\boldsymbol{\epsilon}$ have similar lines of symmetry that are easy to work with. Of course, physical theories about scattering are generally expressed in terms of the scattering matrix, whose elements are the most physically intuitive. In order to choose meaningful values for $\boldsymbol{\epsilon}$, it is thus necessary to know how its elements relate to those of the scattering matrix. In general, the relation between $\bar{\mathbf{M}}$ and $\boldsymbol{\epsilon}$ is opaque due to the nature of the matrix exponential. In the limit of a thin, weakly scattering medium, however, it was seen that $\boldsymbol{\epsilon}$ can be interpreted as a small perturbation to the transfer matrix. In this regime a simple connection can be made between $\boldsymbol{\epsilon}$ and $\bar{\mathbf{S}}$, which will be explored in more detail in Chapter 6.

3.5 Conclusion

To conclude, in this chapter we have introduced the scattering and transfer matrices for an arbitrary scattering medium confined to a region of space with slab geometry. The scattering and transfer matrices are defined with respect to spectra of vectorial plane waves containing both propagating and evanescent components. We have derived the constraints imposed upon these matrices by energy conservation, reciprocity and time reversal symmetry. We have demonstrated that these constraints are generalisations of the more familiar constraints presented in the literature and that the latter follow as limiting cases to those presented here.

The results derived in this chapter will be particularly important in Chapter 6, where we discuss in detail a simulation technique for generating random scattering matrices of realistic scattering media. Before this, however, we first explore the application of random matrix theory to the scattering matrix, which is the subject of the next chapter.

Chapter 4

Random matrix theory

Having introduced the scattering and transfer matrix formalisms, we are now ready to discuss random matrix theory. In Chapter 3, we saw that the elements of the scattering matrix relate the amplitudes, phases and polarisation states of waves that impinge upon a scattering medium and those that emerge from it. In order to actually determine the numerical values of these elements, a physical theory is needed for the scattering medium, which can be given, for example, in terms of the permittivity function ϵ. Once such a theory has been established, the elements of the scattering matrix can in principle be calculated using one of the methods presented in Chapter 2. In a random medium, however, ϵ is a random function of its spatial coordinates whose values may vary unpredictably from one point in space to another, as well as between different realisations of scattering media at a fixed point in space.

Analytic theories for scattering media described by random permittivity functions have been pursued for a long time, both for continuous and discrete random media. In continuous media, where there is no notion of a discrete scatterer, ϵ may vary continuously throughout all of space. For such media, one of the simplest models for ϵ is a Gaussian stationary random process [241]. Gaussian statistics are, when possible, preferable, as high order statistical moments of ϵ can be expanded in terms of two-point correlation functions using Isserlis's theorem [242]. The mean and covariance of the total electric field can be found by solving the Dyson and

Bethe-Salpeter equations respectively [243]. Although these equations are exact, they require approximations to yield analytic solutions, which limits their practical utility [244]. In statistical models for discrete scattering media, instead of specifying the statistics of ϵ, it is typical to give a probability distribution for the positions and properties of the particles within the medium. A similar pair of equations that govern the mean and covariance of the electric field can then be derived under the assumption that the positions of the particles are uncorrelated [245]. These equations, however, come with the same difficulties as in the continuous case.

Instead of trying to calculate the statistical properties of the scattering matrix elements from a more fundamental theory, random matrix theory proposes a statistical model for the scattering matrix directly, often on the basis of more universal considerations. In random matrix theory, one begins by proposing a joint probability distribution p for the elements of the scattering matrix. Given such a distribution, the statistics of the transport properties of the corresponding ensemble of scattering media, which are often expressible in terms of the eigenvalues of different blocks of the scattering matrix, can be analysed [7]. If such an approach is possible, it renders statistical analysis relatively simple and computationally quick, as once p is known there is no need for any further physical modelling or electromagnetic simulations. Rather, a generic instance of a certain class of random media can be studied by simply generating a random scattering matrix from the distribution defined by p. Transport properties of random media may be derivable analytically from the functional form of p, but even if this is not the case, statistical quantities of interest can be approximated numerically by averaging over a large enough number of scattering matrix samples.

The obvious challenge faced by random matrix theory in physics is to give a reasonable choice for the function p that accurately corresponds to a physical system. Indeed, it is not immediately obvious that this problem is any simpler than deriving the properties of the scattering matrix from a more fundamental physical theory. As discussed in Chapter 2, however, it is known by random phasor arguments that, under rather general conditions, certain aspects of the scattered field follows relatively simple Gaussian statistics due to a central limit theorem. It is therefore not unreasonable to suppose that the scattering matrix may also exhibit universal

statistical properties, at least in certain scattering regimes. It should be kept in mind, of course, that the scattering matrix is constrained by the various symmetries discussed in Chapter 3, and such constraints must therefore be respected by probabilistic models.

In this chapter we shall examine one of the simplest random matrix models, namely the circular ensembles, and explore their ramifications for the statistical properties of scattered polarised light. We shall begin by presenting some of the theoretical aspects of the circular ensembles at a level of detail that will be sufficient for subsequent calculations. We will then examine the joint statistics of the elements of matrices drawn from these ensembles and the statistics of diattenuation and retardance associated with different matrix blocks: two important polarimetric quantities that shall be defined more carefully shortly. The results in this chapter can be thought of as establishing a baseline for the ability of classical random matrix theory to model the scattering of polarised light. As shall be seen, these models are highly limited, and in later chapters we will present a more advanced statistical approach that will correspond more accurately to realistic scattering media. Results derived from the circular ensembles, however, will be seen to correspond to limiting statistics of more advanced models, and are therefore still of value. This will be explored in more detail in Chapter 6.

The results presented in this chapter is novel and were recently presented in the literature in Ref. [246].

4.1 Circular ensembles

Random matrix theory was first introduced into physics by Wigner to model the distributions of energy levels of heavy atomic elements [10]. In quantum physics, the energy levels of a system correspond to the eigenvalues of the Hamiltonian operator, which operates in an infinite dimensional Hilbert space. For practical reasons, this operator is truncated to a large, but finite dimensional matrix $\mathbf{H}$. It was postulated that the properties of atomic spectral lines, such as their mean spacing and density per unit energy interval, corresponded to the statistical properties of the eigenvalues of $\mathbf{H}$. Since there is no practical way to determine the precise form of $\mathbf{H}$ for a complex

atomic nucleus, it was instead necessary to model $\mathbf{H}$ probabilistically. Symmetry considerations reveal that $\mathbf{H}$ is a real, symmetric matrix, and several probabilistic models obeying these constraints were proposed [247]. These include, for example, the the Wishart distribution, where $\mathbf{H} = \mathbf{A}\mathbf{A}^{\mathrm{T}}$ for a random matrix $\mathbf{A}$ with real, independent Gaussian entries, and the Gaussian orthogonal ensemble, where $\mathbf{H}$ is instead generated from $\mathbf{H} = (\mathbf{A} + \mathbf{A}^{\mathrm{T}})/2$ [248]. One interesting aspect of random matrix theory is that for sufficiently large matrices, similar statistical properties tend to be observed irrespective of the underlying probability distribution. For example, the joint eigenvalue density of a symmetric or Hermitian matrix with identically distributed, independent entries, when properly normalised, is known to follow the semi-circle law, regardless of the distribution of the matrix elements [249]. This universal aspect of random matrix theory suggests that certain statistical features of random systems may be common to broad classes of problems, and may partly explain why random matrix theory has found application in such a wide range of disciplines, including for example RNA folding [250], complex networks [251] and the study of the zeros of the Riemann zeta function [252].

While the Gaussian orthogonal ensemble and the closely related Gaussian unitary and Gaussian symplectic ensembles are appropriate for modelling Hamiltonians, the matrices do not possess the correct symmetries to model the scattering matrix. A corresponding collection of ensembles appropriate for this task, known as the circular ensembles, was introduced by Dyson, again in the context of quantum physics [253, 254, 255]. Specifically, the circular ensembles model random unitary matrices, and are thus appropriate for far field scattering matrices satisfying energy conservation. Using the notation of Chapter 3, the circular ensembles model the matrix $\bar{\mathbf{S}}_{pp}$, which in this chapter we shall simply refer to as $\mathbf{S}$ for simplicity.

4.1.1 Preliminaries

The simplest of the circular ensembles is the circular unitary ensemble, which can be thought of as a uniform distribution over the unitary group. More rigorously, since the set of unitary matrices is a compact group, it is possible to establish a volume form on the unitary group that defines a corresponding uniform measure [256]. In this chapter we shall adopt similar notation to Ref. [256], so that for a

matrix $\mathbf{X}$, $\mathrm{d}\mathbf{X}$ denotes the corresponding matrix of differentials and $(\mathrm{d}\mathbf{X})$ denotes the wedge product of the independent elements of $\mathrm{d}\mathbf{X}$, which defines a volume form. The form $(\mathrm{d}\mathbf{X})$ can be thought of as an infinitesimal volume within the appropriate ensemble of matrices centred on the matrix $\mathbf{X}$. Given a way of defining volumes in matrix spaces, one can imagine the probability of sampling a matrix from some small subset of the ensemble as being the ratio of the volume of the subset to the volume of the entire matrix ensemble. This intuitive understanding can be made rigorous using measure theory.

With the preceding considerations in mind, the circular unitary ensemble is defined to be the group of unitary matrices, whose elements shall be denoted by $\mathbf{U}$, endowed with the special volume form $(\mathrm{d}_{\mathrm{H}}\mathbf{U})$, known as the Haar form, which is required to satisfy

$$(\mathrm{d}_{\mathrm{H}}\mathbf{U}) = (\mathrm{d}_{\mathrm{H}}\mathbf{U}\mathbf{V}) = (\mathrm{d}_{\mathrm{H}}\mathbf{V}\mathbf{U}) \tag{4.1}$$

for any fixed unitary matrix $\mathbf{V}$. Roughly speaking, Eq. (4.1) implies that the probability of sampling a particular unitary matrix is invariant under left and right multiplication by any other fixed matrix, and it is in this sense that the resulting probability distribution is uniform. By the nature of the uniform probability distribution, matrices drawn from the the circular unitary ensemble, in some sense, describe an isotropic ensemble of scattering media. Of course, individual matrix realisations will possess anisotropic scattering amplitudes due to random fluctuations in the values of the matrix elements. Viewing the ensemble of scattering matrices as a whole, however, all matrix elements are treated on an equal basis and there is no ensemble-wide preference for scattering into any particular channel.

The circular ensemble appropriate for unitary symmetric matrices is known as the circular orthogonal ensemble. Since matrix symmetry is equivalent to reciprocity in the case of scalar waves, as described in Eq. (3.176), this random matrix ensemble is able to describe random scattering media that obey both energy conservation and reciprocity. Unitary symmetric matrices do not comprise a group, and the invariance property of the corresponding volume form must be modified. The simplest way to approach this problem is to note that every unitary symmetric matrix $\mathbf{S}$ admits the

decomposition

$$\mathbf{S} = \mathbf{U}^{\mathrm{T}}\mathbf{U}, \tag{4.2}$$

for some unitary matrix $\mathbf{U}$ [10]. The circular orthogonal ensemble can therefore be constructively defined by first sampling $\mathbf{U}$ from the circular unitary ensemble and then computing $\mathbf{S}$ from Eq. (4.2). While this construction satisfies the reciprocity symmetry for scalar waves, the circular orthogonal ensemble can also be used to generate matrices obeying the corresponding reciprocity symmetry for polarised light given by Eq. (3.163). As a reminder, the polarisation reciprocity relation is of the form $\mathbf{S} = \mathbf{K}\mathbf{S}^{\mathrm{T}}\mathbf{K}$, where $\mathbf{K} = \mathbb{I} \otimes \mathbf{T} \otimes \mathbf{\Sigma}^z$. Since $\mathbf{K}^2 = \mathbb{I}$ and $\mathbf{K} = \mathbf{K}^{\mathrm{T}}$, we have $\mathbf{K}\mathbf{S} = \mathbf{S}^{\mathrm{T}}\mathbf{K} = (\mathbf{K}\mathbf{S})^{\mathrm{T}}$, and so $\mathbf{K}\mathbf{S}$ is symmetric. Therefore, a scattering matrix $\mathbf{S}$ can be generated by first sampling $\mathbf{S}' = \mathbf{K}\mathbf{S}$ from the circular orthogonal ensemble, after which $\mathbf{S}$ can be obtained using $\mathbf{S} = \mathbf{K}\mathbf{S}'$. By considering the structure of $\mathbf{K}$, it is possible to see that multiplying a matrix by $\mathbf{K}$ is equivalent to performing a signed permutation of the matrix elements, which does not lead to an important difference in statistics between $\mathbf{S}$ and $\mathbf{S}'$. It is also worth noting that the circular orthogonal ensemble is known to be the ensemble appropriate for the scattering of spin one particles: a class to which the photon belongs [257].

In order to study the polarisation statistics of matrices drawn from the circular orthogonal ensemble, we shall consider the joint statistics of elements lying within 2×2 blocks of $\mathbf{S}$, which, as discussed in Chapter 3, describe the scattering from one plane wave component to another. We shall henceforth refer to such a block by $\mathbf{T}$, which can be interpreted as a generalised Jones matrix. Due to reciprocity, blocks that lie on the anti-diagonals of the reflection matrices satisfy the symmetry property $\mathbf{T} = \mathbf{T}^{\mathrm{R}}$, which is equivalent to the condition $T_{12} = -T_{21}$. These blocks describe backscattering in the direction opposite to the incident wavevector and, due to their symmetry, have different statistical propreties to other Jones matrices located elsewhere within the scattering matrix. To keep track of which type of block is being considered, we shall introduce the parameter α, where $\alpha = 1$ for the aforementioned back-scattering blocks and $\alpha = 2$ for all other blocks.

The statistical moments of elements of matrices drawn from the circular orthog-

onal ensemble are well known [258]. For the matrix $\mathbf{T}$, we have

$$\langle T_{ij} \rangle = 0, \tag{4.3}$$

for $1 \leq i, j \leq 2$, independent of α. In addition, we have [258]

$$\langle T_{ij} T_{kl}^{*} \rangle = \begin{cases} \frac{\delta_{ik}\delta_{jl}(1+2\delta_{ij})-\delta_{il}\delta_{jk}}{N+1} & \text{if } \alpha = 1, \\ \frac{\delta_{ik}\delta_{jl}}{N+1} & \text{if } \alpha = 2, \end{cases} \tag{4.4}$$

where N is the size of the scattering matrix. The averages in Eq. (4.4) are taken over the circular orthogonal ensemble, i.e. they are integrated over the ensemble with respect to the measure induced by the Haar form. Consider for example the simple case $i = j = k = l = 1$, which corresponds to looking at the statistics of the top-left element of $\mathbf{T}$. The cross-correlations in Eq. (4.4) then become autocorrelations and we see that $\langle |T_{11}|^2 \rangle_{\alpha=1} = 2/(N+1)$ and $\langle |T_{11}|^2 \rangle_{\alpha=2} = 1/(N+1)$. The square modulus of a scattering matrix element can be interpreted physically as the probability of scattering between the pair of modes associated with the matrix element. Evidently there is a factor of two enhancement in the intensity of waves scattered in the back-scattering direction opposite to the incident wave, which can be interpreted physically as a manifestation of the coherent backscattering effect. It is also noteworthy that if $i = k = 1$ and $j = l = 2$, or vice versa, then for off-diagonal terms we find for both values of α that $\langle |T_{12}|^2 \rangle = \langle |T_{21}|^2 \rangle = 1/(N+1)$. Since there are a total of N modes, summing the square moduli of the scattering matrix elements over a column or row gives a total of one, as expected by energy conservation. The fact that each element of $\mathbf{S}$ away from the backscattering direction has the same associated scattering probability, namely $1/(N+1)$, is a reflection of the isotropy of the circular ensembles, as previously mentioned.

For each 2×2 block $\mathbf{T}$ of $\mathbf{S}$, one can define a corresponding ensemble average Mueller matrix $\langle \mathbf{M} \rangle$. Each realisation of $\mathbf{T}$ has a corresponding Jones-Mueller matrix $\mathbf{M}$ [240]. Averaging these Jones-Mueller matrices over the circular orthogonal ensemble then yields $\langle \mathbf{M} \rangle$. It follows from Eq. (4.4) that for $\alpha = 2$, the elements of $\mathbf{T}$ are uncorrelated, which implies that the average Mueller matrix associated with the ensemble of $\mathbf{T}$ matrices is that of a pure depolariser, i.e. $\langle \mathbf{M} \rangle = \mathrm{diag}(1, 0, 0, 0)$.

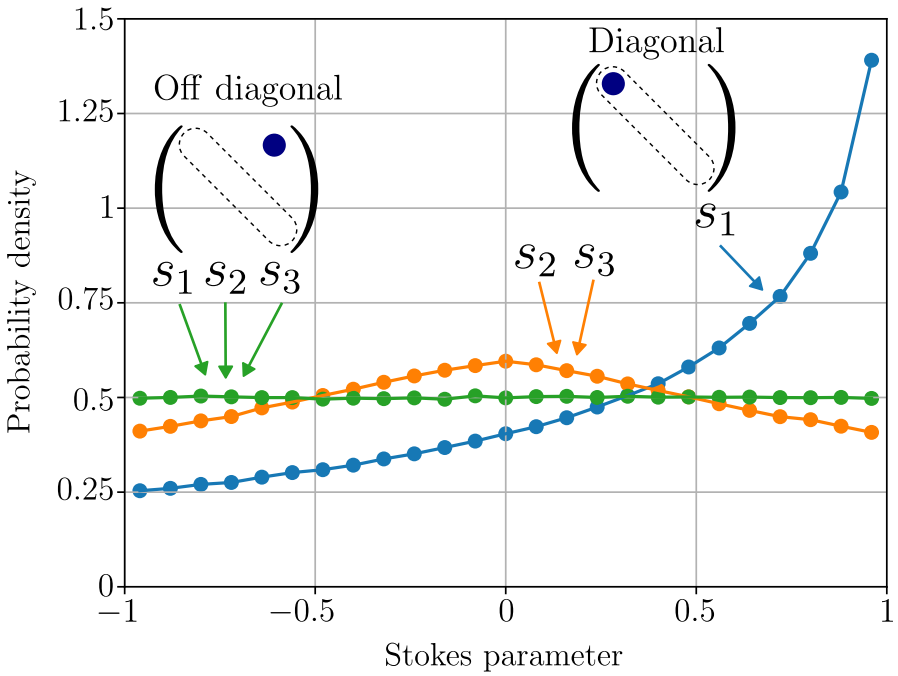

Figure 4.1: Histograms of scattered normalised Stokes parameters in the backscattering direction and a non-backscattering direction for incident x polarised light. Blue and orange data correspond to the backscattering direction, while green data correspond to a non-backscattering direction.

It is worth emphasising that, for a given scattering matrix and incident field, the scattered field is a fully polarised, random polarisation state. The ensemble average Stokes vector of the scattered field, however, is that of fully depolarised light, irrespective of the incident field. In fact, numerical analysis suggests that, for any incident polarisation state, the polarisation states of the scattered field for different scattering matrix realisations are distributed uniformly over the Poincaré sphere.

For $\alpha = 1$, it can instead be shown that $\langle \mathbf{M} \rangle = \mathrm{diag}(1, 1/3, -1/3, 1/3)$. In this case, the average Mueller matrix corresponds to a partial depolariser, which reduces the degree of polarisation of any fully polarised incident state to 1/3. The retention of some degree of polarisation can be understood by noting that, as previously shown, the squared absolute values of the diagonal elements of $\mathbf{T}$ are, on average, twice as large as those of the off-diagonal terms. These elements correspond to scattering into the same polarisation state as the incident wave, i.e. the co-polarised channel. There is thus is a preference for the scattered polarisation state to be parallel to the incident polarisation state, which results in a non-uniform distribution of scattered polarisation states. This can be confirmed by numerical tests, which

show that, for any incident polarisation state, the distribution of the scattered polarisation states on the Poincaré sphere peaks at the incident polarisation state, about which it spreads symmetrically. This behaviour is demonstrated in Figure 4.1, which shows the probability distributions of the scattered Stokes parameters in the backscattering direction and a non-backscattering direction. In particular, we show the normalised scattered Stokes parameters, defined by $s_i = S_i/S_0$, for an incident plane wave polarised in the x direction, i.e. with an incident normalised Stokes vector of $\mathbf{s} = (1, 1, 0, 0)^{\mathrm{T}}$. In the backscattering direction, as described by a diagonal block of the scattering matrix, the blue curve shows the density for s_1, while the orange curve shows the density for both s_2 and s_3, which are equal by symmetry. Collectively, the probability density is highest for $\mathbf{s} = (1, 1, 0, 0)^{\mathrm{T}}$, which is equal to the incident normalised Stokes vector. The green data show the densities of the scattered Stokes parameters in a non-backscattering direction, which is uniform for all three components.

4.1.2 Diattenuation and retardance

In assessing the scattering of polarised light, diattenuation and retardance are two frequently discussed quantities that give a simple description of how the change in amplitude and phase of an incident wave depends on the incident polarisation state. Diattenuation and retardance are associated with a Jones matrix and can be defined using the matrix polar decomposition. Any Jones matrix can be factorised as

$$\mathbf{T} = \mathbf{T}_R \mathbf{T}_D, \tag{4.5}$$

where $\mathbf{T}_D = \sqrt{\mathbf{T}^\dagger \mathbf{T}}$ is a positive semi-definite Hermitian matrix and $\mathbf{T}_R = \mathbf{T}\mathbf{T}_D^{-1}$ is a unitary matrix [259]. $\mathbf{T}$ also admits a reverse polar decomposition $\mathbf{T} = \mathbf{T}'_D \mathbf{T}_R$, where $\mathbf{T}'_D = \sqrt{\mathbf{T}\mathbf{T}^\dagger}$. For our purposes however, either choice of polar decomposition leads to the same results and we shall hence proceed with that of Eq. (4.5). The

diattenuation D and retardance R associated with $\mathbf{T}$ are defined by

$$D = \frac{|s_1^2 - s_2^2|}{s_1^2 + s_2^2}, \tag{4.6}$$

$$R = \min\Big(|\theta_1 - \theta_2|, 2\pi - |\theta_1 - \theta_2|\Big), \tag{4.7}$$

where s_1 and s_2 are the eigenvalues of $\mathbf{T}_D$ and $\exp(i\theta_1)$ and $\exp(i\theta_2)$ are the eigenvalues of $\mathbf{T}_R$. The expression for retardance in Eq. (4.7) is slightly non-standard, but ensures that $0 \leq R \leq \pi$ when θ_1 and θ_2 are not given any particular order. The eigenvector of $\mathbf{T}_D$ with largest eigenvalue, when viewed as a unit vector on the Poincaré sphere, is known as the diattenuation vector. The diattenuation vector represents the polarisation state that is maximally transmitted (or reflected) by the scattering medium for the pair of modes associated with $\mathbf{T}$. Similarly, the eigenvector of $\mathbf{T}_R$ corresponding to the polarisation state that experiences the shortest phase delay is known as the retardance vector. Since $\mathbf{T}$ is random, both D and R are random variables that follow some pair of probability distributions.

Diattenuation is a measure of the extent to which the transmission (reflection) of light by a system depends on the incident polarisation state. When $D = 0$, all incident polarisation states are transmitted (reflected) equally, and when $D = 1$, $\mathbf{T}$ is singular and there exists a polarisation state for which the transmission (reflection) is zero. It should be emphasised that since $\mathbf{S}$ is assumed to be unitary, we are only concerned with scattering-induced diattenuation, rather than polarisation-dependent absorption. A low scattered intensity in one particular plane wave component must be compensated by a larger scattered intensity in another plane wave component so that energy is conserved overall. Similarly, retardance is a measure of the extent to which the optical path length of a system depends on the incident polarisation state.

Diattenuation and retardance may also be defined with respect to Mueller matrices using a corresponding Mueller matrix polar decomposition [260]. If the Mueller matrix is a Mueller-Jones matrix, the values obtained from the Mueller matrix coincide with those from the Jones matrix. If, however, the Mueller matrix is not a Mueller-Jones matrix, but is instead obtained from averaging some ensemble of Mueller-Jones matrices, then the resulting diattenuation and retardance values have

different meanings to their Jones matrix counterparts. While qualitatively similar, the diattenuation and retardance for an average Mueller matrix apply to the transformation of the ensemble averaged Stokes vector and are therefore fixed values, rather than random variables. As demonstrated in the previous section, for the circular orthogonal ensemble the average Mueller matrix takes the form of a pure depolariser for both values of α, and thus does not exhibit any diattenuation or retardance.

Let us now consider the statistics of D and R associated with 2×2 blocks of the scattering matrix, as defined in Eqs. (4.6) and (4.7). We found that the statistics of D and R are independent of whether the scattering matrix symmetry is of the form $\mathbf{S} = \mathbf{S}^{\mathrm{T}}$ or $\mathbf{S} = \mathbf{K}\mathbf{S}^{\mathrm{T}}\mathbf{K}$. For simplicity, we may therefore consider the former case, such that $\alpha = 1$ now corresponds to diagonal blocks of $\mathbf{S}$ that satisfy $\mathbf{T} = \mathbf{T}^{\mathrm{T}}$. For $\alpha = 1$, the joint probability density function for the elements of $\mathbf{T}$ was derived in Ref. [261]. For $\alpha = 2$, which corresponds to any arbitrary off-diagonal Jones matrix, we found numerically that, for large values of N, such matrices are statistically similar to arbitrary 2×2 blocks of matrices drawn from the circular unitary ensemble. As shall be demonstrated, this approximation holds reasonably well even for values as small as $N = 12$. The probability density function for an arbitrary 2×2 block of a matrix sampled from the circular unitary ensemble has also been derived analytically, such as in Ref. [262]. Combining these two results, the probability density function for $\mathbf{T}$ is given by (approximately in the case $\alpha = 2$)

$$p(\mathbf{T}) \sim [\det(\mathbb{I}_2 - \mathbf{T}^{\dagger}\mathbf{T})]^{\alpha(N-6+\alpha)/2}. \tag{4.8}$$

It is interesting to note that Eq. (4.8) is independent of the choice of polarisation basis, as it is invariant under the change of basis transformation $\mathbf{T} \to \mathbf{U}\mathbf{T}\mathbf{U}^{\dagger}$ for all 2×2 unitary matrices $\mathbf{U}$.

The polar decomposition is closely related to the singular value decomposition, in which $\mathbf{T}$ is factorised as

$$\mathbf{T} = \begin{cases} \mathbf{U}\boldsymbol{\Sigma}\mathbf{U}^{\mathrm{T}} & \text{if } \alpha = 1, \\ \mathbf{V}\boldsymbol{\Sigma}\mathbf{W}^{\dagger} & \text{if } \alpha = 2, \end{cases} \tag{4.9}$$

where $\mathbf{U}, \mathbf{V}$ and $\mathbf{W}$ are unitary matrices containing the singular vectors of $\mathbf{T}$ and $\mathbf{\Sigma} = \mathrm{diag}(s_1, s_2)$, which are also the singular values of $\mathbf{T}$ [263]. In the case $\alpha = 1$, we have used a special version of the singular value decomposition known as the Autonne-Takagi factorisation, which exploits the symmetry of $\mathbf{T}$ [264]. Straightforward algebra shows that $\mathbf{T}_D = \mathbf{U}^* \mathbf{\Sigma} \mathbf{U}^{\mathrm{T}}$ and $\mathbf{T}_R = \mathbf{U}\mathbf{U}^{\mathrm{T}}$ for $\alpha = 1$, and $\mathbf{T}_D = \mathbf{W}\mathbf{\Sigma}\mathbf{W}^\dagger$ and $\mathbf{T}_R = \mathbf{V}\mathbf{W}^\dagger$ for $\alpha = 2$. The diattenuation and retardance vectors are therefore closely related to the singular vectors of $\mathbf{T}$.

In order to derive the statistics of diattenuation and retardance, it will be necessary to express the probability $p(\mathbf{T})(\mathrm{d}\mathbf{T})$, in terms of the variables used in Eq. (4.9). The volume form $(\mathrm{d}\mathbf{T})$ is given simply by the product of differentials for each matrix element. Explicitly, $(\mathrm{d}\mathbf{T}) = \mathrm{d}T_{11}\mathrm{d}T_{12}\mathrm{d}T_{22}$ for $\alpha = 1$ and $(\mathrm{d}\mathbf{T}) = \mathrm{d}T_{11}\mathrm{d}T_{12}\mathrm{d}T_{21}\mathrm{d}T_{22}$ for $\alpha = 2$. Changing variables requires computing the Jacobian of the transformation, which we shall now address.

In the case $\alpha = 2$, the Jacobian for the singular value decomposition is well known and is given by [265]

$$\left| \frac{\partial(\mathbf{T})}{\partial(\mathbf{\Sigma}, \mathbf{V}, \mathbf{W})} \right| \sim s_1 s_2 (s_1^2 - s_2^2)^2, \tag{4.10}$$

where the left hand side denotes the Jacobian determinant. In the case $\alpha = 1$, the corresponding Jacobian for the Autonne-Takagi factorisation can be computed relatively straightforwardly. To begin we note that it can be shown from Eq. (4.1) that the Haar form is given by [256]

$$(\mathrm{d}_H \mathbf{U}) \sim (\mathbf{U}^\dagger \mathrm{d}\mathbf{U}). \tag{4.11}$$

Moreover, by differentiating the unitarity condition $\mathbf{U}^\dagger\mathbf{U} = \mathbb{I}$, we see that

$$\mathbf{U}^\dagger \mathrm{d}\mathbf{U} = -\mathrm{d}\mathbf{U}^\dagger \mathbf{U} = -[\mathbf{U}^\dagger \mathrm{d}\mathbf{U}]^\dagger, \tag{4.12}$$

which shows that $\mathbf{U}^\dagger \mathrm{d}\mathbf{U}$ is a skew-Hermitian matrix. We may thus write $\mathbf{U}^\dagger \mathrm{d}\mathbf{U}$ as

$$\mathbf{U}^\dagger \mathrm{d}\mathbf{U} = \begin{pmatrix} i\mathrm{d}_H U_1 & \mathrm{d}_H U_2 + i\mathrm{d}_H U_3 \\ \mathrm{d}_H U_2 - i\mathrm{d}_H U_3 & i\mathrm{d}_H U_4, \end{pmatrix} \tag{4.13}$$

where $\mathrm{d}_H U_1, \mathrm{d}_H U_2, \mathrm{d}_H U_3$ and $\mathrm{d}_H U_4$ are real valued differentials. Differentiating $\mathbf{T} = \mathbf{U}\mathbf{\Sigma}\mathbf{U}^{\mathrm{T}}$, we find

$$\mathrm{d}\mathbf{T} = \mathrm{d}\mathbf{U}\mathbf{\Sigma}\mathbf{U}^{\mathrm{T}} + \mathbf{U}\mathrm{d}\mathbf{\Sigma}\mathbf{U}^{\mathrm{T}} + \mathbf{U}\mathbf{\Sigma}\mathrm{d}\mathbf{U}^{\mathrm{T}}. \tag{4.14}$$

Pre-multiplying Eq. (4.14) by $\mathbf{U}^{\dagger}$ and post-multiplying by $\mathbf{U}^{*}$ gives

$$\begin{aligned} \mathbf{U}^{\dagger}\mathrm{d}\mathbf{T}\mathbf{U}^{*} &= \mathbf{U}^{\dagger}\mathrm{d}\mathbf{U}\mathbf{\Sigma} + \mathbf{\Sigma}\mathrm{d}\mathbf{U}^{\mathrm{T}}\mathbf{U}^{*} + \mathrm{d}\mathbf{\Sigma} \\ &= \mathbf{U}^{\dagger}\mathrm{d}\mathbf{U}\mathbf{\Sigma} + [\mathbf{U}^{\dagger}\mathrm{d}\mathbf{U}\mathbf{\Sigma}]^{\mathrm{T}} + \mathrm{d}\mathbf{\Sigma}. \end{aligned} \tag{4.15}$$

Consider now the volume forms associated with each side of Eq. (4.15), which are obtained by taking wedge products of the independent elements within the matrices on either side. Since $\mathbf{T}$ is symmetric, we need only take the products of elements in the upper-triangular sections of each matrix. For the left hand side, we make use of the fact that $(\mathbf{U}^{\dagger}\mathrm{d}\mathbf{T}\mathbf{U}^{*}) \sim (\mathrm{d}\mathbf{T})$ [256]. Explicit calculation shows that the right hand side of Eq. (4.15) is given by

$$\begin{pmatrix} \mathrm{d}s_1 & \mathrm{d}_H U_2 (s_1 - s_2) \\ -\mathrm{d}_H U_2 (s_1 - s_2) & \mathrm{d}s_2 \end{pmatrix} + i \begin{pmatrix} 2 s_1 \mathrm{d}_H U_1 & \mathrm{d}_H U_3 (s_1 + s_2) \\ -\mathrm{d}_H U_3 (s_1 + s_2) & 2 s_2 \mathrm{d}_H U_4 \end{pmatrix}. \tag{4.16}$$

In order to correctly perform the wedge products, it is necessary take products of the real and imaginary parts separately and multiply the two results together [266]. Ignoring constant factors in Eq. (4.16), we find that

$$(\mathrm{d}\mathbf{T}) \sim s_1 s_2 (s_2 - s_1)(s_2 + s_1) \mathrm{d}s_1 \mathrm{d}s_2 (\mathrm{d}_H \mathbf{U}), \tag{4.17}$$

from which the Jacobian may be read off as the terms that multiply the differentials.

Combining the results of Eqs. (4.17) and (4.10), we may now transform Eq. (4.8) to give

$$p(\mathbf{T})(\mathrm{d}\mathbf{T}) \sim s_1 s_2 |s_1^2 - s_2^2|^{\alpha} [(1 - s_1^2)(1 - s_2^2)]^{\alpha(N-6-\alpha)/2} \mathrm{d}s_1 \mathrm{d}s_2 (\mathrm{d}_H [\mathbf{U}; \mathbf{V}, \mathbf{W}]), \tag{4.18}$$

where

$$(\mathrm{d}_H[\mathbf{U};\mathbf{V},\mathbf{W}]) = \begin{cases} (\mathrm{d}_H\mathbf{U}) & \text{if } \alpha = 1, \\ (\mathrm{d}_H\mathbf{V})(\mathrm{d}_H\mathbf{W}) & \text{if } \alpha = 2. \end{cases} \tag{4.19}$$

Note that in deriving Eq. (4.18) we have also made use of the fact that

$$\det(\mathbb{I}_2 - \mathbf{T}^\dagger\mathbf{T}) = \det(\mathbb{I}_2 - \mathbf{\Sigma}^\dagger\mathbf{\Sigma}) = (1 - s_1^2)(1 - s_2^2). \tag{4.20}$$

Observing the right hand side of Eq. (4.18), we note that the singular values and singular vectors of $\mathbf{T}$ are statistically independent, and that the joint probability density function for s_1 and s_2 is proportional to the function multiplying the differentials. In addition, we see that the matrices $\mathbf{U}$, $\mathbf{V}$ and $\mathbf{W}$ are all uniformly distributed unitary matrices, irrespective of N. It follows that the diattenuation and retardance vectors are uniformly distributed on the surface of the Poincaré sphere, meaning there are no preferentially transmitted (reflected) polarisation states across the entire ensemble of scattering matrices.

We are now in a position to derive the statistics of R and D. For $\alpha = 1$, we see that $\mathbf{T}_R = \mathbf{U}\mathbf{U}^{\mathrm{T}}$ is, by the constructive definition, distributed according to the circular orthogonal ensemble. For $\alpha = 2$ on the other hand, $\mathbf{T}_R = \mathbf{V}\mathbf{W}^\dagger$ is the product of two uniformly distributed unitary matrices and is thus distributed according to circular unitary ensemble. The joint density for the eigenvalues of $\mathbf{T}_R$ are given by the well known result [10]

$$p(\theta_1, \theta_2) \sim |e^{i\theta_1} - e^{i\theta_2}|^\alpha. \tag{4.21}$$

The probability density function for the retardance can therefore be computed by the integral

$$p(R) \sim \int_0^{2\pi}\int_0^{2\pi} |e^{i\theta_1} - e^{i\theta_2}|^\alpha \delta\Big[R - \min\Big(|\theta_1 - \theta_2|, 2\pi - |\theta_1 - \theta_2|\Big)\Big]\mathrm{d}\theta_1\mathrm{d}\theta_2. \tag{4.22}$$

This integral can be tackled using the change of variables $x = \theta_2 - \theta_1$, $y = \theta_2 + \theta_1$ and computing the resulting integrals piecewise. Doing so and normalising the resulting

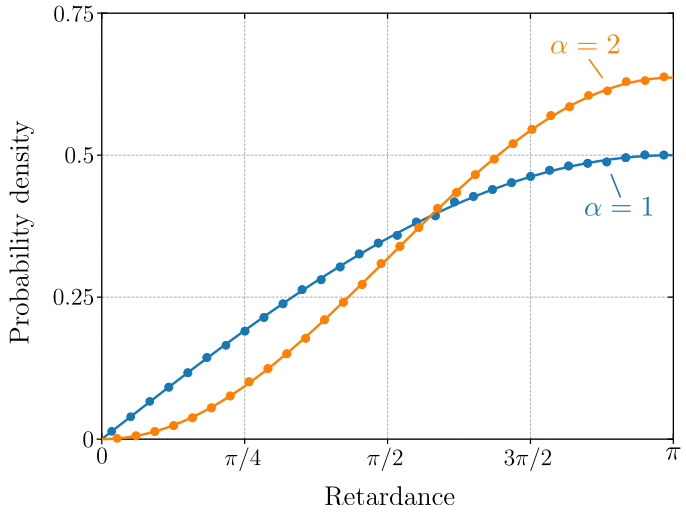

Figure 4.2: Histograms of retardance for on-diagonal blocks ($\alpha = 1$) and off-diagonal blocks ($\alpha = 2$). Data points were calculated from 10^6 realisations of matrices drawn from the circular orthogonal ensemble. Curves are given by Eq. (4.23).

probability density function yields the result

$$p(R) = \begin{cases} \frac{1}{2}\sin(\frac{R}{2}) & \text{if } \alpha = 1, \\ \frac{2}{\pi}\sin^2(\frac{R}{2}) & \text{if } \alpha = 2, \end{cases} \tag{4.23}$$

which we have plotted as solid lines in Figure 4.2. The data points (circles in Figure 4.2) were calculated by randomly generating 10^6 random matrices from the circular orthogonal ensemble and calculating R according to Eq. (4.7) from two different 2×2 blocks of $\mathbf{S}$: one on-diagonal and one off-diagonal. As can be seen, the theoretical curves match the data points excellently. In both cases we see that the density is monotonically increasing and peaks at $R = \pi$. Therefore, in terms of relative phase changes experienced by the incident field, the scattering medium is most likely to behave as a half-wave plate. We note that our result here for $\alpha = 2$ is similar to that derived elsewhere for the retardation angle in optical fibres using a random Jones matrix model, albeit using a slightly different definition for retardance [267].

The probability density function for the diattenuation can be found by integrat-

ing the joint density for s_1 and s_2 in Eq. (4.18). Explicitly, we have

$$p(D) \sim \int_0^1 \int_0^1 s_1 s_2 |s_1^2 - s_2^2|^\alpha [(1-s_1^2)(1-s_2^2)]^{\alpha(N-6-\alpha)/2} \delta\left(D - \frac{|s_1^2 - s_2^2|}{|s_1^2 + s_2^2|}\right) \mathrm{d}s_1 \mathrm{d}s_2, \tag{4.24}$$

which, after some manipulation, can be reduced to

$$p(D) \sim \frac{D^\alpha}{(1+D)^{\alpha+2}} \int_0^1 x^{\alpha+1} \left[(1-x)\left(1 - \frac{1-D}{1+D}x\right)\right]^{\alpha(N-6-\alpha)/2} \mathrm{d}x, \tag{4.25}$$

where x is a dummy variable. The resulting integral in Eq. (4.25) can be expressed in terms of the hypergeometric function ${}_2F_1$ (see 3.197, 3. of Ref. [268]). After normalising the resulting densities, we find that

$$p(D) = \begin{cases} 16 \frac{N-2}{N+1} \frac{D}{(1+D)^3} \, {}_2F_1\left(\frac{5-N}{2}, 3; \frac{N+3}{2}; \frac{1-D}{1+D}\right) & \text{if } \alpha = 1, \\ 48 \frac{N-2}{N} \frac{D^2}{(1+D)^4} \, {}_2F_1\left(4-N, 4; N+1; \frac{1-D}{1+D}\right) & \text{if } \alpha = 2. \end{cases} \tag{4.26}$$

Some example plots of these densities for different values of N are shown in Figure 4.3 for both $\alpha = 1$ and $\alpha = 2$. As with the retardance calculations, the data points were computed from Eq. (4.6) using 10^6 realisations of matrices from the circular orthogonal ensemble for each matrix size. As discussed, our result for $\alpha = 1$ is exact and matches very well for all matrix sizes. For $\alpha = 2$, our result is approximate and was found to match the data reasonably well for $N \geq 12$. While not shown here, for $N < 12$ we observed deviations from the simulated data, particularly in the minimal case $N = 4$, which corresponds to single-mode scattering. As N increases however, the approximation improves.

As can be seen, with the exception of $N = 4$ for $\alpha = 1$, the densities are strictly increasing and peak at $D = 1$ for all values of N. We therefore find that, when measuring the scattered field in any individual mode, it is most probable that the scattering medium behaves like a polarising filter that totally rejects one polarisation state. Since the diattenuation vector is uniformly distributed on the Poincaré sphere, the polarisation state that is rejected is completely random. Furthermore, since different blocks of $\mathbf{S}$ are uncorrelated, the rejected polarisation states in differ-

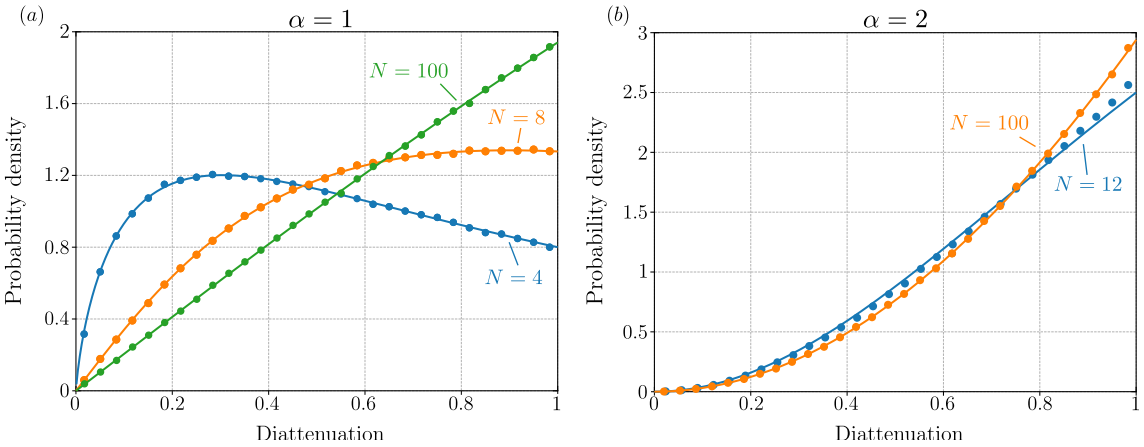

Figure 4.3: Histograms of diattenuation for blocks of scattering matrices of different sizes. Data points were calculated from 10^6 realisations of matrices drawn from the circular orthogonal ensemble. Curves are given by Eq. (4.26).

ent outgoing modes are also uncorrelated. Since the diattenuation and retardance statistics are independent, we can conclude that the most probable behaviour of a Jones matrix within the scattering matrix is that of a perfect diattenuator followed by a half- wave plate, both with randomly oriented and independent eigenvectors.

It is noteworthy that the mean diattenuation is lower for $\alpha = 1$ than for $\alpha = 2$. When diattenuation is large, the scattered polarisation state tends to be similar to the diattenuation vector, regardless of the incident polarisation state. In this case, the correlation between the incident and scattered polarisation states is weaker. As discussed in the previous section, the incident and scattered polarisation states are partially correlated in the back-scattering direction, which is therefore consistent with a lower average diattenuation.

4.1.3 Large matrices and Gaussian statistics

As mentioned in Chapter 3, in optical scattering experiments the number of modes admitted by a system tends to be very large, typically on the order of tens of millions per millimetre of illuminated surface area for visible light [6]. It will therefore be relevant to consider the large N limit of Eq. (4.26). This limit may in fact be taken directly using the asymptotic relation

$$ {}_2F_1(a - N, b; c + N; z) \sim \frac{1}{(1+z)^b}, \tag{4.27} $$

which is valid in the limit $N \to \infty$ for arbitrary a, b and c [269]. Applying this result to Eq. (4.26) and renormalising the resulting densities, we find the simple results

$$p(D)_{N\to\infty} = \begin{cases} 2D & \text{if } \alpha = 1, \\ 3D^2 & \text{if } \alpha = 2. \end{cases} \tag{4.28}$$

Observing again Figure. 4.3, these asymptotic densities closely match the densities for $N = 100$, which is well below the number of modes expected in a typical scattering experiment.

The simplicity of Eq. (4.28) suggests that a simpler statistical model may be applicable in the limit $N \to \infty$ that bypasses the complex machinery of the hypergeometric function. This is indeed the case, as it turns out that for large N the elements of a matrix drawn from the circular orthogonal ensemble converge in probability to zero-mean, uncorrelated, complex Gaussian random variables with varainces given by [270]

$$\langle |S_{ij}|^2 \rangle = \frac{1 + \delta_{ij}}{N}. \tag{4.29}$$

This result should not be too surprising. It is well known after all from the simple phasor sum arguments shown in Chapter 2 that fields scattered from random media often follow Gaussian statistics.

Transmission and reflection matrices with Gaussian statistics have been the subject of a lot of study, and a variety of their statistical properties are known, including for example the quarter-circle or Marchenko-Pastur laws for the distributions of their normalised singular values [271, 272]. Since these laws only hold for uncorrelated Gaussian variables, these results can be used as a reference to assess the degree of correlation between the elements of an experimentally determined matrix [5, 273]. In reality, the assumption of uncorrelated matrix elements is not exactly true, and a variety of different types of correlations exist, such as the short-range memory effect [274] and other long-range correlations [275]. It is also interesting to note that, for experimentally determined transmission and reflection matrices, the degree of correlation between matrix elements is also related to the amount of the matrix that is accessible experimentally. As previously mentioned, not all of the scattered

field may be collected by the detection optics. This effect, sometimes referred to as incomplete control, has been studied theoretically using so-called filtered random matrix ensembles, where the statistics of a truncated sub-section of the total scattering matrix is considered [217].

Using the assumption of Gaussian statistics, a simpler derivation of the asymptotic results in Eq. (4.28) is possible. As before, let $\mathbf{T}$ be a 2×2 block of $\mathbf{S}$, and let $\mathbf{T}' = \sqrt{N}\mathbf{T}$. Notably, $\mathbf{T}'$ has the same diattenuation as $\mathbf{T}$. By considering Eq. (4.29), it can be shown that $\mathbf{T}'$ has joint density given by

$$p(\mathbf{T}') \sim \exp\Big(-\frac{1}{3-\alpha}\mathrm{tr}(\mathbf{T}'^{\dagger}\mathbf{T}')\Big). \tag{4.30}$$

Taking a singular value decomposition of $\mathbf{T}'$ as before and changing variables yields the density for the singular values of $\mathbf{T}'$, s_1 and s_2, which is given by

$$p(s_1, s_2) \sim s_1 s_2 |s_1^2 - s_2^2|^{\alpha} \exp\Big(-\frac{1}{3-\alpha}(s_1^2 + s_2^2)\Big). \tag{4.31}$$

The probability density function for the diattenuation can therefore be calculated from the integral

$$p(D) \sim \int_0^{\infty}\int_0^{\infty} s_1 s_2 |s_1^2 - s_2^2|^{\alpha} \exp\Big(-\frac{1}{3-\alpha}(s_1^2 + s_2^2)\Big)\delta\left(D - \frac{|s_1^2 - s_2^2|}{|s_1^2 + s_2^2|}\right)\mathrm{d}s_1\mathrm{d}s_2, \tag{4.32}$$

which ultimately leads to the same result as Eq. (4.28). It should be pointed out that since under the Gaussian assumption the elements of $\mathbf{T}$ are unbounded, the values of s_1 and s_2 range from zero to infinity. The decaying exponential in the integrand of Eq. (4.32), however, prevents the integral from diverging.

4.2 Conclusion

In this chapter we have explored some of the consequences of the circular ensembles on the scattering of polarised light. To achieve these we analysed the joint statistics of 2×2 blocks of matrices drawn from the circular orthogonal ensemble. One of the key observations is that, with the exception of scattering into the backscattering

direction, no particular polarisation state is favoured over the entire ensemble, either when viewing the scattered field in an arbitrary mode, or with regard to the diattenuation or retardance vectors. All of these vectors are distributed uniformly over the Poincaré sphere and the average Mueller matrix is thus a pure depolariser. In the backscattering direction, the average Mueller matrix is only a partial depolariser and the scattered fields are distributed non-uniformly over the Poincaré sphere, displaying a focus in probability density around the incident polarisation state. The distributions of retardance and diattenuation associated with Jones matrices within $\mathbf{S}$ are non-trivial, but their limiting distributions for large scattering matrices are those predicted by Gaussian statistics.

While the circular ensembles were studied primarily for their simplicity, it is clear that they are inadequate as an effective model for realistic scattering media. Since the circular ensembles do not discriminate between scattering into any particular mode, nor between transmission and reflection, they may only be applicable for random media that scatter isotropically. Random media of this sort, however, generally do not show a lot of interesting polarisation statistics anyway, as the scattered field for such a system is often fully depolarised. The random matrix theory literature, of course, extends well beyond the circular ensembles. The Poisson kernel, for example, generalises the circular ensembles to incorporate a non-zero mean [276]. In order to move forwards however, it will be necessary to develop a more tailored statistical model that is able to account for non-universal aspects of scattering media specific to certain problems. This shall be the subject of the next two chapters, beginning with theoretical work in Chapter 5, followed by numerical simulations in Chapter 6. As shall be seen, the polarisation statistics of the circular ensembles will emerge as limits of the more general model and, given their relative simplicity, are therefore still of value.

Chapter 5

Scattering matrix statistics

Tailoring the statistics of a distribution of random scattering matrices so as to be germane to a particular class of random media requires some degree of physical modelling. In this chapter we will introduce a theoretical framework that will allows us to express the elements of the scattering matrix for a random medium composed of a large number of discrete scatterers in terms of the physical properties of the constituent scatterers. With this framework, we will be able to derive the statistical properties of the scattering matrix elements, which, in Chapter 6, will be used in numerical simulations of multiple scattering of polarised light, and, in Chapter 7, to study the persistence and possible recovery of polarisation information transmitted through a random medium. The theory in this chapter is presented in terms of the continuous scattering matrix, which is mathematically simpler than the discrete scattering matrix. In Chapter 6, we will demonstrate how the theory can be applied to the discrete scattering matrix, which is ultimately what must be used for numerical studies.

We will begin by introducing the far field Foldy-Lax equations, which describe the scattered field due to a discrete collection of particles. Using this, we will be able to derive expressions for the corresponding scattering matrix elements and analyse their statistical properties. The majority of the statistical results in this chapter apply to the matrix $\bar{\mathbf{S}}_{pp}$. A brief discussion on how the theory may be generalised to incorporate evanescent wave components will be given in Section 5.4.

5.1 Multiple scattering equations

Consider the same problem as described in Chapter 3. Suppose that the scattering medium situated within the region $-L/2 \leq z \leq L/2$ is illuminated by an incident, monochromatic plane wave whose complex representation $\mathbf{E}_i(\mathbf{r})$ is given by

$$\mathbf{E}_i(\mathbf{r}) = \mathbf{E}_0 e^{i\mathbf{k}_i \cdot \mathbf{r}} = \int \delta(\boldsymbol{\kappa} - \boldsymbol{\kappa}_i) \mathbf{E}_0 e^{i\mathbf{k}\cdot\mathbf{r}} \mathrm{d}\boldsymbol{\kappa}, \tag{5.1}$$

where $\mathbf{E}_0$ is a constant vector that characterises the incident field's polarisation state. Let us now, however, suppose that the scattering medium consists of a large number N of random, discrete scatterers. These can be thought of as small particles, each occupying a volume V_p, where $1 \leq p \leq N$ indexes the particles . The permittivity varies spatially according to

$$\epsilon(\mathbf{r}) = \epsilon_b + \sum_{p=1}^{N} \epsilon_p(\mathbf{r}), \tag{5.2}$$

where $\epsilon_p(\mathbf{r})$ is only non-zero for $\mathbf{r} \in V_p$. The exact form of $\epsilon_p(\mathbf{r})$ within V_p, of course, depends on the nature of the particle. We shall also define the vector $\mathbf{r}_p$, which points to the centre of the smallest sphere that circumscribes the particle. We may refer to $\mathbf{r}_p$ as the centre of the particle.

We now assume that the particles are widely separated so that each one is located in the far field of all the others. For a measurement point located in the far field of all of the particles in the scattering medium, the total electric field is given by the far field Foldy-Lax equations [27]

$$\mathbf{E}(\mathbf{r}) = \mathbf{E}_i(\mathbf{r}) + \sum_{p_1=1}^{N} G(\mathbf{r} - \mathbf{r}_{p_1}) \left[\mathbf{A}_{p_1}(\widehat{\mathbf{r} - \mathbf{r}_{p_1}}) \mathbf{E}_i(\mathbf{r}_{p_1}) + \sum_{\substack{p_2=1 \\ p_2 \neq p_1}}^{N} \mathbf{A}_{p_1}(\widehat{\mathbf{r} - \mathbf{r}_{p_1}}, \widehat{\mathbf{r}_{p_1} - \mathbf{r}_{p_2}}) \mathbf{E}_{p_1 p_2} \right], \tag{5.3}$$

$$\mathbf{E}_{p_1 p_2} = G(\mathbf{r}_{p_1} - \mathbf{r}_{p_2}) \left[\mathbf{A}_{p_2}(\widehat{\mathbf{r}_{p_1} - \mathbf{r}_{p_2}}) \mathbf{E}_i(\mathbf{r}_{p_2}) + \sum_{\substack{p_3=1 \\ p_3 \neq p_2}}^{N} \mathbf{A}_{p_2}(\widehat{\mathbf{r}_{p_1} - \mathbf{r}_{p_2}}, \widehat{\mathbf{r}_{p_2} - \mathbf{r}_{p_3}}) \mathbf{E}_{p_2 p_3} \right], \tag{5.4}$$

where a hat over a vector signifies that the vector has unit magnitude and the subscripts p_1, p_2 and p_3 index different particles. Eq. (5.4) gives a recursive definition of the field $\mathbf{E}_{p_1 p_2}$, which, physically, can be loosely interpreted as the field exciting particle p_1 due to particle p_2. In the Foldy-Lax equations, $G(\mathbf{r}) = \exp(ik|\mathbf{r}|)/ik|\mathbf{r}|$ is the scalar Green's function and $\mathbf{A}_p$ is the single particle amplitude matrix for the p'th particle, as introduced in Chapter 2. While the Foldy-Lax equations describe multiple scattering, the matrix $\mathbf{A}_p$, which describes the single scattering properties of the p'th particle, must be calculated from a more fundamental single particle scattering theory, such as, for example, Mie theory in the case of spherical scatterers.

Due to their recursive nature, the Foldy-Lax equations may be iterated to yield a formal series expansion for the total scattered field. This series is given by

$$\begin{aligned}
\mathbf{E}(\mathbf{r}) = \mathbf{E}_i(\mathbf{r}) &+ \sum_{p_1=1}^{N} G(\mathbf{r}-\mathbf{r}_{p_1})\mathbf{A}_{p_1}(\widehat{\mathbf{r}-\mathbf{r}_{p_1}}, \widehat{\mathbf{k}}_i)\mathbf{E}_i(\mathbf{r}_{p_1}) \\
&+ \sum_{p_1=1}^{N}\sum_{\substack{p_2=1 \\ p_2\neq p_1}}^{N} G(\mathbf{r}-\mathbf{r}_{p_2})\mathbf{A}_{p_2}(\widehat{\mathbf{r}-\mathbf{r}_{p_2}}, \widehat{\mathbf{r}_{p_2}-\mathbf{r}_{p_1}})G(\mathbf{r}_{p_2}-\mathbf{r}_{p_1})\mathbf{A}_{p_1}(\widehat{\mathbf{r}_{p_2}-\mathbf{r}_{p_1}}, \widehat{\mathbf{k}}_i)\mathbf{E}_i(\mathbf{r}_{p_1}) \\
&+ \sum_{p_1=1}^{N}\sum_{\substack{p_2=1 \\ p_2\neq p_1}}^{N}\sum_{\substack{p_3=1 \\ p_3\neq p_1 \\ p_3\neq p_2}}^{N} G(\mathbf{r}-\mathbf{r}_{p_3})\mathbf{A}_{p_3}(\widehat{\mathbf{r}-\mathbf{r}_{p_3}}, \widehat{\mathbf{r}_{p_3}-\mathbf{r}_{p_2}})G(\mathbf{r}_{p_3}-\mathbf{r}_{p_2}) \\
&\qquad \mathbf{A}_{p_2}(\widehat{\mathbf{r}_{p_3}-\mathbf{r}_{p_2}}, \widehat{\mathbf{r}_{p_2}-\mathbf{r}_{p_1}})G(\mathbf{r}_{p_2}-\mathbf{r}_{p_1})\mathbf{A}_{p_1}(\widehat{\mathbf{r}_{p_2}-\mathbf{r}_{p_1}}, \widehat{\mathbf{k}}_i)\mathbf{E}_i(\mathbf{r}_{p_1}) \\
&+ \quad \ldots,
\end{aligned} \tag{5.5}$$

where the series continues indefinitely with higher order terms containing an increasing number of factors. Each term in Eq. (5.5) can be interpreted as the component of the total field that is the result of a certain number of scattering events and the term containing n summations will be referred to as the term of order n. The term with a single sum is also referred to as the single scattering term, which is followed by the double scattering term and so on. Importantly, Eq. (5.5) makes use of the Twersky approximation [277], which neglects scattering sequences for which two or more of the summation indices coincide. Physically, this approximation neglects recurrent scattering, i.e. sequences of particles in which a particle is visited more than

once. The Twersky approximation is considered valid in the limit $N \to \infty$, provided that the weak scattering condition $kl_s \gg 1$ is met [27]. In the scattering term of order n, the summation involves $N!/(N-n)! = N(N-1)(N-2)\dots(N-n+1)$ terms, which, in the limit $N \to \infty$, grows as $\sim N^n$.

In virtue of Eqs. (3.13) and (5.1), if $z > L/2$, then

$$\begin{aligned}\mathbf{E}(\mathbf{r}) = \int \mathbf{b}(\boldsymbol{\kappa}_j) e^{i\mathbf{k}_j\cdot\mathbf{r}} \mathrm{d}\boldsymbol{\kappa}_j &= \int \left[\int \mathbf{t}(\boldsymbol{\kappa}_j, \boldsymbol{\kappa}) \mathbf{a}(\boldsymbol{\kappa}) \mathrm{d}\boldsymbol{\kappa} \right] e^{i\mathbf{k}_j\cdot\mathbf{r}} \mathrm{d}\boldsymbol{\kappa}_j \\ &= \int \left[\int \mathbf{t}(\boldsymbol{\kappa}_j, \boldsymbol{\kappa}) \mathbf{E}_0 \delta(\boldsymbol{\kappa} - \boldsymbol{\kappa}_i) \mathrm{d}\boldsymbol{\kappa} \right] e^{i\mathbf{k}_j\cdot\mathbf{r}} \mathrm{d}\boldsymbol{\kappa}_j \\ &= \int \mathbf{t}(\boldsymbol{\kappa}_j, \boldsymbol{\kappa}_i) \mathbf{E}_0 e^{i\mathbf{k}_j\cdot\mathbf{r}} \mathrm{d}\boldsymbol{\kappa}_j.\end{aligned} \tag{5.6}$$

Similarly,

$$\mathbf{E}(\mathbf{r}) = \mathbf{E}_0 e^{i\mathbf{k}_i\cdot\mathbf{r}} + \int \mathbf{r}(\boldsymbol{\kappa}_j, \boldsymbol{\kappa}_i) \mathbf{E}_0 e^{i\widetilde{\mathbf{k}}_j\cdot\mathbf{r}} \mathrm{d}\boldsymbol{\kappa}_j \tag{5.7}$$

for $z < -L/2$. Importantly, the incident field in Eq. (5.7) propagates in the opposite direction to the reflected field and therefore cannot be incorporated into the integral. Similar equations for $\mathbf{t}'$ and $\mathbf{r}'$ can be obtained by instead beginning with a left-propagating incident wave. To derive expressions for the scattering matrix elements, it is necessary to decompose the expressions for the scattered field in Eq. (5.5) into angular spectra. To achieve this, we analyse terms of different order separately by defining

$$\mathbf{t}(\boldsymbol{\kappa}_j, \boldsymbol{\kappa}_i) = \sum_{n=0}^{\infty} \mathbf{t}^{(n)}(\boldsymbol{\kappa}_j, \boldsymbol{\kappa}_i) \tag{5.8}$$

In relation to Eq. (5.5), $\mathbf{t}^{(n)}$ will account for the contribution to the total field due to the term of order n. Analogous equations may be defined for the other blocks of the scattering matrix. For simplicity, we shall present calculations primarily for the transmission matrix and state the corresponding results for the other blocks, understanding that the underlying mathematics is similar in all cases.

First, by comparing Eqs. (5.1), (5.5) and (5.6), it is evident that

$$\mathbf{t}^{(0)}(\boldsymbol{\kappa}_j, \boldsymbol{\kappa}_i) = \delta(\boldsymbol{\kappa}_j - \boldsymbol{\kappa}_i)\mathbb{I}_2, \tag{5.9}$$

which describes the unscattered field. For higher order terms, we shall make use of the identity [278]

$$\boldsymbol{\varphi}(\widehat{\mathbf{r}})G(\mathbf{r}) = \frac{1}{2\pi}\int \boldsymbol{\varphi}(\widehat{\mathbf{k}})e^{i\mathbf{k}\cdot\mathbf{r}}\frac{\mathrm{d}\boldsymbol{\kappa}}{k\gamma}, \tag{5.10}$$

which holds for $z > 0$ in the limit $k|\mathbf{r}| \to \infty$ for any vector function $\boldsymbol{\varphi}$. For the first order term of Eq. (5.5), setting

$$\boldsymbol{\varphi}(\widehat{\mathbf{r} - \mathbf{r}_{p_1}}) = \mathbf{A}_{p_1}(\widehat{\mathbf{r} - \mathbf{r}_{p_1}}, \widehat{\mathbf{k}}_i)\mathbf{E}_i(\mathbf{r}_{p_1}) \tag{5.11}$$

and using Eq. (5.10) gives

$$\begin{aligned}\sum_{p_1=1}^{N} G(\mathbf{r} - \mathbf{r}_{p_1})\mathbf{A}_{p_1}(\widehat{\mathbf{r} - \mathbf{r}_{p_1}}, \widehat{\mathbf{k}}_i)\mathbf{E}_i(\mathbf{r}_{p_1}) &= \int \sum_{p_1=1}^{N} \frac{\mathbf{A}^t_{p_1}(\widehat{\boldsymbol{\kappa}}_j, \widehat{\boldsymbol{\kappa}}_i)\mathbf{E}_0 e^{i\mathbf{k}_i\cdot\mathbf{r}_{p_1}}}{2\pi k\gamma_j} e^{i\mathbf{k}_j\cdot(\mathbf{r}-\mathbf{r}_{p_1})}\mathrm{d}\boldsymbol{\kappa}_j \\ &= \int \left[\frac{1}{2\pi k\gamma_j}\sum_{p_1=1}^{N} \mathbf{A}^t_{p_1}(\widehat{\boldsymbol{\kappa}}_j, \widehat{\boldsymbol{\kappa}}_i)e^{i\mathbf{r}_{p_1}\cdot(\mathbf{k}_i-\mathbf{k}_j)}\right]\mathbf{E}_0 e^{i\mathbf{k}_j\cdot\mathbf{r}}\mathrm{d}\boldsymbol{\kappa}_j,\end{aligned} \tag{5.12}$$

where we have defined

$$\mathbf{A}^t_{p_1}(\widehat{\boldsymbol{\kappa}}_j, \widehat{\boldsymbol{\kappa}}_i) = \mathbf{A}_{p_1}(\widehat{\mathbf{k}}_j, \widehat{\mathbf{k}}_i). \tag{5.13}$$

The reason for defining $\mathbf{A}^t_{p_1}$ is that, unlike $\mathbf{A}_{p_1}$, it is only a function of transverse wavevectors. From Eq. (5.12), the first order transmission matrix can be read off as

$$\mathbf{t}^{(1)}(\boldsymbol{\kappa}_j, \boldsymbol{\kappa}_i) = \frac{1}{2\pi k\gamma_j}\sum_{p_1=1}^{N} \mathbf{A}^t_{p_1}(\widehat{\boldsymbol{\kappa}}_j, \widehat{\boldsymbol{\kappa}}_i)e^{i\mathbf{r}_{p_1}\cdot(\mathbf{k}_i-\mathbf{k}_j)}. \tag{5.14}$$

A similar sequence of calculations can be performed for the reflection matrix. In

this case we first define

$$\mathbf{A}^r_{p_1}(\widehat{\boldsymbol{\kappa}}_j, \widehat{\boldsymbol{\kappa}}_i) = \mathbf{A}_{p_1}(\widetilde{\widehat{\mathbf{k}}}_j, \widehat{\mathbf{k}}_i), \tag{5.15}$$

where the tilde above $\widehat{\mathbf{k}}_j$ is necessary as the scattered wavevector has z component with opposite sign to the incident field. Note first that, since the incident field propagates to the right, we have $\mathbf{r}^{(0)}(\boldsymbol{\kappa}_j, \boldsymbol{\kappa}_i) = \mathbf{0}$. The first order reflection matrix can be derived by noting that, for $z < 0$, a similar identity to Eq. (5.10) holds, but with $\mathbf{k}$ replaced with $\widetilde{\mathbf{k}}$ on the right hand side. Using this, we find

$$\mathbf{r}^{(1)}(\boldsymbol{\kappa}_j, \boldsymbol{\kappa}_i) = \frac{1}{2\pi k \gamma_j} \sum_{p_1=1}^{N} \mathbf{A}^r_{p_1}(\widehat{\boldsymbol{\kappa}}_j, \widehat{\boldsymbol{\kappa}}_i) e^{i\mathbf{r}_{p_1}\cdot(\mathbf{k}_i - \widetilde{\mathbf{k}}_j)}. \tag{5.16}$$

Similar calculations can be performed for $\mathbf{t}'$ and $\mathbf{r}'$, which involve the matrices $\mathbf{A}^{t'}$ and $\mathbf{A}^{r'}$ that can be defined analogously to $\mathbf{A}^t$ and $\mathbf{A}^r$ with the appropriate choice of tildes that give the correct sign for the z components of the incident and scattered wavevectors.

Higher order terms of the scattering matrix elements can be derived by repeated use of Eq. (5.10). It is necessary, however, to consider the relative z components of the positions of the particles. Consider, for example a two-particle scattering sequence and suppose that the first and second particles have z coordinates z_1 and z_2 respectively. With respect to its z coordinate, the second particle may be in front of ($z_2 > z_1$) or behind ($z_2 < z_1$) the first particle. Depending on which of these is the case, in expressing the angular spectrum of the field illuminating the second particle (which arises from scattering by the first particle) it will either be necessary to apply Eq. (5.10) directly, or the corresponding identity that applies for the case $z < 0$, as was used for the first order term of the reflection matrix. For ease of notation, we shall suppose that the particles are indexed in order of increasing z component, i.e. such that $z_1 < z_2 \cdots < z_N$. Separating different cases into different

sums and making further use of Eq. (5.10), we find

$$\mathbf{t}^{(2)}(\boldsymbol{\kappa}_j,\boldsymbol{\kappa}_i)=\int\frac{1}{(2\pi k)^2\gamma_j\gamma_{12}}\Bigg[\sum_{p_2=p_1+1}^{N}\sum_{p_1=1}^{N-1}\mathbf{A}^{t}_{p_2}(\widehat{\boldsymbol{\kappa}}_j,\widehat{\boldsymbol{\kappa}}_{12})\mathbf{A}^{t}_{p_1}(\widehat{\boldsymbol{\kappa}}_{12},\widehat{\boldsymbol{\kappa}}_i)e^{i[\mathbf{r}_{p_1}\cdot(\mathbf{k}_i-\mathbf{k}_{12})+\mathbf{r}_{p_2}\cdot(\mathbf{k}_{12}-\mathbf{k}_j)]} + \sum_{p_2=1}^{p_1-1}\sum_{p_1=2}^{N}\mathbf{A}^{r'}_{p_2}(\widehat{\boldsymbol{\kappa}}_j,\widehat{\boldsymbol{\kappa}}_{12})\mathbf{A}^{r}_{p_1}(\widehat{\boldsymbol{\kappa}}_{12},\widehat{\boldsymbol{\kappa}}_i)e^{i[\mathbf{r}_{p_1}\cdot(\mathbf{k}_i-\widetilde{\mathbf{k}}_{12})+\mathbf{r}_{p_2}\cdot(\widetilde{\mathbf{k}}_{12}-\mathbf{k}_j)]}\Bigg]\mathrm{d}\boldsymbol{\kappa}_{12}, \tag{5.17}$$

where $\boldsymbol{\kappa}_{12}$ is an intermediate transverse wavevector that describes the field that propagates from the first particle to the second. The two different terms in Eq. (5.17) have straightforward physical interpretations. The first describes scattering sequences that involve two forward-directed scattering events, while the second involves backscattering from the incident field into a left-propagating field, following by another backscattering event whose scattered wavevector is again right-propagating. Similarly, the second order term for the reflection matrix is given by

$$\mathbf{r}^{(2)}(\boldsymbol{\kappa}_j,\boldsymbol{\kappa}_i)=\int\frac{1}{(2\pi k)^2\gamma_j\gamma_{12}}\Bigg[\sum_{p_2=1}^{p_1-1}\sum_{p_1=2}^{N}\mathbf{A}^{t'}_{p_2}(\widehat{\boldsymbol{\kappa}}_j,\widehat{\boldsymbol{\kappa}}_{12})\mathbf{A}^{r}_{p_1}(\widehat{\boldsymbol{\kappa}}_{12},\widehat{\boldsymbol{\kappa}}_i)e^{i[\mathbf{r}_{p_1}\cdot(\mathbf{k}_i-\widetilde{\mathbf{k}}_{12})+\mathbf{r}_{p_2}\cdot(\widetilde{\mathbf{k}}_{12}-\widetilde{\mathbf{k}}_j)]} + \sum_{p_2=p_1+1}^{N}\sum_{p_1=1}^{N-1}\mathbf{A}^{r}_{p_2}(\widehat{\boldsymbol{\kappa}}_j,\widehat{\boldsymbol{\kappa}}_{12})\mathbf{A}^{t}_{p_1}(\widehat{\boldsymbol{\kappa}}_{12},\widehat{\boldsymbol{\kappa}}_i)e^{i[\mathbf{r}_{p_1}\cdot(\mathbf{k}_i-\mathbf{k}_{12})+\mathbf{r}_{p_2}\cdot(\mathbf{k}_{12}-\widetilde{\mathbf{k}}_j)]}\Bigg]\mathrm{d}\boldsymbol{\kappa}_{12}, \tag{5.18}$$

whose different terms again describe different types of two-particle scattering sequences. This time, however, the final wavevector $\widetilde{\mathbf{k}}_j$ has negative z component and thus describes a left-propagating wave. Similar calculations can be performed for higher order terms, which will involve more complex types of multi-particle scattering sequences.

Observing Eqs. (5.14), (5.16), (5.17) and (5.18), the expressions for the transmission and reflection matrix elements are ultimately random phasor sums. As previously discussed, such expressions are known to be asymptotically Gaussian random variables as $N\to\infty$ [49]. For this to hold, we require the assumption that

a scatterer's morphology is statistically independent of its position, which we shall take to be the case.

Suppose that all of the independent elements of the scattering matrix are collated into a vector $\mathbf{z}$ of complex random variables. In virtue of the previous comments, each element of $\mathbf{z}$ is marginally Gaussian distributed. It is worth nothing that while a multivariate Gaussian distribution has Gaussian marginals, the converse is not true. Nevertheless, we shall assume that $\mathbf{z}$ follows a multivariate Gaussian distribution, both for the mathematical simplicity afforded by this assumption, and because of historical precedent, as this assumption is typically taken to be the case [49]. The statistics of a complex multivariate Gaussian distribution are fully described by three parameters: the mean, covariance matrix and pseudo covariance matrix [279]. In the following section we shall define these quantities more precisely and derive expressions for them.

5.2 Mean matrix elements

We now consider the problem of computing the mean transmission and reflection matrices, i.e. $\langle \mathbf{t}(\boldsymbol{\kappa}_j, \boldsymbol{\kappa}_i) \rangle$ and $\langle \mathbf{r}(\boldsymbol{\kappa}_j, \boldsymbol{\kappa}_i) \rangle$ where the average is over the ensemble of all realisations of the scattering medium. Observing the form of the matrix elements, such as in Eqs. (5.14) and (5.17), it can be seen that the randomness arises from two physical sources: the positions of the scatterers, which contribute to the complex exponential terms, and the morphological properties of the scatterers, which contribute to the amplitude matrix factors. We shall assume that these two factors are independent, so that no particular type of scatterer is more likely to exist than any other at any specific location.

5.2.1 Single scattering

In this section we shall consider the first order terms of the transmission and reflection matrices. Consider first the transmission matrix, whose mean is given by

$$\langle \mathbf{t}^{(1)}(\boldsymbol{\kappa}_j, \boldsymbol{\kappa}_i)\rangle = \frac{1}{2\pi k\gamma_j}\sum_{p_1=1}^{N}\langle \mathbf{A}^t_{p_1}(\widehat{\boldsymbol{\kappa}}_j, \widehat{\boldsymbol{\kappa}}_i)\rangle\langle e^{i\mathbf{r}_{p_1}\cdot(\mathbf{k}_i-\mathbf{k}_j)}\rangle \tag{5.19}$$

$$= \frac{N}{2\pi k\gamma_j}\langle \mathbf{A}^t(\widehat{\boldsymbol{\kappa}}_j, \widehat{\boldsymbol{\kappa}}_i)\rangle\langle e^{i\mathbf{r}\cdot(\mathbf{k}_i-\mathbf{k}_j)}\rangle, \tag{5.20}$$

where we have made use of the fact that, after averaging, the particle index becomes redundant, allowing us to replace the sum with a factor of N. In order to evaluate the average of the complex exponential, it is necessary to specify a probability distribution for the position vector $\mathbf{r}$. Since we assume that no particular position within the medium is favoured over any other, we shall suppose that $\mathbf{r}$ is distributed uniformly within the scattering medium, so that the single particle distribution function is given by $p(\mathbf{r}) = 1/V$, where V is the volume of the scattering medium. This assumption is reasonable given that each scatterer lies in the far field of all of the others. For simplicity, let us suppose that the transverse extent (x and y directions) of the scattering medium is confined to the rectangular cross section $-L_x/2 < x < L_x/2, -L_y/2 < y < L_y/2$, so that the volume of the scattering medium is given by $V = L_xL_yL$. We then find that

$$\begin{aligned} N\langle e^{i\mathbf{r}\cdot(\mathbf{k}_i-\mathbf{k}_j)}\rangle &= N\int_{-L/2}^{L/2}\int_{-L_y/2}^{L_y/2}\int_{-L_x/2}^{L_x/2}\frac{1}{V}e^{i\mathbf{r}\cdot(\mathbf{k}_i-\mathbf{k}_j)}\mathrm{d}x\mathrm{d}y\mathrm{d}z \\ &= nL_x\mathrm{sinc}\Big((k_{ix}-k_{jx})\frac{L_x}{2}\Big)L_y\mathrm{sinc}\Big((k_{iy}-k_{jy})\frac{L_y}{2}\Big)L\mathrm{sinc}\Big((\gamma_i-\gamma_j)\frac{L}{2}\Big), \end{aligned} \tag{5.21}$$

where $n = N/V$ is the particle number density and $\mathrm{sinc}(x) = \sin(x)/x$. We now take the limit of an infinite slab by letting $L_x, L_y \to \infty$. In taking this limit it also follows that $N \to \infty$, but we shall suppose that n is held constant to avoid divergences. To perform this limit, we make use of the fact that the sinc function satisfies the weak

limit [44]

$$\lim_{L\to\infty} L\mathrm{sinc}\Big(\frac{Lx}{2}\Big) = 2\pi\delta(x), \tag{5.22}$$

which allows us to deduce

$$N\langle e^{i\mathbf{r}\cdot(\mathbf{k}_i-\mathbf{k}_j)}\rangle \to (2\pi)^2 nL\mathrm{sinc}\Big((\gamma_i-\gamma_j)\frac{L}{2}\Big)\delta(k_{ix}-k_{jx})\delta(k_{iy}-k_{jy}). \tag{5.23}$$

Since the delta functions appearing in Eq. (5.23) effectively enforce the constraint $\boldsymbol{\kappa}_i = \boldsymbol{\kappa}_j$, which implies that $\gamma_i = \gamma_j$, the sinc term can be evaluated to unity and we find that

$$\langle \mathbf{t}^{(1)}(\boldsymbol{\kappa}_j, \boldsymbol{\kappa}_i)\rangle = \delta(\boldsymbol{\kappa}_i - \boldsymbol{\kappa}_j)\frac{2\pi nL}{k\gamma_j}\langle \mathbf{A}^t(\widehat{\boldsymbol{\kappa}}_j, \widehat{\boldsymbol{\kappa}}_i)\rangle. \tag{5.24}$$

Clearly the transmitted field is non-zero only in the direction parallel to the incident field. The origin of this fact is relatively transparent from a simple physical argument. According to Eq. (5.14), the transmitted field is the sum of a large number of complex phasors, which, given our assumptions, will have uniformly distributed phases in the interval $[0, 2\pi)$. A sufficiently large sum of such phasors will tend to interfere destructively, resulting in a mean amplitude of zero. The only way for this effect to not occur is for the arguments of the complex phasors to be zero, which is indeed the case when $\boldsymbol{\kappa}_j = \boldsymbol{\kappa}_i$. Physically, the phase accrued by waves that are transmitted in the forward direction is independent of the scatterer position.

Analogous calculations show that the first order mean reflection matrix is given by

$$\langle \mathbf{r}^{(1)}(\boldsymbol{\kappa}_j, \boldsymbol{\kappa}_i)\rangle = \delta(\boldsymbol{\kappa}_i - \boldsymbol{\kappa}_j)\frac{2\pi nL}{k\gamma_j}\mathrm{sinc}(\gamma_i L)\langle \mathbf{A}^r(\widehat{\boldsymbol{\kappa}}_j, \widehat{\boldsymbol{\kappa}}_i)\rangle, \tag{5.25}$$

where the argument of the sinc is no longer zero as the argument of the complex exponentials being averaged this time take the form $\sim \mathbf{r}\cdot(\mathbf{k}_i - \widetilde{\mathbf{k}}_j) = \boldsymbol{\rho}\cdot(\boldsymbol{\kappa}_i - \boldsymbol{\kappa}_j) + z(\gamma_i + \gamma_j)$. The phase accrued by backscattered waves is path-dependent, regardless of which direction scattering occurs in. The delta function appearing in Eq. (5.25) means that the mean reflected field is non-zero only in the specular reflection direction, which is the direction in which the transverse wavevector is

conserved [280].

5.2.2 Multiple scattering

For scattering order greater than one, which is also known as multiple scattering, calculating the mean transmission and reflection matrices is a complex problem. As demonstrated in Eqs. (5.17) and (5.18), high order terms contain different contributions from different types of sequences of particles, all of which must be averaged separately and then summed together. In the case of the transmission matrix, however, a simple result for the ensemble average is obtainable when all of the particles in the medium are identical. To achieve this we will begin by showing that, for any given scattering order, the component of the mean transmission matrix that represents a sequence of consecutive forward scattering events is dominant in the limit $L \to \infty$. This will allow us to neglect all other types of scattering sequences and, as shall be shown, the surviving terms can be summed using the matrix exponential. We shall first demonstrate this property for the double scattering term and then sketch a proof for arbitrary scattering order. For simplicity, we shall only use single integral signs in this section, even if multiple integration variables are present.

Consider the two terms in Eq. (5.17), which we shall refer to as the tt and $r'r$ terms respectively. As was the case for the first order terms, after averaging the sums are replaced by combinatorial factors that count how many different scattering sequences there are. In either case, the number of terms in the sums is $N(N-1)/2$, which grows as $\sim N^2/2$ in the limit $N \to \infty$. Assuming all the particles in the medium are identical, the $\mathbf{A}$ terms are non-random and can be factored out of the sums, leaving only the exponentials to be averaged. Focusing first on the tt term, it is necessary to take the average of the expression $\langle e^{i[\mathbf{r}_1\cdot(\mathbf{k}_i-\mathbf{k}_{12})+\mathbf{r}_2\cdot(\mathbf{k}_{12}-\mathbf{k}_j)]}\rangle$, where $\mathbf{r}_1$ and $\mathbf{r}_2$ are random position vectors. This requires specifying the joint probability density function $p(\mathbf{r}_1, \mathbf{r}_2)$, which is often given in terms of the pair distribution function $g(\mathbf{r}_1, \mathbf{r}_2)$, which satisfies [241]

$$p(\mathbf{r}_1, \mathbf{r}_2) = \frac{g(\mathbf{r}_1, \mathbf{r}_2)}{V^2} \frac{N}{N-1}. \tag{5.26}$$

A sparse collection of scatterers, for which the positions may be assumed to be

independent, corresponds to the case $g(\mathbf{r}_1, \mathbf{r}_2) = 1$. Although not entirely physical, this choice of pair distribution function greatly simplifies calculations and shall be made in this thesis. For dense particulate media, however, where particle positions are correlated and the possibility of two particles overlapping cannot be neglected, it may be more appropriate to use different models for the joint position statistics [281].

Although we assume that particle positions are independent, it is still necessary to respect the order of the z components of each particle's position vector, as described previously. This can be achieved by introducing the Heaviside step function H, which is defined by

$$H(x) = \begin{cases} 1 & \text{if } x > 0, \\ 0 & \text{if } x \leq 0. \end{cases} \tag{5.27}$$

For large N, a joint uniform probability density function for $\mathbf{r}_1$ and $\mathbf{r}_2$, constrained such that $z_2 > z_1$ is given by

$$p(\mathbf{r}_1, \mathbf{r}_2) = \frac{H(z_2 - z_1)}{V^2/2}, \tag{5.28}$$

which is normalised by virtue of the fact that $\int\int H(z_2 - z_1)\mathrm{d}\mathbf{r}_1\mathrm{d}\mathbf{r}_2 = V^2/2$. Averaging the complex exponential for the tt term thus amounts to the evaluation of the integral

$$\frac{N^2}{2}\langle e^{i[\mathbf{r}_1\cdot(\mathbf{k}_i-\mathbf{k}_{12})+\mathbf{r}_2\cdot(\mathbf{k}_{12}-\mathbf{k}_j)]}\rangle = n^2\int e^{i[\mathbf{r}_1\cdot(\mathbf{k}_i-\mathbf{k}_{12})+\mathbf{r}_2\cdot(\mathbf{k}_{12}-\mathbf{k}_j)]}H(z_2 - z_1)\mathrm{d}\mathbf{r}_1\mathrm{d}\mathbf{r}_2. \tag{5.29}$$

Separating transverse and z components of $\mathbf{r}_1$ and $\mathbf{r}_2$, the transverse integral in the infinite medium limit is given by

$$\int e^{i[\boldsymbol{\rho}_1\cdot(\boldsymbol{\kappa}_i-\boldsymbol{\kappa}_{12})+\boldsymbol{\rho}_2\cdot(\boldsymbol{\kappa}_{12}-\boldsymbol{\kappa}_j)]}\mathrm{d}\boldsymbol{\rho}_1\mathrm{d}\boldsymbol{\rho}_2 = (2\pi)^4\delta(\boldsymbol{\kappa}_i - \boldsymbol{\kappa}_{12})\delta(\boldsymbol{\kappa}_{12} - \boldsymbol{\kappa}_j). \tag{5.30}$$

One of the delta functions in Eq. (5.30) will be eliminated after performing the integral over $\boldsymbol{\kappa}_{12}$ in Eq. (5.17). In any case, the remaining delta function will be

$\delta(\boldsymbol{\kappa}_i - \boldsymbol{\kappa}_j)$, and so, overall, we have the effective constraint $\boldsymbol{\kappa}_i = \boldsymbol{\kappa}_j = \boldsymbol{\kappa}_{12}$, from which it also follows that $\gamma_i = \gamma_{12} = \gamma_j$. The z integral contained in Eq. (5.29) is thus given by

$$\int e^{i[z_1\cdot(\gamma_i-\gamma_{12})+z_2\cdot(\gamma_{12}-\gamma_j)]}H(z_2-z_1)\mathrm{d}z_1\mathrm{d}z_2 = \int H(z_2-z_1)\mathrm{d}z_1\mathrm{d}z_2 = \frac{L^2}{2} \tag{5.31}$$

Overall, we have

$$\frac{N^2}{2}\langle e^{i[\mathbf{r}_1\cdot(\mathbf{k}_i-\mathbf{k}_{12})+\mathbf{r}_2\cdot(\mathbf{k}_{12}-\mathbf{k}_j)]}\rangle = \frac{1}{2}L^2n^2(2\pi)^4\delta(\boldsymbol{\kappa}_i-\boldsymbol{\kappa}_j), \tag{5.32}$$

which is quadratic in L. Performing analogous calculations for the $r'r$ term of Eq. (5.17), a similar cancellation in the z integral does not occur. Instead, the integral is of the form

$$\int e^{2i\gamma_i(z_1-z_2)}H(z_1-z_2)\mathrm{d}z_1\mathrm{d}z_2 = -\frac{1+e^{-2i\gamma_iL}+2i\gamma_iL}{4\gamma_i^2}, \tag{5.33}$$

which is instead linear in L in the limit $L\to\infty$. Therefore, for large L, the $r'r$ term will be dominated by the tt term and may thus be neglected.

This trend outlined for double scattering continues for higher order terms, assuming that the positions of the particles are jointly uniform and constrained only by the ordering previously discussed. To see this, note that for arbitrary order n, the corresponding z integral for any type of scattering sequence will be of the form

$$I_n(\mathbf{x},L) = \int_{[-L/2,L/2]^n} e^{i\mathbf{x}\cdot\mathbf{z}}f(\mathbf{z})\mathrm{d}\mathbf{z} = L^n\int_{[-1/2,1/2]^n} e^{iL\mathbf{x}\cdot\mathbf{z}}f(\mathbf{z})\mathrm{d}\mathbf{z} = L^n\int_{\mathcal{S}} e^{iL\mathbf{x}\cdot\mathbf{z}}\mathrm{d}\mathbf{z}, \tag{5.34}$$

where $\mathbf{z} = (z_1, z_2, \ldots, z_n)$, $\mathbf{x}$ is a vector independent of $\mathbf{z}$ that depends on the type of scattering sequence being considered, $f(\mathbf{z})$ is some product of Heaviside functions that enforces the correct particle ordering, and $\mathcal{S}$ is some subset of the hypercube $[-1/2,1/2]^n$ as determined by $f(\mathbf{z})$. For example, in the case of Eq. (5.33), we have $n=2$, $\mathbf{z}=(z_1,z_2)$, $\mathbf{x}=2\gamma_i(1,-1)$, $f(\mathbf{z})=H(z_1-z_2)$, and $\mathcal{S}$ is the half of the cube

$[-1/2, 1/2]^2$ for which $z_1 > z_2$. Noting that for $\mathbf{x} \neq \mathbf{0}$

$$e^{iL\mathbf{x}\cdot\mathbf{z}} = -\frac{i}{L|\mathbf{x}|^2}\mathbf{x}\cdot\nabla e^{iL\mathbf{x}\cdot\mathbf{z}}, \tag{5.35}$$

and, using the identity [282]

$$\int_{\mathcal{S}} \mathbf{u}\cdot\nabla v \mathrm{d}\mathbf{r} = \int_{\partial\mathcal{S}} v\mathbf{u}\cdot\widehat{\mathbf{n}}\mathrm{d}A - \int_{\mathcal{S}} v\nabla\cdot\mathbf{u}\mathrm{d}\mathbf{r}, \tag{5.36}$$

where $\partial\mathcal{S}$ is the boundary of $\mathcal{S}$ and $\widehat{\mathbf{n}}$ is a unit vector normal to the boundary, we have

$$I_n(\mathbf{x}, L) = -i\frac{L^{n-1}}{|\mathbf{x}|^2}\int_{\mathcal{S}} \mathbf{x}\cdot\nabla e^{iL\mathbf{x}\cdot\mathbf{z}}\mathrm{d}\mathbf{z} = -i\frac{L^{n-1}}{|\mathbf{x}|^2}\int_{\partial\mathcal{S}} e^{iL\mathbf{x}\cdot\mathbf{z}}\mathbf{x}\cdot\widehat{\mathbf{n}}\mathrm{d}A, \tag{5.37}$$

where we have made use of the fact that that $\nabla\cdot\mathbf{x} = 0$. Finally, we have

$$|I_n(\mathbf{x}, L)| \leq \frac{L^{n-1}}{|\mathbf{x}|^2}\left|\int_{\partial\mathcal{S}} e^{iL\mathbf{x}\cdot\mathbf{r}}\mathbf{x}\cdot\widehat{\mathbf{n}}\mathrm{d}A\right| \leq \frac{L^{n-1}}{|\mathbf{x}|^2}\int_{\partial\mathcal{S}} |\mathbf{x}\cdot\widehat{\mathbf{n}}|\mathrm{d}A = c(\mathbf{x})L^{n-1}, \tag{5.38}$$

where $c(\mathbf{x})$ is a geometric factor independent of L. Thus, we see that $|I_n(\mathbf{x}, L)|$ grows as $\sim L^{n-1}$ for large L. In the special case $\mathbf{x} = \mathbf{0}$, which corresponds to a sequence of consecutive forward scattering events, we have

$$I_n(\mathbf{x}, L) = \int_{[-L/2,L/2]^n} H(z_2 - z_1)H(z_3 - z_2)\ldots H(z_n - z_{n-1})\mathrm{d}\mathbf{z} = \frac{L^n}{n!}, \tag{5.39}$$

which grows as $\sim L^n$.

Neglecting all terms but those corresponding to chains of forward scattering events, the transmission matrix of order n is given by

$$\mathbf{t}^{(n)}(\boldsymbol{\kappa}_j, \boldsymbol{\kappa}_i) = \frac{1}{(2\pi k)^n\gamma_j}\int \sum_{z_{p_1}<\cdots<z_{p_n}} \prod_{s=0}^{n-1} \mathbf{A}^t_{p_{n-s}}(\widehat{\boldsymbol{\kappa}}_{n-s}, \widehat{\boldsymbol{\kappa}}_{n-s-1})e^{i\mathbf{r}_{p_{n-s}}\cdot(\mathbf{k}_{n-s-1}-\mathbf{k}_{n-s})}\prod_{s=1}^{n-1}\frac{\mathrm{d}\boldsymbol{\kappa}_s}{\gamma_s}, \tag{5.40}$$

where $\boldsymbol{\kappa}_s$ is an intermediate transverse wavevector for $1 \leq s \leq n-1$ and we have defined $\boldsymbol{\kappa}_0 = \boldsymbol{\kappa}_i$, $\boldsymbol{\kappa}_n = \boldsymbol{\kappa}_j$. Note that the matrix product should be taken in the

order

$$\prod_{s=0}^{n-1} \mathbf{A}^t_{p_{n-s}}(\widehat{\boldsymbol{\kappa}}_{n-s}, \widehat{\boldsymbol{\kappa}}_{n-s-1}) = \mathbf{A}^t_{p_n}(\widehat{\boldsymbol{\kappa}}_n, \widehat{\boldsymbol{\kappa}}_{n-1})\mathbf{A}^t_{p_{n-1}}(\widehat{\boldsymbol{\kappa}}_{n-1}, \widehat{\boldsymbol{\kappa}}_{n-2}) \dots \mathbf{A}^t_{p_1}(\widehat{\boldsymbol{\kappa}}_1, \widehat{\boldsymbol{\kappa}}_0). \quad (5.41)$$

In taking the ensemble average, we following similar steps to those taken in the explicit examples already shown. Assuming that the positions of the particles are jointly uniform, we may make the following substitutions in the limit $N \to \infty$

$$\begin{aligned} \sum_{z_{p_1} < z_{p_2} < \dots < z_{p_n}} &\to \frac{N^n}{n!}, \\ \left\langle \prod_{s=0}^{n-1} e^{i\mathbf{r}_{p_{n-s}} \cdot (\mathbf{k}_{n-s-1} - \mathbf{k}_{n-s})} \right\rangle &\to \frac{(2\pi)^{2n} L^n}{V^n} \prod_{s=0}^{n-1} \delta(\boldsymbol{\kappa}_{n-s-1} - \boldsymbol{\kappa}_{n-s}). \end{aligned} \quad (5.42)$$

Integrating the delta functions over the intermediate wavevectors enforces the chain of equalities $\boldsymbol{\kappa}_0 = \boldsymbol{\kappa}_1 = \dots = \boldsymbol{\kappa}_n$ and ultimately leads to

$$\langle \mathbf{t}^{(n)}(\boldsymbol{\kappa}_j, \boldsymbol{\kappa}_i) \rangle = \frac{1}{n!} \left(\frac{2\pi n L}{k\gamma_i} \mathbf{A}^t(\widehat{\boldsymbol{\kappa}}_j, \widehat{\boldsymbol{\kappa}}_i) \right)^n \delta(\boldsymbol{\kappa}_j - \boldsymbol{\kappa}_i). \quad (5.43)$$

Finally, summing over all scattering orders and recognising the emerging exponential series, the mean scattering matrix is given by

$$\langle \mathbf{t}(\boldsymbol{\kappa}_j, \boldsymbol{\kappa}_i) \rangle = \delta(\boldsymbol{\kappa}_j - \boldsymbol{\kappa}_i) \exp \left(\frac{2\pi n L}{k\gamma_i} \mathbf{A}^t(\widehat{\boldsymbol{\kappa}}_j, \widehat{\boldsymbol{\kappa}}_i) \right). \quad (5.44)$$

Eq. (5.44) can be written in a more physically intuitive form using the optical theorem. The ensemble average scattering cross section for an incident plane wave with transverse wavevector $\boldsymbol{\kappa}_i$ and polarisation state represented by α is given by [1]

$$\langle \sigma(\boldsymbol{\kappa}_i, \alpha) \rangle = -\frac{4\pi}{k^2} \mathrm{Re}\Big(\mathbf{e}^\dagger_\alpha \langle \mathbf{t}(\boldsymbol{\kappa}_i, \boldsymbol{\kappa}_i) \rangle \mathbf{e}_\alpha \Big). \quad (5.45)$$

In Eq. (5.45), $\mathbf{e}_\alpha$ is a complex unit vector characterising the incident polarisation state. Taking for example the case of isotropic spheres, it can be shown that $\mathbf{A}^t(\widehat{\boldsymbol{\kappa}}_i, \widehat{\boldsymbol{\kappa}}_i) = A\mathbb{I}_2$ for some complex constant A. In this case, it is clear that the

cross section is independent of the incident wavevector or polarisation state. Simplifying the notation so that $\langle \sigma(\boldsymbol{\kappa}_i, \theta) \rangle = \sigma$, the optical theorem then reduces to $\mathrm{Re}(A) = -k^2\sigma/4\pi$. Therefore, the mean transmission matrix element is given by

$$\langle \mathbf{t}(\boldsymbol{\kappa}_j, \boldsymbol{\kappa}_i) \rangle = \delta(\boldsymbol{\kappa}_j - \boldsymbol{\kappa}_i) \exp\left(-\frac{1}{2}\frac{L}{l_s}\sec(\theta_i) \right) \exp\left(-i\frac{1}{2}\frac{L}{l_p}\sec(\theta_i) \right) \mathbb{I}_2, \tag{5.46}$$

where l_s is the scattering mean free path, θ_i is the angle between $\mathbf{k}_i$ and the optical axis, and we have also defined

$$l_p = \frac{-k^2}{4\pi n \mathrm{Im}(A)}. \tag{5.47}$$

Observing Eq. (5.46), it can be seen that the amplitude of the mean scattered field decays exponentially over a length scale given by l, while the phase evolves over the length scale l_p. Note that $L\sec(\theta_i)$ is the length of a line segment parallel to the incident wavevector passing through the scattering medium. A grazing incident wave therefore, for which $\sec(\theta_i)$ is large, effectively 'sees' a thicker scattering medium than a normally incident mode for which $\sec(\theta_i) = 1$.

If the forward scattering amplitude matrix is not a constant factor of the identity matrix, then while the optical theorem can still be applied, the scattering cross section, and thus the mean free path, will depend on the incident polarisation state. Optically active spheres, for example, for which left and right circular polarised light experience different refractive indices, in a circular polarisation basis have a forward scattering amplitude matrix that can be written as $\mathbf{A}^t(\widehat{\boldsymbol{\kappa}}_i, \widehat{\boldsymbol{\kappa}}_i) = \mathrm{diag}(A_1, A_2)$, where A_1 and A_2 are different complex valued matrix elements. In a Cartesian basis, however, the mean transmission matrix cannot be reduced to a scalar equation as in Eq. (5.46), and the length scales over which the amplitude and phase of the scattered field evolve will depend on the helicity of the incident field. This effect will be revisited in the next chapter in Section 6.2.2.3.

5.3 Correlation functions

So far we have only considered the mean values of the scattering matrix elements. In this section we shall look at correlations between different scattering matrix elements, which are also required for a full description of Gaussian random processes. Specifically, we shall consider correlations of the form

$$C^{tt}_{(j,i)ba(v,u)dc} = \langle t_{(j,i)ba} t^{*}_{(v,u)dc} \rangle := \langle \widehat{\mathbf{e}}_b^{\dagger} \mathbf{t}(\boldsymbol{\kappa}_j, \boldsymbol{\kappa}_i) \widehat{\mathbf{e}}_a \widehat{\mathbf{e}}_c^{\dagger} \mathbf{t}^{\dagger}(\boldsymbol{\kappa}_v, \boldsymbol{\kappa}_u) \widehat{\mathbf{e}}_d \rangle, \tag{5.48}$$

where $\widehat{\mathbf{e}}_a, \widehat{\mathbf{e}}_b, \widehat{\mathbf{e}}_c$ and $\widehat{\mathbf{e}}_d$ are some collection of basis polarisation states. Similarly, we shall define $C^{rr}_{(j,i)ba(v,u)dc}$ to be the analogous correlation function between elements of the reflection matrix; $C^{tr}_{(j,i)ba(v,u)dc}$ to be cross correlations between the transmission and reflection matrices and so on for other combinations of blocks of the scattering matrix. In general, correlation functions of this type do not give a full description of the second order statistics of a collection of complex random variables. It is also necessary to consider correlations of the form

$$\widehat{C}^{tt}_{(j,i)ba(v,u)dc} = \langle t_{(j,i)ba} t_{(v,u)dc} \rangle := \langle \widehat{\mathbf{e}}_b^{\dagger} \mathbf{t}(\boldsymbol{\kappa}_j, \boldsymbol{\kappa}_i) \widehat{\mathbf{e}}_a \widehat{\mathbf{e}}_c^{\dagger} \mathbf{t}(\boldsymbol{\kappa}_v, \boldsymbol{\kappa}_u) \widehat{\mathbf{e}}_d \rangle, \tag{5.49}$$

which, in contrast to Eq. (5.48), does not involve a complex conjugate on the second transmission matrix factor. As before, in general it will also be necessary to consider $\widehat{C}^{rr}_{(j,i)ba(v,u)dc}$, $\widehat{C}^{tr}_{(j,i)ba(v,u)dc}$ and so on. Moving forwards, we shall refer to the term defined in Eq. (5.48) as a 'regular' correlation and that defined in Eq. (5.49) as a 'pseudo' correlation. In many circumstances, such as correlations between different spatial points in a typical speckle pattern, pseudo correlations are typically not observed and thus neglected in probabilistic models [283]. A vector of complex random variables whose corresponding pseudo correlation matrix is zero is sometimes referred to as 'proper' [284]. We note that propriety of a collection of complex random variables is implied by the stronger condition of circular symmetry, but is not equivalent to it.

Correlations of the scattering matrix elements appear in calculations involving correlations between different components of the scattered field. Consider for example two right-propagating incident plane waves with transverse wavevectors $\boldsymbol{\kappa}_i$ and

$\boldsymbol{\kappa}_u$ and polarisation states $\widehat{\mathbf{e}}_a$ and $\widehat{\mathbf{e}}_c$ respectively. Let $\mathbf{E}_1$ and $\mathbf{E}_2$ be the total electric fields on the right side of the medium caused by the scattering of these incident fields individually. Then by Eq. (5.6), projecting the total fields onto states $\widehat{\mathbf{e}}_b$ and $\widehat{\mathbf{e}}_d$, we have

$$\begin{aligned}\langle \widehat{\mathbf{e}}_b^\dagger \mathbf{E}_1(\mathbf{r}_1)\mathbf{E}_2^\dagger(\mathbf{r}_2)\widehat{\mathbf{e}}_d\rangle &= \int\int \langle \widehat{\mathbf{e}}_b^\dagger \mathbf{t}(\boldsymbol{\kappa}_j,\boldsymbol{\kappa}_i)\widehat{\mathbf{e}}_a \widehat{\mathbf{e}}_c^\dagger \mathbf{t}^\dagger(\boldsymbol{\kappa}_v,\boldsymbol{\kappa}_u)\widehat{\mathbf{e}}_d\rangle e^{i(\mathbf{k}_j\cdot\mathbf{r}_1-\mathbf{k}_v\cdot\mathbf{r}_2)}\mathrm{d}\boldsymbol{\kappa}_j\mathrm{d}\boldsymbol{\kappa}_v \\ &= \int\int C^{tt}_{(j,i)ba(v,u)dc} e^{i(\mathbf{k}_j\cdot\mathbf{r}_1-\mathbf{k}_v\cdot\mathbf{r}_2)}\mathrm{d}\boldsymbol{\kappa}_j\mathrm{d}\boldsymbol{\kappa}_v.\end{aligned} \tag{5.50}$$

Similarly, it can also be shown that pseudo correlations of the scattered field satisfy the analogous equation

$$\langle \widehat{\mathbf{e}}_b^\dagger \mathbf{E}_1(\mathbf{r}_1)\mathbf{E}_2^{\mathrm{T}}(\mathbf{r}_2)\widehat{\mathbf{e}}_d\rangle = \int\int \widehat{C}^{tt}_{(j,i)ba(v,u)dc} e^{i(\mathbf{k}_j\cdot\mathbf{r}_1+\mathbf{k}_v\cdot\mathbf{r}_2)}\mathrm{d}\boldsymbol{\kappa}_j\mathrm{d}\boldsymbol{\kappa}_v. \tag{5.51}$$

5.3.1 Single scattering

Unlike the calculation of the mean transmission matrix in Section 5.2.2, a complete theory of the correlation functions introduced so far that incorporates all scattering orders is much more complicated mathematically. We will therefore be limited to the study of a couple of special cases, the simplest of which is single scattering. Although single scattering is only accurate for thin scattering media, the correlation functions are exactly solvable and take relatively simple forms that offer interesting physical insight.

Recalling the form of the transmission matrix as given by Eq. (5.14), the single scattering correlation function is given by

$$\langle t^{(1)}_{(j,i)ba} t^{(1)*}_{(v,u)dc}\rangle = \frac{1}{(2\pi k)^2\gamma_j\gamma_v}\sum_{p_1=1}^{N}\sum_{q_1=1}^{N}\langle A^t_{p_1(j,i)ba} A^{t*}_{q_1(v,u)dc}\rangle\langle e^{i[\mathbf{r}_{p_1}\cdot(\mathbf{k}_i-\mathbf{k}_j)-\mathbf{r}_{q_1}\cdot(\mathbf{k}_u-\mathbf{k}_v)]}\rangle. \tag{5.52}$$

The terms in the sums in Eq. (5.52) can be separated into two types: those for which $p_1 = q_1$ and those for which $p_1 \neq q_1$. If $p_1 \neq q_1$, then by the assumption that the statistical properties of the particles are independent, the terms in the

sums completely decouple and the averages can be performed over each particle separately, yielding the product of the means $\langle t^{(1)}_{(j,i)ba}\rangle\langle t^{(1)*}_{(v,u)dc}\rangle$. If, however, $p_1 = q_1$, then $\mathbf{r}_{p_1} = \mathbf{r}_{q_1} = \mathbf{r}$ and, using Eq. (5.23), the exponential average becomes

$$N\langle e^{i\mathbf{r}\cdot(\mathbf{k}_i-\mathbf{k}_j-\mathbf{k}_u+\mathbf{k}_v)}\rangle \to (2\pi)^2 nL\mathrm{sinc}\Big((\gamma_i-\gamma_j-\gamma_u+\gamma_v)\frac{L}{2}\Big)\delta(\boldsymbol{\kappa}_i-\boldsymbol{\kappa}_j-\boldsymbol{\kappa}_u+\boldsymbol{\kappa}_v). \tag{5.53}$$

The argument of the delta function appearing in Eq. (5.53) is zero precisely when

$$k_{ix}-k_{jx} = k_{ux}-k_{vx}, \tag{5.54}$$

$$k_{iy}-k_{jy} = k_{uy}-k_{vy}. \tag{5.55}$$

This condition is precisely that of the memory effect [44], which manifests here as a correlation between certain pairs of blocks of the scattering blocks. Overall, we find that the covariance of the transmission matrix elements is given by

$$\begin{aligned}\langle t^{(1)}_{(j,i)ba}t^{(1)*}_{(v,u)dc}\rangle - \langle t^{(1)}_{(j,i)ba}\rangle\langle t^{(1)*}_{(v,u)dc}\rangle = \\ \delta(\boldsymbol{\kappa}_i-\boldsymbol{\kappa}_j-\boldsymbol{\kappa}_u+\boldsymbol{\kappa}_v)\frac{nL}{k^2\gamma_j\gamma_v}\langle A^t_{(j,i)ba}A^{t*}_{(v,u)dc}\rangle\mathrm{sinc}\Big((\gamma_i-\gamma_j-\gamma_u+\gamma_v)\frac{L}{2}\Big).\end{aligned} \tag{5.56}$$

An analogous result can be derived for the pseudo covariance, which is given by

$$\begin{aligned}\langle t^{(1)}_{(j,i)ba}t^{(1)}_{(v,u)dc}\rangle - \langle t^{(1)}_{(j,i)ba}\rangle\langle t^{(1)}_{(v,u)dc}\rangle = \\ \delta(\boldsymbol{\kappa}_i-\boldsymbol{\kappa}_j+\boldsymbol{\kappa}_u-\boldsymbol{\kappa}_v)\frac{nL}{k^2\gamma_j\gamma_v}\langle A^t_{(j,i)ba}A^{t}_{(v,u)dc}\rangle\mathrm{sinc}\Big((\gamma_i-\gamma_j+\gamma_u-\gamma_v)\frac{L}{2}\Big).\end{aligned} \tag{5.57}$$

This time, the argument of the delta function vanishes under the condition

$$k_{ix}-k_{jx} = -(k_{ux}-k_{vx}), \tag{5.58}$$

$$k_{iy}-k_{jy} = -(k_{uy}-k_{vy}). \tag{5.59}$$

Suppose that the variables i and j, which denote an incident and scattered plane wave component respectively, are fixed. The polarisation statistics of the scattered

field are classically expressed using regular correlations, i.e. the type appearing in Eq. (5.56), at a fixed point in space, or scattered direction. Choosing also $u = i$ and $v = j$ means that Eq. (5.56) describes correlations between the four complex elements of the 2×2 block of the transmission matrix $\mathbf{t}_{(j,i)}$. In fact, supposing for simplicity that $i \neq j$ so that $\langle \mathbf{t}_{(j,i)} \rangle = \mathbf{0}$, enumerating all 16 choices for variables a, b, c and d allows for the construction of an autocorrelation matrix associated with the elements of $\mathbf{t}_{(j,i)}$. The elements of the mean Mueller matrix associated with the ensemble of $\mathbf{t}_{(j,i)}$ is then given by linear combinations of the autocorrelation matrix. Since the Mueller matrix is fully determined by regular correlations, pseudo correlations have no impact on the polarisation properties of scattered wave in a fixed direction. This is also immediately evident by noting that the argument of the delta function appearing in Eq. (5.57) does not in general vanish under the conditions $i = u$ and $j = v$, save for the trivial case when $i = j$ also holds.

In addition to being proper, given that non-diagonal blocks of the transmission matrix also have zero mean, it follows that every element within a non-diagonal block of the transmission matrix is a circularly symmetric complex random variable [279]. The joint statistics of all of the elements of the transmission matrix, however, do not obey circular symmetry, owing to the existence of non-zero pseudo correlations, as described by Eq. (5.57). Consider for example the pair of blocks $\mathbf{t}_{(j,i)}$ and $\mathbf{t}_{(i,j)}$, which are related by swapping the incident and outgoing plane wave directions. Referring to Eq. (5.14), the complex exponential terms for these blocks are given by $\exp[i(\mathbf{k}_i - \mathbf{k}_j) \cdot \mathbf{r}]$ and $\exp[i(\mathbf{k}_j - \mathbf{k}_i) \cdot \mathbf{r}] = \exp[-i(\mathbf{k}_i - \mathbf{k}_j) \cdot \mathbf{r}]$ respectively. Thus, regardless of the distribution of the particles within the medium, the complex exponential terms associated with $\mathbf{t}_{(i,j)}$ are always the complex conjugates of those associated with $\mathbf{t}_{(j,i)}$, which manifests as a non-zero pseudo correlation. It is also straightforward to see that these blocks also satisfy Eqs. (5.58) and (5.59).

The statistics of the reflection matrix elements are given by

$$\langle r^{(1)}_{(j,i)ba} r^{(1)*}_{(v,u)dc} \rangle - \langle r^{(1)}_{(j,i)ba} \rangle \langle r^{(1)*}_{(v,u)dc} \rangle = \delta(\boldsymbol{\kappa}_i - \boldsymbol{\kappa}_j - \boldsymbol{\kappa}_u + \boldsymbol{\kappa}_v) \frac{nL}{k^2 \gamma_j \gamma_v} \langle A^r_{(j,i)ba} A^{r*}_{(v,u)dc} \rangle \mathrm{sinc}\Big((\gamma_i + \gamma_j - \gamma_u - \gamma_v) \frac{L}{2} \Big), \tag{5.60}$$

$$\langle r^{(1)}_{(j,i)ba} r^{(1)}_{(v,u)dc} \rangle - \langle r^{(1)}_{(j,i)ba} \rangle \langle r^{(1)}_{(v,u)dc} \rangle = \delta(\boldsymbol{\kappa}_i - \boldsymbol{\kappa}_j + \boldsymbol{\kappa}_u - \boldsymbol{\kappa}_v) \frac{nL}{k^2 \gamma_j \gamma_v} \langle A^r_{(j,i)ba} A^{r}_{(v,u)dc} \rangle \mathrm{sinc}\Big((\gamma_i + \gamma_j + \gamma_u + \gamma_v) \frac{L}{2} \Big). \tag{5.61}$$

Similar results for the other blocks of the scattering matrix, as well as correlations between different blocks also take the same form as those presented here, but with the appropriate choice of superscripts on the $\mathbf{A}$ matrices and the correct signs on the γ terms within the sinc.

5.3.2 Physical picture

In this section we shall examine in more detail some of the physical consequences of the correlation functions discussed thus far. Although we have discussed correlations between different field components, it is more common to work with scattered field intensity correlation functions, which are more accessible experimentally.

Suppose that a plane wave with transverse wavevector $\boldsymbol{\kappa}_i$ and polarisation state $a \in \{\theta, \phi\}$ is incident upon the scattering medium and let $\langle I_{(j,i)a} \rangle$ denote the mean transmitted intensity in the direction associated with $\boldsymbol{\kappa}_j$, defined by

$$\langle I_{(j,i)a} \rangle = \langle t_{(j,i)\theta a} t^*_{(j,i)\theta a} \rangle + \langle t_{(j,i)\phi a} t^*_{(j,i)\phi a} \rangle. \tag{5.62}$$

Similarly, let $\langle I_{(v,u)c} \rangle$ denote the corresponding mean transmitted intensity in direction $\boldsymbol{\kappa}_v$ for an incident plane wave with transverse wavevector $\boldsymbol{\kappa}_u$ and polarisation state $c \in \{\theta, \phi\}$. For simplicity, we shall suppose that $i \neq j$ and $u \neq v$, so that the corresponding matrix elements are zero-mean. A common choice for a normalised

intensity correlation function is [285]

$$C^{I}_{(j,i)a(v,u)c} = \frac{\langle \delta I_{(j,i)a} \delta I_{(v,u)c} \rangle}{\langle I_{(j,i)a} \rangle \langle I_{(v,u)c} \rangle} = \frac{\langle I_{(j,i)a} I_{(v,u)c} \rangle}{\langle I_{(j,i)a} \rangle \langle I_{(v,u)c} \rangle} - 1, \tag{5.63}$$

where $\delta I_{(j,i)a} = I_{(j,i)a} - \langle I_{(j,i)a} \rangle$ describes intensity fluctuations about the mean. The correlation $\langle I_{(j,i)a} I_{(v,u)c} \rangle$ is given by

$$\langle I_{(j,i)a} I_{(v,u)c} \rangle = \langle (t_{(j,i)\theta a} t^{*}_{(j,i)\theta a} + t_{(j,i)\phi a} t^{*}_{(j,i)\phi a})(t_{(v,u)\theta c} t^{*}_{(v,u)\theta c} + t_{(v,u)\phi c} t^{*}_{(v,u)\phi c}) \rangle, \tag{5.64}$$

which involves terms containing the products of four different elements of the transmission matrix. Writing each transmission matrix term in Eq. (5.64) in terms of its real and imaginary parts so that, for example, $t_{(j,i)\theta a} = t^{\mathrm{Re}}_{(j,i)\theta a} + i t^{\mathrm{Im}}_{(j,i)\theta a}$, allows us to rewrite Eq. (5.64) in the form

$$\langle I_{(j,i)a} I_{(v,u)c} \rangle = \sum_{\substack{p,q \in \{\mathrm{Re,Im}\} \\ b,d \in \{\theta,\phi\}}} \langle (t^{p}_{(j,i)ba} t^{q}_{(v,u)dc})^2 \rangle, \tag{5.65}$$

where the terms within the sum are real quantities. Since the matrix elements are assumed to be Gaussian, we may apply Isserlis's theorem, a special version of which states that if (a, b) follow a zero-mean multivariate Gaussian distribution then [242]

$$\langle a^2 b^2 \rangle = \langle a^2 \rangle \langle b^2 \rangle + 2 \langle ab \rangle^2. \tag{5.66}$$

Applying this theorem to Eq. (5.65) and noting that

$$\sum_{\substack{p,q \in \{\mathrm{Re,Im}\} \\ b,d \in \{\theta,\phi\}}} \langle t^{p}_{(j,i)ba} t^{p}_{(j,i)ba} \rangle \langle t^{q}_{(v,u)dc} t^{q}_{(v,u)dc} \rangle = \langle I_{(j,i)a} \rangle \langle I_{(v,u)c} \rangle, \tag{5.67}$$

we find that

$$\langle I_{(j,i)a} I_{(v,u)c} \rangle - \langle I_{(j,i)a} \rangle \langle I_{(v,u)c} \rangle = 2 \sum_{\substack{p,q \in \{\mathrm{Re,Im}\} \\ b,d \in \{\theta,\phi\}}} \langle t^{p}_{(j,i)ba} t^{q}_{(v,u)dc} \rangle^2. \tag{5.68}$$

Now, making use of the fact that [279]

$$C^{tt}_{(j,i)ba(v,u)dc} = t^{\mathrm{Re}}_{(j,i)ba} t^{\mathrm{Re}}_{(v,u)dc} + t^{\mathrm{Im}}_{(j,i)ba} t^{\mathrm{Im}}_{(v,u)dc} + i(t^{\mathrm{Im}}_{(j,i)ba} t^{\mathrm{Re}}_{(v,u)dc} - t^{\mathrm{Re}}_{(j,i)ba} t^{\mathrm{Im}}_{(v,u)dc}), \quad (5.69)$$

$$\widehat{C}^{tt}_{(j,i)ba(v,u)dc} = t^{\mathrm{Re}}_{(j,i)ba} t^{\mathrm{Re}}_{(v,u)dc} - t^{\mathrm{Im}}_{(j,i)ba} t^{\mathrm{Im}}_{(v,u)dc} + i(t^{\mathrm{Im}}_{(j,i)ba} t^{\mathrm{Re}}_{(v,u)dc} + t^{\mathrm{Re}}_{(j,i)ba} t^{\mathrm{Im}}_{(v,u)dc}), \quad (5.70)$$

it follows after some algebra that

$$C^{I}_{(j,i)a(v,u)c} = \frac{\sum_{b,d\in\{\theta,\phi\}} \left(|C^{tt}_{(j,i)ba(v,u)dc}|^2 + |\widehat{C}^{tt}_{(j,i)ba(v,u)dc}|^2 \right)}{\left(C^{tt}_{(j,i)\theta a(j,i)\theta a} + C^{tt}_{(j,i)\phi a(j,i)\phi a} \right) \left(C^{tt}_{(v,u)\theta c(v,u)\theta c} + C^{tt}_{(v,u)\phi c(v,u)\phi c} \right)}. \quad (5.71)$$

Finally, using Eqs. (5.56) and (5.57) and assuming independent particles, we arrive at

$$C^{I}_{(j,i)a(v,u)c} = \delta^R \mathrm{sinc}^2\left((c_i - c_j - c_u + c_v)\frac{kL}{2} \right) + \delta^P \mathrm{sinc}^2\left((c_i - c_j + c_u - c_v)\frac{kL}{2} \right), \quad (5.72)$$

where δ^R is equal to one if Eqs. (5.54) and (5.55) are satisfied and zero otherwise and, similarly, δ^P is equal to one if Eqs. (5.58) and (5.59) are satisfied and zero otherwise. c_i is defined by $c_i = \gamma_i/k$, and all other c terms are defined similarly. Note that the domains for which δ^R and δ^P are non-zero are mutually exclusive, except for special cases, such as $i = j$ and $u = v$, which we excluded at the outset. Note also that in deriving Eq. (5.72) we have supposed that the 'infinities' related to the delta functions in the numerator and denominator cancel and that the constraints enforced by the delta functions of the numerators now manifest in the δ^R and δ^P factors. In reality, of course, one would be concerned with scattered field correlations, rather than scattering matrix element correlations, and the delta functions would be resolved by intermediate integrals, eventually resulting in the same expression as Eq. (5.72).

Eq. (5.72), notably, shows no dependence on polarisation. Polarisation dependence, if at all, must enter into the function via the amplitude matrices, which, in Eq. (5.71) completely cancel in the numerator and denominator. This is partly a result of our choice of correlation function, as well as the fact that the particles are identical and independent. The polarisation properties of similar correlation

functions will be explored in more detail in Chapter 7.

Consider first the regular correlations described by the first term of Eq. (5.72). Since the envelope of sinc is a decaying function, regular correlations are generally larger when the argument of the sinc is small. In fact, Eq. (5.72) suggests that perfect correlation is achievable under the condition

$$c_i - c_j - c_u + c_v = 0, \tag{5.73}$$

irrespective of L, remembering of course that Eq. (5.72) is only accurate in the single scattering regime. Eq. (5.73) essentially states that the total phase change in the z direction incurred by transmission from an incident plane wave with wavevector $\mathbf{k}_i$ to one with wavevector $\mathbf{k}_j$, is equal to the corresponding phase change by the corresponding pair of waves with wavevectors $\mathbf{k}_u$ and $\mathbf{k}_v$. The actual set of wavevectors that satisfy this condition, however, is not completely trivial.

In order to better visualise solutions of Eq. (5.73), it is helpful to think of transverse wavevectors as points in k-space. For simplicity, we shall suppose that all wavevectors are normalised by k so that the set of all homogeneous wavevectors lies within the unit circle $|\boldsymbol{\kappa}| = 1$. Suppose that $\boldsymbol{\kappa}_i$ and $\boldsymbol{\kappa}_j$ are fixed. For example, let $\boldsymbol{\kappa}_i = (0, 0)$ and $\boldsymbol{\kappa}_j = (0.5, 0)$. The difference between these vectors is $\Delta\boldsymbol{\kappa}_{ji} = \boldsymbol{\kappa}_j - \boldsymbol{\kappa}_i = (0.5, 0)$. In order for there to be regular correlations, the pair of transverse wavevectors $\boldsymbol{\kappa}_u$ and $\boldsymbol{\kappa}_v$ must be such that $\Delta\boldsymbol{\kappa}_{vu} = \boldsymbol{\kappa}_v - \boldsymbol{\kappa}_u$ satisfies $\Delta\boldsymbol{\kappa}_{ji} = \Delta\boldsymbol{\kappa}_{vu}$. Note that choosing one of either $\boldsymbol{\kappa}_v$ or $\boldsymbol{\kappa}_u$ automatically determines the other, and so there is only a single degree of freedom, which we shall take to be the position of $\boldsymbol{\kappa}_u$. Consider now the left panel in Figure 5.1, where $\Delta\boldsymbol{\kappa}_{ji}$ is shown by the black arrow emanating from the origin. A choice of $\boldsymbol{\kappa}_u$ (and thus $\boldsymbol{\kappa}_v$) for which the memory effect condition is satisfied will be such that the resulting $\Delta\boldsymbol{\kappa}_{vu}$ is related to $\Delta\boldsymbol{\kappa}_{ji}$ by a simple translation in the plane. It must be remembered, however, that $\boldsymbol{\kappa}_u$ cannot be chosen too close to the circular boundary, as this may result in the corresponding position of $\boldsymbol{\kappa}_v$ lying outside of the circle. For a given choice of $\boldsymbol{\kappa}_u$ and $\boldsymbol{\kappa}_v$ satisfying these conditions, there will be non-zero correlations between the corresponding matrix blocks $\mathbf{t}_{(j,i)}$ and $\mathbf{t}_{(v,u)}$.

Not all possible choices of $\boldsymbol{\kappa}_u$ have equal correlation strength. As discussed, the

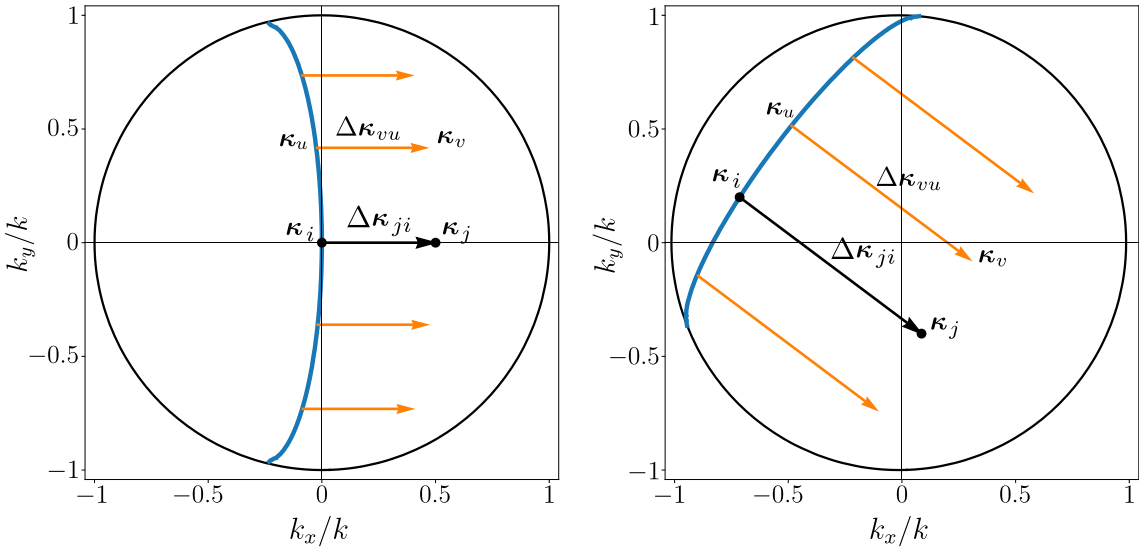

Figure 5.1: Diagram of k-space depicting elliptical bands that describe positions of $\boldsymbol{\kappa}_u$ for which the block $\mathbf{t}_{(v,u)}$ has perfect regular correlation with $\mathbf{t}_{(j,i)}$. In the left panel $\boldsymbol{\kappa}_i = (0, 0)$ and $\boldsymbol{\kappa}_j = (0, 0.5)$ and in the right panel $\boldsymbol{\kappa}_i = (-0.7, 0.2)$ and $\boldsymbol{\kappa}_j = (0.1, -0.4)$.

correlation function is maximised when Eq. (5.73) holds. In terms of normalised transverse wavevectors, this is equivalent to

$$\sqrt{1 - |\boldsymbol{\kappa}_i|^2} - \sqrt{1 - |\boldsymbol{\kappa}_j|^2} - \sqrt{1 - |\boldsymbol{\kappa}_u|^2} + \sqrt{1 - |\boldsymbol{\kappa}_v|^2} = 0. \tag{5.74}$$

For fixed $\boldsymbol{\kappa}_i$ and $\boldsymbol{\kappa}_j$, the locus of points (k_{ux}, k_{uy}) that satisfy Eq. (5.74), after some algebra, can be shown to be one branch of an ellipse, which is shown in the left panel of Figure 5.1 as a solid blue line. Regular correlations will therefore be maximised when $\boldsymbol{\kappa}_u$ is chosen to lie on this ellipse. Some examples of such positions for $\boldsymbol{\kappa}_u$ are demonstrated in Figure 5.1, where the orange arrows represent $\Delta\boldsymbol{\kappa}_{vu}$. If $\boldsymbol{\kappa}_u$ does not lie on the ellipse, correlations will still exist, but, since the argument of the sinc function in Eq. (5.72) will be non-zero, regular correlations will be weaker. Regular correlations, in fact, become increasingly weak as $\boldsymbol{\kappa}_u$ is moved away from the elliptical band. The shape of the ellipse depends on the choices for $\boldsymbol{\kappa}_i$ and $\boldsymbol{\kappa}_j$, and another example is shown in the right panel of Figure 5.1, where $\boldsymbol{\kappa}_i = (-0.7, 0.2)$ and $\boldsymbol{\kappa}_j = (0.1, -0.4)$. In general, we find that the vector $\Delta\boldsymbol{\kappa}_{ji}$ is normal to the ellipse at the point $\boldsymbol{\kappa}_i$.

While pseudo correlations have no effect on the intensity statistics in a single scattered direction, Eq. (5.72) shows that they manifest in the joint intensity statis-

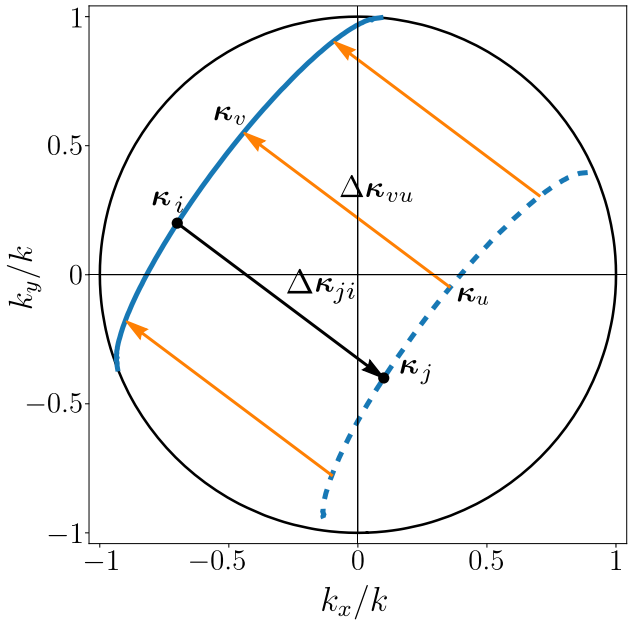

Figure 5.2: Diagram of k-space depicting a dashed elliptical band that describe positions of $\boldsymbol{\kappa}_u$ for which the block $\mathbf{t}_{(v,u)}$ has perfect pseudo correlation with $\mathbf{t}_{(j,i)}$. The solid elliptical band is the same as in Fig 5.1 and describes positions for $\boldsymbol{\kappa}_u$ where regular correlations are maximally strong. In addition, $\boldsymbol{\kappa}_i = (-0.7, 0.2)$ and $\boldsymbol{\kappa}_j = (0.1, -0.4)$. For $\boldsymbol{\kappa}_u$ on the dashed elliptical band, $\boldsymbol{\kappa}_v$ is constrained to satisfy $\Delta\boldsymbol{\kappa}_{vu} = \Delta\boldsymbol{\kappa}_{ji}$.

tics for a pair of scattering directions. Suppose for example that $\boldsymbol{\kappa}_i = \boldsymbol{\kappa}_u = \boldsymbol{\kappa}_0$, so that we are considering the joint statistics of different directions in a single angular intensity speckle pattern. Although $\delta^R = 0$ for all choices of $\boldsymbol{\kappa}_u$ and $\boldsymbol{\kappa}_v$ apart from $\boldsymbol{\kappa}_u = \boldsymbol{\kappa}_v$ meaning no regular correlations exist between different scattering directions, Eqs. (5.58) and (5.59) reduce to $\boldsymbol{\kappa}_0 = (\boldsymbol{\kappa}_j + \boldsymbol{\kappa}_v)/2$, which means that the intensities of two directions whose corresponding transverse wavevectors are positioned symmetrically about $\boldsymbol{\kappa}_0$ are correlated. Note that this condition on the transverse wavevectors does not imply the same constraint for the z components of the wavevectors. In general, even when $\delta^P = 1$, it will not be the case that $c_0 = (c_j + c_v)/2$, which means that pseudo correlations will generally decay with increasing L, as the argument of the corresponding sinc in Eq. (5.72) will be non-zero. Further analysis shows that correlations of this type are maximised when $\boldsymbol{\kappa}_0 = \mathbf{0}$, i.e. normally incident light, and when $\boldsymbol{\kappa}_u$ and $\boldsymbol{\kappa}_v$ are as close to the origin as possible. Correlations of this type are known in the field of rough surface scattering [286] and have also been referred to as the conjugate memory effect [287].

A corresponding ellipse representing positions of $\boldsymbol{\kappa}_u$ that exhibit maximal pseudo

correlation strength can be found by considering the argument of the sinc in the second term of Eq. (5.72). Suppose that once again we have $\boldsymbol{\kappa}_i = (-0.7, 0.2)$ and $\boldsymbol{\kappa}_j = (0.1, -0.4)$. The ellipse is shown in Fig. 5.2 as a dashed blue line. This time, however, the vector $\Delta\boldsymbol{\kappa}_{vu}$ must be directed opposite to $\Delta\boldsymbol{\kappa}_{ji}$ so as to satisfy the condition $\Delta\boldsymbol{\kappa}_{vu} = -\Delta\boldsymbol{\kappa}_{ji}$.

If one instead derives the intensity correlation function for the reflected field, an analogous expression to Eq. (5.72) can be derived, but which instead has a different pattern of + and − symbols inside the sinc functions so as to accord with Eqs. (5.60) and (5.61). This time, the corresponding set of points of maximal regular correlations is a closed ellipse, as shown in the left panel in Figure 5.3, for which $\boldsymbol{\kappa}_i = (0.1, 0.5)$ and $\boldsymbol{\kappa}_j = (0.6, 0.2)$. As before, if the vector $\boldsymbol{\kappa}_u$ is chosen to lie on this ellipse, the corresponding pair of blocks of the reflection matrix will be perfectly correlated. It is also interesting to note that the point $\boldsymbol{\kappa}_u = -\boldsymbol{\kappa}_j$, which we shall call the reciprocal point and which is indicated in Figure 5.3, always lies on the ellipse. If this point is chosen for $\boldsymbol{\kappa}_u$, then it automatically follows that $\boldsymbol{\kappa}_v = -\boldsymbol{\kappa}_i$, which means that $\mathbf{r}_{(v,u)} = \mathbf{r}_{(-i,-j)}$, which is the block related to $\mathbf{r}_{(j,i)}$ by reciprocity. Since reciprocity enforces a deterministic relationship between $\mathbf{r}_{(j,i)}$ and $\mathbf{r}_{(-i,-j)}$, regardless of the disorder of the scattering medium, these blocks must always be perfectly correlated. It should be stressed that, although the elliptical path is a consequence of single scattering theory, reciprocity holds under more general conditions, including in the multiple scattering regime. The existence of perfect correlation at the reciprocal point has been noted before in the literature, and has been referred to as the time-reversed memory effect [288].

A similar time-reversed memory effect occurs for the transmission matrix. Unlike the reflection matrix, however, the reciprocal counterpart to $\mathbf{t}_{(j,i)}$ is $\mathbf{t}'_{(-i,-j)}$, which does not lie in the transmission matrix. Considering correlations between the elements of $\mathbf{t}_{(j,i)}$ and $\mathbf{t}'_{(v,u)}$, leads to another ellipse of maximal correlations, which is depicted by a dashed blue line in the right panel of Fig. 5.3. If $\boldsymbol{\kappa}_u$ is chosen to lie on this path, then $\mathbf{t}_{(j,i)}$ and $\mathbf{t}'_{(v,u)}$ are perfectly correlated. The reciprocal point, corresponding to the block $\mathbf{t}'_{(-i,-j)}$ is again shown. As with the previous case, this correlation is not limited to single scattering.

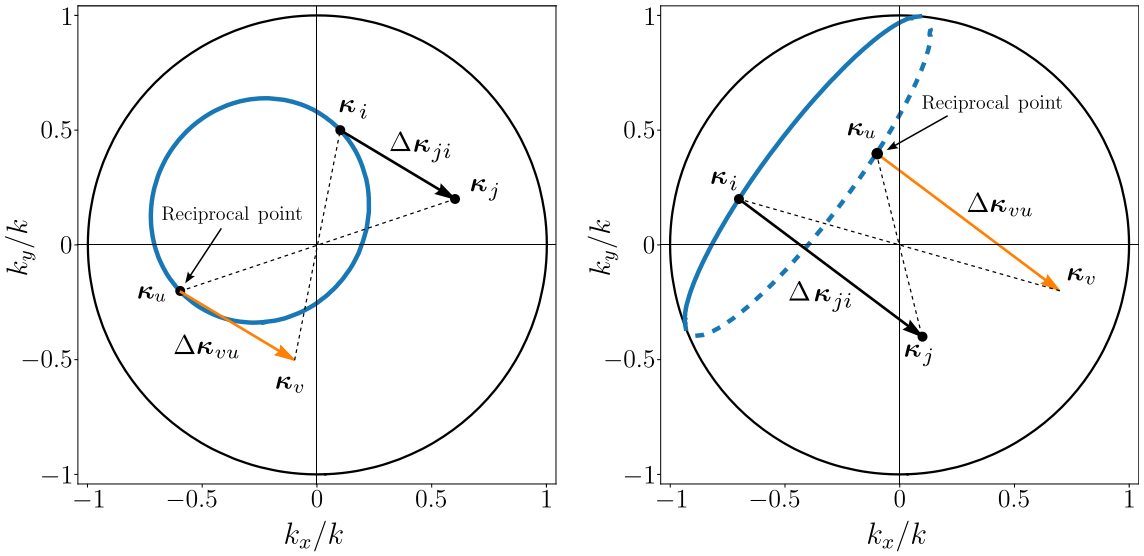

Figure 5.3: Diagram of k-space depicting ellipses that describe positions of $\boldsymbol{\kappa}_u$ for which regular correlations between scattering matrix blocks are maximised. In the left figure $\boldsymbol{\kappa}_i = (0.1, 0.5)$ and $\boldsymbol{\kappa}_j = (0.6, 0.2)$, and the ellipse shows positions of $\boldsymbol{\kappa}_u$ that maximise regular correlations between $\mathbf{r}_{(j,i)}$ and $\mathbf{r}_{(v,u)}$. The reciprocal point is related to the time-reversed memory effect, as discussed in the text. In the right figure $\boldsymbol{\kappa}_i = (-0.7, 0.2)$ and $\boldsymbol{\kappa}_j = (0.1, -0.4)$. The dashed blue curve shows positions of $\boldsymbol{\kappa}_u$ that maximise regular correlations between $\mathbf{t}_{(j,i)}$ and $\mathbf{t}'_{(v,u)}$. The reciprocal point again is related to the time-reversed memory effect.

5.3.3 Multiple scattering

For multiple scattering, calculating the correlation functions becomes much more difficult. Within the framework presented in this chapter, it would be necessary to calculated correlations between terms of different scattering order, which themselves contained numerous sub-terms for different types of scattering sequences. A full mathematical analysis of this problem is beyond the scope of this thesis. Nevertheless we shall present some preliminary results that offer some insight towards the multiple scattering characteristics of correlation functions of the type explored in the preceding sections. We shall restrict our discussion to regular correlations between different elements of the transmission matrix. The results in this section will later be compared against simulated data in Chapter 7.

In diagrammatic theories of multiple scattering, the total correlation is the solution of the Bethe-Salpeter equation, which expresses the correlation function as an infinite sum over all possible so-called strongly connected diagrams [241]. Although it is infeasible to solve this equation exactly, it is common to use the ladder approx-

imation in the weak scattering regime ($kl_s \gg 1$). In the ladder approximation, one only considers correlations between pairs of scattering sequences (one for $\boldsymbol{\kappa}_i \to \boldsymbol{\kappa}_j$ and one for $\boldsymbol{\kappa}_u \to \boldsymbol{\kappa}_v$) that involve the same set of particles, traversed in the same order. In addition, it is assumed that the fields within the medium that propagate between different particles in the scattering sequences are the previously derived mean fields, which, as shown in Eq. (5.46), decay in amplitude as they propagate. It is the use of the decaying mean field that incorporates multiple scattering effects. The ladder approximation allows one to express the total correlation function $C^{L}_{(j,i)ba(v,u)dc}$ as an infinite series over a different kind of scattering order. The ladder term of order n, which we shall denote by $C^{L_n}_{(j,i)ba(v,u)dc}$, represents correlations due to a pair of scattering sequences that share exactly n particles in common. We therefore have

$$C^{L}_{(j,i)ba(v,u)dc} = \sum_{n=0}^{\infty} C^{L_n}_{(j,i)ba(v,u)dc}. \tag{5.75}$$

Scattering sequences captured in the zero order term $C^{L_0}_{(j,i)ba(v,u)dc}$ contain no particles in common and the correlation function is thus given by the mean product

$$\begin{aligned} C^{L_0}_{(j,i)ba(v,u)dc} &= \langle t_{(j,i)ba} \rangle \langle t^{*}_{(v,u)dc} \rangle \\ &= \delta(\boldsymbol{\kappa}_j - \boldsymbol{\kappa}_i)\delta(\boldsymbol{\kappa}_v - \boldsymbol{\kappa}_u)\widehat{\mathbf{e}}^{\dagger}_b \exp\left(\frac{2\pi n L}{k\gamma_i}\mathbf{A}^{t}_{(j,i)}\right)\widehat{\mathbf{e}}_a \widehat{\mathbf{e}}^{\dagger}_c \exp\left(\frac{2\pi n L}{k\gamma_u}\mathbf{A}^{t\dagger}_{(v,u)}\right)\widehat{\mathbf{e}}^{\dagger}_c. \end{aligned} \tag{5.76}$$

The first order term $C^{L_1}_{(j,i)ba(v,u)dc}$ can be interpreted physically as single scattering of the mean field and is sometimes referred to as 'first order multiple scattering' [163]. Truncating the ladder series to give the approximation $C^{L}_{(j,i)ba(v,u)dc} \approx C^{L_0}_{(j,i)ba(v,u)dc} + C^{L_1}_{(j,i)ba(v,u)dc}$ is also sometimes known as the distorted Born approximation [241]. To derive the first order term, we begin with the fact that, if $\mathbf{E}_1$ and $\mathbf{E}_2$ are two scattered fields as defined in Eq. (5.50), then the ladder approximation is equivalent

to the series [289]

$$\begin{aligned}\langle\widehat{\mathbf{e}}_b^\dagger\mathbf{E}^1(\mathbf{r}_1)\widehat{\mathbf{e}}_a\widehat{\mathbf{e}}_c^\dagger\mathbf{E}^{2\dagger}(\mathbf{r}_2)\widehat{\mathbf{e}}_d\rangle - \langle\widehat{\mathbf{e}}_b^\dagger\mathbf{E}^1(\mathbf{r}_1)\widehat{\mathbf{e}}_a\rangle\langle\widehat{\mathbf{e}}_c^\dagger\mathbf{E}^{2\dagger}(\mathbf{r}_2)\widehat{\mathbf{e}}_d\rangle = \\ n\int\widehat{\mathbf{e}}_b^\dagger\mathbf{V}(\mathbf{r}_1-\mathbf{r}_{p_1},\mathbf{k}_i)\mathbf{U}(\mathbf{r}_{p_1};\mathbf{k}_i)\widehat{\mathbf{e}}_a\widehat{\mathbf{e}}_c^\dagger\mathbf{U}^\dagger(\mathbf{r}_{p_1};\mathbf{k}_u)\mathbf{V}^\dagger(\mathbf{r}_2-\mathbf{r}_{p_1},\mathbf{k}_u)\widehat{\mathbf{e}}_d\mathrm{d}\mathbf{r}_{p_1} \\ +n^2\int\widehat{\mathbf{e}}_b^\dagger\mathbf{V}(\mathbf{r}_1-\mathbf{r}_{p_2},\mathbf{r}_{p_2}-\mathbf{r}_{p_1})\mathbf{V}(\mathbf{r}_{p_2}-\mathbf{r}_{p_1},\mathbf{k}_i)\mathbf{U}(\mathbf{r}_{p_1};\mathbf{k}_i)\widehat{\mathbf{e}}_a \\ \widehat{\mathbf{e}}_c^\dagger\mathbf{U}^\dagger(\mathbf{r}_{p_1};\mathbf{k}_u)\mathbf{V}^\dagger(\mathbf{r}_{p_2}-\mathbf{r}_{p_1},\mathbf{k}_u)\mathbf{V}^\dagger(\mathbf{r}_2-\mathbf{r}_{p_2},\mathbf{r}_{p_2}-\mathbf{r}_{p_1})\widehat{\mathbf{e}}_d\mathrm{d}\mathbf{r}_{p_1}\mathrm{d}\mathbf{r}_{p_2} \\ +\ldots\end{aligned} \tag{5.77}$$

where

$$\begin{aligned}\mathbf{V}(\mathbf{u},\mathbf{v}) &= G(\mathbf{u})\exp\left(\frac{2\pi n}{k^2}|\mathbf{u}|\mathbf{A}^t(\widehat{\mathbf{u}},\widehat{\mathbf{u}})\right)\mathbf{A}^t(\widehat{\mathbf{u}},\widehat{\mathbf{v}}), \\ \mathbf{U}(\mathbf{r}_{p_1};\mathbf{k}_i) &= \exp\left(\frac{2\pi n}{k\gamma_i}(z_{p_1}+L/2)\mathbf{A}^t(\boldsymbol{\kappa}_i,\boldsymbol{\kappa}_i)\right)e^{i\mathbf{k}_i\cdot\mathbf{r}_{p_1}},\end{aligned} \tag{5.78}$$

and the vector $\mathbf{r}_{p_m}$ denotes the position of the m'th particle common to both scattering sequences. The integrals on the right hand side of Eq. (5.78) correspond precisely to terms of different order in the ladder approximation. Consider the first integral on the right hand side of Eq. (5.77). We shall apply Eq. (5.10) twice, using the vector functions

$$\begin{aligned}\boldsymbol{\varphi}_1(\widehat{\mathbf{r}_1-\mathbf{r}_{p_1}}) &= \exp\left(\frac{2\pi n}{k^2}\frac{L/2-z_{p_1}}{\widehat{\mathbf{r}_1-\mathbf{r}_{p_1}}\cdot\widehat{\mathbf{z}}}\mathbf{A}^t(\widehat{\mathbf{r}_1-\mathbf{r}_{p_1}},\widehat{\mathbf{r}_1-\mathbf{r}_{p_1}})\right)\mathbf{A}^t(\widehat{\mathbf{r}_1-\mathbf{r}_{p_1}},\boldsymbol{\kappa}_i)\mathbf{e}_a e^{i\mathbf{k}_i\cdot\mathbf{r}_{p_1}}, \\ \boldsymbol{\varphi}_2(\widehat{\mathbf{r}_2-\mathbf{r}_{p_1}}) &= e^{-i\mathbf{k}_u\cdot\mathbf{r}_{p_1}}\mathbf{e}_c^\dagger\mathbf{A}^{t\dagger}(\widehat{\mathbf{r}_2-\mathbf{r}_{p_1}},\boldsymbol{\kappa}_u)\exp\left(\frac{2\pi n}{k^2}\frac{L/2-z_{p_1}}{\widehat{\mathbf{r}_2-\mathbf{r}_{p_1}}\cdot\widehat{\mathbf{z}}}\mathbf{A}^{t\dagger}(\widehat{\mathbf{r}_2-\mathbf{r}_{p_1}},\widehat{\mathbf{r}_2-\mathbf{r}_{p_1}})\right).\end{aligned} \tag{5.79}$$

The first integral of Eq. (5.77), which we denote I_1, becomes

$$I_1 = n \int \Bigg[\int \int \widehat{\mathbf{e}}_b^{\dagger} \exp\left(\frac{2\pi n}{k^2}(L/2 - z_{p_1}) s_j \mathbf{A}^t_{(j,j)} \right) \mathbf{A}^t_{(j,i)} \exp\left(\frac{2\pi n}{k^2}(z_{p_1} + L/2) s_i \mathbf{A}^t_{(i,i)} \right) \widehat{\mathbf{e}}_a \widehat{\mathbf{e}}_c^{\dagger} \exp\left(\frac{2\pi n}{k^2}(z_{p_1} + L/2) s_u \mathbf{A}^{t\dagger}_{(u,u)} \right) \mathbf{A}^{t\dagger}_{(q,p)} \exp\left(\frac{2\pi n}{k^2}(L/2 - z_{p_1}) s_v \mathbf{A}^{t\dagger}_{(v,v)} \right) \widehat{\mathbf{e}}_d e^{i\mathbf{r}_{p_1}\cdot(\mathbf{k}_i - \mathbf{k}_j - \mathbf{k}_u + \mathbf{k}_v)} e^{i(\mathbf{k}_j \cdot \mathbf{r}_1 - \mathbf{k}_v \cdot \mathbf{r}_2)} \frac{\mathrm{d}\boldsymbol{\kappa}_j \mathrm{d}\boldsymbol{\kappa}_v}{(2\pi k)^2 \gamma_j \gamma_v} \Bigg] \mathrm{d}\mathbf{r}_{p_1}, \tag{5.80}$$

where $s_i = \sec(\theta_i)$, with θ_i satisfying $\gamma_i = k\cos(\theta_i)$, and similarly for s_j, s_u and s_v.

In order to simplify Eq. (5.80), it is necessary to perform the integral over $\mathbf{r}_{p_1}$, which involves integrating the numerous exponentials within the integral. We consider again the simplest case of isotropic scatterers where, for forward scattering we have $\mathbf{A}^t = A\mathbb{I}_2$. In addition, recalling from Section 5.2.2 that $2\pi n \mathrm{Re}(A)/k^2 = -1/(2l_s)$ and $2\pi n \mathrm{Im}(A)/k^2 = -1/(2l_p)$, the integral then simplifies to

$$I_1 = n \int \int e^{-\frac{1}{4}\frac{L}{l_s}(s_i + s_j + s_u + s_v) + i\frac{1}{4}\frac{L}{l_p}(s_i + s_j - s_u - s_v)} \widehat{\mathbf{e}}_b^{\dagger} \mathbf{A}^t_{(j,i)} \widehat{\mathbf{e}}_a \widehat{\mathbf{e}}_c^{\dagger} \mathbf{A}^{t\dagger}_{(v,u)} \widehat{\mathbf{e}}_d \left[\int e^{i\boldsymbol{\rho}_{p_1}\cdot(\boldsymbol{\kappa}_i - \boldsymbol{\kappa}_j - \boldsymbol{\kappa}_u + \boldsymbol{\kappa}_v) + z_{p_1}[-\frac{1}{2l_s}(s_i - s_j + s_u - s_v) + i\frac{1}{2l_p}(s_i - s_j - s_u + s_v)]} \mathrm{d}\mathbf{r}_{p_1} \right] e^{i(\mathbf{k}_j \cdot \mathbf{r}_1 - \mathbf{k}_v \cdot \mathbf{r}_2)} \frac{\mathrm{d}\boldsymbol{\kappa}_j \mathrm{d}\boldsymbol{\kappa}_v}{(2\pi k)^2 \gamma_j \gamma_v}. \tag{5.81}$$

The integral over $\mathbf{r}_{p_1}$ contained within I_1 in Eq. (5.81) simplifies to

$$\delta(\boldsymbol{\kappa}_i - \boldsymbol{\kappa}_j - \boldsymbol{\kappa}_u + \boldsymbol{\kappa}_v)(2\pi)^2 L \mathrm{sinhc}\Bigg(-\frac{1}{4}\frac{L}{l_s}(s_i - s_j + s_u - s_v) + i\left[\frac{1}{4}\frac{L}{l_p}(s_i - s_j - s_u + s_v) + \frac{kL}{2}(c_i - c_j - c_u + c_v) \right] \Bigg), \tag{5.82}$$

where $\mathrm{sinhc}(z) = \sinh(z)/z$ [290] and $c_i = 1/s_i$. Thus, overall, comparing Eqs.

(5.50) and (5.81), the correlation function can be read off as

$$C^{L_1}_{(j,i)ba(v,u)dc} = \delta(\boldsymbol{\kappa}_i - \boldsymbol{\kappa}_j - \boldsymbol{\kappa}_u + \boldsymbol{\kappa}_v)\frac{nL}{k^2\gamma_j\gamma_v}\langle A^t_{(j,i)ba}A^{t*}_{(v,u)dc}\rangle \\ e^{-\frac{1}{4}\frac{L}{l_s}(s_i+s_j+s_u+s_v)+i\frac{1}{4}\frac{L}{l_p}(s_i+s_j-s_u-s_v)} \\ \operatorname{sinhc}\Bigg(-\frac{1}{4}\frac{L}{l_s}(s_i-s_j+s_u-s_v) \\ +i\left[\frac{1}{4}\frac{L}{l_p}(s_i-s_j-s_u+s_v)+\frac{kL}{2}(c_i-c_j-c_u+c_v)\right]\Bigg). \tag{5.83}$$

It is noteworthy that Eq. (5.83) has obvious parallels with Eq. (5.56). The difference between these equations is that Eq. (5.83) contains sinhc instead of sinc, as well as an additional exponential term. A closer comparison can be drawn using some relatively crude approximations. Numerical calculations for spherical particles suggest that l_p is the same order of magnitude as l_s. Since we have assumed that $kl_s \gg 1$, we have $kL \gg L/l_s$ and thus $kL \gg L/l_p$. The imaginary part of the argument of the sinhc function is therefore dominated by the latter term. Suppose now that all four wavevectors are close to the optical axis, so that c_i, c_j, c_u, c_v are all close to unity. For scattering media that are not too thick, say on the order of up to five mean free paths, $L/(4l_s)$ will be on the order of 1 and we may approximate the real part of the argument of the sinhc function to be zero. Finally, using the identity $\operatorname{sinhc}(iz) = \operatorname{sinc}(z)$, the sinhc function simplifies to $\operatorname{sinc}(kL/2(c_i - c_j - c_p + c_q))$, which appears in the single scattering result in Eq. (5.56). We also have $s_i + s_j + s_p + s_q \approx 4$, which simplifies the exponential term to yield the approximation

$$C^{L_1}_{(j,i)ba(v,u)dc} \approx \delta(\boldsymbol{\kappa}_i - \boldsymbol{\kappa}_j - \boldsymbol{\kappa}_u + \boldsymbol{\kappa}_v)\frac{nL}{k^2\gamma_j\gamma_v}\langle A_{(j,i)ba}A^*_{(q,p)dc}\rangle \\ \operatorname{sinc}\left((\gamma_i - \gamma_j - \gamma_u + \gamma_v)\frac{L}{2}\right)e^{-\frac{L}{l_s}}. \tag{5.84}$$

What is noteworthy is that Eq. (5.84) is identical to the single scattering result, save for an additional exponential term, indicating that the correlation function decays with medium thickness. The normalised intensity correlation function that would result from Eq. (5.84), as discussed in the previous section, would also exhibit the

same elliptical bands in k-space as the single scattering theory.

5.4 Near field scattering

In deriving the results in this chapter we have made heavy use of the identity Eq. (5.10), which is valid only in the far field of a scatterer. This is appropriate under the assumptions that the scatterers are sparsely distributed within the scattering medium and that the source and observation point lie in the far fields of all the scatterers. If either of these assumptions is violated, as may be the case for dense particulate media, when the scattering medium is illuminated by an evanescent wave, or when the scattered field is measured close to the boundary of the scattering medium, Eq. (5.10) is no longer applicable. In fact, the expression for the Green's function G and the whole concept of the far field amplitude matrix $\mathbf{A}$, both of which first appeared in the Foldy-Lax equations, are inappropriate for near field scattering. Extending the statistical theory in this chapter to incorporate near field scattering therefore requires an alternative mathematical approach, which will be briefly discussed in this section.

More general formulations of the Foldy-Lax equations that make use of the so-called transition dyadic are able to incorporate evanescent fields [291, 292]. Expressed in this form, the resulting theories, however, are not immediately translatable into the formalism presented in this chapter. An alternative approach makes use of the T-matrix theory, which, as shall be seen, will allow us to formulate the scattering of evanescent waves by redefining the amplitude matrix in a more general form, after which the results of this chapter can then be applied, naturally with some caveats that shall be discussed. This approach is based on the use of the electromagnetic multipole fields, which we shall proceed to define rigorously. Most of the mathematical notation used in this chapter is based upon the work in Refs. [293, 294].

To begin, we define the spherical harmonic Y_l^m as

$$Y_l^m(\theta,\phi) = \sqrt{\frac{(2l+1)(l-m)!}{4\pi(l+m)!}} P_l^m(\cos\theta) e^{im\phi}, \tag{5.85}$$

where P_l^m is the associated Legendre polynomial of degree l and order m. The parameters θ and ϕ refer to the polar and azimuthal angle in spherical polar coordaintes. The spherical harmonics constitute a complete set of functions defined on the unit sphere and are orthonormal in the sense that

$$\int_0^{2\pi}\int_0^{\pi} Y_l^m(\theta,\phi)Y_{l'}^{m'*}(\theta,\phi)\sin\theta \mathrm{d}\theta\mathrm{d}\phi = \delta_{ll'}\delta_{mm'}. \tag{5.86}$$

In order to describe vectorial fields, we require the vector spherical harmonics $\mathbf{Y}_l^m$, which are defined by

$$\mathbf{Y}_l^m(\theta,\phi) = \mathcal{L}_r Y_l^m(\theta,\phi) = -i\mathbf{r}\times\nabla Y_l^m(\theta,\phi), \tag{5.87}$$

where $\mathcal{L}_r = -i\mathbf{r}\times\nabla$ is the so-called 'orbital angular momentum operator' in $\mathbf{r}$ space. The vector spherical harmonics form an orthogonal set of functions, this time in the sense that

$$\int_0^{2\pi}\int_0^{\pi} \mathbf{Y}_l^m(\theta,\phi)\cdot\mathbf{Y}_{l'}^{m'*}(\theta,\phi)\sin\theta \mathrm{d}\theta\mathrm{d}\phi = l(l+1)\delta_{ll'}\delta_{mm'}. \tag{5.88}$$

The vector spherical harmonics, together with the corresponding collection of functions $\widehat{\mathbf{r}}\times\mathbf{Y}_l^m$, form an orthogonal basis for all well-behaved functions defined on and tangential to the unit sphere. For practical purposes, it can be useful to express the vector spherical harmonics in Cartesian coordinates using the identity [293]

$$\mathbf{Y}_l^m(\theta,\phi) = a_- Y_l^{m+1}(\theta,\phi)\mathbf{u}_- + a_+ Y_l^{m-1}(\theta,\phi)\mathbf{u}_- + mY_l^m(\theta,\phi)\widehat{\mathbf{z}}, \tag{5.89}$$

where

$$a_\pm = \sqrt{(l\pm m)(l\mp m+1)}, \tag{5.90}$$

$$\mathbf{u}_\pm = \frac{1}{2}(\widehat{\mathbf{x}}\pm i\widehat{\mathbf{y}}), \tag{5.91}$$

and $\widehat{\mathbf{x}},\widehat{\mathbf{y}}$ and $\widehat{\mathbf{z}}$ are the usual Cartesian basis vectors.

We define the scalar multipole fields as

$$\Lambda_l^m(\mathbf{r}) = j_l(kr)Y_l^m(\theta,\phi), \tag{5.92}$$

$$\Pi_l^m(\mathbf{r}) = h_l^{(1)}(kr)Y_l^m(\theta,\phi), \tag{5.93}$$

where j_l is the spherical Bessel function of the first kind and $h_l^{(1)}$ is the spherical Hankel function of the first kind. Using these, we may define the electromagnetic multipole fields as

$$\mathbf{M}_{lm} = \frac{1}{\sqrt{l(l+1)}}\nabla\times\Big(\mathbf{r}\Pi_l^m(\mathbf{r})\Big), \tag{5.94}$$

$$\mathbf{N}_{lm} = \frac{1}{k\sqrt{l(l+1)}}\nabla\times\Big[\nabla\times\Big(\mathbf{r}\Pi_l^m(\mathbf{r})\Big)\Big], \tag{5.95}$$

$$\mathrm{Rg}\mathbf{M}_{lm} = \frac{1}{\sqrt{l(l+1)}}\nabla\times\Big(\mathbf{r}\Lambda_l^m(\mathbf{r})\Big), \tag{5.96}$$

$$\mathrm{Rg}\mathbf{N}_{lm} = \frac{1}{k\sqrt{l(l+1)}}\nabla\times\Big[\nabla\times\Big(\mathbf{r}\Lambda_l^m(\mathbf{r})\Big)\Big]. \tag{5.97}$$

Note that the fields $\mathrm{Rg}\mathbf{M}_{lm}$ and $\mathrm{Rg}\mathbf{N}_{lm}$ are regularised (finite) at the origin, whereas the fields $\mathbf{M}_{lm}$ and $\mathbf{N}_{lm}$ diverge, since $|h_l^{(1)}(kr)|\to\infty$ as $r\to 0$.

Suppose that a scatterer of arbitrary shape is situated at the co-ordinate origin and let R be the radius of the smallest sphere that circumscribes the scatterer. Suppose also that the scatterer is illuminated by the incident field as defined in Eq. (5.1), which may now be an evanescent plane wave (corresponding to $|\boldsymbol{\kappa}_i| > k$). The incident field can be expanded in terms of the regularised multipole fields $\mathrm{Rg}\mathbf{M}_{ml}$ and $\mathrm{Rg}\mathbf{N}_{ml}$ in the form

$$\mathbf{E}_i(\mathbf{r}) = \sum_{l=1}^{\infty}\sum_{m=-l}^{m=l}\Big[a_{lm}\mathrm{Rg}\mathbf{M}_{lm}(\mathbf{r}) + b_{lm}\mathrm{Rg}\mathbf{N}_{lm}(\mathbf{r})\Big], \tag{5.98}$$

where a_{lm} and b_{lm} are given by [294]

$$a_{lm} = i\frac{4\pi i^l}{\sqrt{l(l+1)}}\mathbf{Y}_l^{m*}(\theta_i,\phi_i)\cdot\mathbf{E}_0, \tag{5.99}$$

$$b_{lm} = \frac{4\pi i^l}{\sqrt{l(l+1)}}\Big[\widehat{\mathbf{u}}_i\times\mathbf{Y}_l^m(\theta_i,\phi_i)\Big]^*\cdot\mathbf{E}_0, \tag{5.100}$$

where $\widehat{\mathbf{u}}_i = \mathbf{k}_i/k$ is the normalised incident wavevector and (θ_i, ϕ_i) are the polar co-orindates associated with $\widehat{\mathbf{u}}_i$. The scattered field $\mathbf{E}_s$, on the other hand, can be expressed as an infinite sum of the multipole fields $\mathbf{M}_{lm}$ and $\mathbf{N}_{lm}$ in the form

$$\mathbf{E}_s(\mathbf{r}) = \sum_{l=1}^{\infty} \sum_{m=-l}^{m=l} \Big[p_{lm} \mathbf{M}_{lm}(\mathbf{r}) + q_{lm} \mathbf{N}_{lm}(\mathbf{r}) \Big], \tag{5.101}$$

where p_{lm} and q_{lm} are constants. The coefficients p_{lm} and q_{lm} are related linearly to a_{lm} and b_{lm} by the elements of the T-matrix. Writing these relations explicitly, we have

$$p_{lm} = \sum_{l'=1}^{\infty} \sum_{m'=-l'}^{l'} \Big(T^{11}_{lml'm'} a_{l'm'} + T^{12}_{lml'm'} b_{l'm'} \Big), \tag{5.102}$$

$$q_{lm} = \sum_{l'=1}^{\infty} \sum_{m'=-l'}^{l'} \Big(T^{21}_{lml'm'} a_{l'm'} + T^{22}_{lml'm'} b_{l'm'} \Big), \tag{5.103}$$

where the T-matrix elements $T^{ij}_{lml'm'}$ depend only on the physical characteristics of the scatterer and are independent of the propagation directions and polarisation states of the incident and scattered fields. The T-matrix elements can be computed numerically. For a more detailed discussion, we refer the interested reader to Ref. [294].

In order to relate the multipole expansion of the scattered field to the scattering matrix, it is necessary to expand the electromagnetic multipole fields as angular spectra. For $|z| > R$, the electromagnetic multipole fields can be expressed as [293]

$$\mathbf{M}_{lm}(\mathbf{r}) = \frac{(-i)^l}{\sqrt{l(l+1)}} \frac{1}{2\pi} \int_{-\pi}^{\pi} \int_{C^{\pm}} \mathbf{Y}_l^m(\theta, \phi) e^{ik\widehat{\mathbf{u}}\cdot\mathbf{r}} \sin\theta \mathrm{d}\theta \mathrm{d}\phi, \tag{5.104}$$

$$\mathbf{N}^e_{lm}(\mathbf{r}) = \frac{(-i)^l}{\sqrt{l(l+1)}} \frac{i}{2\pi} \int_{-\pi}^{\pi} \int_{C^{\pm}} \widehat{\mathbf{u}} \times \mathbf{Y}_l^m(\theta, \phi) e^{ik\widehat{\mathbf{u}}\cdot\mathbf{r}} \sin\theta \mathrm{d}\theta \mathrm{d}\phi, \tag{5.105}$$

where $\widehat{\mathbf{u}}$ is a unit vector with polar co-ordinates (θ, ϕ) and $C^{\pm}$ are the integration contours shown in Figure 5.4. The contour C^+ applies for $z > R$ and C^- applies for $z < -R$. It is important to stress that while the condition $|z| > R$ ensures that the angular spectra are taken outside of the scatterer, we do not require $\mathbf{r}$ to be in the far field of the scatterer. Combining Eqs. (5.101), (5.104) and (5.105), the scattered

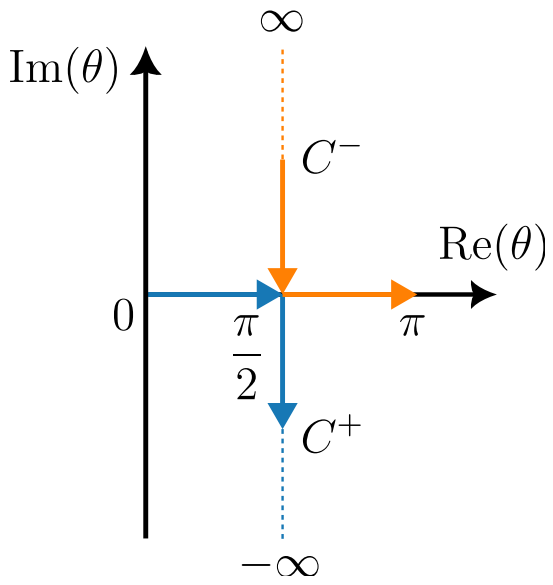

Figure 5.4: Integration contours for the angular spectrum representations of the scattered field. The blue path shows C^+ and the red path shows C^-.

field can be expressed as

$$\mathbf{E}_s(\mathbf{r}) = \frac{1}{2\pi}\int_{-\pi}^{\pi}\int_{C^\pm}\sum_{l=1}^{\infty}\sum_{m=-l}^{l}\frac{(-i)^l}{\sqrt{l(l+1)}}\Big[p_{lm}\mathbf{Y}_l^m(\theta,\phi)+iq_{lm}\widehat{\mathbf{u}}\times\mathbf{Y}(\theta,\phi)\Big]e^{ik\widehat{\mathbf{u}}\cdot\mathbf{r}}\sin\theta\mathrm{d}\theta\mathrm{d}\phi, \tag{5.106}$$

which is an angular spectrum representation of the scattered field.

To draw a comparison with the far field theory, we begin by noting that Eq. (5.106) can be written in the form

$$\mathbf{E}_s(\mathbf{r}) = \frac{1}{2\pi}\int_{-\pi}^{\pi}\int_{C^\pm}\mathbf{B}(\widehat{\mathbf{u}},\widehat{\mathbf{u}}_i)\mathbf{E}_0 e^{ik\widehat{\mathbf{u}}\cdot\mathbf{r}}\sin\theta\mathrm{d}\theta\mathrm{d}\phi, \tag{5.107}$$

where, after making use of Eqs. (5.102) and (5.103),

$$\begin{aligned}\mathbf{B}(\widehat{\mathbf{u}},\widehat{\mathbf{u}}_i)=\sum_{l=1}^{\infty}\sum_{m=-l}^{l}\sum_{l'=1}^{\infty}\sum_{m'=-l'}^{l'}\frac{4\pi i^{l'-l}}{\sqrt{l(l+1)l'(l'+1)}}\Big[&\\ iT^{11}_{lml'm'}\mathbf{Y}_l^m(\theta,\phi)[\mathbf{Y}_{l'}^{m'}(\theta_i,\phi_i)]^\dagger&\\ +T^{12}_{lml'm'}\mathbf{Y}_l^m(\theta,\phi)[\widehat{\mathbf{u}}_i\times\mathbf{Y}_{l'}^{m'}(\theta_i,\phi_i)]^\dagger&\\ -T^{21}_{lml'm'}[\widehat{\mathbf{u}}\times\mathbf{Y}_l^m(\theta,\phi)][\mathbf{Y}_{l'}^{m'}(\theta_i,\phi_i)]^\dagger&\\ +iT^{22}_{lml'm'}[\widehat{\mathbf{u}}\times\mathbf{Y}_l^m(\theta,\phi)][\widehat{\mathbf{u}}_i\times\mathbf{Y}_{l'}^{m'}(\theta_i,\phi_i)]^\dagger\Big].&\end{aligned}\tag{5.108}$$

The matrix $\mathbf{B}$, similarly to $\mathbf{A}$, relates the polarisation state of the incident wave with wavevector $\mathbf{k}_i$ to the plane wave component of the scattered field with wavevector $\mathbf{k}$. For $\mathbf{B}$, however, $\mathbf{k}_i$ and $\mathbf{k}$, may be wavevectors of evanescent plane wave components. Eq. (5.107) may be expressed in terms of the transverse wavevector $\boldsymbol{\kappa}$ by making the change of variables $(\theta,\phi)\rightarrow(k_x,k_y)$, for which the Jacobian is given by

$$\sin\theta\mathrm{d}\theta\mathrm{d}\phi=\frac{\mathrm{d}k_x\mathrm{d}k_y}{k\gamma}.\tag{5.109}$$

For $z>R$ we have

$$\mathbf{E}_s(\mathbf{r})=\int_{\mathbb{R}^2}\frac{1}{2\pi k|\gamma|}\mathbf{B}(\widehat{\mathbf{u}},\widehat{\mathbf{u}}_i)\mathbf{E}_0e^{i(\boldsymbol{\kappa}\cdot\boldsymbol{\rho}+\gamma z)}\mathrm{d}\boldsymbol{\kappa},\tag{5.110}$$

and for $z<-R$

$$\mathbf{E}_s(\mathbf{r})=\int_{\mathbb{R}^2}\frac{1}{2\pi k|\gamma|}\mathbf{B}(\widetilde{\widehat{\mathbf{u}}},\widehat{\mathbf{u}}_i)\mathbf{E}_0e^{i(\boldsymbol{\kappa}\cdot\boldsymbol{\rho}-\gamma z)}\mathrm{d}\boldsymbol{\kappa},\tag{5.111}$$

where $\widehat{\mathbf{u}}=(k_x,k_y,\gamma)^{\mathrm{T}}/k$ and $\widetilde{\widehat{\mathbf{u}}}=(k_x,k_y,-\gamma)^{\mathrm{T}}/k$. The evaluation of $\mathbf{B}(\widehat{\mathbf{u}},\widehat{\mathbf{u}}_i)$ and $\mathbf{B}(\widetilde{\widehat{\mathbf{u}}},\widehat{\mathbf{u}}_i)$ requires the evaluation of $\mathbf{Y}_l^m(\widehat{\mathbf{u}})$ and $\mathbf{Y}_l^m(\widetilde{\widehat{\mathbf{u}}})$. By virtue of Eq. (5.89), it is required that we are able to evaluate the scalar spherical harmonics $Y_l^m(\widehat{\mathbf{u}})$ and $Y_l^m(\widetilde{\widehat{\mathbf{u}}})$. It is straightforward to show, however, that

$$Y_l^m(\widehat{\mathbf{u}})=\sqrt{\frac{(2l+1)(l-m)!}{4\pi(l+m)!}}P_l^m(u_z)\left(\frac{u_x+iu_y}{\sqrt{u_x^2+u_y^2}}\right)^m,\tag{5.112}$$

and similarly for $Y_l^m(\widetilde{\widehat{\mathbf{u}}})$, but with u_z replaced by $-u_z$. Note that for evanescent components, the argument of the Legendre polynomial is imaginary.

A multiple scattering theory incorporating near field components requires a more general form of the Foldy-Lax equations [295]. Such a theory is beyond the scope of this thesis. Nevertheless, we shall show how the single scattering component of the scattering matrix can be express in an analogous manner to the theory developed in this chapter for far field scattering.

Using the same notation as in Section 5.1, suppose again that there are N scatterers within the slab confined to the region $-L/2 < z < L/2$ with random positions described by vectors $\mathbf{r}_p$ for $1 \leq p \leq N$. Let $\mathbf{r}'_p = \mathbf{r} - \mathbf{r}_p$ be the position vector of the measurement point relative to the p'th particle. The incident field can be written as

$$\mathbf{E}_i(\mathbf{r}) = \mathbf{E}_0 e^{i\mathbf{k}_i \cdot \mathbf{r}} = e^{i\mathbf{k}_i \cdot \mathbf{r}_p} \mathbf{E}_0 e^{i\mathbf{k}_i \cdot \mathbf{r}'_p}. \tag{5.113}$$

Expanding $\mathbf{E}_0 e^{i\mathbf{k}_i \cdot \mathbf{r}'_p}$ in terms of the regularised electromagnetic multipole fields as in Eq. (5.98), we find that the expansion coefficients a_{lm} and b_{lm} for $\mathbf{E}_i$ will be as before, but with $\mathbf{E}_0$ replaced by $\mathbf{E}_0 e^{i\mathbf{k}_i \cdot \mathbf{r}_p}$. Furthermore, since we originally assumed the scatterer was located at the origin, it is necessary to make the replacement $\mathbf{r} \to \mathbf{r}'_p$ within the integrals in Eq. (5.110) and (5.111). Overall, this has the effect of introducing a factor of $e^{i(\mathbf{k}_i - \mathbf{k}) \cdot \mathbf{r}_p}$ into Eq. (5.110) and $e^{i(\mathbf{k}_i - \widetilde{\mathbf{k}}) \cdot \mathbf{r}_p}$ into Eq. (5.111). Summing over the scattered fields for each particle and using a j subscript for scattered wavevectors, we finally arrive at

$$\mathbf{E}_s(\boldsymbol{\rho}, L/2) = \int_{\mathbb{R}^2} \frac{1}{2\pi k |\gamma_j|} \sum_{n=1}^{N} \mathbf{B}_p^t(\widehat{\boldsymbol{\kappa}}_j, \widehat{\boldsymbol{\kappa}}_i) e^{i(\mathbf{k}_i - \mathbf{k}_j) \cdot \mathbf{r}_p} \mathbf{E}_0 e^{i\mathbf{k}_j \cdot \mathbf{r}} \mathrm{d}\boldsymbol{\kappa}_j, \tag{5.114}$$

$$\mathbf{E}_s(\boldsymbol{\rho}, -L/2) = \int_{\mathbb{R}^2} \frac{1}{2\pi k |\gamma_j|} \sum_{n=1}^{N} \mathbf{B}_p^r(\widehat{\boldsymbol{\kappa}}_j, \widehat{\boldsymbol{\kappa}}_i) e^{i(\mathbf{k}_i - \widetilde{\mathbf{k}}_j) \cdot \mathbf{r}_p} \mathbf{E}_0 e^{i\widetilde{\mathbf{k}}_j \cdot \mathbf{r}} \mathrm{d}\boldsymbol{\kappa}_j, \tag{5.115}$$

where

$$\mathbf{B}_p^t(\widehat{\boldsymbol{\kappa}}, \widehat{\boldsymbol{\kappa}}_i) = \mathbf{B}_p(\widehat{\mathbf{u}}, \widehat{\mathbf{u}}_i), \tag{5.116}$$

$$\mathbf{B}_p^r(\widehat{\boldsymbol{\kappa}}, \widehat{\boldsymbol{\kappa}}_i) = \mathbf{B}_p(\widetilde{\widehat{\mathbf{u}}}, \widehat{\mathbf{u}}_i). \tag{5.117}$$

The corresponding transmission and reflection matrices contained within Eqs. (5.114) and (5.115) are virtually identical to the far field forms given in Eqs. (5.14) and (5.16). The key differences are that the **A** matrix has been replaced with **B** and that the domain of integration now extends to the infinite two dimensional plane.

Calculating the statistics of the near field components of the scattering matrix in the single scattering regime is fundamentally the same as the process outlined for the far field components. Some of the assumptions made in the far field case, however, need to be reanalysed. Most notably, in deriving the far field scattering matrix statistics, we assumed that the positions of the particles were distributed jointly uniformly. Since near field scattering is only relevant in the case where the particles are packed together with appreciable density, this assumption may no longer be appropriate, and a more general particle distribution function may be required. In particular, the sinc functions appearing in, for example, Eq. (5.56), which ultimately arise due to their being the Fourier transform of a uniform probability density function, would be replaced by the corresponding Fourier transform of the particle distribution function. Even if a uniform distribution were chosen, it should also be noted that the arguments of the sinc functions would, in general, be complex, as the γ term for an evanescent plane wave component is imaginary. For a general complex number $x + iy$, straightforward trigonometry shows that

$$|\mathrm{sinc}(x+iy)| = \sqrt{\frac{\cos^2(x)\sinh^2(y) + \sin^2(x)\cosh^2(y)}{x^2+y^2}}. \tag{5.118}$$

We can therefore see that evanescent plane wave components, which will contribute to the imaginary part of the argument of sinc, may have scattering matrix correlation functions with large magnitudes. Physically, this is counteracted by the decaying exponentials in the scattered field angular spectra, so that, overall, the scattered field correlation functions remain finite.

5.5 Conclusion

In this chapter, beginning with the far-field Foldy Lax equations, we presented a theoretical framework for the scattering matrix that describes a random medium con-

taining a large number of discrete particles with given physical properties. Through repeated use of Eq. (5.10), we were able to derive expressions for the scattering matrix elements in terms of different types of scattering sequences. We then applied a simple statistical model to derive the mean values of the matrix elements, as well as regular correlations and pseudo correlations between different matrix elements. We found in Eq. (5.44) an exact exponential law for the mean transmission matrix elements, which incorporates all scattering orders. Although a corresponding law is not known for correlations, we found exact results for correlations between transmission and reflection matrix elements under the assumption of single scattering which are summarised in Eqs. (5.56), (5.57), (5.60) and (5.61). Regular correlations, it was found, exist precisely when the wavevectors corresponding to the pair of matrix blocks being considered accord with the memory effect condition. Pseudo correlations were instead found to exist provided that a corresponding conjugate memory effect condition was satisfied. For regular transmission matrix correlations, we were able to extend the single scattering result to Eq. (5.83), which incorporates first order multiple scattering effects in the ladder approximation. In Section 5.3.2, we also gave an extended discussion of the geometric nature of both regular and pseudo correlations, specifically with regard to how the strength of the correlations depends on the positions of the different wavevectors in k-space. Though all of these results rested on the assumption of far-field scattering, in Section 5.4 we discussed a possible extension to our theory that is able to incorporate evanescent wave components, which are pertinent for scattering in dense particulate media.

The results of this chapter form the basis of a theoretical understanding of the scattering of polarised light in discrete random media. The type of analytic approach pursued, however, is clearly limited, as moving to high order scattering terms quickly becomes mathematically unfeasible, even when using numerous approximations. In the following chapter, we will introduce a numerical approach for studying the statistics of the scattering matrix that is able to access the multiple scattering regime. As shall be seen, our approach will make use of the results in this chapter, particularly those for single scattering, but will allow us to generate numerical data for random media of arbitrary thicknesses.

Chapter 6

Random matrix simulations

In Chapter 5, we derived exact results for the statistics of scattering matrices describing discrete random media. These results, however, were limited to special cases, such as the single scattering regime, or first order multiple scattering for correlations between different matrix elements. A full multiple scattering theory able to account for correlations of all scattering orders, if at all derivable, requires further work and greater mathematical sophistication. In absence of such a theory, in this chapter we turn to an alternative, more tractable approach, namely numerical simulations. In particular, in this chapter we apply the theoretical framework of the scattering matrix outlined in previous chapters and present a numerical method for generating random scattering matrices that describe far field scattering of polarised light by disordered media containing randomly positioned, discrete scatterers. Our method randomly samples the propagating-propagating block of the discrete scattering matrix ($\bar{\mathbf{S}}_{pp}$ in Chapter 3, which, for simplicity, shall henceforth be referred to as just $\bar{\mathbf{S}}$) in the single scattering regime using the statistical results of Chapter 5 and accesses the multiple scattering regime using a matrix cascade technique.

We begin by outlining in detail the algorithm underpinning our simulation method. Afterwards, we present numerical results and validate our approach by demonstrating its ability to reproduce known polarisation phenomena. We shall also show how the random matrix theory discussed in Chapter 4 relates to the matrices generated from our simulations. Finally, we end with a quantitative performance analysis of

different aspects of the method and discuss some of the shortcomings and possible avenues of future research.

The method presented in this chapter is novel and were recently presented in the literature in Ref. [296].

6.1 Algorithm

6.1.1 Mode discretisation

To begin, since we are working with the propagating-propagating block of the discrete scattering matrix, it is necessary to select a cubature scheme for the circle in k-space of radius k that will allow us to approximate continuous angular spectra as finite sums, as described in Section 3.3 and shown in Figure 3.2. In general, there are many ways to achieve this, and cubature schemes are typically chosen with the form of the function being approximated in mind [297]. For simplicity, we decided to distribute our modes on a Cartesian grid in k space with grid spacings Δk_x and Δk_y, and whose origin aligns with $\boldsymbol{\kappa} = (0, 0)$. Of course, as the boundary of k space is a circle, the interior cannot be fully tessellated by a Cartesian grid and modes close to the boundary have associated weights not given by the product $\Delta k_x \Delta k_y$. To ensure that the weight for each mode is equal and that the weights are correctly normalised, we decided to give each mode the weight $w = \pi k^2/(2N_p + 1)$. This value differs slightly to the product $\Delta k_x \Delta k_y$, but this discrepancy decreases as the number of modes increases. Some discussion of more general cubature schemes and technical difficulties associated with them will be given in Section 6.3.4.

6.1.2 Input statistics

Let us now consider the statistics of the elements of $\bar{\mathbf{S}}$. We follow all of the assumptions of Chapter 5 and suppose that the scattering medium lies in the region $-\Delta L/2 < z < \Delta L/2$, where ΔL is sufficiently small so as to satisfy the single scattering approximation. This will allow us to use the single scattering results from Sections 5.2.1 and 5.3.1 as the input statistics for our simulations.

Consider first the mean transmission and reflection matrix expressions given in

Eqs. (5.24) and (5.25). In order to discretise these equations, we replace the Dirac delta function with a Kronecker delta by making the substitution $\delta(\boldsymbol{\kappa}_i - \boldsymbol{\kappa}_j) \to \delta_{ij}/w$, where w is the constant weight associated with the cubature scheme. In light of Eq. (3.115), however, working with the normalised scattering matrix it is also necessary to multiply each block by an additional factor of w, meaning that overall we have $\delta(\boldsymbol{\kappa}_i - \boldsymbol{\kappa}_j) \to \delta_{ij}$ in Eqs. (5.24) and (5.25). Expressions for the mean discrete transmission and reflection matrices are thus given by

$$\langle \bar{\mathbf{t}}_{(j,i)} \rangle = \delta_{ij} \left(\mathbb{I}_2 + \frac{2\pi n \Delta L}{k\gamma_i} \langle \mathbf{A}^t_{(j,i)} \rangle \right). \tag{6.1}$$

and

$$\langle \bar{\mathbf{r}}_{(j,i)} \rangle = \delta_{ij} \frac{2\pi n \Delta L}{k\gamma_i} \mathrm{sinc}\Big(\gamma_i \Delta L\Big) \langle \mathbf{A}^r_{(j,i)} \rangle. \tag{6.2}$$

Note that there are no additional γ factors introduced into these expressions by the transformation given in Eq. (3.115) as the mean blocks are non-zero only for $i = j$.

Expressions for the covariance and pseudo covariance can be derived similarly starting from, for example, the transmission matrix covariance given by Eq. (5.56), which contains the delta function $\delta(\boldsymbol{\kappa}_i - \boldsymbol{\kappa}_j - \boldsymbol{\kappa}_u + \boldsymbol{\kappa}_v)$. This time we discretise the delta function to give $\delta(\boldsymbol{\kappa}_i - \boldsymbol{\kappa}_j - \boldsymbol{\kappa}_u + \boldsymbol{\kappa}_v) \to \delta^{\mathrm{R}}/w$, where $\delta^{\mathrm{R}} = 1$ when the memory effect condition (Eqs. (5.54) and (5.55)) is satisfied and 0 otherwise. The superscript R stands for 'regular', soon to be contrasted with P for 'pseudo'. Applying again the normalisation given by Eq. (3.115) to each transmission matrix, we find that

$$\begin{aligned} &\langle \bar{t}_{(j,i)ba} \bar{t}^*_{(v,u)dc} \rangle - \langle \bar{t}_{(j,i)ba} \rangle \langle \bar{t}^*_{(v,u)dc} \rangle \\ &\qquad = \delta^R \frac{wn\Delta L}{k^2 \sqrt{\gamma_i \gamma_j \gamma_u \gamma_v}} \langle A^t_{(j,i)ba} A^{t*}_{(v,u)dc} \rangle \mathrm{sinc}\Big(\frac{\Delta L}{2} (\gamma_i - \gamma_j - \gamma_u + \gamma_v) \Big). \end{aligned} \tag{6.3}$$

Table 6.1: Summary of the regular and pseudo covariances of the elements of the scattering matrix.

Type	Block $\bar{B}$	Expression
Regular	$\bar{t}$	$\delta^R C_{ijuv}\langle A^t_{(j,i)ba} A^{t*}_{(j,i)dc}\rangle \mathrm{sinc}(\frac{L}{2}(\gamma_i - \gamma_j - \gamma_u + \gamma_v))$
	$\bar{r}$	$\delta^R C_{ijuv}\langle A^r_{(j,i)ba} A^{r*}_{(j,i)dc}\rangle \mathrm{sinc}(\frac{L}{2}(\gamma_i + \gamma_j - \gamma_u - \gamma_v))$
	$\bar{t}'$	$\delta^R C_{ijuv}\langle A^{t'}_{(j,i)ba} A^{t'*}_{(j,i)dc}\rangle \mathrm{sinc}(\frac{L}{2}(-\gamma_i + \gamma_j + \gamma_u - \gamma_v))$
	$\bar{r}'$	$\delta^R C_{ijuv}\langle A^{r'}_{(j,i)ba} A^{r'*}_{(j,i)dc}\rangle \mathrm{sinc}(\frac{L}{2}(-\gamma_i - \gamma_j + \gamma_u - \gamma_v))$
Pseudo	$\bar{t}$	$\delta^P C_{ijuv}\langle A^t_{(j,i)ba} A^t_{(j,i)dc}\rangle \mathrm{sinc}(\frac{L}{2}(\gamma_i - \gamma_j + \gamma_u - \gamma_v))$
	$\bar{r}$	$\delta^P C_{ijuv}\langle A^r_{(j,i)ba} A^r_{(j,i)dc}\rangle \mathrm{sinc}(\frac{L}{2}(\gamma_i + \gamma_j + \gamma_u + \gamma_v))$
	$\bar{t}'$	$\delta^P C_{ijuv}\langle A^{t'}_{(j,i)ba} A^{t'}_{(j,i)dc}\rangle \mathrm{sinc}(\frac{L}{2}(-\gamma_i + \gamma_j - \gamma_u + \gamma_v))$
	$\bar{r}'$	$\delta^P C_{ijuv}\langle A^{r'}_{(j,i)ba} A^{r'}_{(j,i)dc}\rangle \mathrm{sinc}(\frac{L}{2}(-\gamma_i - \gamma_j - \gamma_u - \gamma_v))$

Similarly, the pseudo covariance for the transmission matrix is given by

$$\begin{aligned}\langle \bar{t}_{(j,i)ba}\bar{t}_{(v,u)dc}\rangle - \langle \bar{t}_{(j,i)ba}\rangle\langle \bar{t}_{(v,u)dc}\rangle \\ = \delta^P \frac{wn\Delta L}{k^2\sqrt{\gamma_i\gamma_j\gamma_u\gamma_v}}\langle A^t_{(j,i)ba}A^t_{(v,u)dc}\rangle \mathrm{sinc}\Big(\frac{\Delta L}{2}(\gamma_i - \gamma_j + \gamma_u - \gamma_v)\Big),\end{aligned} \tag{6.4}$$

where $\delta^{\mathrm{P}} = 1$ when Eqs. (5.58) and (5.59) hold and 0 otherwise.

Analogous expressions for the statistics of the other blocks of the scattering matrix can be derived similarly. A summary of these results is given in Table 6.1, which contains a list of expressions for the covariances and pseudo covariances of the elements of the scattering matrix. Referring to the first column of Table 6.1, type 'Regular' refers to the covariance of the form $\langle \bar{B}_{(j,i)ba}\bar{B}^*_{(v,u)dc}\rangle - \langle \bar{B}_{(j,i)ba}\rangle\langle \bar{B}^*_{(v,u)dc}\rangle$, where $\bar{B}$ denotes an arbitrary block of the scattering matrix (i.e. one of $\bar{r}$, $\bar{t}$, $\bar{t}'$ or $\bar{r}'$). Type 'Pseudo' refers to the pseudo covariance of the form $\langle \bar{B}_{(j,i)ba}\bar{B}_{(v,u)dc}\rangle - \langle \bar{B}_{(j,i)ba}\rangle\langle \bar{B}_{(v,u)dc}\rangle$. To save space, we define the symbol

$$C_{ijuv} = \frac{wn\Delta L}{k^2\sqrt{\gamma_i\gamma_j\gamma_u\gamma_v}}. \tag{6.5}$$

As can be seen, expressions for each block are all similar, save for the superscript of the $\mathbf{A}$ matrices and the argument of the sinc term.

In order to use the expressions for the statistics of the scattering matrix elements, it is necessary to compute the single particle $\mathbf{A}$ matrix terms. In virtually all of the

scattering literature (e.g. Refs. [1, 27, 28]), these matrices are defined with respect to the scattering plane, rather than the local polar coordinate systems associated with each wavevector introduced in Section 3.3. For completeness, we present here the geometric transformations necessary to convert between these different coordinate systems.

Consider a particular pair of incident and outgoing plane waves with wavevectors $\mathbf{k}_i$ and $\mathbf{k}_j$ respectively. Let $\hat{\mathbf{e}}_{ki}$, $\hat{\mathbf{e}}_{\phi i}$, $\hat{\mathbf{e}}_{\theta i}$ $\hat{\mathbf{e}}_{kj}$, $\hat{\mathbf{e}}_{\phi j}$ and $\hat{\mathbf{e}}_{\theta j}$ be the associated spherical polar vectors as defined in Eqs. (3.80)-(3.82). The vectors $\hat{\mathbf{e}}_{ki}$ and $\hat{\mathbf{e}}_{kj}$ define the scattering plane, whose unit normal vector is given by $\hat{\mathbf{e}}_{\perp} = (\hat{\mathbf{e}}_{ki} \times \hat{\mathbf{e}}_{kj})/|\hat{\mathbf{e}}_{ki} \times \hat{\mathbf{e}}_{kj}|$. We then define the vectors $\hat{\mathbf{e}}_{\parallel i} = \hat{\mathbf{e}}_{\perp} \times \hat{\mathbf{e}}_{ki}$ and $\hat{\mathbf{e}}_{\parallel j} = \hat{\mathbf{e}}_{\perp} \times \hat{\mathbf{e}}_{kj}$ so that $(\hat{\mathbf{e}}_{\parallel i}, \hat{\mathbf{e}}_{\perp i}, \hat{\mathbf{e}}_{ki})$ and $(\hat{\mathbf{e}}_{\parallel j}, \hat{\mathbf{e}}_{\perp j}, \hat{\mathbf{e}}_{kj})$ form right-handed triads. In the case that $\hat{\mathbf{e}}_{ki}$ and $\hat{\mathbf{e}}_{kj}$ are parallel, we take $\hat{\mathbf{e}}_{\parallel i} = \hat{\mathbf{e}}_{\theta i}$, $\hat{\mathbf{e}}_{\parallel j} = \hat{\mathbf{e}}_{\theta j}$ and $\hat{\mathbf{e}}_{\perp i} = \hat{\mathbf{e}}_{\perp j} = \hat{\mathbf{e}}_{\phi i}$.

Consider now the incident wavevector $\mathbf{k}_i$ and let us temporarily drop the subscript i. The vectors $\hat{\mathbf{e}}_{\theta}, \hat{\mathbf{e}}_{\phi}, \hat{\mathbf{e}}_{\parallel}$ and $\hat{\mathbf{e}}_{\perp}$ all lie in the same plane with unit normal vector given by $\hat{\mathbf{e}}_k$. In general, however, the vectors $\hat{\mathbf{e}}_{\theta}$ and $\hat{\mathbf{e}}_{\phi}$ will not align with $\hat{\mathbf{e}}_{\parallel}$ and $\hat{\mathbf{e}}_{\perp}$. Let α be the angle between $\hat{\mathbf{e}}_{\theta}$ and $\hat{\mathbf{e}}_{\parallel}$, defined such that $-\pi < \alpha < \pi$, where $\alpha > 0$ if $(\hat{\mathbf{e}}_{\theta} \times \hat{\mathbf{e}}_{\parallel})/|\hat{\mathbf{e}}_{\theta} \times \hat{\mathbf{e}}_{\parallel}| = \hat{\mathbf{e}}_k$ (i.e. $\hat{\mathbf{e}}_{\parallel}$ is an anti-clockwise rotation of $\hat{\mathbf{e}}_{\theta}$ about $\hat{\mathbf{e}}_k$) and $\alpha < 0$ if $(\hat{\mathbf{e}}_{\theta} \times \hat{\mathbf{e}}_{\parallel})/|\hat{\mathbf{e}}_{\theta} \times \hat{\mathbf{e}}_{\parallel}| = -\hat{\mathbf{e}}_k$ (i.e. $\hat{\mathbf{e}}_{\parallel}$ is a clockwise rotation of $\hat{\mathbf{e}}_{\theta}$ about $\hat{\mathbf{e}}_k$). See Figure 6.1 for a graphical representation of these vectors, along with the electric field vector $\mathbf{E}$, which also lies in the same plane.

Given α, the electric field vector, which can be written as $\mathbf{E} = (E_{\theta}, E_{\phi})^{\mathrm{T}}$ with respect to the basis vectors $\hat{\mathbf{e}}_{\theta}$ and $\hat{\mathbf{e}}_{\phi}$, can be transformed to $\mathbf{E} = (E_{\parallel}, E_{\perp})^{\mathrm{T}}$ with respect to $\hat{\mathbf{e}}_{\parallel}$ and $\hat{\mathbf{e}}_{\perp}$ by

$$\begin{pmatrix} E_{\parallel} \\ E_{\perp} \end{pmatrix} = \mathbf{R}(\alpha) \begin{pmatrix} E_{\theta} \\ E_{\phi} \end{pmatrix}, \qquad \mathbf{R}(\alpha) = \begin{pmatrix} \cos(\alpha) & \sin(\alpha) \\ -\sin(\alpha) & \cos(\alpha) \end{pmatrix}. \tag{6.6}$$

Note that conventions for the directions of the unit vectors described here are not consistent throughout the literature. For example, in Ref [1], the normal to the scattering plane is taken to be $\hat{\mathbf{e}}'_{\perp} = -\hat{\mathbf{e}}_{\perp}$. In this case, the electric field component perpendicular to the scattering plane is given by $E'_{\perp} = -E_{\perp}$. Following the

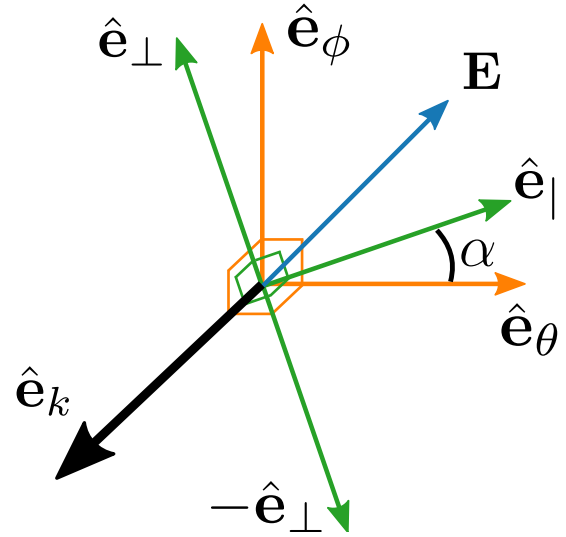

Figure 6.1: Vectors used in scattering calculations. The vectors $\mathbf{E}, \hat{\mathbf{e}}_\theta, \hat{\mathbf{e}}_\phi, \hat{\mathbf{e}}_\parallel$ and $\hat{\mathbf{e}}_\perp$ all lie in the plane perpendicular to $\hat{\mathbf{e}}_k$. The angle θ is positive in the diagram.

convention used in Ref [1], it can ultimately be shown that

$$\begin{pmatrix} E_{\theta j} \\ E_{\phi j} \end{pmatrix} = \mathbf{R}(-\alpha_j)\boldsymbol{\sigma}_z \begin{pmatrix} \mathcal{A}_2 & \mathcal{A}_3 \\ \mathcal{A}_4 & \mathcal{A}_1 \end{pmatrix} \boldsymbol{\sigma}_z \mathbf{R}(\alpha_i) \begin{pmatrix} E_{\theta i} \\ E_{\phi i} \end{pmatrix}, \tag{6.7}$$

where $\mathcal{A}_1$, $\mathcal{A}_2$, $\mathcal{A}_3$ and $\mathcal{A}_4$ are scattering coefficients defined with respect to the scattering plane and α_i and α_j are the angles between $\hat{\mathbf{e}}_{\theta i}$, $\hat{\mathbf{e}}_{\parallel i}$ and $\hat{\mathbf{e}}_{\theta j}$, $\hat{\mathbf{e}}_{\parallel j}$ respectively. Finally, the matrix $\mathbf{A}^{t/r}_{(j,i)}$, which is used in our simulations, is given by the product of the five matrices in Eq. (6.7).

Once all of the covariances and pseudo covariances have been computed, their values constitute the elements of a pair of large, complex covariance and pseudo covariance matrices $\boldsymbol{\Sigma}_R$ and $\boldsymbol{\Sigma}_P$ that describe regular covariances and pseudo covariances between all of the elements of the scattering matrix. Since correlations between scattering elements exist only for pairs of blocks satisfying the memory or conjugate memory effects, these matrices will be sparse, as most of their elements will be zero. In order to generate random scattering matrices, it is easier in practice to generate real Gaussian variables than complex Gaussian variables. Using the complex covariance and pseudo covariance matrices, we can form the real-valued covariance matrix for the real and imaginary parts of the elements of the scattering

matrix $\mathbf{\Sigma}$ using the equation [279]

$$\mathbf{\Sigma} = \frac{1}{2}\begin{pmatrix} \mathrm{Re}(\mathbf{\Sigma}_R + \mathbf{\Sigma}_P) & \mathrm{Im}(-\mathbf{\Sigma}_R + \mathbf{\Sigma}_P) \\ \mathrm{Im}(\mathbf{\Sigma}_R + \mathbf{\Sigma}_P) & \mathrm{Re}(\mathbf{\Sigma}_R - \mathbf{\Sigma}_P) \end{pmatrix}. \tag{6.8}$$

Rather than using $\mathbf{\Sigma}$ directly to sample Gaussian random variables, it is more efficient to compute the Cholesky decomposition $\mathbf{C}$ of $\mathbf{\Sigma}$, generate a vector of standard, zero-mean Gaussian random variables $\mathbf{x}$, and then compute $\mathbf{z} = \mathbf{C}\mathbf{x}$. The vector $\mathbf{z}$ computed in this manner will then contain the real and imaginary parts of the elements of a single realisation of the scattering matrix possessing the correct regular covariances and pseudo covariances as described by $\mathbf{\Sigma}_R$ and $\mathbf{\Sigma}_P$. Finally, the non-zero mean values can be corrected for by adding to the generated matrix the mean values described by Eq. (6.1) and (6.2).

6.1.3 Symmetrisation

A randomly generated scattering matrix will not in general satisfy the symmetry constraints discussed in Chapter 3 (energy conservation, reciprocity and time reversal symmetry). It is important however that these constraints are obeyed so that the scattering matrices correspond to physically realisable scattering media.

In order to generate a random scattering matrix that automatically satisfies these symmetry constraints, it is first necessary to identity a set of independent parameters that fully capture the degrees of freedom of the matrix. These parameters may be, for example, a subset of the matrix elements, or parameters associated with a certain matrix decomposition. Once these parameters have been determined, the full set of matrix elements can be uniquely determined from the constraints. Importantly, the set of independent parameters must be chosen so that their statistics can be related to the physical properties of the scattering medium, in our case using the results presented in Section 6.1.2. While it is straightforward to accommodate the reciprocity constraint, unitarity, which manifests as a large system of quadratic equations, is far less trivial to satisfy. In theoretical studies, a commonly used set of parameters is the generalised polar decomposition, previously shown in Eq. (3.134). The connection between the singular vectors of the scattering matrix blocks and

the raw elements of the scattering matrix, however, is non-trivial and unintuitive. Furthermore, the matrices $\mathbf{U}$, $\mathbf{V}$, $\mathbf{U}'$ and $\mathbf{V}'$ appearing in Eq. (3.134) are still unitary, and thus the problem of how to randomly sample a unitary matrix with given statistics remains.

Instead of directly generating a random unitary matrix, an alternative strategy is to first generate a non-unitary scattering matrix $\bar{\mathbf{S}}'$ with desired statistical properties and to then find a unitary matrix $\bar{\mathbf{S}}$ that closely approximates $\bar{\mathbf{S}}'$. One can think of $\bar{\mathbf{S}}$ as a 'symmetrised' version of $\bar{\mathbf{S}}'$. Naturally, the resulting unitary matrix $\bar{\mathbf{S}}$ from this procedure will not possess the exact same statistical properties as those prescribed for $\bar{\mathbf{S}}'$. Provided that the matrix $\bar{\mathbf{S}}$ is sufficiently 'close' to $\bar{\mathbf{S}}'$ (in the sense that $||\bar{\mathbf{S}}' - \bar{\mathbf{S}}||$ is small for some choice of matrix norm), however, this issue becomes unimportant. Given any arbitrary matrix $\bar{\mathbf{S}}'$, it is well known that the closest unitary approximation $\bar{\mathbf{S}}$ of $\bar{\mathbf{S}}'$ is given by the unitary matrix that appears in the polar decomposition of $\bar{\mathbf{S}}'$ [298]. More rigorously, given some arbitrary matrix $\bar{\mathbf{S}}'$, the unitary matrix $\bar{\mathbf{S}}$ produced from this procedure minimises the value of $||\bar{\mathbf{S}}' - \bar{\mathbf{S}}||$ over the set of all unitary matrices for any unitarily invariant matrix norm. Equivalently, if $\bar{\mathbf{S}}' = \mathbf{U}\mathbf{\Lambda}\mathbf{V}^\dagger$ is a singular value decomposition of $\bar{\mathbf{S}}'$, then the closest unitary approximation is given by $\bar{\mathbf{S}} = \mathbf{U}\mathbf{V}^\dagger$. For this reason, we shall refer to this method as 'SVD'.

While the SVD method yields the overall most faithful approximation of the unsymmetrised scattering matrix in the sense just described, it is not the only way to perform the symmetrisation. Another class of methods make use of the differential transfer matrix discussed in Section 3.4.2. In the single scattering regime, writing the scattering matrix in the perturbative form

$$\bar{\mathbf{S}} = \begin{pmatrix} \bar{\mathbf{r}}^{(1)} & \mathbb{I} + \bar{\mathbf{t}}'^{(1)} \\ \mathbb{I} + \bar{\mathbf{t}}^{(1)} & \bar{\mathbf{r}}'^{(1)} \end{pmatrix}, \tag{6.9}$$

where $\bar{\mathbf{r}}^{(1)}, \bar{\mathbf{t}}^{(1)}, \bar{\mathbf{t}}'^{(1)}$ and $\bar{\mathbf{r}}'^{(1)}$ are the single scattering contributions to each block, we may find expressions for the differential transfer matrix in terms of these blocks, first by finding the transfer matrix using Eqs. (3.120)-(3.123), and then by using

the matrix logarithm to infer the differential transfer matrix, since

$$\boldsymbol{\epsilon} = \log(\bar{\mathbf{M}}) = \sum_{n=0}^{\infty} (-1)^{n+1} (\bar{\mathbf{M}} - \mathbb{I})^n / n. \tag{6.10}$$

Following through the algebra, we find that the blocks of the differential transfer matrix, in terms of the scattering matrix blocks, are given by

$$\boldsymbol{\epsilon}_\alpha = \bar{\mathbf{t}}^{(1)} - \frac{1}{2}\left(\bar{\mathbf{r}}'^{(1)}\bar{\mathbf{r}}^{(1)} + \bar{\mathbf{t}}^{(1)}\bar{\mathbf{t}}^{(1)}\right) + \ldots, \tag{6.11}$$

$$\boldsymbol{\epsilon}_\beta = \bar{\mathbf{r}}'^{(1)} - \frac{1}{2}\left(\bar{\mathbf{t}}^{(1)}\bar{\mathbf{r}}'^{(1)} + \bar{\mathbf{r}}'^{(1)}\bar{\mathbf{t}}'^{(1)}\right) + \ldots, \tag{6.12}$$

$$\boldsymbol{\epsilon}_\gamma = -\bar{\mathbf{r}}^{(1)} + \frac{1}{2}\left(\bar{\mathbf{t}}'^{(1)}\bar{\mathbf{r}}^{(1)} + \bar{\mathbf{r}}^{(1)}\bar{\mathbf{t}}^{(1)}\right) + \ldots, \tag{6.13}$$

$$\boldsymbol{\epsilon}_\delta = -\bar{\mathbf{t}}'^{(1)} + \frac{1}{2}\left(\bar{\mathbf{r}}^{(1)}\bar{\mathbf{r}}'^{(1)} + \bar{\mathbf{t}}'^{(1)}\bar{\mathbf{t}}'^{(1)}\right) + \ldots, \tag{6.14}$$

where the series continue indefinitely and involve products of increasing numbers of matrices. In converting from the scattering matrix to the transfer matrix in deriving Eqs. (6.11)-(6.14), we have made use of the Neumann series

$$(\mathbb{I} - \mathbf{A})^{-1} = \sum_{n=0}^{\infty} \mathbf{A}^n. \tag{6.15}$$

The convergence of the series in Eq. (6.15) is justified by the fact that $\mathbf{A}$ represents the single scattering component of one of the blocks of the scattering matrix, the elements of which are assumed to be much smaller than one in magnitude. As progressive terms in Eqs. (3.120)-(3.123) are assumed to become increasingly small, in practice the series may be truncated after some finite number of terms. Retaining only the first terms of the series, it can be seen that each block of the differential transfer matrix corresponds to a different block of the scattering matrix.

Given a collection of randomly generated $\bar{\mathbf{r}}^{(1)}, \bar{\mathbf{t}}^{(1)}, \bar{\mathbf{t}}'^{(1)}$ and $\bar{\mathbf{r}}'^{(1)}$ matrices, the differential transfer matrix can be computed, either by performing the entire conversion numerically, or by using the truncated series in Eqs. (3.120)-(3.123) to yield a reasonable approximation. In Section 3.4.2, however, in particular observing the form of Eqs. (3.192)-(3.195), it was shown that only two of the four blocks of $\boldsymbol{\epsilon}$ are independent. The block $\boldsymbol{\epsilon}_\alpha$ is required to be skew-Hermitian, which is not automat-

ically satisfied by Eq. (6.11) and must therefore be enforced manually. This can be achieved by taking the skew-Hermitian part of $\boldsymbol{\epsilon}_\alpha$ by making the transformation

$$\boldsymbol{\epsilon}_\alpha \to (\boldsymbol{\epsilon}_\alpha - \boldsymbol{\epsilon}_\alpha^\dagger)/2. \tag{6.16}$$

Having done this, the block $\boldsymbol{\epsilon}_\delta$ can be computed using the relation

$$\boldsymbol{\epsilon}_\delta = (\mathbf{J}^p \otimes \boldsymbol{\Sigma}_1^z)\boldsymbol{\epsilon}_\alpha^{pp*}(\mathbf{J}^p \otimes \boldsymbol{\Sigma}_1^z). \tag{6.17}$$

It is noteworthy that the reciprocity symmetry of the matrices $\bar{\mathbf{r}}^{(1)}, \bar{\mathbf{t}}^{(1)}, \bar{\mathbf{t}}'^{(1)}$ and $\bar{\mathbf{r}}'^{(1)}$, which is also built into their statistical properties, means that $\boldsymbol{\epsilon}_\beta$ and $\boldsymbol{\epsilon}_\gamma$ automatically satisfy the reciprocity constraint given by Eq. (3.197). Furthermore, unitarity of $\bar{\mathbf{S}}$ corresponds to requiring that $\boldsymbol{\epsilon}_\beta$ and $\boldsymbol{\epsilon}_\gamma$ are a Hermitian conjugate pair, which is not automatically enforced during random generation. There is therefore freedom in which of the two matrices is calculated from the scattering matrix blocks, as any one of them fully determines the other. One can, for example, calculate $\boldsymbol{\epsilon}_\beta$ and then specify that $\boldsymbol{\epsilon}_\gamma = \boldsymbol{\epsilon}_\beta^\dagger$, foregoing the need to calculate $\boldsymbol{\epsilon}_\gamma$ numerically. We shall refer to this method as 'β'. Alternatively, one can instead calculate $\boldsymbol{\epsilon}_\gamma$ and then specify that $\boldsymbol{\epsilon}_\beta = \boldsymbol{\epsilon}_\gamma^\dagger$, which we shall refer to as 'γ'. Each of these approaches, in some sense, favours one matrix over the other. A more impartial approach is to calculate both $\boldsymbol{\epsilon}_\beta$ and $\boldsymbol{\epsilon}_\gamma$ separately and make the transformations

$$\boldsymbol{\epsilon}_\beta \to (\boldsymbol{\epsilon}_\beta + \boldsymbol{\epsilon}_\gamma^\dagger)/2, \tag{6.18}$$

$$\boldsymbol{\epsilon}_\gamma \to (\boldsymbol{\epsilon}_\gamma + \boldsymbol{\epsilon}_\beta^\dagger)/2. \tag{6.19}$$

This approach, which shall be referred to as 'Mix', also yields a Hermitian conjugate pair of matrices, but combines the information contained in the initial pair of $\boldsymbol{\epsilon}_\beta$ and $\boldsymbol{\epsilon}_\gamma$ matrices computed from the scattering matrix. A quantitative comparison of the four methods outlined in this section will be given in Section 6.3.1.

6.1.4 Matrix cascade

Given the assumption of single scattering, we may only directly generate scattering matrices for thin slabs. Matrices for slabs of arbitrary thickness, however, can

be found by cascading many independent realisations of thin slabs. This is easily achieved using transfer matrices, which possess the useful property that the transfer matrix for a system composed of two contiguous slabs is given by the correctly-ordered product of the transfer matrices of the individual slabs [7]. Specifically, if two spatially disjoint scattering media $\mathcal{S}_1$ and $\mathcal{S}_2$, with transfer matrices $\bar{\mathbf{M}}_1$ and $\bar{\mathbf{M}}_2$ respectively are positioned such that $\mathcal{S}_2$ is to the right of $\mathcal{S}_1$, i.e. $z_1 < z_2$ where z_1 and z_2 are the z coordinates of the centres of the two media, then the transfer matrix $\bar{\mathbf{M}}$ for the combined scattering medium $\mathcal{S}$ is given by

$$\bar{\mathbf{M}} = \bar{\mathbf{M}}_2 \bar{\mathbf{M}}_1. \tag{6.20}$$

A corresponding composition law for scattering matrices also exists, but is more complicated. If $\bar{\mathbf{S}}_1$ and $\bar{\mathbf{S}}_2$ are the scattering matrices for $\mathcal{S}_1$ and $\mathcal{S}_2$ respectively, where

$$\bar{\mathbf{S}}_1 = \begin{pmatrix} \bar{\mathbf{r}}_1 & \bar{\mathbf{t}}'_1 \\ \bar{\mathbf{t}}_1 & \bar{\mathbf{r}}'_1 \end{pmatrix}, \tag{6.21}$$

$$\bar{\mathbf{S}}_2 = \begin{pmatrix} \bar{\mathbf{r}}_2 & \bar{\mathbf{t}}'_2 \\ \bar{\mathbf{t}}_2 & \bar{\mathbf{r}}'_2 \end{pmatrix}, \tag{6.22}$$

then the scattering matrix $\bar{\mathbf{S}}$ for $\mathcal{S}$ can be shown to be given by

$$\bar{\mathbf{S}} = \begin{pmatrix} \bar{\mathbf{r}} & \bar{\mathbf{t}}' \\ \bar{\mathbf{t}} & \bar{\mathbf{r}}' \end{pmatrix} = \begin{pmatrix} \bar{\mathbf{r}}_1 + \bar{\mathbf{t}}'_1 \bar{\mathbf{r}}_2 \mathbf{Q} \bar{\mathbf{t}}_1 & (\mathbf{J}_{2N_k+1} \otimes \boldsymbol{\sigma}_z)(\bar{\mathbf{t}}_2 \mathbf{Q} \bar{\mathbf{t}}_1)^{\mathrm{T}} (\mathbf{J}_{2N_k+1} \otimes \boldsymbol{\sigma}_z) \\ \bar{\mathbf{t}}_2 \mathbf{Q} \bar{\mathbf{t}}_1 & \bar{\mathbf{r}}'_2 + \bar{\mathbf{t}}_2 \mathbf{Q} \bar{\mathbf{r}}'_1 \bar{\mathbf{t}}'_2 \end{pmatrix}, \tag{6.23}$$

where $\mathbf{Q} = (\mathbb{I} - \bar{\mathbf{r}}'_1 \bar{\mathbf{r}}_2)^{-1}$.

A problem with cascading matrices is that the statistical results in Section 6.1.2 are based on the assumption that the scattering medium is centred at $z = 0$. This led to the emergence of the sinc factors in the expressions for the covariances and pseudo covariances associated with the scattering matrix elements. If instead the scattering medium were centred at an arbitrary position $z = L_0$, these factors would be different.

Suppose that a scattering medium is contained within the region $L_0 - \Delta L/2 <$

$z < L_0 + \Delta L/2$. Observing Eqs. (5.14) and (5.16), it is clear that only the complex exponential terms are affected by such a shift in z coordinate. Furthermore, if $\bar{\mathbf{t}}^{L_0}_{(j,i)}$, $\bar{\mathbf{t}}'^{L_0}_{(j,i)}$, $\bar{\mathbf{r}}^{L_0}_{(j,i)}$ and $\bar{\mathbf{r}}'^{L_0}_{(j,i)}$ are blocks of the scattering matrix for the medium centred at the plane $z = L_0$, then by extracting a constant exponential from each term, we have

$$\bar{\mathbf{t}}^{L_0}_{(j,i)} = \bar{\mathbf{t}}^{0}_{(j,i)} e^{i(\gamma_i - \gamma_j)L_0}, \tag{6.24}$$

$$\bar{\mathbf{t}}'^{L_0}_{(j,i)} = \bar{\mathbf{t}}'^{0}_{(j,i)} e^{i(-\gamma_i + \gamma_j)L_0}, \tag{6.25}$$

$$\bar{\mathbf{r}}^{L_0}_{(j,i)} = \bar{\mathbf{r}}^{0}_{(j,i)} e^{i(\gamma_i + \gamma_j)L_0}, \tag{6.26}$$

$$\bar{\mathbf{r}}'^{L_0}_{(j,i)} = \bar{\mathbf{r}}'^{0}_{(j,i)} e^{i(-\gamma_i - \gamma_j)L_0}, \tag{6.27}$$

where $\bar{\mathbf{t}}^{0}_{(j,i)}$, $\bar{\mathbf{t}}'^{0}_{(j,i)}$, $\bar{\mathbf{r}}^{0}_{(j,i)}$ and $\bar{\mathbf{r}}'^{0}_{(j,i)}$ are corresponding scattering matrix blocks that describe the same physical scattering medium if it were instead centred at the origin. Eqs. (6.24)-(6.27) imply that

$$\bar{\mathbf{t}}^{L_0} = \Lambda^{L_0}_{-} \bar{\mathbf{t}}^{0} \Lambda^{L_0}_{+}, \tag{6.28}$$

$$\bar{\mathbf{t}}'^{L_0} = \Lambda^{L_0}_{+} \bar{\mathbf{t}}'^{0} \Lambda^{L_0}_{-}, \tag{6.29}$$

$$\bar{\mathbf{r}}^{L_0} = \Lambda^{L_0}_{+} \bar{\mathbf{r}}^{0} \Lambda^{L_0}_{+}, \tag{6.30}$$

$$\bar{\mathbf{r}}'^{L_0} = \Lambda^{L_0}_{-} \bar{\mathbf{r}}'^{0} \Lambda^{L_0}_{-}, \tag{6.31}$$

where

$$\Lambda^{L_0}_{+} = \begin{pmatrix} e^{i\gamma_{-N_k} L_0} & \dots & 0 \\ \vdots & \ddots & \vdots \\ 0 & \dots & e^{i\gamma_{N_k} L_0} \end{pmatrix} \otimes \begin{pmatrix} 1 & 0 \\ 0 & 1 \end{pmatrix} \tag{6.32}$$

and $\Lambda^{L_0}_{-} = (\Lambda^{L_0}_{+})^*$. Considering the block structure of the scattering matrix, overall we find that

$$\bar{\mathbf{S}}^{L_0} = \begin{pmatrix} \bar{\mathbf{r}}^{L_0} & \bar{\mathbf{t}}'^{L_0} \\ \bar{\mathbf{t}}^{L_0} & \bar{\mathbf{r}}'^{L_0} \end{pmatrix} = \Lambda^{L_0}_{\pm} \bar{\mathbf{S}}^{0} \Lambda^{L_0}_{\pm} = \begin{pmatrix} \Lambda^{L_0}_{+} & \mathbb{O} \\ \mathbb{O} & \Lambda^{L_0}_{-} \end{pmatrix} \begin{pmatrix} \bar{\mathbf{r}}^{0} & \bar{\mathbf{t}}'^{0} \\ \bar{\mathbf{t}}^{0} & \bar{\mathbf{r}}'^{0} \end{pmatrix} \begin{pmatrix} \Lambda^{L_0}_{+} & \mathbb{O} \\ \mathbb{O} & \Lambda^{L_0}_{-} \end{pmatrix}. \tag{6.33}$$

Using the Eqs. (3.120)-(3.123), it can also be shown that the blocks of the transfer

matrix satisfy

$$\bar{\boldsymbol{\alpha}}^{L_0} = \Lambda_-^{L_0}\boldsymbol{\alpha}^0\Lambda_+^{L_0}, \tag{6.34}$$

$$\bar{\boldsymbol{\beta}}^{L_0} = \Lambda_-^{L_0}\boldsymbol{\beta}^0\Lambda_-^{L_0}, \tag{6.35}$$

$$\bar{\boldsymbol{\gamma}}^{L_0} = \Lambda_+^{L_0}\boldsymbol{\gamma}^0\Lambda_+^{L_0}, \tag{6.36}$$

$$\bar{\boldsymbol{\delta}}^{L_0} = \Lambda_+^{L_0}\boldsymbol{\delta}^0\Lambda_-^{L_0}, \tag{6.37}$$

where the superscripts are defined analogously to those of the scattering matrix blocks. It follows that

$$\bar{\mathbf{M}}^{L_0} = \begin{pmatrix} \bar{\boldsymbol{\alpha}}^{L_0} & \bar{\boldsymbol{\beta}}^{L_0} \\ \bar{\boldsymbol{\gamma}}^{L_0} & \bar{\boldsymbol{\delta}}^{L_0} \end{pmatrix} = \Lambda_\mp^{L_0}\bar{\mathbf{M}}^0\Lambda_\pm^{L_0} = \begin{pmatrix} \Lambda_-^{L_0} & \mathbb{O} \\ \mathbb{O} & \Lambda_+^{L_0} \end{pmatrix} \begin{pmatrix} \bar{\boldsymbol{\alpha}}^0 & \bar{\boldsymbol{\beta}}^0 \\ \bar{\boldsymbol{\gamma}}^0 & \bar{\boldsymbol{\delta}}^0 \end{pmatrix} \begin{pmatrix} \Lambda_+^{L_0} & \mathbb{O} \\ \mathbb{O} & \Lambda_-^{L_0} \end{pmatrix}. \tag{6.38}$$

Therefore, in order to generate a random matrix describing a scattering medium centred at $z = L_0$, we can first generate $\bar{\mathbf{S}}^0$, whose statistics are given by the results of Section 6.1.2, and then compute $\bar{\mathbf{S}}^{L_0}$ using Eq. (6.33).

Suppose now that a series of N scattering layers are situated with centres located at (from left to right) $L_1, L_2, \ldots L_N$ and let $\bar{\mathbf{M}}_i^{L_i}$ denote the transfer matrix of the i'th layer. Using Eq. (6.38), the overall transfer matrix is given by

$$\begin{aligned} \bar{\mathbf{M}} &= \bar{\mathbf{M}}_N^{L_N} \ldots \bar{\mathbf{M}}_3^{L_3}\bar{\mathbf{M}}_2^{L_2}\bar{\mathbf{M}}_1^{L_1} \\ &= \Lambda_\mp^{L_N}\bar{\mathbf{M}}_N^0\Lambda_\pm^{L_N} \ldots \Lambda_\mp^{L_3}\bar{\mathbf{M}}_3^0\Lambda_\pm^{L_3}\Lambda_\mp^{L_2}\bar{\mathbf{M}}_2^0\Lambda_\pm^{L_2}\Lambda_\mp^{L_1}\bar{\mathbf{M}}_1^0\Lambda_\pm^{L_1}, \\ &= \Lambda_\mp^{L_N}\bar{\mathbf{M}}_N^0 \ldots \bar{\mathbf{M}}_3^0\Lambda_\pm^{L_3-L_2}\bar{\mathbf{M}}_2^0\Lambda_\pm^{L_2-L_1}\bar{\mathbf{M}}_1^0\Lambda_\pm^{L_1} \end{aligned} \tag{6.39}$$

Deriving the final line of Eq. (6.39) makes use of the identity $\Lambda_\pm^{L_2}\Lambda_\mp^{L_1} = \Lambda_\pm^{L_2-L_1}$, which follows trivially from the definitions. In the special case $L_1 = 0$ and $L_{i+1} - L_i = \Delta L$ for $1 \leq i \leq N-1$, as would be the case for contiguous slabs of equal thicknesses ΔL, Eq. (6.39) can be written in the form

$$\bar{\mathbf{M}} = \Lambda_\mp^{N\Delta L}\prod_{i=1}^{N}\Lambda_\pm^{\Delta L}\bar{\mathbf{M}}_i^0. \tag{6.40}$$

Therefore, a transfer matrix for a medium of thickness $N\Delta L$ can be computed by

cascading N matrices of the form $\Lambda_{\pm}^{\Delta L}\bar{\mathbf{M}}^0$. Note that the final matrix $\Lambda_{\mp}^{N\Delta L}$ outside of the product in Eq. (6.40) imparts global phase terms onto each 2×2 block of $\bar{\mathbf{M}}$ (and $\bar{\mathbf{S}}$) and therefore does not alter any of the intensity or polarisation statistics of the random matrix given by the product. If necessary, scattering at the boundaries of the slab can also be incorporated into the matrix cascade by including additional scattering or transfer matrices that capture the surface effects at either interface.

As shall be discussed in more detail in Section 6.3.2, it is computationally faster to cascade transfer matrices than scattering matrices. One problem that can arise when cascading transfer matrices, however, is that it is possible for the transfer matrix elements to diverge numerically. This happens because the transfer matrix group $\mathcal{G}$ is not a compact group [299]. Because of this, there exist sequences of transfer matrices corresponding to physically realisable scattering media for which the matrix elements are unbounded. While this problem does not occur for thin scattering media, for which the corresponding transfer matrices are numerically close to the identity matrix, in the multiple scattering regime it is common for the transfer matrix elements to become too large to reasonably represent on a computer. It is therefore necessary to monitor the growth of the transfer matrix elements during the cascade process. If it is discovered that the transfer matrix elements are becoming too large, it is required that the matrices are converted to scattering matrices, which, by unitarity, do not suffer from the same problem. After converting to scattering matrices, the cascade can be continued indefinitely, albeit at a slower computation speed.

In order to access the multiple scattering regime, it is necessary to cascade at least $\sim l/\Delta L$ transfer matrices of thin slabs, which, as shall be seen, can be on the order of 10^2 matrices. Additionally, in order to compute good statistics, it is necessary to have a large number of scattering matrices at any given thickness. This point shall be explored in more detail in Section 6.3.3. Consequently, in total, a large number of random matrices are required to generate data for random media with thicknesses beyond a mean free path. To alleviate this computational burden, we incorporated a bootstrapping approach that reuses a relatively small number of matrices. Specifically, we generated two pools of random matrices, which we shall refer to as the single pool and the multi pool. Working with transfer matrices, the

single pool contains random transfer matrices describing slabs of thicknesses ΔL centred at the origin and multiplied by the fixed propagator matrix as discussed previously. The multi pool contains random transfer matrices describing scattering medium of some larger prescribed thickness $\delta L > \Delta L$ (e.g. $\delta L = 0.5l$) and are generated by taking random products of matrices from the single pool.

If the multi pool is sufficiently large, then in generating the multi pool it is clear by the pigeonhole principle that some matrices from the single pool will be reused, which may introduce unwanted statistical correlations between members of the multi pool. Suppose that N_s and N_m are the sizes of the single and multi pools respectively and that each member of the multi pool is generated by taking the product of N_Δ elements of the single pool. Since matrix multiplication is not commutative, there are a total of $N_t = N_s!/(N_s - N_\Delta)!$ different possible members of the multi pool. This number is immensely large for any realistic choices of N_s and N_Δ. For example, if $N_s = 10^4$ and $N_\Delta = 100$, then $N_t \sim 10^{400}$, which, of course, is far bigger than any realistic size of N_m. Practically speaking, each member of the multi pool is therefore guaranteed to be unique. While we have not conducted a full study of the statistical implications of members of the multi pool having repeated matrices in their products or having matrices in common with those contained within the products of other multi pool members, numerical evidence suggest that these effects are negligible for the number of matrices used in our simulations.

A final set of matrices independent of the pools is used to describe actual realisations of the scattering media being modelled at different thicknesses. It is this final set of matrices that is used to calculate all the statistical data presented in this chapter. This final set of matrices is initially equated to the single pool, and thus, at the beginning of the simulation, describes an ensemble of scattering media of thickness ΔL. In order for the simulation to progress to greater thicknesses, each matrix from this final set is multiplied by a randomly selected matrix from the multi pool, which progresses the thickness of the scattering media described by the final set of matrices by δL. This process can be repeated indefinitely and, after n steps, the final set of matrices will correspond to scattering media of thickness $\Delta L + n\delta L$. Using this approach, after the single and multi pools have been generated, no further random matrices are required, and progressing to greater thicknesses only requires matrix

products, or the corresponding operations required to cascade scattering matrices.

6.2 Physical validation

To validate our model, we simulated two types of scattering media: one containing spherical, optically inactive particles and one containing spherical, chiral particles exhibiting circular birefringence. In either case, the single particle scattering properties are known theoretically (see, for example, Ref. [1]). We used a Cartesian cubature scheme with mode spacing given by $\Delta k_x = \Delta k_y = 0.1715k$, which resulted in a total of 101 modes. This means that our scattering and transfer matrices were of size 404. We chose the wavelength $\lambda = 500\,\text{nm}$ and considered isotropic spheres of three different sizes, namely $x = 1, 2$ and 4, where $x = ka$ is the dimensionless size parameter and a is the particle radius. For each particle size, we used the same relative refractive index $m = 1.2$ and calculated the $\mathbf{A}_{(j,i)}^{t/r/r'}$ factors using Mie theory. In addition, we performed simulations for chiral spheres of two different size parameters, $x = 1$ and 4. For both size parameters, we chose a mean relative refractive index $\bar{m} = 1.2$ and circular birefringence $2\Delta m = 0.088$ so that $m_l = \bar{m} + \Delta m$ and $m_r = \bar{m} - \Delta m$ were the relative refractive indices experienced by incident left and right handed circular polarisation respectively.

For a given type of particle, the volume density n and slab thickness ΔL are free parameters. It is important, however, to choose these parameters in a way that does not violate any of the assumptions made in our model. To ensure that this was the case, we identified three conditions that must be simultaneously satisfied. Firstly, we require $kd \gg 1$, where $d = (1/n)^{1/3}$ is a measure of the average spacing between the particles in the medium. This condition ensures that the particles are all in the far field of each other. Secondly, we require $l/\Delta L \gg 1$, which ensures that the single scattering approximation holds since, under this constraint, the mean transmission matrix element appearing in Eq. (5.46) will have magnitude much less than one. Since this second condition requires that the slab thickness ΔL is small, we identified a third condition $\Delta L/2a > 1$ that ensures that the slab is thick enough to contain the particles.

Instead of specifying n directly, it was simpler to start with a particle volume

Table 6.2: Summary of the physical parameters used in simulations.

Input			Calculated Parameters					Physical Checks		
x	$\overline{m}$	Δm	$n/\mu\text{m}^{-3}$	$\Delta L/\mu\text{m}$	$l/\mu\text{m}$	a/nm	$d/\mu\text{m}$	kd	$\Delta L/2a$	$l/\Delta L$
1	1.2	0	4.737	1.177	311.57	79.58	0.595	7.48	7.34	264.7
2	1.2	0	0.592	1.126	88.08	159.15	1.191	14.96	3.53	78.2
4	1.2	0	0.074	1.173	35.87	318.31	2.382	29.93	1.84	30.6
1	1.2	0.044	4.737	0.969	311.57	79.58	0.595	7.48	6.09	321.7
4	1.2	0.044	0.074	0.969	35.87	318.31	2.382	29.93	1.52	37.0

fraction ϕ and calculate the density via $n = \phi/V_p$, where V_p is the volume of a single particle. For all simulations we chose the value $\phi = 0.01$. In specifying ΔL, a problem we encountered was that, given the appearance of $1/\gamma_i$ factors in, for example, Eq. (6.1), the numerical values of the means and covariances can become large for grazing incidence modes. As discussed in Section 5.2.2, grazing modes effectively see a larger thickness for the scattering medium, which, if not managed carefully, may result in a violation of the single scattering assumption. To overcome this problem, we set an arbitrary threshold value $\delta = 0.1$ and demanded that the elements of the mean transmission matrix were smaller than δ for all incident modes. Specifically, in light of Eq. (6.1), we solved the equation $\delta = 2\pi n \Delta L s_{\text{max},i}/(k\gamma_i)$ for ΔL for $1 < i < 2N_p + 1$, where $s_{\text{max},i}$ is the largest singular value of $\langle \mathbf{A}^t_{(i,i)} \rangle$. We then took the actual value of ΔL used in the simulations to be the minimum of all these values. This method was found to give parameter sets that satisfied all of the previously discussed conditions. A summary of all the simulation parameters is given in Table 6.2, where each row corresponds to a different parameter set. For chiral particles, the presented mean free path is that calculated from Mie theory for an isotropic sphere with the same size parameter.

For each parameter set we generated the matrices $\bar{\mathbf{t}}$, $\bar{\mathbf{r}}$ and $\bar{\mathbf{r}}'$ using a multivariate Gaussian distribution, calculating $\bar{\mathbf{t}}'$ from $\bar{\mathbf{t}}$ using Eq. (3.154). For each matrix $\bar{\mathbf{S}}'$ we computed the unitary approximation $\bar{\mathbf{S}}$ (and its associated transfer matrix $\bar{\mathbf{M}}$) using the SVD method. To properly account for propagation along the z axis when cascading multiple slabs, we then pre-multiplied each of these transfer matrices by the constant matrix $\Lambda^{\Delta L}_{\pm}$. These matrices constitute the single pool, which was of size $N_s = 10^4$ for each parameter set. We generated multi pools of size $N_m = 10^4$

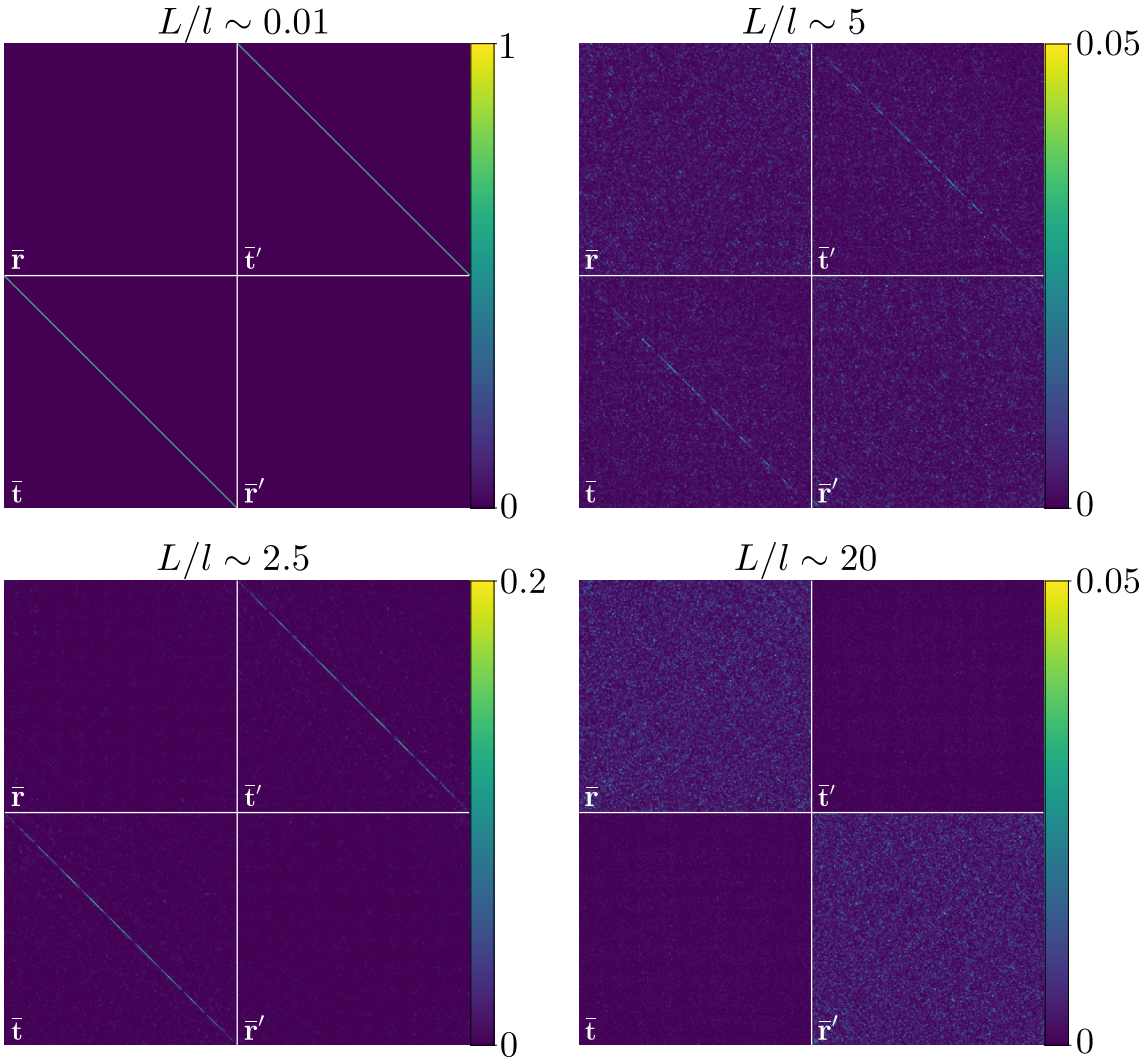

Figure 6.2: Square moduli of elements of random scattering matrices describing random media of thicknesses $L/l \sim 0.01, 2.5, 5$ and 20. Matrices were generated using isotropic spheres with size parameter $x = 2$.

representing scattering media of step size $\delta L = 0.5l$. Finally, for data collection, we used a final set of matrices as previously discussed, also of size 10^4. Using this final set of matrices, we progressed to a final thickness of $L = 30l$, collecting data at each step.

Examples of scattering matrices are shown in Fig 6.2, which shows the square modulus (scattering probability) of the elements of a single realisation of the scattering matrix at different thicknesses. As can be seen, for $L/l \sim 0.01$, the moduli of all of the matrix elements are virtually zero, save for the diagonal elements of the transmission matrix, which are large due to the dominance of the incident field. As the

thickness of the medium increases, the moduli of the diagonal elements decay as light is scattered away from the incident field into other directions. Correspondingly, the moduli of elements elsewhere within the scattering matrix gradually increase with thickness. For $L/l \sim 20$, very little light is able to penetrate through the medium, resulting in the moduli of the elements of the transmission matrix becoming small relative to those of the reflection matrix. In addition, the reflection matrices are relatively isotropic, which is characteristic of multiple scattering.

In the following section we present a variety of statistical data pertinent to polarisation, calculated from our simulations for thicknesses L ranging from the single to multiple scattering regimes. As we have access to the entire scattering matrix, in addition to analysing more familiar characteristics of the scattered field in individual modes, such as the intensity and degree of polarisation, we may also calculate parameters that are functions of larger sections of $\bar{\mathbf{S}}$, such as correlations between different matrix blocks and the transmission eigenvalues. In all of the following data, averages were computed over all 10^4 realisations of the scattering matrix for each thickness.

6.2.1 Isotropic spheres

The following results are for optically inactive spheres whose parameters are given in the first three rows of Table 6.2.

6.2.1.1 Transmission eigenvalues and eigenvectors

Figure 6.3(a) shows the mean transmission eigenvalue $\langle\tau\rangle = \langle \mathrm{tr}(\bar{\mathbf{t}}^\dagger\bar{\mathbf{t}})\rangle/(4N_p + 2)$, where tr denotes the trace operator as a function of medium thickness. When all incident light is transmitted, regardless of incident mode or polarisation state, $\langle\tau\rangle = 1$, whereas $\langle\tau\rangle = 0$ when no light is transmitted. By conservation of energy, a decrease in $\langle\tau\rangle$ must be compensated for by an increase in the mean reflection eigenvalue $\langle\rho\rangle = 1 - \langle\tau\rangle = \langle \mathrm{tr}(\bar{\mathbf{r}}^\dagger\bar{\mathbf{r}})\rangle/(4N_p + 2)$. The key characteristics of Figure 6.3 are that $\langle\tau\rangle$ decreases monotonically with increasing medium thickness, as is known to occur for isotropic systems [3], and that the rate of decrease is smaller for larger size parameters. The dependence on particle size can be explained by single particle scattering anisotropy: larger particles preferentially scatter light in

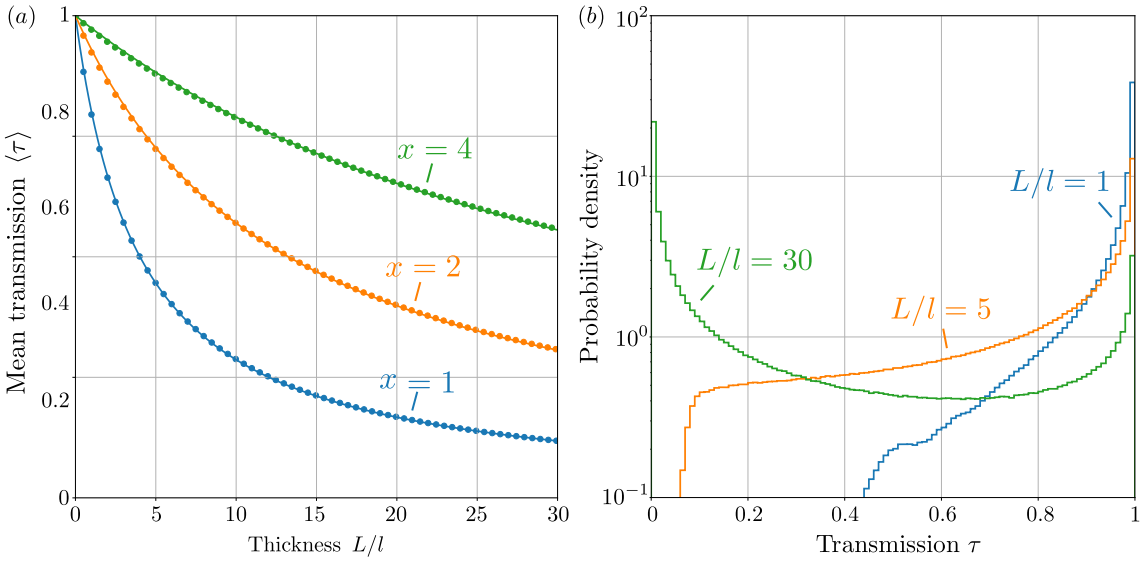

Figure 6.3: (a) Mean transmission as a function of thickness for size parameters $x = 1, 2$ and 4. Fitting curves are of the form $\langle\tau\rangle = (1+L/\alpha l)^{-1}$, where α was calculated from the data points. (b) Probability density functions of transmission eigenvalues for thicknesses $L/l = 1, 5$ and 30 for size parameter $x = 2$.

the forward direction, which results in a slower decay rate for $\langle\tau\rangle$. In Ref. [300], it was found that in a quasi-one dimensional system with isotropic scattering, to lowest order, the mean transmission eigenvalue decays as $\langle\tau\rangle = (1+L/l)^{-1}$. We found that our curves were reasonably well fit by functions of the form $\langle\tau\rangle = (1+L/\alpha l)^{-1}$, where α is a fitting parameter given by 4.02, 13.25 and 37.51 for $x = 1, 2$ and 4 respectively. Physically, αl can be interpreted as a length scale over which the random medium scatters isotropically, similar to the transport mean free path $l_t = l/(1-g)$ [17]. We found however that our value for α was larger than $1/(1-g)$. To explain this, we note that the expression $1/(1-g)$ only accounts for randomisation of direction, whereas α also incorporates isotropisation of polarisation state.

Figure 6.3(b) shows the probability density function for the transmission eigenvalues of scattering matrices at thicknesses $L/l = 1, 5$ and 30 for size parameter $x = 2$. The distribution transitions from being highly peaked at $\tau = 1$ for small thicknesses to highly peaked at $\tau = 0$ for large thicknesses. Notably, even for the largest thickness $L/l = 30$, there still exist channels for which $\tau = 1$. These open eigenchannels are well known and have been studied extensively, both theoretically and experimentally, particularly for scalar waves [3, 6]. In our simulations however, these eigenchannels also have a specific polarisation structure. In order to construct

such an eigenchannel experimentally, such as in a wavefront shaping experiment, it would be necessary to control both the relative intensity and polarisation state of each plane wave component of the incident field. Considering the eigenchannel with largest transmission, we found that altering the polarisation state of any individual plane wave component while keeping its relative intensity constant resulted in a decrease of the total transmitted intensity. Careful control of the incident polarisation state may therefore lead to enhanced transmission over the case of scalar waves. We found similar behaviour for $x = 1$ and 4, but the rate at which the distribution evolves with thickness is greater for $x = 1$ and smaller for $x = 4$, as expected due to scattering anisotropy.

Figures 6.4 and 6.5 show the statistics of the polarisation structure of the maximally and minimally transmitting eigenchannels for different scattering medium realisations of different thicknesses for the parameter set for which $x = 2$. These eigenchannels can be calculated numerically as the singular vectors of the transmission matrix with largest and smallest singular values. In general, the eigenchannels are composed of a collection of plane waves, each travelling in different directions and with different polarisation states. For each realisation, we computed the total Stokes vectors $(S_0, S_1, S_2, S_3)^{\mathrm{T}}$ of these eigenchannels, summed over different plane wave directions. It should be noted that for different plane wave components, since the electric field vibrates within a different plane, these parameters must be calculated with respect to the local coordinate systems associated with each plane wave component. Given the total Stokes vectors, we then computed the degree of linear polarisation and degree of circular polarisation, which are defined by $\sqrt{S_1^2 + S_2^2}/S_0$ and $|S_3|/S_0$ and respectively. These quantities were then averaged over different matrix realisations, and the distributions are presented in Figures 6.4 and 6.5. The polarisation structures of a selection of example singular vectors are also presented as circular insets. These circles, which represent the region of k-space bounded by the circle of radius k, show Lissajous figures for the polarisation states of plane wave components whose wavevectors lie at the position in the k-space occupied by the curve. The colours red and black differentiate elliptical polarisation states of opposite helicity.

The distributions within Figures 6.4 and 6.5 reveal that the eigenchannels do not

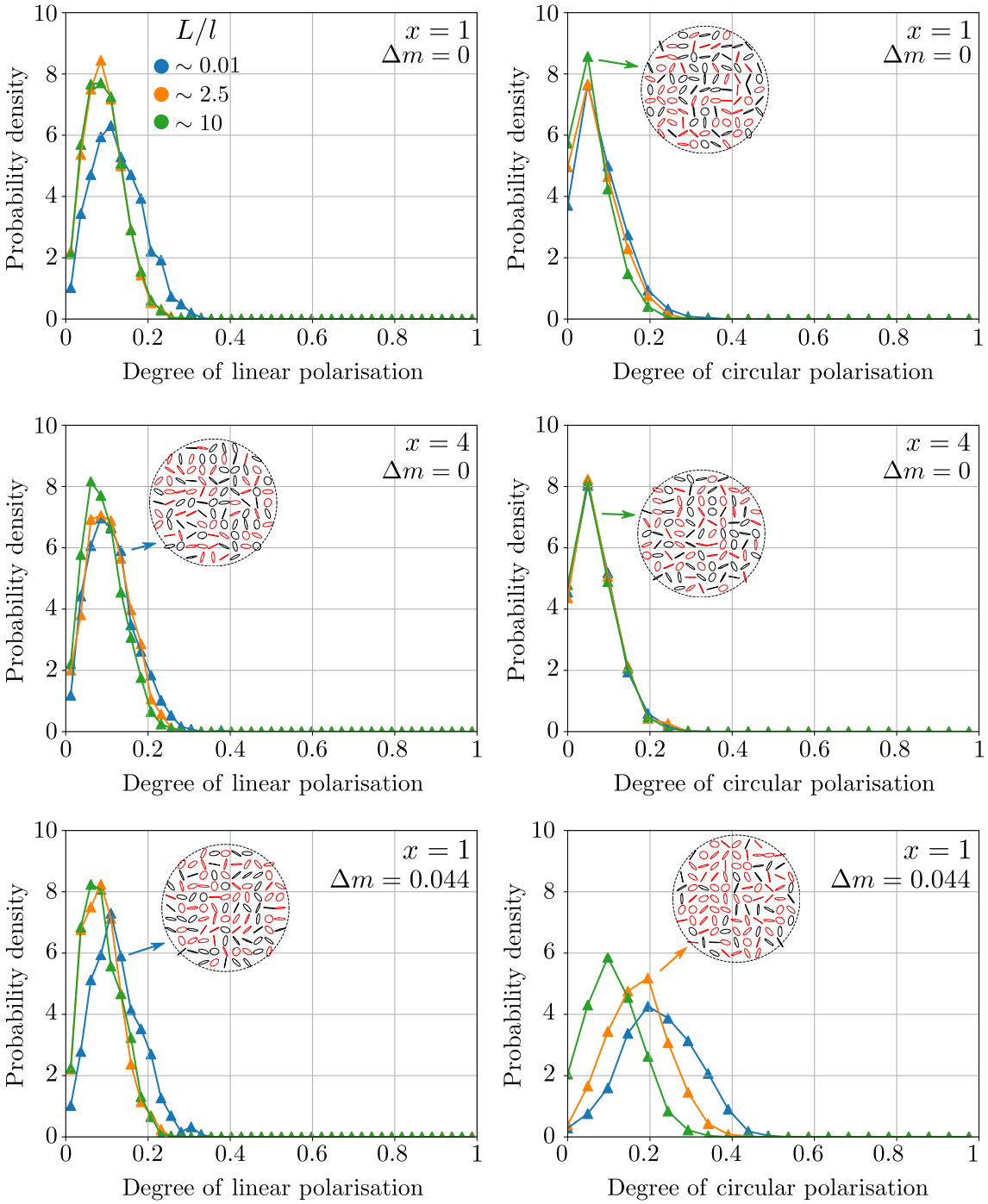

Figure 6.4: Probability distributions for the degrees of linear and circular polarisation associated with the mean Stokes vectors averaged across different scattering directions for the maximally transmitting eigenchannel. Different rows correspond to different simulation parameter sets, as indicated by the text contained within. Sample polarisation profiles are presented within the figures, showing Lissajous polarisation curves of different plane wave components.

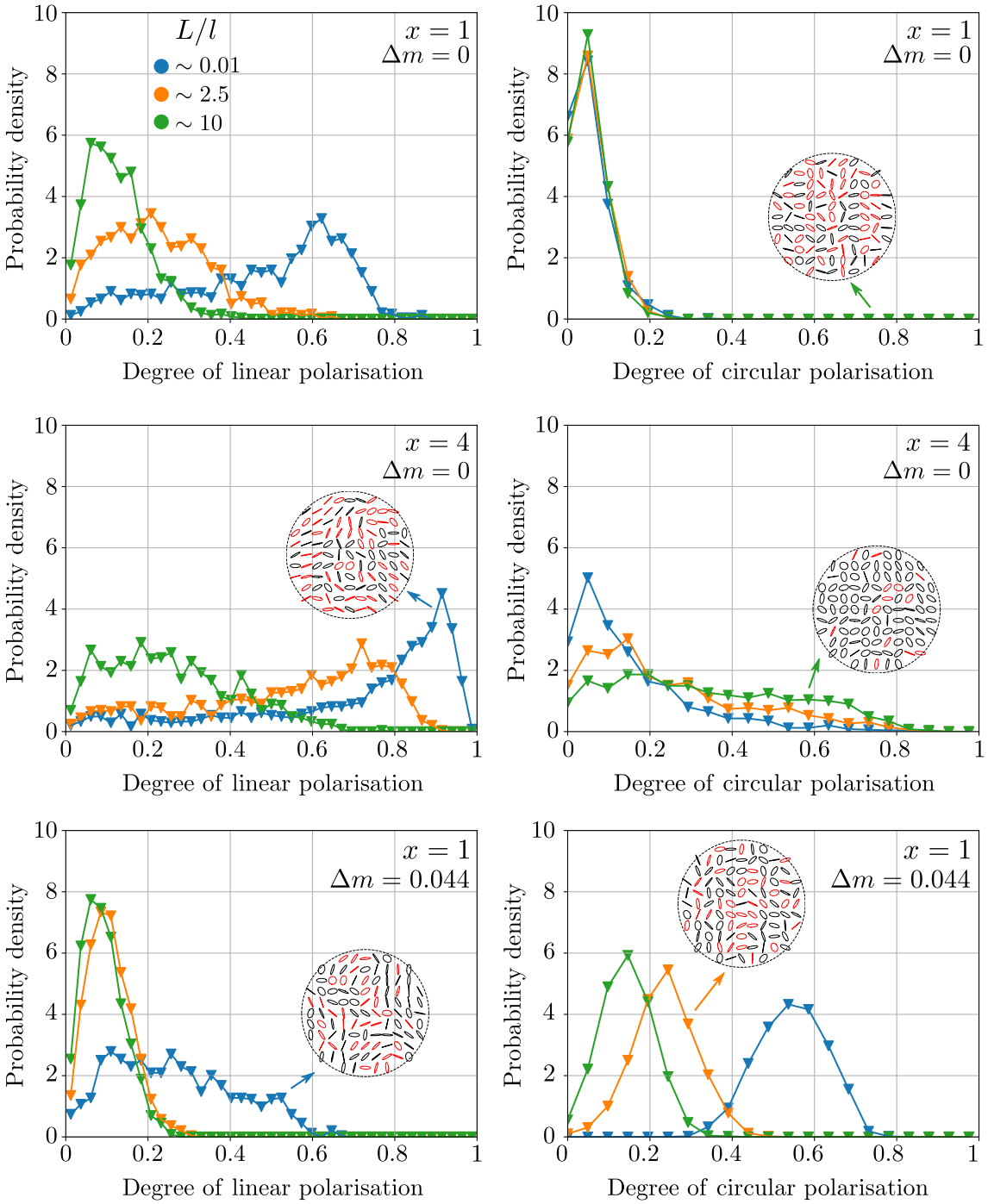

Figure 6.5: As Figure 6.4, but for the minimally transmitting eigenchannels.

possess trivial, isotropic distributions of polarisation states. The most interesting behaviour can be observed in Figure 6.5, which shows data for the minimally transmitting eigenchannel. In the left column of Figure 6.5, which shows the statistics of the degree of linear polarisation, it can be seen that for small thicknesses, the

minimally transmitting eigenchannel (maximally reflected incident waves) tend to have a large number of relatively linear polarisation states throughout their wavefronts. This can also be observed in the sample singular vectors presented within the panels, which generally show a large number of linear states. With regard to the degree of circular polarisation, it can be seen that the statistics in the multiple scattering regime ($L/l \sim 10$) show dependence on particle size. In particular, there tends to be a larger number of relatively circular polarisation states for the $x = 4$ than for $x = 1$. While further analysis is necessary to fully appreciate the intricacies of the polarisation structures of the transmission eigenchannels, these results are, to our knowledge, some of the earliest demonstrations of their kind, and further highlight the importance of controlling the polarisation state of light in scattering experiments.

6.2.1.2 Scattered intensity

Figures 6.6(a) and (b) show the mean plane wave intensity $\langle I \rangle$ in a selection of outgoing modes for a normally incident plane wave and size parameters $x = 1$ and 2. We focused our attention on four different modes: the transmitted wave parallel to the incident field (forward transmission, or FT); the transmitted wave for which $\boldsymbol{\kappa}/k \approx (3\Delta k_x, 0)^{\mathrm{T}}$ (oblique transmission, or OT); the reflected wave for which $\boldsymbol{\kappa}/k = (3\Delta k_x, 0)^{\mathrm{T}}$ (oblique backscattering, or OB) and the backscattered wave propagating in the opposite direction to the incident field (direct backscattering, or DB). For each mode, $\langle I \rangle$ was calculated by taking the ensemble average vector norm of the first column of the appropriate matrix block.

Observing FT in Figure 6.6(a), we see that $\langle I \rangle$ decays exponentially, but the decay rate changes at around $L/l \sim 10$, becoming smaller for large thicknesses. The initial exponential decay is consistent with the intensity computed from Eq. (5.46), which is shown in the figure as a black line. For larger thicknesses, the change in decay rate occurs as there is an increasing amount of light scattered back into the forward direction. The notable bend in the decay curve can therefore be thought of as a transition to the multiple scattering regime. Before this transition occurs, our data points are systematically larger than those predicted by the black line, which we attribute to numerical inaccuracies stemming from our discretisation.

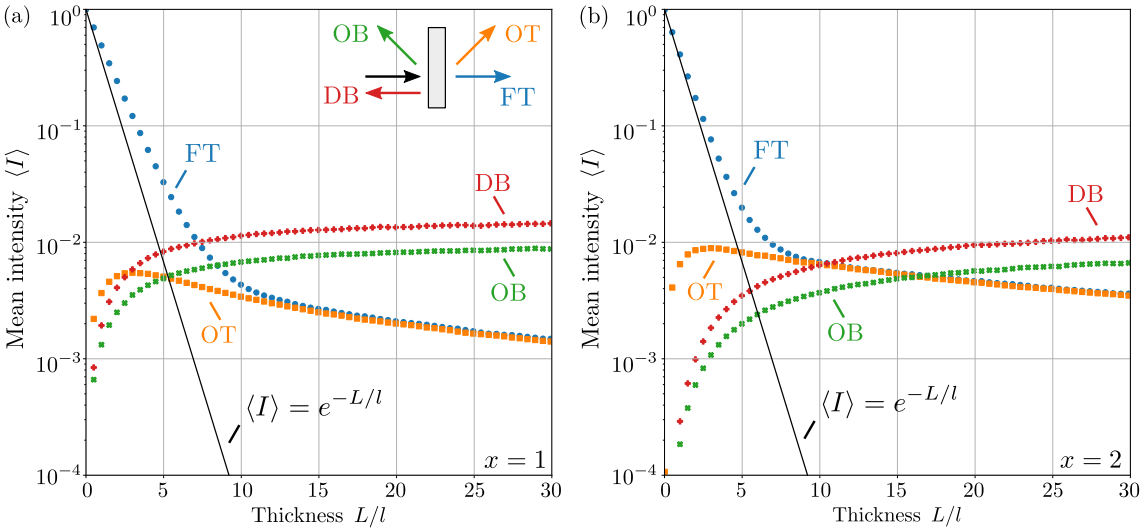

Figure 6.6: Mean intensity as a function of thickness for size parameters (a) $x = 1$ and (b) $x = 2$. The intensity is shown in four different outgoing modes: forward transmission (FT), oblique transmission (OT), oblique backscattering (OB) and direct backscattering (DB). A visual aid is provided in (a).

Looking at OT in Figure 6.6(a), for small thicknesses we see that the intensity is small and increases with thickness. In this regime, scattering is weak and intensity increases as more light is scattered away from FT and into OT. For large thicknesses, the intensity behaviour is similar to FT, settling on a limiting decay trajectory. The behaviour in reflection is conjugate to that of transmission. In OB, the intensity is initially small, but increases monotonically. The same behaviour is observed in DB, but the intensity values are ~ 1.8 times larger. This intensity enhancement is a signature of the coherent backscattering effect, which emerges naturally in our simulations from the reciprocity symmetry of the scattering matrices. This enhancement is less than ideal (a factor of 2), which we attribute to the fact that each mode occupies a non-zero size in k-space and thus needs to account for scattering over a non-zero solid angle. Figure 6.6(b) shows similar trends to Figure 6.6(a). The most notable differences between the two are that the reflected intensities increase at slower rates and the transmitted intensities decay at a slower rate, both of which are also a result of scattering anisotropy.

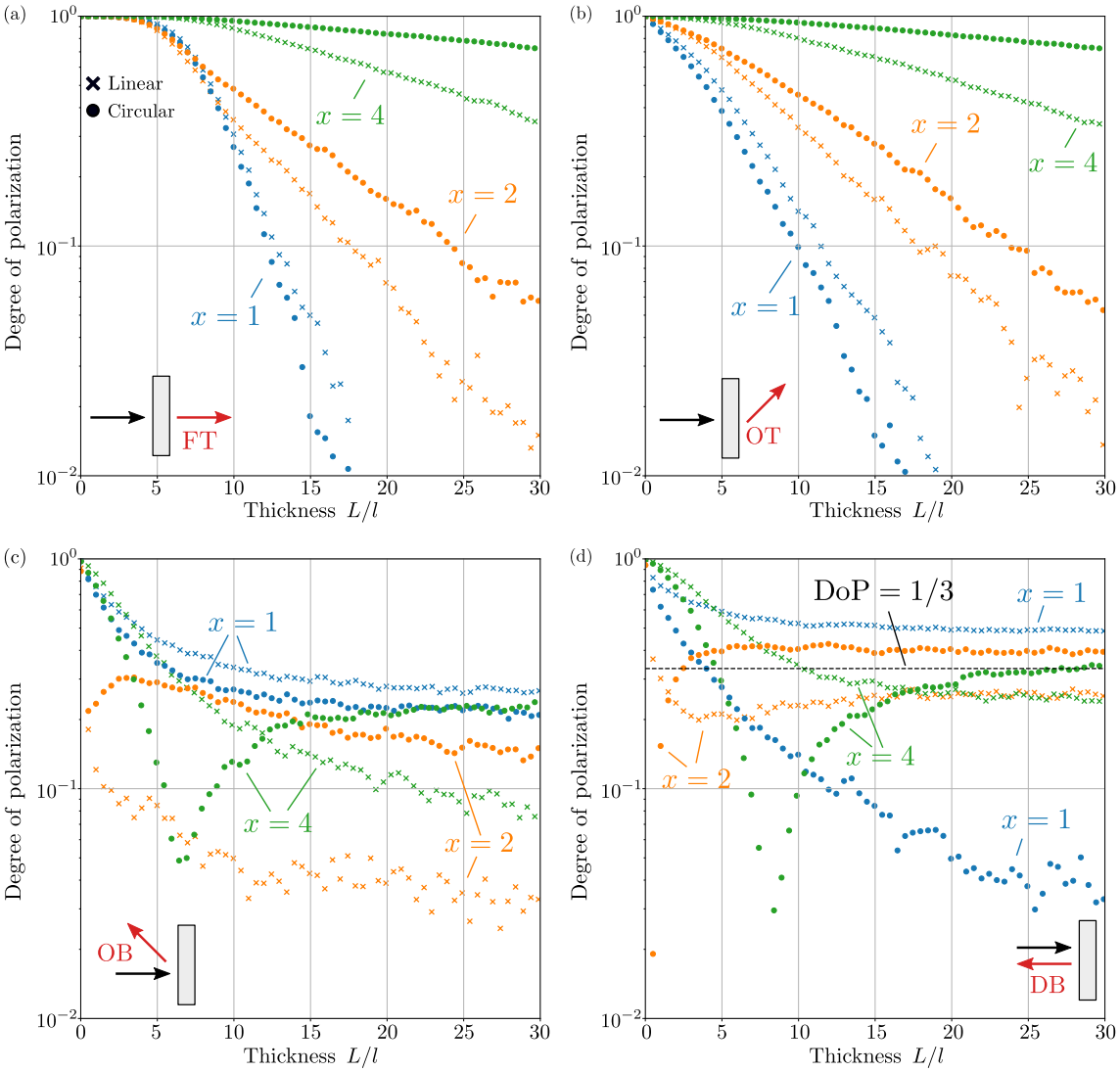

Figure 6.7: Degree of polarisation as a function of thickness for incident linearly (× markers) and circularly (∘ markers) polarised light and size parameters $x = 1$ (blue), 2 (orange) and 4 (green) in (a) forward transmission (FT), (b) oblique transmission (OT), (c) oblique backscattering (OB) and (d) direct backscattering (DB).

6.2.1.3 Degree of polarisation

In Figure 6.7, we show the degree of polarisation in the same four modes discussed in Section 6.2.1.2 for both a linearly and circularly polarised, normally incident plane wave. As discussed in Chapter 4, the degree of polarisation can be found by calculating the ensemble average Mueller matrix for each mode, from which the average scattered Stokes vector for different incident polarisation states, and thus the degree of polarisation, can be deduced.

Figure 6.7(a) shows the degree of polarisation versus thickness in FT. As is evident from the graph, the degree of polarisation decays more slowly for larger particles, regardless of the incident polarisation state. Furthermore, for $x = 1$, we see that linear polarisation better preserves its degree of polarisation over greater thicknesses than circular polarisation, but the opposite is true for $x = 2$ and 4. This phenomenon is a manifestation of the polarisation memory effect discussed in Chapter 2. A similar trend can be observed in Figure 6.7(b), which shows the degree of polarisation in OT. The most notable difference is that, particularly for $x = 1$, the degree of polarisation begins to decay immediately, as opposed to at $L/l \sim 5$ for FT. This is due to the presence of the incident field in FT and absence thereof in OT.

The behaviour of the degree of polarisation in OB, as shown in Figure 6.7(c) is much more interesting. The most obvious feature is that the degree of polarisation retains a residual, non-zero value as $L/l \to \infty$ for all particle sizes and polarisation states. This residual degree of polarisation can be explained by noting that in reflection, unlike transmission, a significant contribution to the total field comes from low-order scattering sequences that occur close to the medium's surface [301]. Another striking feature is the non-monotonicity of the degree of polarisation for circular polarisation and size parameters $x = 2, 4$ (and the absence of such behaviour for $x = 1$). Specifically, the degree of polarisation can be seen to dip to a minimum value before increasing again and settling on a limiting value. This occurs at $L/l \sim 0.5$ for $x = 2$ and at $L/l \sim 6.5$ for $x = 4$. There is also a non-trivial dependence between the limiting degree of polarisation value, size parameter and incident polarisation state.

To explain some of these phenomena, we note that, roughly speaking, the reflected field is the sum of three types of contributions: low scattering order contributions from scattering sequences occurring close to the medium's surface (type I); polarisation-randomising, high order scattering contributions from long, circuitous sequences deep within the medium (type II) and polarisation-maintaining, high order scattering contributions from long, largely forward-directed sequences deep within the medium (type III). As type I contributions occur near the slab boundary, their overall magnitude should be largely independent of thickness. The latter two con-

tributions, however, should increase in magnitude with thickness.

For $x = 1$, since large angle scattering is more probable than for $x = 2$ or 4, type I contributions dominate the total backscattered field for all thicknesses. The degree of polarisation decays relatively slowly as type II contributions gradually increase with thickness, which give a polarisation-randomising background. As scattering is relatively isotropic, type III contributions are comparatively weak and thus less relevant. To verify this claim, we observed distributions of scattered polarisation states over the Poincaré sphere for different thicknesses. We found that for all thicknesses, these distributions remained concentrated at the polarisation state that would result from a single backscattering event, with an increasing isotropic background for larger thicknesses.

The situation is different for $x = 2$ and 4. Since larger particles scatter more strongly in the forward direction, type I contributions, which require large angle scattering events, are comparatively much weaker. For incident linearly polarised light, type I and III contributions both tend to preserve the incident polarisation state. Although type I contributions are weaker for $x = 4$ than $x = 2$, type III contributions are greater for $x = 4$ than $x = 2$. There is thus a non-trivial relationship between the relative magnitudes of these contributions as particle size changes, the exact balance of which dictates the non-monotonicity of the limiting value of the degree of polarisation for linear polarisation.

For $x = 2$ and 4, the situation is again different for incident circularly polarised light. While type III contributions maintain incident helicity, type I contributions result in a helicity flip. Therefore, in transitioning from small to large thicknesses, the distribution of scattered states on the Poincaré sphere must transition from being highly focused at the helicity flipped pole (a single scattering, type I dominant regime) to being relatively isotropic, but concentrated at the pole with the same helicity as the incident field (a multiple scattering, type III dominant regime). Although both of these extremes correspond to relatively large values for the degree of polarisation, in performing this transition, there is an intermediate thickness at which the distribution of scattered states on the Poincaré sphere shows no preference for either pole, in which case the degree of polarisation is small. It is precisely this thickness that corresponds to the dips in the degree of polarisation. The dip

is more obvious for $x = 4$ than $x = 2$ and occurs at a larger thickness because photons are able to penetrate further into the medium for $x = 4$ before their directions are randomised. This behaviour has been observed experimentally in oblique backscattering from suspensions of polystyrene spheres [302].

As a final remark, we note that in Figure 6.7(d), which shows similar trends to Figure 6.7(c), the degree of polarisation tends to values close to 1/3 for $x = 2$ and 4. This is the value predicted for scattering matrices drawn from the circular orthogonal ensemble in the direct backscattering direction, as discussed in Section 4.1.1 [246]. For $x = 1$, the dominance of type I contributions to the reflected field means that the phase function of the slab better resembles that of the individual particles in the medium, which is not isotropic. This may explain why the degree of polarisation for $x = 1$ deviates strongly from this value, particularly for incident circularly polarised light. The assumption of isotropic scattering, which is necessary for the circular ensemble to be an appropriate model, is better satisfied at large thicknesses for $x = 2$ and 4, whose scattered fields are dominated by multiply scattered light.

6.2.1.4 Diattenuation and retardance

An additional pair of parameters that can be useful in assessing the polarimetric properties of a scattering medium are diattenuation and retardance, which were defined previously in Section 4.1.2. As we have access to the full scattering matrix, these can computed for any 2×2 block using the polar decomposition. Unlike the degree of polarisation, which is dependent on the incident polarisation state, diattenuation and retardance are computed from the entire 2×2 block.

Figure 6.8(a) shows a heat map of probability density functions for diattenuation D in FT at different thicknesses for $x = 1$. The values of the color bar are dimensionless and represent probability density. The color bar values are accurate for thicknesses beyond $10l$, but are saturated for shorter thicknesses in a small region close to the origin as outlined by the dashed contour. In this region, D is strongly peaked close to 0, as a weakly scattering medium, which largely preserves the incident field, cannot be strongly diattenuating. In Figure 6.8(b), density functions for a selection of thicknesses as indicated by the horizontal dashed lanes in Figure 6.8(a) are shown more clearly. As can be seen, the diattenuation density

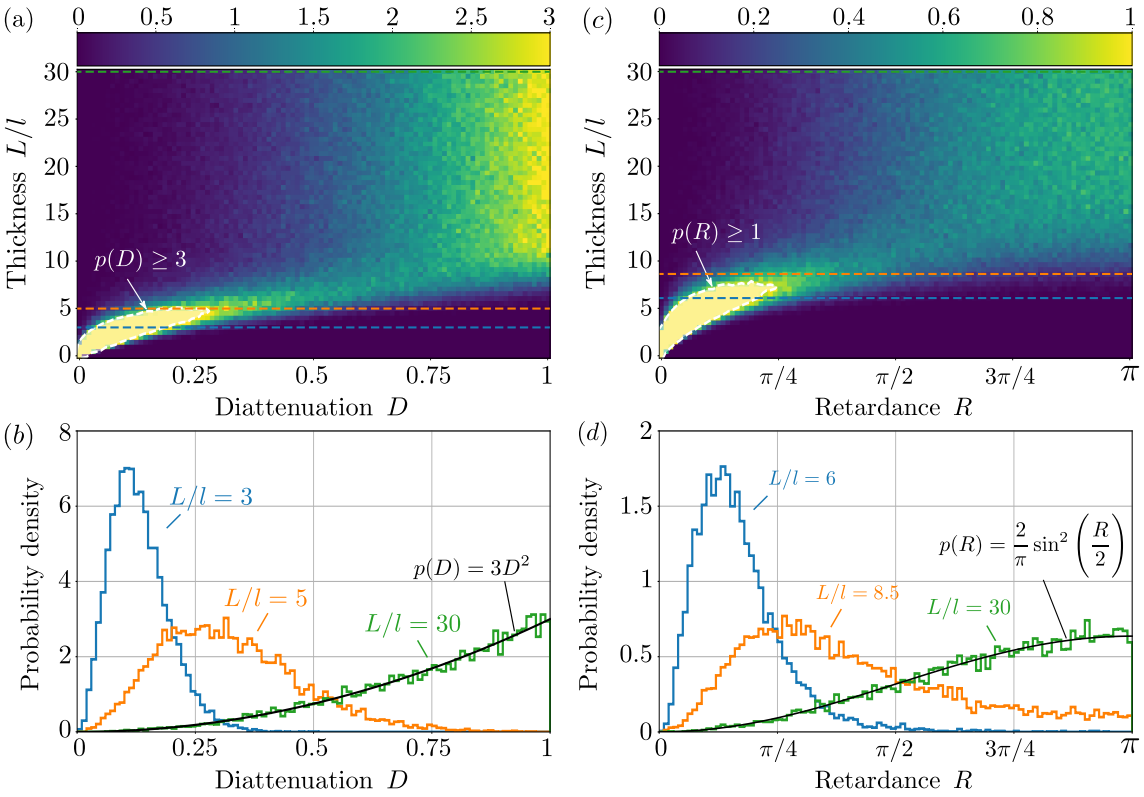

Figure 6.8: Diattenuation and retardance histograms for size parameter $x = 1$ in forward transmission. (a) shows a heatmap of probability distribution functions for diattenuation at different thicknesses. The dashed contour close to the origin indicates a region in which the colors are saturated and the probability density is greater than 3. (b) shows a selection of histograms corresponding to horizontal cross-sections of data in (a). (c) and (d) show analogous data for retardance, with the dashed contour in (c) showing a region for which the probability density is greater than 1.

function transitions from being a delta function $p(D) = \delta(D)$ at $L = 0$ to a limiting distribution given by $p(D) = 3D^2$ as $L \to \infty$. This limiting distribution is precisely that predicted by a random 2×2 matrix of uncorrelated, complex Gaussian entries, and is consistent with the $\alpha = 2$ case of Eq. (4.28). The transition of the diattenuation distribution is therefore related to the decorrelation of the elements of the scattering matrix. Figures 6.8(c) and 6.8(d) show analogous data for retardance in FT. Qualitatively, the behaviour is similar to diattenuation and the density function makes a similar transition from $p(R) = \delta(R)$ to the limiting distribution $p(R) = 2\sin^2(R/2)/\pi$, which is is consistent with the $\alpha = 2$ case of Eq. (4.23). For small thicknesses, we found that the distributions of the diattenuation and retardance vectors were concentrated at polarisation states expected from single scattering theory. These distributions however became isotropic over the Poincaré

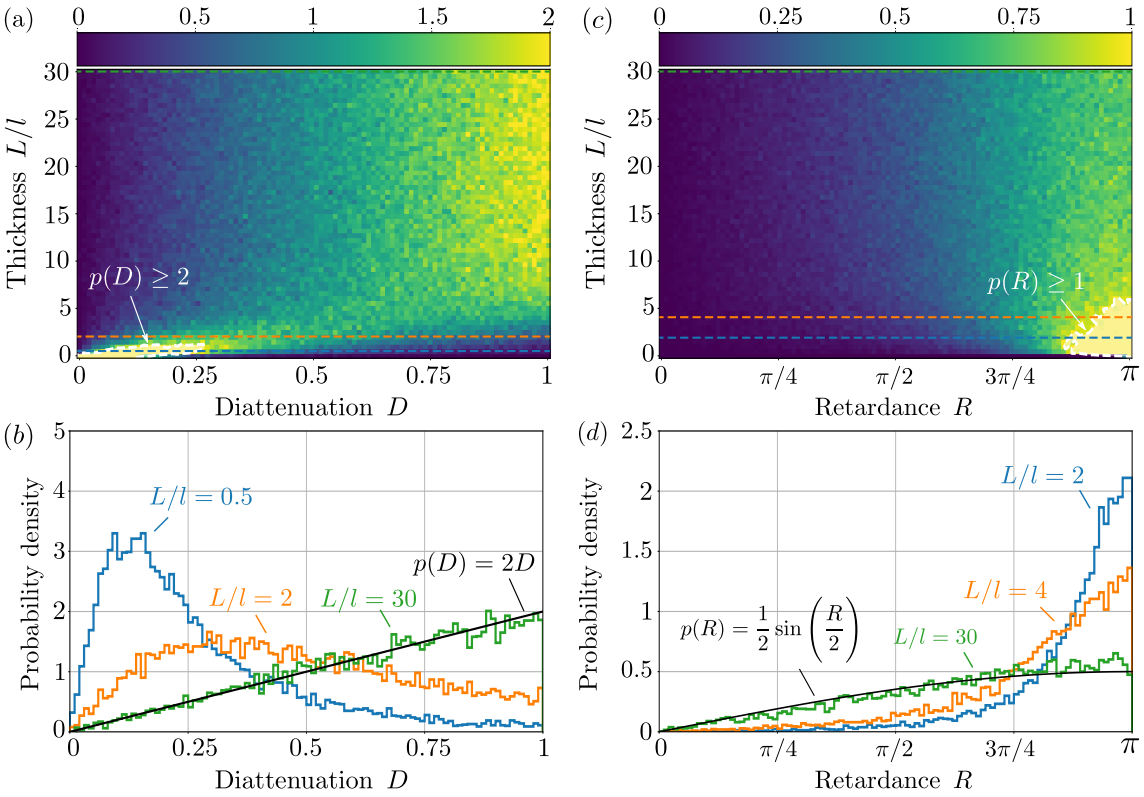

Figure 6.9: As per Figure 6.8, albeit for scatterers with size parameter $x = 4$ and direct backscattering (DB). Dashed contours in (a) and (c) demarcate regions for which the heat map has been clipped for probability densities ≥ 2 and ≥ 1 respectively.

sphere for large thicknesses, meaning that no particular polarisation state is preferentially scattered on average in the large thickness limit. For individual medium realisations, however, as diattenuation tends to be quite large ($\langle D \rangle = 0.75$), there will exist random polarisation states that are transmitted much more strongly than others.

Figure 6.9 shows a similar set of plots to those of Figure 6.8, but for particle size $x = 4$ and for DB. The main differences between Figures 6.8 and 6.9 are the behaviour of retardance, the rates of evolution of the density functions and the limiting probability density functions. As shown in Figures 6.9(a) and 6.9(b), owing to the absence of the incident field, the diattenuation distribution tends to the circular ensemble limiting distribution (this time given by the $\alpha = 1$ case of Eq. (4.28), $p(D) = 2D$) at a shorter thickness. In Figure 6.9(c), for small thicknesses, the retardance is peaked close to $R = \pi$, which is the value expected by single particle backscattering. The retardance distribution evolves to the $\alpha = 1$ case of

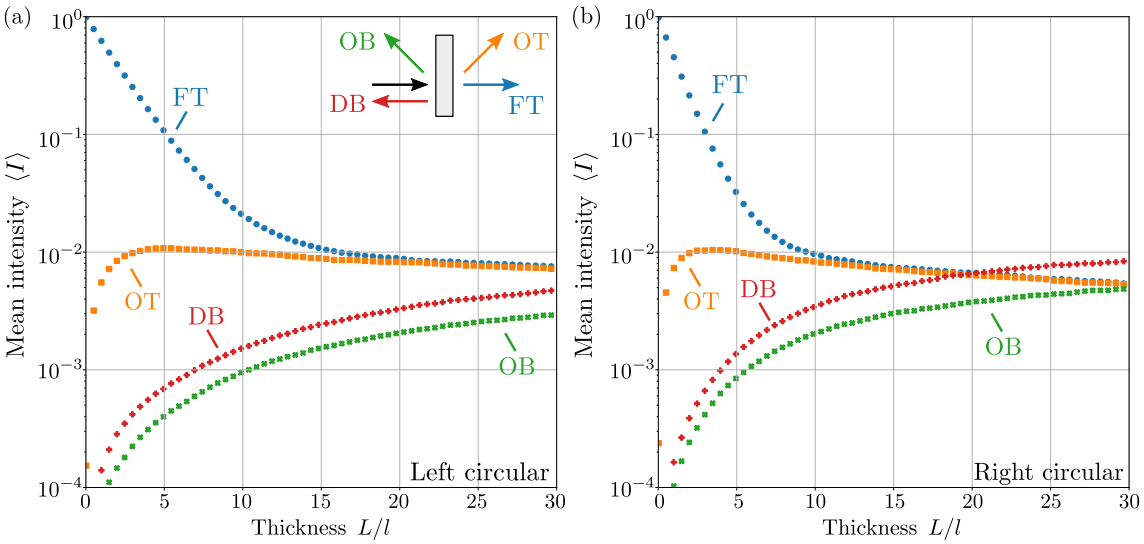

Figure 6.10: Mean intensity as a function of thickness for size parameter $x = 4$ and incident (a) left and (b) right circular polarisation. The intensity is shown in four different outgoing modes: forward transmission (FT), oblique transmission (OT), oblique backscattering (OB) and direct backscattering (DB). A visual aid is provided in (a).

Eq. (4.23), namely $p(R) = \sin(R/2)/2$ at larger thicknesses, as can be seen in Figure 6.9(d). The fact that these limiting densities differ to those in Figure 6.8 is another peculiarity of the DB direction.

6.2.2 Chiral spheres

The following results are for chiral spheres, whose parameter sets are given in the final two rows of Table 6.2. For these particles, since the mean free path depends on the incident polarisation state, to better illustrate the polarisation dependence of the statistics of the scattered field we decided to normalise the medium thickness L by the mean free path calculated for an optically inactive sphere with the same size parameter.

6.2.2.1 Transmission and reflection

Figures 6.10(a) and 6.10(b) show the mean scattered intensity for chiral spheres with size parameter $x = 4$ for incident left handed circularly polarised light (LHC) and right handed circularly polarised light (RHC) respectively. While the overall trends closely resemble those in Figure 6.6, there is now a clear polarisation dependence. As was the case with the isotropic spheres, much of the behaviour can be explained

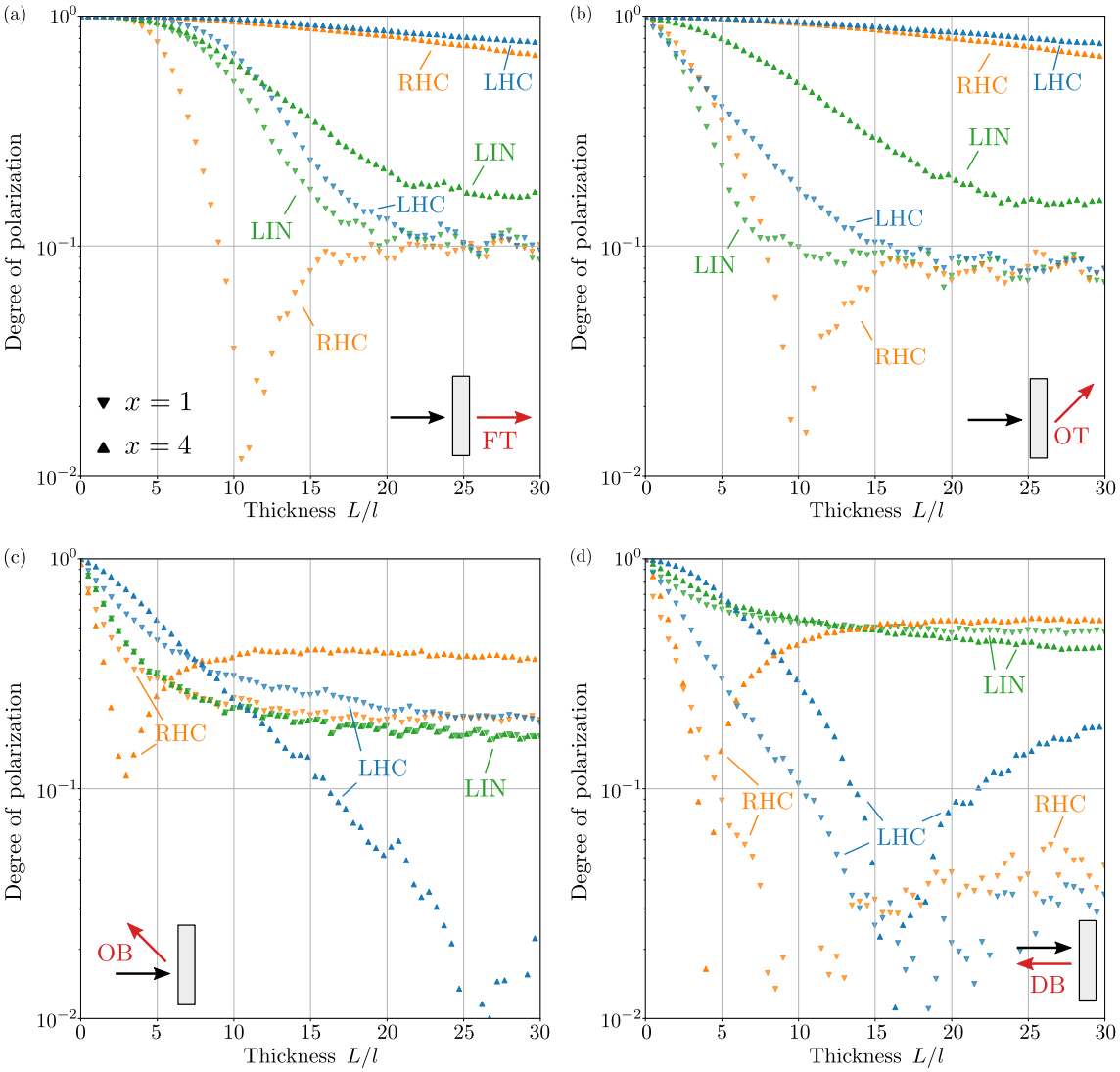

Figure 6.11: DoP as a function of thickness for incident linearly polarised light (LIN), left handed circularly polarised light (LHC) and right handed circularly polarised light (RHC) for size parameters $x = 1$ (▼ markers) and 4 (▲ markers) in outgoing modes (a) forward transmission (FT), (b) oblique transmission (OT), (c) oblique backscattering (OB) and (d) direct backscattering (DB).

through consideration of scattering anisotropy. LHC, which is more preferentially forward scattered than RHC, decays slower in FT. For RHC, the mean intensity is correspondingly larger in the backscattering directions. Similar behaviour was seen for size parameter $x = 1$.

6.2.2.2 Degree of polarisation

The degree of polarisation statistics for chiral spheres of size parameters $x = 1$ and 4 (indicated by downward and upward pointing triangles respectively) are shown in Figure 6.11. We have included three different incident polarisation states: LHC, RHC and LIN, the last of which refers to incident linearly polarised light. The trends we see are similar to those for isotropic spheres in Figure 6.7, but with a few interesting differences. In Figure 6.11(a), a dip in the degree of polarisation can now be seen in FT for RHC and $x = 1$. For isotropic spheres, these dips in the degree of polarisation were only present in reflection for larger spheres. We can explain this phenomenon however by invoking a similar argument to before. For RHC and a thin medium, the distribution of scattered polarisation states on the Poincaré sphere was sharply peaked at the pole corresponding to RHC. For large thicknesses, however, we found that this distribution transitioned to one that was relatively isotropic, but with a slight concentration towards the LHC pole due to the particle chirality. Thus, as before, in transitioning between these two distributions, there exists an intermediate thickness at which the degree of polarisation attains a minimum value. This does not occur for incident LHC, as the initial distribution of scattered states is already concentrated at the LHC pole and no such transition occurs as thickness increases. For incident LIN, the distribution is initially focused at a point on the equator of the Poincaré sphere and, in transitioning towards a distribution focused at the LHC pole, there is no intermediate thickness at which the distribution is isotropic across the entire sphere. Therefore, no such dip in the degree of polarisation occurs. We note that we also expect a dip in the degree of polarisation to occur for incident RHC and $x = 4$, but as the degree of polarisation decay rate is small for this size parameter, the medium is not thick enough, even at $30l$, for the dip to occur. In OT, as shown in Figure 6.11(b), we see that the behaviour resembles FT in the same way that Figure 6.7(b) resembles Figure 6.7(a).

In Figure 6.11(c), we see that for $x = 1$ the degree of polarisation behaviour is similar to that of Figure 6.7(c), but note that the degree of polarisation decays more quickly for RHC than for LHC. All three incident polarisation states settle on similar limiting degree of polarisation values, with LHC and RHC ~ 0.2 and LIN ~ 0.17. For $x = 4$, dips in the degree of polarisation are again visible for RHC and

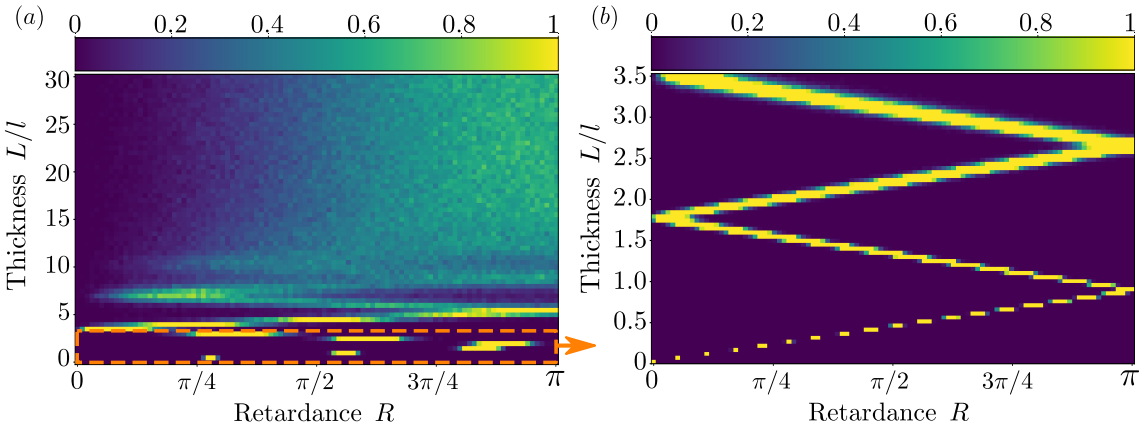

Figure 6.12: Retardance histogram for chiral particles with size parameter $x = 1$ in forward transmission. (a) shows a heatmap of probability distribution functions for retardance at different thicknesses up to $30l$. (b), which is effectively a blow-up of the orange box indicated in (a) shows similar data computed from a separate simulation performed with finer resolution in thickness.

LHC. Unlike in Figure 6.11(a), these dips arise due to the flipping or preservation of helicity for different scattered field contributions, as was the case in Figure 6.7(c). For LHC, which scatters more anisotropically, this dip occurs at a larger thickness ($L/l \sim 27$) than for RHC ($L/l \sim 3$). In Figure 6.11(d), we see that while linearly polarised light retains a large degree of polarisation for large thicknesses irrespective of particle size, dips in the degree of polarisation occur again for LHC and RHC and $x = 4$. For $x = 1$ and incident circularly polarised light, we also see dips in the degree of polarisation, but the exact trends are unclear. For degree of polarisation on the order of 10^{-2} a larger number of realisations than was used is required for good numerical convergence.

6.2.2.3 Retardance

The diattenuation statistics for chiral spheres were not found to differ substantially to those for isotropic spheres. We found, however, interesting behaviour for the retardance. Figure 6.12(a) shows retardance distributions in forward transmission for $x = 1$. Although the limiting behaviour is identical to that of Figure 6.8, we notice that for small thicknesses, enclosed within the orange dashed box, the retardance is a highly peaked function whose position varies with increasing thickness. Figure 6.12(b) shows data from a separate simulation that used the same physical

parameters as in Figure 6.12(a), but a finer step size of $\delta L = 0.05l$, which allowed us to probe the range of thicknesses $0 < L < 3.5$ with greater resolution. Figure 6.12(b) shows that the peak retardance in fact oscillates between 0 and π and, as thickness increases, becomes less sharply peaked. This behaviour is in contrast to our data for isotropic spheres in Figure 6.8, for which the retardance remains close to 0 for small thicknesses.

To explain this phenomenon it should be noted that for thin scattering media, diagonal blocks of the transmission matrix will only display small fluctuations about their non-zero mean values. The behaviour can therefore be probed by investigating the form of the mean transmission matrix. Unlike for isotropic spheres, for which the mean transmission matrix is essentially an identity matrix, for chiral particles, the forward transmission matrix $\mathbf{A}^t_{(i,i)}$ takes the form

$$\mathbf{A}^t_{(i,i)} = \begin{pmatrix} a & b \\ -b & a \end{pmatrix}, \tag{6.41}$$

where $a = \mathrm{Re}(a) + i\mathrm{Im}(a)$ and $b = \mathrm{Re}(b) + i\mathrm{Im}(b)$ are both non-zero complex numbers. Using Eq. (5.44), the mean transmission matrix is given by

$$\langle \bar{\mathbf{t}}_{(i,i)} \rangle = \exp\left[\frac{2\pi n L}{k\gamma_i} \begin{pmatrix} a & b \\ -b & a \end{pmatrix} \right] = \frac{1}{2} \begin{pmatrix} i & -i \\ 1 & 1 \end{pmatrix} \begin{pmatrix} e^{\beta(a-ib)kL} & 0 \\ 0 & e^{\beta(a+ib)kL} \end{pmatrix} \begin{pmatrix} -i & 1 \\ i & 1 \end{pmatrix}, \tag{6.42}$$

where $\beta = 2\pi n/k^3$ is a real, dimensionless constant. Eq. (6.42) shows that right and left handed circularly polarised light are in fact the eigenvectors of the transmission matrix and the electric field vector is multiplied by the factor $e^{\beta(a+ib)kL}$ for right handed circularly polarised light and by $e^{\beta(a-ib)kL}$ for left handed circularly polarised light. The changes in phase experienced by these incident polarisation states, θ_r and θ_l, for right and left handed circularly polarised light respectively, are therefore given by the imaginary parts of the arguments of these exponential functions, which can

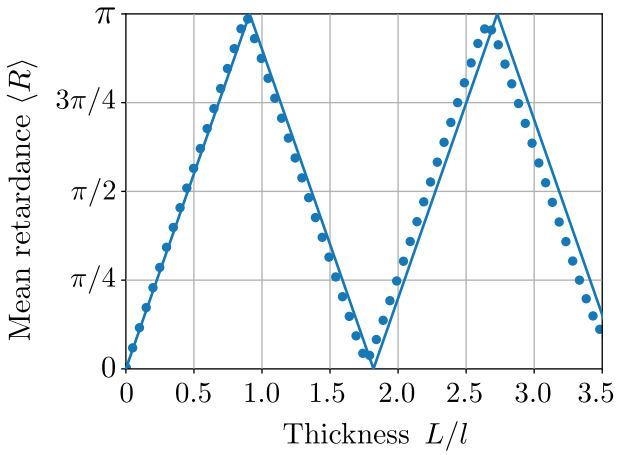

Figure 6.13: Mean retardance against thickness for chiral particles with size parameter $x = 1$. Data points were computed from numerical simulations, whereas the blue lines were calculated theoretically as discussed in the text.

be shown to be

$$\theta_r = \beta[\mathrm{Im}(a) + \mathrm{Re}(b)]kL, \tag{6.43}$$

$$\theta_l = \beta[\mathrm{Im}(a) - \mathrm{Re}(b)]kL. \tag{6.44}$$

Reducing θ_l and θ_r modulo 2π, the retardance can be computed using Eq. (4.7). Figure 6.13 shows the mean retardance as a function of thickness, where the data points show the mean retardances of the distributions shown in Figure 6.12(b) and the straight lines were computed theoretically in light of the above discussion. We see that the theory and data match very closely, although the theoretical result drifts relative to the data for large thickness, which we attribute to numerical inaccuracies inherent with the discrete nature of our model. Physically, since the mean transmitted fields for incident right and left handed circularly polarised light propagate with different effective wavevectors, they progressively go in and out of phase, causing the retardance, which describes the difference in phase between these two fields, to oscillate. Of course, for thick scattering media, the mean field will have decayed, causing the prominence of the retardance peak due to the mean field to weaken, and fluctuations about the mean to increase. This leads to the broadening of the retardance distributions in Figure 6.12(b) for large thicknesses.

6.3 Performance analysis

As with all simulation techniques, the method presented in this chapter is limited in terms of computational efficiency, numerical accuracy and precision. To better assess these limitations, in this section we present a quantitative analysis of the performance of different aspects of the method and explain in more detail some of the choices that were made by contrasting them with alternatives. This analysis will allow us to identify more precisely the shortcomings and limiting elements of the method, as well as areas that require further research and optimisation in order to improve performance.

6.3.1 Symmetrisation method comparison

In Section 6.1.3, we introduced four different methods for symmetrising the randomly generated scattering matrices, which we referred to as SVD, β, γ, and Mix. This symmetrisation step was necessary primarily to enforce unitarity of the scattering matrix. As previously discussed, the SVD method is known to be 'best' in that it yields the matrix that is 'closest' to the unsymmetrised matrix in the sense previously described. Nevertheless, it is interesting to compare SVD with the other three methods to have a clearer understanding of their relative advantages and disadvantages. As we are unable to compare the different methods analytically, the analysis performed in this section was performed numerically using simulated data.

Table 6.3 shows data comparing the mean percentage difference of different blocks

Method	Matrix				
	$\bar{\mathbf{S}}$	$\bar{\mathbf{t}}$	$\bar{\mathbf{t}}'$	$\bar{\mathbf{r}}$	$\bar{\mathbf{r}}'$
β	3.981	0.331	0.336	131.250	5.261
γ	3.982	0.341	0.344	5.482	131.183
Mix	2.832	0.288	0.288	65.988	65.944
SVD	2.828	0.295	0.295	65.873	65.828

Table 6.3: Comparison of different scattering matrix symmetrisation methods. Methods are described in more detail in Section 6.1.3. Numbers in the table show the statistic $100\langle||\mathbf{A} - \mathbf{A}_0||/||\mathbf{A}_0||\rangle$, where $\mathbf{A}$ stands for any of the five matrices shown, averaged over 10^4 scattering matrix realisations. The $x = 1$ parameter set described in Section 6.2 was used.

of the unsymmetrised matrix $\bar{\mathbf{S}}_0$ with the symmetrised matrix $\bar{\mathbf{S}}$. Here we are only considering the case of a single, thin slab. Using the $x = 1$ parameter set for isotropic spheres, we generated 10^4 unsymmetrised matrices, which were then symmetrised using the four different methods. We then computed the quantity $100\langle||\mathbf{A} - \mathbf{A}_0||/||\mathbf{A}_0||\rangle$, where $\mathbf{A}$ stands in place of $\bar{\mathbf{S}}, \bar{\mathbf{t}}, \bar{\mathbf{t}}', \bar{\mathbf{r}}$ and $\bar{\mathbf{r}}'$, averaged over the set of matrices, which gives a measure of the percentage difference between the matrices before and after symmetrisation. Ideally, this quantity should be as small as possible, so that the symmetrisation process does not alter the elements of the scattering matrix too drastically, nor their associated statistics.

Observing the column of the table showing data for $\mathbf{A} = \bar{\mathbf{S}}$, it is clear that SVD is indeed optimal among the four methods. β and γ perform notably worse, although the difference between Mix and SVD is only on the order of 0.01%. Interestingly, Mix outperforms SVD when comparing the transmission matrices $\bar{\mathbf{t}}$ and $\bar{\mathbf{t}}'$, but fares worse with respect to the reflection matrices. The comparison of the reflection matrices before and after symmetrisation is most interesting. With respect to our statistics, both Mix and SVD alter the reflection matrices rather significantly compared to the transmission matrices, with errors on the order of 66%. γ performs by far the best with respect to $\bar{\mathbf{r}}$, with an error at around 5%, but does poorly with respect to $\bar{\mathbf{r}}'$, with an error of over 100%. The opposite situation is true for β with $\bar{\mathbf{r}}$ and $\bar{\mathbf{r}}'$ reversed. It is worth remembering by viewing the first order terms of Eqs. (6.12) and (6.13) that $\boldsymbol{\epsilon}_\beta$ and $\boldsymbol{\epsilon}_\gamma$ are closely related to $\bar{\mathbf{r}}$ and $\bar{\mathbf{r}}'$. Methods β and γ can thus be said to bias one of the reflection matrices, giving a relatively good symmetrised result at the expense of a poor one for the other reflection matrix.

To further examine how different components of the scattering matrix are affected by the different symmetrisation methods, we compared the elements of the scattering matrix before and after symmetrisation on a 2×2 block basis. Figure 6.14 shows scattering matrix diagrams where the colours at different positions show how β, γ and Mix each perform in comparison to SVD for the block at that position. More specifically, taking Figure 6.14(a) as an example, we computed the same statistic as before, averaged over 10^4 realisations, both for β and SVD. We then observed which of the two quantities was smaller. If the statistic computed from β was smaller than SVD, indicating that β performed better for the 2×2 block in question, then the

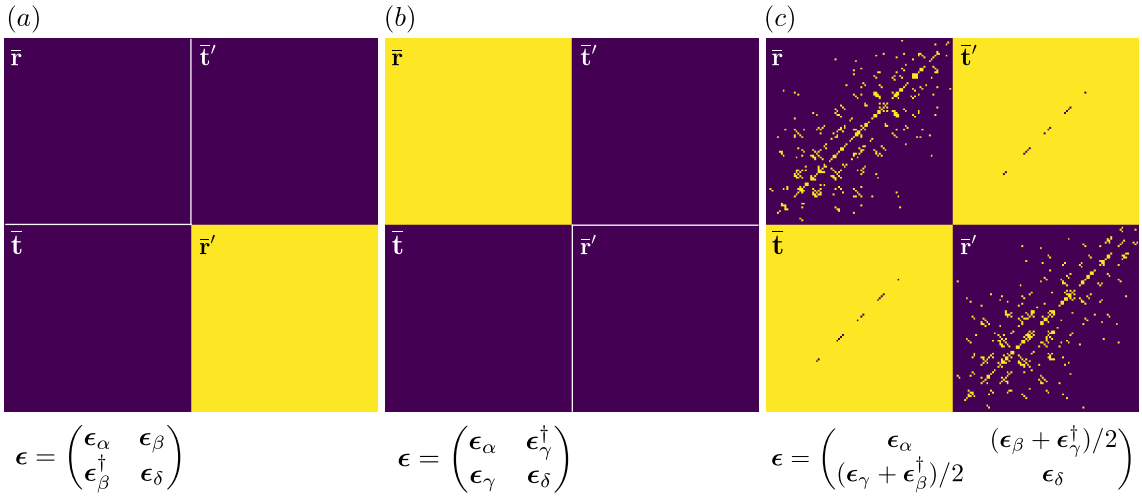

Figure 6.14: Comparisons of methods (a) β, (b) γ and (c) Mix against SVD. Yellow pixels denote 2×2 blocks of the scattering matrix for which the method outperforms SVD, whereas dark pixels denote blocks for which SVD performs better.

pixel in Figure 6.14(a) at the position of the block was coloured yellow. If, however, SVD performed better, then the pixel was coloured a dark purple. Yellow regions in Figure 6.14 therefore correspond to sections of the matrix for which SVD performed worse than the method being compared against. Figures 6.14(b) and (c) show the same information, but compare γ and Mix to SVD respectively.

Figures 6.14(a) and (b) show that β and γ perform better than SVD for the entirety of one of the reflection matrices, but perform worse for all other sections of the matrix. Figures 6.14(c), which compares Mix with SVD, shows that Mix generally performs better than SVD for the transmission matrices, except for some blocks on the anti-diagonals. For the reflection matrices, SVD performs better for a greater number of blocks, but Mix performs better for certain blocks lying on or close to the anti-diagonals. The symmetry of the patterns about the anti-diagonal are due to the reciprocity symmetry of the reflection matrices.

Figure 6.15 shows a scattering matrix diagram that compares the four different methods against each other, again for different 2×2 blocks of the scattering matrix. Unlike Figure 6.14, which compared SVD with the other three methods individually, in Figure 6.15, the same statistic as before is computed for each method and then compared between all four methods simultaneously. The method with the smallest percentage difference for a particular realisation was awarded a point. After all 10^4 realisation, points were tallied and compared for each block and the method that

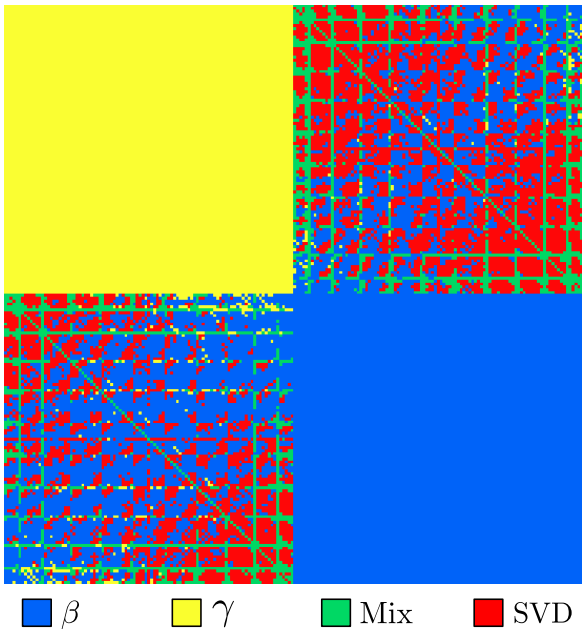

Figure 6.15: Comparison of the performance of different symmetrisation methods for different 2×2 blocks within the scattering matrix. Colours indicate the method that performed best using the metric described in the text.

accrued the greatest number of points was deemed best for that block. For each position within the scattering matrix, the pixel in Figure 6.15 corresponding to that position is coloured according to which method performed best, using the colour code indicated within the figure.

As before, β and γ are clearly dominant with respect to the elements of the reflection matrices. Within the transmission matrix, the situation is much more complicated. A few general observations are that Mix tends to performs best for diagonal blocks of the transmission matrices, as well as along certain lines within each matrix. We note that the existence of such lines is partially an artefact of the way in which the modes are ordered. In k-space, modes are distributed on a Cartesian grid within the circle of radius k, but are ordered numerically in a raster scan pattern. Therefore, there are numerous large jumps between the positions of sequentially numbered modes, which occur at the positions of the green lines in Figure 6.15. It is interesting to note that, although SVD performs best for the scattering matrix overall, it did not perform best for the greatest number of 2×2 blocks within the scattering matrix. This is a statistical effect that is akin to vote splitting in elections. For blocks where SVD did perform best, it tended

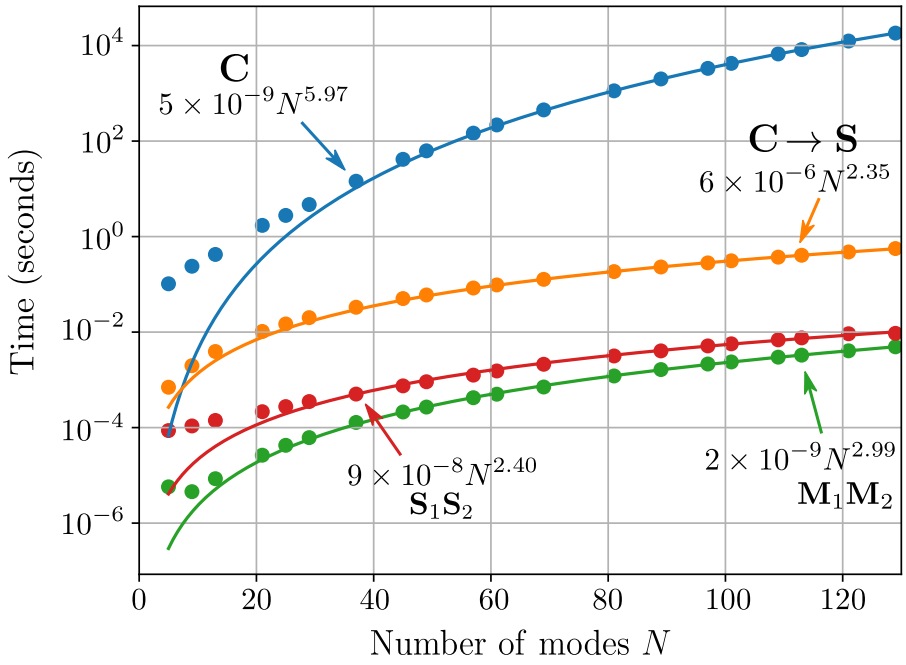

Figure 6.16: Computation time t in seconds against number of modes N for various steps in the simulations. Blue data points describe the time to set up the covariance matrix, orange data points describe the time to generate realisations of random scattering matrices, green data points describe the time to cascade transfer matrices, and red data points describe the time to cascade scattering matrices.

to outperform the other methods by a relatively large margin, enabling SVD to perform best for the scattering matrix overall, despite not amassing the greatest number of individual victories among different blocks. As a final comment, we note that although β clearly outperforms γ for our data, observing the numerical data for a selection of blocks revealed that the difference between the two methods was relatively small, and a repetition of our simulation with more realisations may show γ performing better for a larger number of blocks.

6.3.2 Computation speed

Among all of the steps performed in our algorithm, we identified three that require a significant amount of computation time. These are attaining the Cholesky decomposition $\mathbf{C}$ (described in Section 6.1.2), generating instances of random scattering matrices, and cascading matrices, either by matrix products for transfer matrices, or using the previously discussed formulae for scattering matrices. We timed each of these steps experimentally, making one measurement for acquiring the Cholesky

decomposition, and averaging over 10^4 repetitions for the other steps. Figure 6.16 shows a summary of how the computation time of each of these processes scales with the number of modes, represented here using the symbol N. Within Figure 6.16, blue data points show the time taken for setting up the covariance matrix, orange points show the time taken to generate random scattering matrices, green points show the time taken to multiply two transfer matrices, and red points show the time taken to cascade two scattering matrices. All curves are numerical fits of the form $t = aN^b$, where t is the computation time in seconds and a and b are fitting parameters. It is worth noting that the value of a includes overhead time and may vary on different computers. The exponent b, on the other hand, is related to the complexity of the underlying algorithm and, in principle, is system independent.

The blue data points in Figure 6.16 describe the time required to calculate all of the statistics described in Section 6.1.2 and, ultimately, to obtain $\mathbf{C}$. Ignoring leading coefficients, a scattering matrix with N nodes contains N^2 elements. Since, in principle, all of these elements may be correlated, the associated covariance and pseudo covariance matrices $\mathbf{\Sigma}_R$ and $\mathbf{\Sigma}_P$ are of size $N^2 \times N^2$ and thus contains N^4 elements. The naive approach to setting up these matrices to loop through all N^4 elements, check whether or not the memory effect conditions are satisfied for each element and, if so, compute the correlation and insert its value into the matrix. Naturally, for a large number of modes, this takes a lot of time and scales poorly with N. Once these matrices have been constructed, computing $\mathbf{C}$ from $\mathbf{\Sigma}$ can be done very quickly using standard numerical library functions. In theory, there is a lot of room for optimisation in setting up $\mathbf{\Sigma}$, particularly as $\mathbf{\Sigma}$ is sparse. The number of computational steps can be heavily reduced by first identifying minimal sets of scattering matrix elements that are mutually correlated, rather than checking all possible pairs of elements of $\bar{\mathbf{S}}$. Using techniques of this kind, we were able to reduce the time for this process to $5 \times 10^{-9} N^{5.97}$ seconds. Because of the relatively large power of N, this step represents the greatest bottleneck for large numbers of modes. With our current implementation, for $N = 101$, computing $\mathbf{C}$ takes around an hour. This time increases to ~ 80 hours for $N = 201$ and thus quickly becomes impractical. Once $\mathbf{C}$ has been computed, however, it can be saved and reused for multiple simulations, provided that the physical parameters of the simulation do not

need to be changed.

Comparing the red and green data points and curves, it is clear that cascading transfer matrices is faster than scattering matrices. Interestingly, we see that cascading scattering matrices ($N^{2.4}$) scales better than transfer matrices ($N^{2.99}$) for large N, but is slower than cascading transfer matrices for the number of modes presented due to the relatively large leading coefficient. The difference in scaling may be explained by the fact that, as can be seen in Eq. (6.23), cascading scattering matrices involves a series of operations on the transmission and reflection blocks, each of which are half the size of the scattering matrix. Using the formulae presented, we expect the scattering matrix cascade to outperform the transfer matrix cascade for $N \sim 635$, which is, at present, practically unrealisable due to the large associated time required to compute $\mathbf{C}$.

6.3.3 Convergence

Our method is a Monte Carlo method and requires the computation of a large number of samples in order to approximate average quantities with high precision. Suppose that X is some random variable with true mean μ and variance σ^2. Given N_d samples of X, namely X_i for $1 \leq i \leq N_d$, the sample mean $\langle X \rangle = (X_1 + \ldots + X_{N_d})/N_d$ converges to a Gaussian random variable for large N_d by the central limit theorem. In particular, it can be shown that for for large N_d we have [303]

$$\langle X \rangle_{N_d \to \infty} \to \mu + \frac{\sigma}{\sqrt{N_d}}. \tag{6.45}$$

The difference between the true mean and the sample mean therefore scales as $\sim 1/\sqrt{N_d}$, which is a relatively slowly decaying function of N_d. Because of this, a large number of samples is generally required to attain high numerical precision, which, naturally, comes at the expense of additional computation time and computer memory requirements. Of course, the value of σ also plays an important role in the rate of convergence of the sample mean to the true mean. If a particular precision threshold has been decided upon, then a smaller value of σ will allow one to surpass the threshold with fewer samples.

Figure 6.17 shows how the values of certain statistics computed from our simula-

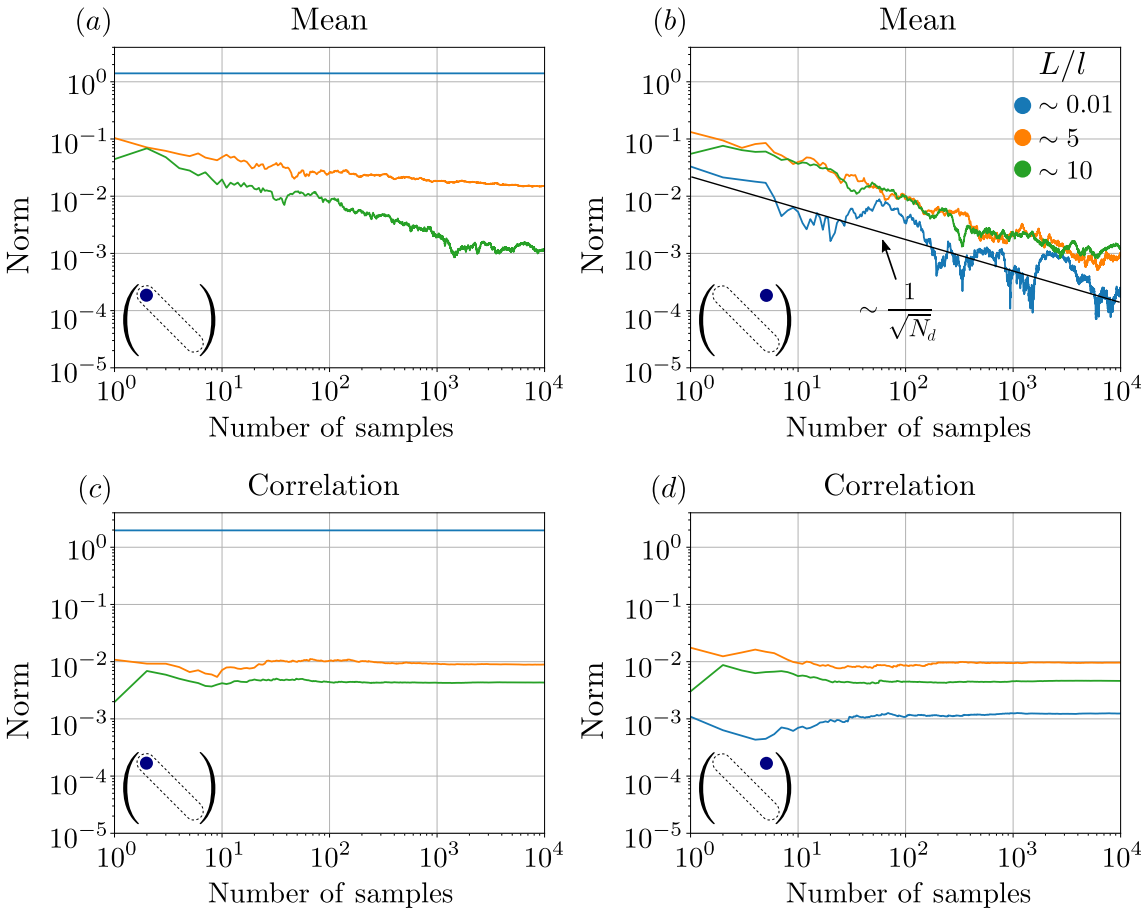

Figure 6.17: Matrix norm against number of samples of mean ((a)) and ((b)) or correlation ((c)) and ((d)) matrix associated with different blocks of the scattering matrix. Figures (a) and (c) show results for blocks lying on the diagonal of the transmission matrix, whereas figures (b) and (d) show results for off-diagonal blocks. Colours show results for different scattering medium thicknesses as indicated.

tion data vary with the number of samples used in their computation. Figure 6.17(a) shows the norm of the mean value of a 2×2 block taken from the diagonal of the transmission matrix, where the mean is computed using different numbers of samples up to 10^4. For these data, the parameter set for isotropic spheres with $x = 1$ was used. The norm was used to reduce the statistics of a 2×2 matrix of complex numbers to a single real number. The blue curve shows results computed for a thin medium with thickness $L/l \sim 0.01$. In this regime, fluctuations about the mean are small and the data quickly converges to the true mean. For larger thicknesses, however, depicted by the orange ($L/l \sim 5$) and green ($L/l \sim 10$) curves, the data shows large fluctuations for small numbers of samples, and a large number of samples N_d are required before the data begins to stabilise. The green curve, for example, only

stabilises for $N_d > 10^3$. Since the mean decays with thickness, an increasing number of samples are required to approximate the true mean at larger thicknesses as, for fixed N_d, the error $\sigma/\sqrt{N_d}$ becomes larger relative to μ as μ decreases.

Figure 6.17(b) shows similar data, but for a block of the transmission matrix lying away from the diagonal. For such blocks, the mean is known to be exactly zero. In this case, since $\mu = 0$, the data describe purely the previously discussed error term, and we do not expect the norm to stabilise at a non-zero value. The scaling of the norm with N_d is thus clearer, and the black line displayed on top of the data, which is of the form $a/\sqrt{N_d}$ for an arbitrarily chosen a, demonstrates the scaling law. Figures 6.17(c) and (d) again show similar data, but computed from the norm of the 4×4 correlation matrix associated with the same 2×2 blocks. In contrast to the means, these correlations do not decay as quickly with thickness, and the norms thus stabilise for relatively few samples, even at large thicknesses.

6.3.4 Cubature schemes and numerical accuracy

In our simulations, a Cartesian cubature scheme was employed because of its theoretical simplicity. In principle, more general cubature schemes offer the possibility of producing more accurate numerical data, as non-Cartesian schemes may yield discrete angular spectra that better approximate the full continuous angular spectra. Moving towards general cubature schemes, however, poses numerous, as of yet unresolved, theoretical complications, which we shall briefly outline in this section.

Consider again Eq. (6.3), which contains the factor w. Suppose instead that an arbitrary cubature scheme were used, consisting of a collection of different weights. Referring back to the normalisation introduced in Eq. (3.115), the corresponding factor that would appear in Eq. (6.3) for a more general scheme would be given by

$$f = \frac{\sqrt{w_i w_j w_u w_v}}{\delta_w}, \tag{6.46}$$

where δ_w is the factor that is introduced when discretising the Dirac delta functions that appear in the continuous equations. For the Cartesian scheme used in this chapter, for which $w_i = w_j = w_u = w_v = w$, we took $\delta_w = w$. In this case Eq. (6.46) reduces to simply $f = w$. In the absence of a careful theoretical investigation, it is

not immediately obvious what the form of δ_w should be in the most general case and naive choices can lead to theoretical inconsistencies.

Consider, for example, the special case $i = u$ and $j = v$. In this case the statistics appearing in Eq. (6.3) are correlations between elements lying within the same 2×2 block of the transmission matrix and the factor f reduces to $f = w_i w_j/\delta_w$. Consider now summing the expression on the right hand side of Eq. (6.3) over the index j, i.e. the scattered wavevector. If we also sum the corresponding reflection matrix correlations and add the results together, intuitively, since we are effectively summing the intensities of the scattered field over all scattering directions, we should expect to obtain an expression describing the power removed from the incident field due to scattering. Performing the calculation, and also summing over the scattered polarisation basis states b, we obtain

$$\frac{w_i}{\delta_w}\frac{n\Delta L}{k\gamma_i}\sum_{j=-N}^{N}\left(\sum_{b\in\{\theta,\phi\}}\left[\langle|A^t_{(j,i)ba}|^2\rangle+\langle|A^r_{(j,i)ba}|^2\rangle\right]\right)\frac{w_j}{k\gamma_j}. \tag{6.47}$$

In the case of a Cartesian scheme, the term on the far right $w_j/(kk_j)$ would reduce to $\Delta k_x\Delta k_y/(kk_j)$. The sum in Eq. (6.47) could then be written as

$$\begin{aligned}
&\sum_{j=-N}^{N}\left(\sum_{b\in\{\theta,\phi\}}\left[\langle|A^t_{(j,i)ba}|^2\rangle+\langle|A^r_{(j,i)ba}|^2\rangle\right]\right)\frac{\Delta k_x\Delta k_y}{k\gamma_j},\\
&\approx\int_{\Gamma_p}\sum_{b\in\{\theta,\phi\}}\left[\langle|A^t_{(j,i)ba}|^2\rangle+\langle|A^r_{(j,i)ba}|^2\rangle\right]\frac{\mathrm{d}\boldsymbol{\kappa}_j}{k\gamma_j},\\
&=\int_{S}\sum_{b\in\{\theta,\phi\}}\left[\langle|A^t_{(j,i)ba}|^2\rangle+\langle|A^r_{(j,i)ba}|^2\rangle\right]\sin\theta\mathrm{d}\theta\mathrm{d}\phi=k^2\sigma,
\end{aligned} \tag{6.48}$$

where the final integral is over the sphere S describing scattered wavevectors with polar coordinates θ and ϕ. In changing coordinates we have used the Jacobian given in Eq. (5.109). The final line follows from the definition of the cross section. Using the result of Eq. (6.48), Eq. (6.47) reduces to $(w_i/\delta_w)\Delta L/l\sec\theta_i$. Comparing this result to Eq. (5.46), this expression is, to first scattering order, equal to the power eliminated from the incident field, provided that $w_i = \delta_w$.

With the above discussion in mind, one may expect δ_w to take a general form such

as $\delta_w = \sqrt{w_i w_u}$, so as to cancel the weights associated with the incident modes. Since this expression does not include weights associated with outgoing modes, however, it leads to inconsistencies when one considers reciprocity. Consider the correlation $\langle \bar{r}_{(j,i)\theta\theta} \bar{r}_{(v,u)\theta\theta} \rangle$, whose formula also contains the factor $f = \sqrt{w_i w_j w_u w_v}/\delta_w$. Using the postulated expression for δ_w reduces this factor to $f = \sqrt{w_j w_v}$. Consider now the reciprocal correlation $\langle \bar{r}_{(-i,-j)\theta\theta} \bar{r}_{(-u,-v)\theta\theta} \rangle$. By reciprocity, we have $\bar{r}_{(j,i)\theta\theta} = \bar{r}_{(-i,-j)\theta\theta}$ and $\bar{r}_{(v,u)\theta\theta} = \bar{r}_{(-u,-v)\theta\theta}$, and so the two correlations must be equal. Using the formula for δ_w, however, the factor f appearing in the correlation $\langle \bar{r}_{(-i,-j)\theta\theta} \bar{r}_{(-u,-v)\theta\theta} \rangle$ is given by $f = \sqrt{w_{-i} w_{-u}}$. If our cubature scheme is symmetric about the origin of k-space so that in general $w_{-i} = w_i$, this is equal to $f = \sqrt{w_i w_u}$. Since i, j, u and v are arbitrary, however, there is no necessary connection between $\sqrt{w_j w_v}$ and $\sqrt{w_i w_u}$, and thus the two correlations are not guaranteed to be equal, violating reciprocity.

The essence of the problem lies in deciding how best to approximate a delta function within a numerical cubature scheme. Since a delta function is not a bonafide mathematical function in the usual sense, this question is non-trivial. For one dimensional integrals, the problem is relatively simple and we can appeal to the sifting property of the delta function. Given the identity

$$\int f(x)\delta(x - x_j)\mathrm{d}x = f(x_j), \tag{6.49}$$

and the cubature scheme

$$\int g(x)\mathrm{d}x \approx \sum_i f(x_i) w_i, \tag{6.50}$$

a natural way to discretise $\delta(x - x_j)$ that has been used previously in this thesis is to use the normalised Kronecker delta δ_{ij}/w_i so that Eq. (6.49) is preserved, since

$$\int f(x)\delta(x - x_j)\mathrm{d}x \approx \sum_i f(x_i) \frac{\delta_{ij}}{w_i} w_i = f(x_j). \tag{6.51}$$

The situation becomes less clear however in higher dimensions. Consider, for

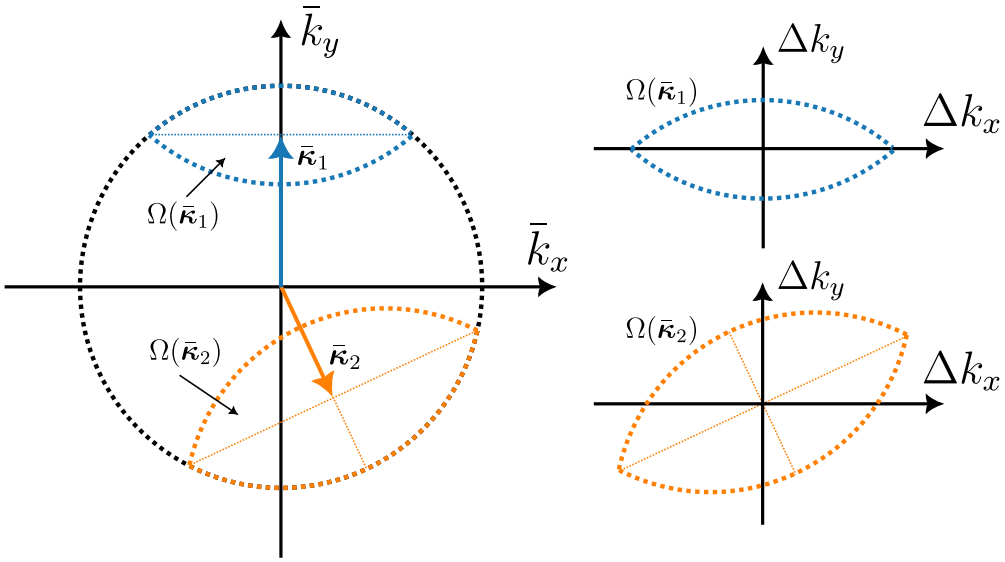

Figure 6.18: Examples of integration regions for $\Delta\boldsymbol{\kappa}$ for different values of $\mathrm{d}\bar{\boldsymbol{\kappa}}$ in the integral in Eq. (6.55).

example

$$\int_{\Gamma_p}\int_{\Gamma_p} f(\boldsymbol{\kappa}_i,\boldsymbol{\kappa}_j)\delta(\boldsymbol{\kappa}_i-\boldsymbol{\kappa}_j)\mathrm{d}\boldsymbol{\kappa}_i\mathrm{d}\boldsymbol{\kappa}_j. \tag{6.52}$$

Note that integrals of this type appear in computing scattered field correlations, such as in Eq. (5.50). By making the change of coordinates

$$\Delta\boldsymbol{\kappa} = \boldsymbol{\kappa}_i - \boldsymbol{\kappa}_j, \tag{6.53}$$

$$\bar{\boldsymbol{\kappa}} = \frac{\boldsymbol{\kappa}_i + \boldsymbol{\kappa}_j}{2}, \tag{6.54}$$

Eq. (6.52) becomes

$$\int_{\Gamma_p}\left(\int_{\Omega(\bar{\boldsymbol{\kappa}})} f(\bar{\boldsymbol{\kappa}},\Delta\boldsymbol{\kappa})\delta(\Delta\boldsymbol{\kappa})\mathrm{d}\Delta\boldsymbol{\kappa}\right)\mathrm{d}\bar{\boldsymbol{\kappa}}. \tag{6.55}$$

Although the delta function appearing in Eq. (6.55) is independent of $\bar{\boldsymbol{\kappa}}$, the domain of integration for $\Delta\boldsymbol{\kappa}$ is no longer a circle in k-space, but instead a more complex region composed of two circular sections that depends on the value of $\bar{\boldsymbol{\kappa}}$. An example of this integration domain is shown in Figure 6.18. We note that when these domains are are considered as regions of $\Delta\boldsymbol{\kappa}$ space, they have an area 4 times that of the

corresponding regions shown in $\bar{\boldsymbol{\kappa}}$ space.

Suppose now that some cubature scheme has been chosen for the circle in k-space. We can imagine that Eq. (6.55) will admit some corresponding cubature scheme with weights given by w_Δ and w_m, which are to be used in approximating the integrals over $\Delta\boldsymbol{\kappa}$ and $\bar{\boldsymbol{\kappa}}$ respectively. Given the preceding discussion, it is natural to suppose that the delta function in Eq. (6.55) may be discretised to a Kronecker delta normalised by the weight w_Δ. Given that the transformation described by Eqs. (6.53) and (6.54) have unit Jacobian determinant, we also have that the weights should satisfy

$$w_i w_j = w_\Delta w_m, \tag{6.56}$$

where w_i and w_j are the weights associated with the cubature scheme over the circle that may be used to discretise Eq. (6.56). Eq. (6.56), however, does not uniquely determine the form of w_Δ in terms of w_i and w_j, and it remains an open question what the form of w_Δ is or should be so as to resolve the previous problems and potentially improve the numerical accuracy of our integral approximations.

To conclude this section, and to better motivate the desire for moving beyond a Cartesian cubature scheme, we present in more detail some issues inherent with the Cartesian method and how the mode spacing affects the numerical accuracy of our simulations.

In order to assess the accuracy of the Cartesian method, we computed the optical cross section of isotropic spheres of different sizes by numerically integrating the square moduli of the elements of the $\mathbf{A}$ matrices computed from Mie theory using cubature schemes with different mode spacings. More specifically, in a similar vein to Eq. (6.48), the cross section was calculated for isotropic spheres of sizes $x = 1, 2$ and 4 by

$$\sigma \approx \frac{1}{k^2} \sum_{j=-N}^{N} \left(\sum_{b\in\{\theta,\phi\}} \left[\langle |A^t_{(j,i)ba}|^2 \rangle + \langle |A^r_{(j,i)ba}|^2 \rangle \right] \right) \frac{\Delta k_x \Delta k_y}{k\gamma_j} \tag{6.57}$$

for different spacings $\Delta k_x = \Delta k_y = \Delta k$ in the range $0.15 < \Delta k < 0.2$. It is important to note that the value of the computed cross section will depend on

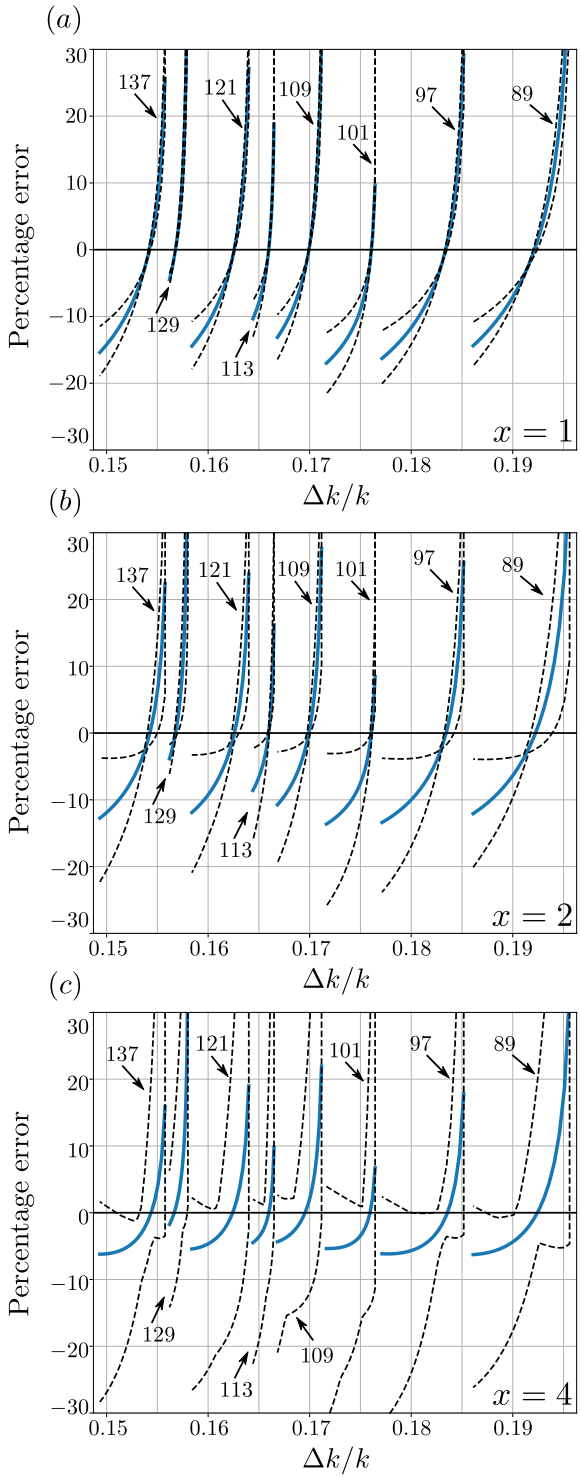

Figure 6.19: Percentage error between theoretical cross section and cross sections computed approximately using a Cartesian cubature scheme for different grid spacings Δk. Blue lines show the mean error averaged over different incident modes and dashed lines show the maximum and minimum errors. Different figures show data for different particle sizes as indicated.

the choice of incident mode. Although in the continuous case this is not true by symmetry, for a finite, discrete grid of modes, each different choice of incident mode will effectively see a different set of scattering angles, and there will therefore be a different set of values for the $\mathbf{A}$ matrices appearing in Eq. (6.57).

Figure 6.19 shows the percentage error between the cross section as calculated by Eq. (6.57) and the true value computed from Mie theory. The blue lines show the mean error averaged over all incident modes and the dashed lines above and below the blue curves show the maximum and minimum errors across all incident modes respectively, thus delineating the range of errors. As is clear from the figure, there are discontinuities in the curves, as once Δk passes certain threshold values, the number of modes in the Cartesian grid within the circle in k-space increases. The number of modes associated with each branch of the figure is indicated. What is clear from the graph is that the error is very sensitive to the choice of spacing. Once a new number of modes has been reached, new modes will lie very close to the circular boundary in k-space. For these modes, the $1/\gamma_j$ factor appearing in Eq. (6.57) will be very large, resulting in spuriously large errors. As can be seen, however, for a fixed number of modes, there is typically some spacing for which the mean error is zero. It is however difficult to determine what spacing values achieve this condition without computing data in the manner presented here.

It is also interesting to note that the error is strongly dependent on the particle size parameter. In particular, the error tends to increase as the size parameter increases. This can be understood by considering scattering anisotropy. Roughly speaking, since a Cartesian scheme weighs each point in k-space equally, it is more ideally suited for smaller particles that scatter more isotropically. For larger particles, which preferentially scatter close to the incident field direction, it would be better in principle to use a cubature scheme that samples more finely modes close to the incident direction. Of course, since in the scattering matrix all possible incident modes must be considered, it is not clear that one may have a single cubature scheme that is simultaneously optimised for every possible incident mode.

While the data in Figure 6.19 are interesting, they are not entirely relevant to the data produced from our simulations, as the statistics of the elements of the scattering matrix are also altered by the symmetrisation process. Figure 6.20 shows the error

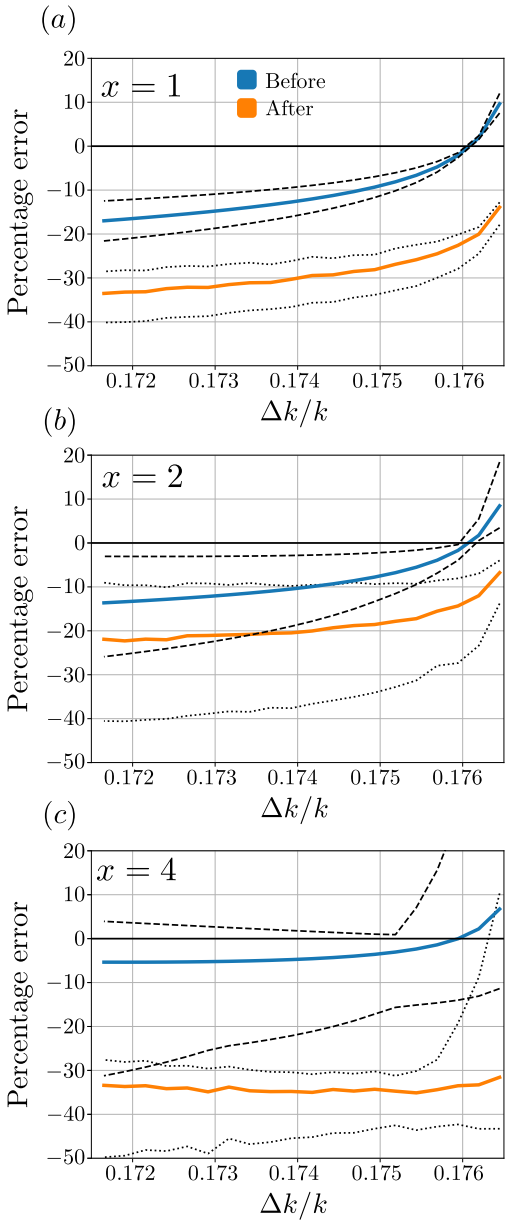

Figure 6.20: Percentage error between theoretical cross section and cross sections computed (blue) as in Figure 6.19 and (orange) averaging over 10^4 realisations of symmetrised scattering matrices using. Dashed lines show the maximum and minimum errors and different figures show data for different particle sizes as indicated.

between the theoretical cross section and that calculated from symmetrised scattering matrices produced from the simulations for thin slabs. The cross section can be computed in two different ways: either by subtracting the zero order scattering matrix (describing the incident field) and summing over columns in a similar manner to Eq. (6.48), or, in light of the optical theorem, by considering the real part of the

elements on the diagonal of the transmission matrix. Figure 6.20 specifically shows a restricted range of Δk values: specifically those for which the number of modes is 101. The blue curve is identical to that in Figure 6.19, whereas the orange curve is computed from the symmetrised scattering matrices. Data for the orange curve was averaged over 10^4 scattering matrix realisations. We note that it is difficult to generate data for a large number of mode spacings as for large numbers of modes it takes a long time to set up the covariance matrices, as discussed previously. As was the case in Figure 6.19, solid curves show the percentage error averaged over all incident modes, whereas the dashed curves show the range of errors over all different incident modes.

The most obvious feature of Figure 6.20 is that the percentage error computed after symmetrisation is notably larger in magnitude than that computed before, which, at present, we are unable to explain. What is particularly notable is that after symmetrisation, there is no choice of Δk for which the mean percentage error is exactly zero. As with Figure 6.19, the magnitude of the error varies with size parameter x. Interestingly, the mean error is generally smallest for size parameter $x = 2$, which may explain why the intensity decay in the forward direction, as presented in Figure 6.6, more closely matches the Beer-Lambert law for $x = 2$ than $x = 1$.

6.4 Conclusion

To conclude, we have presented a method for randomly generating scattering matrices for sparse, complex media that incorporates the polarisation properties of light, scattering anisotropy and the physical constraints of unitarity and reciprocity. Furthermore, we are able to model random media in the multiple scattering regime using a matrix cascade, only requiring knowledge of the single scattering properties of the particles contained within the medium.

We have validated our model by reproducing known behaviour for systems consisting of randomly distributed spherical particles, such as the dependence of the rate of depolarisation on the incident polarisation state. We have also shown that some of the polarisation statistics of our scattering matrices in the large thickness

limit can be related to those of random Gaussian matrices and diagonal blocks of matrices drawn from the circular orthogonal ensemble. We have demonstrated the flexibility of our approach by considering the example of a medium containing chiral particles, for which we found that the polarisation properties of the scattered field depend on the helicity of the incident polarisation state. We were able to analyse the more intricate details of the rate of decay of degree of polarisation by considering the evolution of scattered polarisation state distributions on the Poincaré sphere, which is easily done in our framework given that we have access to the entire scattering matrix. In addition to the data presented here, other possible studies include analyzing the polarisation properties of the transmission eigenchannels and the polarisation properties of correlations between different matrix blocks, such as, for example, the memory effect. We reserve these topics for future studies.

We have also benchmarked out approach by analysing its computational efficiency, numerical accuracy and precision. The biggest limitation of our model is the currently achievable angular resolution of the scattered field, as this directly influences the size of the scattering matrix, which, when large, requires a lot of memory and computation time when a large number of samples is required for the study of statistical quantities. The largest bottleneck currently is the time required to set up the covariance matrix, although this step may be amenable to further algorithmic optimisation. Despite this, generation of individual scattering matrices is very fast, taking only seconds or minutes, depending on the medium thickness and number of modes. We therefore envisage that our method will serve as a complement to the already existing Monte Carlo techniques and may prove advantageous in certain applications, particularly where correlations between different matrix elements are of interest.

Chapter 7

Polarisation recovery

With the presentation of our random matrix framework complete, we now turn briefly to consider some of its applications. In particular, in this chapter we commence a theoretical study of the extent to which polarimetric information is preserved upon transport through a random medium. Without further clarification, this is a broad, vague problem that may be studied in a multitude of ways. For concreteness, we shall consider in this chapter the toy problem of attempting to recover an unknown field incident upon a scattering medium, given some measurements of the transmitted field. To achieve this, we will make use of the polarisation properties of the memory effect, which has featured in previous chapters as a correlation between certain blocks of the transmission matrix, e.g. as in Eq. (5.56).

The memory effect has received widespread attention in the literature, originally as a theoretical curiosity [274], and later as the basis of methods for imaging objects hidden behind random media [304, 305, 306]. In a typical imaging experiment, a target object is hidden behind or within a scattering medium and an experimenter only has access to light that has interacted with the object and subsequently passed through part of the scattering medium. Under rather general conditions, it can be shown that the angular intensity autocorrelation function of the light transmitted through the scattering medium is, save for global scaling factors, equal to that of light that has only interacted with the object. Therefore, by measuring random speckle correlations in the transmitted light, one can estimate the intensity correla-

tion function of the light that has interacted with the hidden object, from which an image of the object can then be recovered using phase retrieval methods [307].

Virtually all studies and applications of the memory effect, to our knowledge, assume scalar fields and relatively little work has been done on its polarisation properties [308]. A generalised, vectorial memory effect, however, may enable the recovery of the polarimetric information of a hidden object, such as the full set of Stokes parameters associated with the light scattered by the object, rather than just the intensity. In this chapter we work towards realising this goal by establishing a theoretical framework for exploring the preservation of polarisation correlations through random media and discussing a possible polarisation reconstruction algorithm. Although the findings in this chapter are preliminary, we hope that our work may motivate, or form the basis of, a more in-depth, future study.

7.1 Introduction

We shall begin by setting up the problem more rigorously and outlining the notation that will be used. We will then describe the genesis of an algorithm for reconstructing a hidden object using transmitted field measurements. This will be followed by some numerical results that show the process in action, as well as its current limitations and challenges.

Suppose that a field $\mathbf{E}_i$, where

$$\mathbf{E}_i = \int \mathbf{a}(\boldsymbol{\kappa}) e^{i[(\boldsymbol{\kappa}\cdot\boldsymbol{\rho})+\gamma z]} \mathrm{d}\boldsymbol{\kappa}, \tag{7.1}$$

is incident upon the left side of a random medium. In this chapter we only consider propagating waves and the domain of all integrals, unless stated otherwise, will be assumed to be Γ_p. The transmitted field on the right side of the medium $\mathbf{E}_t$, where

$$\mathbf{E}_t = \int \mathbf{b}(\boldsymbol{\kappa}) e^{i[(\boldsymbol{\kappa}\cdot\boldsymbol{\rho})+\gamma z]} \mathrm{d}\boldsymbol{\kappa}, \tag{7.2}$$

is related to the incident field via the transmission matrix, since

$$\mathbf{b}(\boldsymbol{\kappa}) = \int \bar{\mathbf{t}}(\boldsymbol{\kappa}, \boldsymbol{\kappa}') \mathbf{a}(\boldsymbol{\kappa}') \mathrm{d}\boldsymbol{\kappa}'. \tag{7.3}$$

We suppose that an observer is situated on the right side of the medium so that only the transmitted field and its spectral components $\mathbf{b}(\boldsymbol{\kappa})$ are measurable quantities. The exact form of the incident field and the transmission matrix will be assumed to be unknown. A natural problem to consider is to what degree the incident field, or its spectral components $\mathbf{a}(\boldsymbol{\kappa})$, can be recovered from measurements of the transmitted field. In reality, $\mathbf{a}$ may represent the light scattered by a hidden object of interest, or a message that is to be passed through a scattering medium. For simplicity, we shall thus refer to $\mathbf{a}$ as the 'object' field and $\mathbf{b}$ as the 'image' field.

Since nothing is known about particular realisations of the transmission matrix, statistical averages are necessary. Consider, for example, taking ensemble averages of Eq. (7.3). We assume that $\mathbf{a}$ has a fixed functional form and is therefore constant with respect to averaging. In the case of a monodisperse scattering medium, using the expression in Eq. (5.44) for the mean transmission matrix yields

$$\langle \mathbf{b}(\boldsymbol{\kappa}) \rangle = \exp\left(\frac{2\pi n L}{k\gamma_i}\mathbf{A}(\boldsymbol{\kappa},\boldsymbol{\kappa})\right)\mathbf{a}(\boldsymbol{\kappa}), \tag{7.4}$$

which can be inverted to solve for $\mathbf{a}(\boldsymbol{\kappa})$. Therefore, if the exponential term in Eq. (7.4) is known, the object field is recoverable from $\langle \mathbf{b}(\boldsymbol{\kappa}) \rangle$. Assuming ergodicity, the ensemble average required to measure $\langle \mathbf{b}(\boldsymbol{\kappa}) \rangle$ in practice may be most simply achieved by temporally averaging the field transmitted through a dynamic random medium.

Recovering an object using Eq. (7.4) poses several practical difficulties. For large thicknesses, the modulus of $\langle \mathbf{b}(\boldsymbol{\kappa}) \rangle$ will be very small and the required measurements may therefore have poor signal to noise ratio. In addition, measurements of the complex field components of $\mathbf{b}$ requires a potentially complicated interferometric experimental setup that is able to measure both the phase and polarisation state of different plane wave components of the scattered field. Finally, this method does not readily generalise to partially polarised or partially coherent fields, which cannot be described by fixed, complex field vectors. These problems can be largely resolved however, by instead considering second order correlation functions of the field components.

Using spherical polar coordinates, the object and image vectors can be decom-

posed as

$$\begin{aligned}\mathbf{a}(\boldsymbol{\kappa}) &= a_\theta(\boldsymbol{\kappa})\hat{\mathbf{e}}_\theta(\boldsymbol{\kappa}) + a_\phi(\boldsymbol{\kappa})\hat{\mathbf{e}}_\phi(\boldsymbol{\kappa}),\\ \mathbf{b}(\boldsymbol{\kappa}) &= b_\theta(\boldsymbol{\kappa})\hat{\mathbf{e}}_\theta(\boldsymbol{\kappa}) + b_\phi(\boldsymbol{\kappa})\hat{\mathbf{e}}_\phi(\boldsymbol{\kappa}).\end{aligned} \tag{7.5}$$

We define the correlation functions

$$\begin{aligned}\mathcal{H}^O_{\alpha\beta}(\boldsymbol{\kappa}_i, \boldsymbol{\kappa}_p) &= a_\alpha(\boldsymbol{\kappa}_i)a^*_\beta(\boldsymbol{\kappa}_p),\\ \mathcal{H}^I_{\gamma\delta}(\boldsymbol{\kappa}_j, \boldsymbol{\kappa}_q) &= \langle b_\gamma(\boldsymbol{\kappa}_j)b^*_\delta(\boldsymbol{\kappa}_q)\rangle,\end{aligned} \tag{7.6}$$

where the subscripts α, β, γ and δ stand in place of either θ or ϕ, and the superscripts correspond to 'object' and 'image' as previously described. As before, since $\mathbf{a}$ is assumed to be non-random, no averaging is necessary for the object correlation function. $\mathcal{H}^O$ can be thought of as containing information about the relative amplitudes and phases of the different plane wave components contained within the object field. Using Eqs. (7.2) and (7.3), $\mathcal{H}^O$ and $\mathcal{H}^I$ can be shown to be related by

$$\begin{aligned}\mathcal{H}^I_{\gamma\delta}(\boldsymbol{\kappa}_j, \boldsymbol{\kappa}_q) =& \langle b_\gamma(\boldsymbol{\kappa}_j)b^*_\delta(\boldsymbol{\kappa}_q)\rangle\\ =& \left\langle \int \sum_{\alpha\in\{\theta,\phi\}} \bar{t}_{\gamma\alpha}(\boldsymbol{\kappa}_j, \boldsymbol{\kappa}_i)a_\alpha(\boldsymbol{\kappa}_i)\mathrm{d}\boldsymbol{\kappa}_i \left(\int \sum_{\beta\in\{\theta,\phi\}} \bar{t}_{\delta\beta}(\boldsymbol{\kappa}_j, \boldsymbol{\kappa}_p)a_\beta(\boldsymbol{\kappa}_p)\mathrm{d}\boldsymbol{\kappa}_p \right)^* \right\rangle\\ =& \sum_{\alpha,\beta\in\{\theta,\phi\}} \int\int \langle \bar{t}_{\gamma\alpha}(\boldsymbol{\kappa}_j, \boldsymbol{\kappa}_i)\bar{t}^*_{\delta\beta}(\boldsymbol{\kappa}_q, \boldsymbol{\kappa}_p)\rangle \mathcal{H}^O_{\alpha\beta}(\boldsymbol{\kappa}_i, \boldsymbol{\kappa}_p)\mathrm{d}\boldsymbol{\kappa}_i\mathrm{d}\boldsymbol{\kappa}_p.\end{aligned} \tag{7.7}$$

Moving forward, it will be convenient to rewrite Eq. (7.7) as a matrix equation. Let

$$\mathcal{H}^I(\boldsymbol{\kappa}_j, \boldsymbol{\kappa}_q) = [\mathcal{H}^I_{\theta\theta}(\boldsymbol{\kappa}_j, \boldsymbol{\kappa}_q), \mathcal{H}^I_{\theta\phi}(\boldsymbol{\kappa}_j, \boldsymbol{\kappa}_q), \mathcal{H}^I_{\phi\theta}(\boldsymbol{\kappa}_j, \boldsymbol{\kappa}_q), \mathcal{H}^I_{\phi\phi}(\boldsymbol{\kappa}_j, \boldsymbol{\kappa}_q)]^{\mathrm{T}} \tag{7.8}$$

and let $\mathcal{H}^O(\boldsymbol{\kappa}_i, \boldsymbol{\kappa}_p)$ be defined analogously. Eq. (7.7) can then be written as

$$\mathcal{H}^I(\boldsymbol{\kappa}_j, \boldsymbol{\kappa}_q) = \int\int \mathbf{C}(\boldsymbol{\kappa}_j, \boldsymbol{\kappa}_i; \boldsymbol{\kappa}_q, \boldsymbol{\kappa}_p)\mathcal{H}^O(\boldsymbol{\kappa}_i, \boldsymbol{\kappa}_p)\mathrm{d}\boldsymbol{\kappa}_i\mathrm{d}\boldsymbol{\kappa}_p, \tag{7.9}$$

where $\mathbf{C}$ is a matrix given by (using the discrete transmission matrix notation for

brevity)

$$\mathbf{C}(\boldsymbol{\kappa}_j, \boldsymbol{\kappa}_i; \boldsymbol{\kappa}_q, \boldsymbol{\kappa}_p) = \begin{pmatrix} \langle \bar{t}_{(j,i)\theta\theta} \bar{t}_{(q,p)\theta\theta} \rangle & \langle \bar{t}_{(j,i)\theta\theta} \bar{t}_{(q,p)\theta\phi} \rangle & \langle \bar{t}_{(j,i)\theta\phi} \bar{t}_{(q,p)\theta\theta} \rangle & \langle \bar{t}_{(j,i)\theta\phi} \bar{t}_{(q,p)\theta\phi} \rangle \\ \langle \bar{t}_{(j,i)\theta\theta} \bar{t}_{(q,p)\phi\theta} \rangle & \langle \bar{t}_{(j,i)\theta\theta} \bar{t}_{(q,p)\phi\phi} \rangle & \langle \bar{t}_{(j,i)\theta\phi} \bar{t}_{(q,p)\phi\theta} \rangle & \langle \bar{t}_{(j,i)\theta\phi} \bar{t}_{(q,p)\phi\phi} \rangle \\ \langle \bar{t}_{(j,i)\phi\theta} \bar{t}_{(q,p)\theta\theta} \rangle & \langle \bar{t}_{(j,i)\phi\theta} \bar{t}_{(q,p)\theta\phi} \rangle & \langle \bar{t}_{(j,i)\phi\phi} \bar{t}_{(q,p)\theta\theta} \rangle & \langle \bar{t}_{(j,i)\phi\phi} \bar{t}_{(q,p)\theta\phi} \rangle \\ \langle \bar{t}_{(j,i)\phi\theta} \bar{t}_{(q,p)\phi\theta} \rangle & \langle \bar{t}_{(j,i)\phi\theta} \bar{t}_{(q,p)\phi\phi} \rangle & \langle \bar{t}_{(j,i)\phi\phi} \bar{t}_{(q,p)\phi\theta} \rangle & \langle \bar{t}_{(j,i)\phi\phi} \bar{t}_{(q,p)\phi\phi} \rangle \end{pmatrix}. \tag{7.10}$$

An alternative presentation and discussion of the object and image field correlations is possible using the generalised Stokes parameters [154]. We define the generalised image Stokes vector $\mathcal{S}^I(\boldsymbol{\kappa}_j, \boldsymbol{\kappa}_q)$ as

$$\mathcal{S}^I(\boldsymbol{\kappa}_j, \boldsymbol{\kappa}_q) = [\mathcal{S}_0^I(\boldsymbol{\kappa}_j, \boldsymbol{\kappa}_q), \mathcal{S}_1^I(\boldsymbol{\kappa}_j, \boldsymbol{\kappa}_q), \mathcal{S}_2^I(\boldsymbol{\kappa}_j, \boldsymbol{\kappa}_q), \mathcal{S}_3^I(\boldsymbol{\kappa}_j, \boldsymbol{\kappa}_q)]^{\mathrm{T}}, \tag{7.11}$$

for which the components are defined in relation to the image correlation function by

$$\begin{pmatrix} \mathcal{S}_0^I(\boldsymbol{\kappa}_j, \boldsymbol{\kappa}_q) \\ \mathcal{S}_1^I(\boldsymbol{\kappa}_j, \boldsymbol{\kappa}_q) \\ \mathcal{S}_2^I(\boldsymbol{\kappa}_j, \boldsymbol{\kappa}_q) \\ \mathcal{S}_3^I(\boldsymbol{\kappa}_j, \boldsymbol{\kappa}_q) \end{pmatrix} = \begin{pmatrix} 1 & 0 & 0 & 1 \\ 1 & 0 & 0 & -1 \\ 0 & 1 & 1 & 0 \\ 0 & -i & i & 0 \end{pmatrix} \begin{pmatrix} \mathcal{H}_{\theta\theta}^I(\boldsymbol{\kappa}_j, \boldsymbol{\kappa}_q) \\ \mathcal{H}_{\theta\phi}^I(\boldsymbol{\kappa}_j, \boldsymbol{\kappa}_q) \\ \mathcal{H}_{\phi\theta}^I(\boldsymbol{\kappa}_j, \boldsymbol{\kappa}_q) \\ \mathcal{H}_{\phi\phi}^I(\boldsymbol{\kappa}_j, \boldsymbol{\kappa}_q) \end{pmatrix}. \tag{7.12}$$

The generalised object Stokes vector $\mathcal{S}^O(\boldsymbol{\kappa}_j, \boldsymbol{\kappa}_q)$ can be defined analogously. In terms of information content, it is clear from Eq. (7.12) that $\mathcal{H}^I$ and $\mathcal{S}^I$ are equivalent. Given its closer alignment with results presented in previous chapters, we shall proceed using $\mathcal{H}^I$ in our theoretical discussion. We note, however, that $\mathcal{S}^I$ may be more readily measurable experimentally [309].

To address the question of how the correlations discussed in this section might be measured in practice, we present in Figure 7.1 a hypothetical experiment that uses a self-interferometric setup. Suppose for example that one wishes to compute $\mathcal{H}_{xy}^I(\boldsymbol{\kappa}, \boldsymbol{\kappa} + \Delta\boldsymbol{\kappa})$, where $\Delta\boldsymbol{\kappa}$ denotes the difference between the two wavevector arguments. For simplicity, we shall use the x and y directions instead of θ and ϕ as polarisation bases. The core idea of the experiment is to introduce a wavevector shift of $\Delta\boldsymbol{\kappa}$ into the y component of the image field $\mathbf{b}$ and to feed the resulting fields

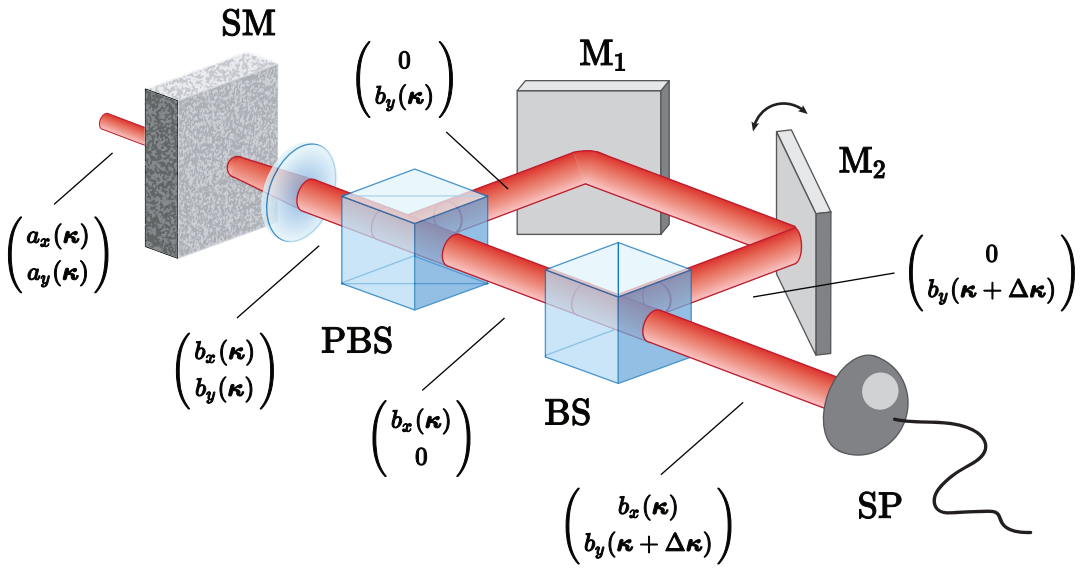

Figure 7.1: Hypothetical experimental setup for measuring $\mathcal{H}^I_{xy}(\boldsymbol{\kappa}, \boldsymbol{\kappa}+\Delta\boldsymbol{\kappa})$. SM = scattering medium, PBS = polarising beam splitter, BS = beam splitter, SP = Stokes polarimeter, M_1 and M_2 = adjustable mirrors.

into a standard Stokes polarimeter. To achieve this we first use a polarising beam splitter to separate the two field components into different arms of the apparatus. In the arm carrying the y component of the field, a tilt in the wavevector can be introduced using, for example, a rotatable mirror. Using another beam splitter, the two components can be recombined and subsequently fed into a traditional Stokes polarimeter. The desired correlation is then given by

$$\mathcal{H}^I_{xy}(\boldsymbol{\kappa}, \boldsymbol{\kappa}+\Delta\boldsymbol{\kappa}) = \frac{1}{2}(S_2 - iS_3), \tag{7.13}$$

where S_2 and S_3 are the regular Stokes parameters measured by the Stokes polarimeter.

A different experimental setup would be required to measure $\mathcal{H}^I_{xx}(\boldsymbol{\kappa}, \boldsymbol{\kappa}+\Delta\boldsymbol{\kappa})$ and $\mathcal{H}^I_{yy}(\boldsymbol{\kappa}, \boldsymbol{\kappa}+\Delta\boldsymbol{\kappa})$. Taking $\mathcal{H}^I_{xx}(\boldsymbol{\kappa}, \boldsymbol{\kappa}+\Delta\boldsymbol{\kappa})$ as an example, one could imagine first using a polarising filter before the initial beam splitter to remove the y component of the scattered field. Replacing the polarising beam splitter by a regular beam splitter would then result in the field vector $(b_x(\boldsymbol{\kappa}), 0)^{\mathrm{T}}$ propagating in both arms of the apparatus. In one arm, an optical rotator could be used to transform the field into $(0, b_x(\boldsymbol{\kappa}))^{\mathrm{T}}$, after which the measurement would proceed as before. We stress

that the design of our experiment is not intended to be optimal, but rather serves to illustrate that such correlations are experimentally accessible.

The most straightforward approach to recovering the object polarisation states using second order correlations is to first measure the regular image Stokes parameters (i.e. taking $\boldsymbol{\kappa}_j = \boldsymbol{\kappa}_q$) for different far field scattering directions using regular Stokes polarimetry. This is equivalent to setting $\Delta\boldsymbol{\kappa} = 0$ in the experiment in Figure 7.1. These components can then be used as an approximation for the Stokes parameters of the hidden object field. The most obvious problem with this method, however, is that, even after statistical averaging, the relationship between the object and image Stokes parameters is not that of a block diagonal matrix, as was the case for the complex field components as shown in Eq. (7.4). Instead, the image Stokes parameters are a complicated mixture of the object Stokes parameters that is non-trivial to invert. Furthermore, at large thicknesses, depolarisation means that not all of the information contained with the object Stokes parameters will be present within the image Stokes parameters, and full polarimetric information about the object field may therefore be unrecoverable.

At a conceptual level, the information contained within the regular Stokes parameters constitutes only a small subset of the total information contained within the image field. Efforts to reconstruct the object field may therefore be improved upon by taking into consideration the full set of information contained within the generalised Stokes parameters, which includes correlations between different scattered plane wave components, i.e. those for which $\Delta\boldsymbol{\kappa} \neq 0$. As has been shown in Chapter 5, these additional correlations arise due to the memory effect, which we shall thus attempt to exploit.

7.2 Reconstruction algorithm

As discussed in Section 7.1, classical Stokes polarimetry suffers from numerous issues that arise due to multiple scattering. In this section we will explore the possibility of reconstructing the object field using the full set of second order correlations that exist within the image field.

Once $\mathcal{H}^I$ has been measured, the recovery of $\mathbf{a}$ can be thought of as a two step

process. First it is necessary to estimate $\mathcal{H}^O$ from $\mathcal{H}^I$, which is tantamount to inverting Eq. (7.9). Secondly, it is necessary to recover $\mathbf{a}$ from $\mathcal{H}^O$. The first of these two steps requires physical insight into the form of Eq. (7.9), whereas the latter is a phase retrieval problem. We shall examine both of these steps separately.

7.2.1 Recovering the correlation function

To proceed it is necessary to say something about the form of $\mathbf{C}(\boldsymbol{\kappa}_j, \boldsymbol{\kappa}_i; \boldsymbol{\kappa}_q, \boldsymbol{\kappa}_p)$ in Eq. (7.9). In Chapter 5, exact results for this function were found in the case of single scattering and first order multiple scattering in the ladder approximation, for which the correlation function is only non-zero provided that the memory effect condition is satisfied, i.e. $\Delta\boldsymbol{\kappa} = \Delta\boldsymbol{\kappa}_{qj} = \boldsymbol{\kappa}_q - \boldsymbol{\kappa}_j = \boldsymbol{\kappa}_p - \boldsymbol{\kappa}_i = \Delta\boldsymbol{\kappa}_{pi}$. Motivated by these results, we thus suppose that $\mathbf{C}(\boldsymbol{\kappa}_j, \boldsymbol{\kappa}_i; \boldsymbol{\kappa}_q, \boldsymbol{\kappa}_p)$ takes the general form

$$\begin{aligned}\mathbf{C}(\boldsymbol{\kappa}_j, \boldsymbol{\kappa}_i; \boldsymbol{\kappa}_q, \boldsymbol{\kappa}_p) = \delta(\boldsymbol{\kappa}_i - \boldsymbol{\kappa}_j)\delta(\boldsymbol{\kappa}_p - \boldsymbol{\kappa}_q)\mathbf{C}_b(\boldsymbol{\kappa}_i, \boldsymbol{\kappa}_p) \\ + \delta(\Delta\boldsymbol{\kappa}_{qj} - \Delta\boldsymbol{\kappa}_{pi})C_s(\boldsymbol{\kappa}_j, \boldsymbol{\kappa}_i; \boldsymbol{\kappa}_q, \boldsymbol{\kappa}_p),\end{aligned} \tag{7.14}$$

where, physically, $\mathbf{C}_b$ describes contributions due to the unscattered, or ballistic, field and $\mathbf{C}_s$ describes contributions due to the scattered field. Inserting Eq. (7.14) into Eq. (7.9) and integrating the delta functions yields

$$\begin{aligned}\mathcal{H}^I(\boldsymbol{\kappa}_j, \boldsymbol{\kappa}_j + \Delta\boldsymbol{\kappa}) =& \mathbf{C}_b(\boldsymbol{\kappa}_j, \boldsymbol{\kappa}_j + \Delta\boldsymbol{\kappa})\mathcal{H}^O(\boldsymbol{\kappa}_j, \boldsymbol{\kappa}_j + \Delta\boldsymbol{\kappa}) \\ &+ \int_{\Omega(\Delta\boldsymbol{\kappa})} \mathbf{C}_s(\boldsymbol{\kappa}_j, \boldsymbol{\kappa}_i; \boldsymbol{\kappa}_j + \Delta\boldsymbol{\kappa}, \boldsymbol{\kappa}_i + \Delta\boldsymbol{\kappa})\mathcal{H}^O(\boldsymbol{\kappa}_i, \boldsymbol{\kappa}_i + \Delta\boldsymbol{\kappa})\mathrm{d}\boldsymbol{\kappa}_i,\end{aligned} \tag{7.15}$$

where $\Omega(\Delta\boldsymbol{\kappa})$ is the domain of physically allowable wavevectors $\boldsymbol{\kappa}_i$ such that $|\boldsymbol{\kappa}_i + \Delta\boldsymbol{\kappa}| < k$, ensuring that all wavevectors are propagating. Simple physical considerations show that for $L \to 0$, $\mathbf{C}_b \to \mathbb{I}$ and $\mathbf{C}_s \to \mathbb{O}$, which results in $\mathcal{H}^I(\boldsymbol{\kappa}_j, \boldsymbol{\kappa}_j + \Delta\boldsymbol{\kappa}) = \mathcal{H}^O(\boldsymbol{\kappa}_j, \boldsymbol{\kappa}_j + \Delta\boldsymbol{\kappa})$ for an infinitesimally thin medium. For $L \to \infty$ on the other hand, we have $\mathbf{C}_b \to \mathbb{O}$ and thus the first term of Eq. (7.15) can be neglected.

In order to better understand the consequences of Eq. (7.15), let us consider a simple example. Suppose that the object field contains precisely two modes with transverse wavevectors $\boldsymbol{\kappa}_0$ and $-\boldsymbol{\kappa}_0$ for some arbitrary choice of $\boldsymbol{\kappa}_0 \neq \mathbf{0}$. The object

correlation function will be non-zero precisely at the four values $\mathcal{H}^O(-\boldsymbol{\kappa}_0, -\boldsymbol{\kappa}_0)$, $\mathcal{H}^O(-\boldsymbol{\kappa}_0, \boldsymbol{\kappa}_0)$, $\mathcal{H}^O(\boldsymbol{\kappa}_0, -\boldsymbol{\kappa}_0)$ and $\mathcal{H}^O(\boldsymbol{\kappa}_0, \boldsymbol{\kappa}_0)$. Considering the arguments of $\mathcal{H}^O$ for these values, it is clear that there are precisely three different values for the difference between the pair of wavevector arguments of the object correlation function, namely $\Delta\boldsymbol{\kappa} = -2\boldsymbol{\kappa}_0, \mathbf{0}$ and $2\boldsymbol{\kappa}_0$. Consider now the $\mathbf{C}_b$ term of Eq. (7.15). This term will only contribute to the image correlation function provided that the pair of scattered wavevectors $\boldsymbol{\kappa}_j$ and $\boldsymbol{\kappa}_j + \Delta\boldsymbol{\kappa}$ are chosen to align with one of the four pairs of wavevectors for which the object correlation function is non-zero. For example, suppose that $\boldsymbol{\kappa}_j = -\boldsymbol{\kappa}_0$ and $\Delta\boldsymbol{\kappa} = 2\boldsymbol{\kappa}_0$, so that $\boldsymbol{\kappa}_j + \Delta\boldsymbol{\kappa} = \boldsymbol{\kappa}_0$. Clearly, since $\mathcal{H}^O(-\boldsymbol{\kappa}_0, \boldsymbol{\kappa}_0) \neq \mathbf{0}$, the $\mathbf{C}_b$ term will result in a non-zero contribution to $\mathcal{H}^I(-\boldsymbol{\kappa}_0, \boldsymbol{\kappa}_0)$. If, however, $\boldsymbol{\kappa}_j = -2\boldsymbol{\kappa}_0$ and $\Delta\boldsymbol{\kappa} = 2\boldsymbol{\kappa}_0$, so that $\boldsymbol{\kappa}_j + \Delta\boldsymbol{\kappa} = \mathbf{0}$, then, since $\mathcal{H}^O(-2\boldsymbol{\kappa}_0, \mathbf{0}) = \mathbf{0}$, the $\mathbf{C}_b$ term will not contribute to the value of $\mathcal{H}^I(-2\boldsymbol{\kappa}_0, \mathbf{0})$.

For the $\mathbf{C}_s$ term of Eq. (7.15), the situation is different due to the presence of the integral. Notably, the $\mathbf{C}_s$ term can yield a non-zero contribution to $\mathcal{H}^I(\boldsymbol{\kappa}_j, \boldsymbol{\kappa}_j + \Delta\boldsymbol{\kappa})$, even in the case that $\mathcal{H}^O(\boldsymbol{\kappa}_j, \boldsymbol{\kappa}_j + \Delta\boldsymbol{\kappa}) = \mathbf{0}$. Consider again the example $\boldsymbol{\kappa}_j = -2\boldsymbol{\kappa}_0$ and $\Delta\boldsymbol{\kappa} = 2\boldsymbol{\kappa}_0$, so that $\boldsymbol{\kappa}_j + \Delta\boldsymbol{\kappa} = \mathbf{0}$. Since $\mathcal{H}^O(\boldsymbol{\kappa}_i, \boldsymbol{\kappa}_i + \Delta\boldsymbol{\kappa})$ is integrated over $\boldsymbol{\kappa}_i$, there will be a non-zero contribution to the integral around the point $\boldsymbol{\kappa}_i = -\boldsymbol{\kappa}_0$, since $\mathcal{H}^O(-\boldsymbol{\kappa}_0, \boldsymbol{\kappa}_0) \neq \mathbf{0}$. This will result in a non-zero contribution to $\mathcal{H}^I(-2\boldsymbol{\kappa}_0, \mathbf{0})$, even though $\mathcal{H}^O(-2\boldsymbol{\kappa}_0, \mathbf{0}) = \mathbf{0}$. In other words, provided that $\Delta\boldsymbol{\kappa}$ is chosen so that $\mathcal{H}^O$ is non-zero *somewhere*, there will be non-zero contributions to $\mathcal{H}^I$ due to the $\mathbf{C}_s$ term in Eq. (7.15) *everywhere*, i.e. for any choice of $\boldsymbol{\kappa}_j$.

To make better use of all of the information contained within the image field, it is helpful to define the integrated correlation functions $\bar{\mathcal{H}}^I(\Delta\boldsymbol{\kappa})$ and $\bar{\mathcal{H}}^O(\Delta\boldsymbol{\kappa})$, where

$$\bar{\mathcal{H}}^I(\Delta\boldsymbol{\kappa}) = \int_{\Omega(\Delta\boldsymbol{\kappa})} \mathcal{H}^I(\boldsymbol{\kappa}_j, \boldsymbol{\kappa}_j + \Delta\boldsymbol{\kappa}) \mathrm{d}\boldsymbol{\kappa}_j \tag{7.16}$$

and $\bar{\mathcal{H}}^O(\Delta\boldsymbol{\kappa})$ can be defined analogously. By integrating Eq. (7.15), we then find

$$\begin{aligned}\bar{\mathcal{H}}^I(\Delta\boldsymbol{\kappa}) = &\int_{\Omega(\Delta\boldsymbol{\kappa})} \mathbf{C}_b(\boldsymbol{\kappa}_j, \boldsymbol{\kappa}_j + \Delta\boldsymbol{\kappa}) \mathcal{H}^O(\boldsymbol{\kappa}_j, \boldsymbol{\kappa}_j + \Delta\boldsymbol{\kappa}) \mathrm{d}\boldsymbol{\kappa}_j \\ &+ \int_{\Omega(\Delta\boldsymbol{\kappa})} \left[\int_{\Omega(\Delta\boldsymbol{\kappa})} \mathbf{C}_s(\boldsymbol{\kappa}_j, \boldsymbol{\kappa}_i; \boldsymbol{\kappa}_j + \Delta\boldsymbol{\kappa}, \boldsymbol{\kappa}_i + \Delta\boldsymbol{\kappa}) \mathrm{d}\boldsymbol{\kappa}_j \right] \mathcal{H}^O(\boldsymbol{\kappa}_i, \boldsymbol{\kappa}_i + \Delta\boldsymbol{\kappa}) \mathrm{d}\boldsymbol{\kappa}_i.\end{aligned} \tag{7.17}$$

In order to make further progress, we shall make several assumptions. First, let us suppose that the support of $\mathbf{a}$ is contained within a small circle of radius kr, with $0 \leq r \ll 1$. Physically, this means that the incident field only contains paraxial plane wave components that propagate close to the optical axis. The maximum value of $|\Delta\boldsymbol{\kappa}|$ for which $\mathcal{H}^O(\boldsymbol{\kappa}, \boldsymbol{\kappa} + \Delta\boldsymbol{\kappa})$ is non-zero is then $2kr$, which is also assumed to be small. The integrals in Eq. (7.17), can hence be restricted to the support of $\mathbf{a}$ (denoted by $\mathcal{S}_a$), for which we can assume both that $|\boldsymbol{\kappa}|/k \ll 1$ and $|\Delta\boldsymbol{\kappa}|/k \ll 1$. In addition, for paraxial plane waves components, we may use the x and y directions as a pair of global polarisation base states.

In light of Eq. (5.44), the only dependence of $\mathbf{C}_b$ on the wavevectors is in the $1/k_z$ factor, which, for modes close to the axis, can be assumed to have a constant value of $1/k$. The matrix $\mathbf{C}_b$ can thus be assumed to be a constant matrix independent of $\boldsymbol{\kappa}_j$ and $\Delta\boldsymbol{\kappa}$. Furthermore, for thin scattering media, the $\mathbf{C}_s$ term in Eq. (7.17) can be ignored to give

$$\bar{\mathcal{H}}^I(\Delta\boldsymbol{\kappa}) \sim \mathbf{C}_b \bar{\mathcal{H}}^O(\Delta\boldsymbol{\kappa}), \tag{7.18}$$

which shows that the image correlation function is related to the object correlation function by a simple matrix product. Calculations from Mie theory show that, for isotropic spheres, we have $\mathbf{C}_b \sim e^{-L/l}\mathbb{I}_4$, i.e. $\mathbf{C}_b$ is a scaled identity matrix. For other particle types, such as chiral spheres, $\mathbf{C}_b$ takes a more complex form, but Eq. (7.18) still holds. Of course, due to the presence of the exponential function in Eq. (7.18), ballistic contributions to the image correlation function decay quickly with thickness.

The second term in Eq. (7.17) involving $\mathbf{C}_s$ requires a more careful analysis. In particular there are two cases to consider, namely $\Delta\boldsymbol{\kappa} = 0$ and $\Delta\boldsymbol{\kappa} \neq 0$. In the special case $\Delta\boldsymbol{\kappa} = 0$, the elements of $\mathbf{C}_s(\boldsymbol{\kappa}_j, \boldsymbol{\kappa}_i; \boldsymbol{\kappa}_j, \boldsymbol{\kappa}_i)$ describe correlations between the four complex elements of the 2×2 block of the transmission matrix $\bar{\mathbf{t}}(\boldsymbol{\kappa}_j, \boldsymbol{\kappa}_i)$. Under the assumptions made thus far, it is well known that $\mathbf{C}_s$ takes a universal

form given by, up to constant factors, [310, 311, 312, 313]

$$\mathbf{C}_s \sim \begin{pmatrix} 1 & 0 & 0 & \rho \\ 0 & \Gamma & \delta & 0 \\ 0 & \delta^* & \Gamma^* & 0 \\ \rho & 0 & 0 & 1 \end{pmatrix}, \tag{7.19}$$

where ρ, known as the 'depolarisation', is a real parameter, and Γ and δ are complex parameters satisfying the rule $|\Gamma + \delta| = 1 - \rho$. Notably, the magnitudes of the elements of $\mathbf{C}_s$, unlike those of $\mathbf{C}_b$, decay sub-exponentially with thickness. Physical intuition for the form of $\mathbf{C}_s$ can be obtained by considering its associated Mueller matrix, which is given by

$$\mathbf{M} \sim \begin{pmatrix} 1+\rho & 0 & 0 & 0 \\ 0 & 1-\rho & 0 & 0 \\ 0 & 0 & \mathrm{Re}(\Gamma+\delta) & \mathrm{Im}(\delta-\Gamma) \\ 0 & 0 & \mathrm{Im}(\delta+\Gamma) & \mathrm{Re}(\Gamma-\delta) \end{pmatrix}. \tag{7.20}$$

We found from simulations that for isotropic spheres, Γ and δ are both real quantities and thus the Mueller matrix in Eq. (7.20) reduces to a diagonal depolariser matrix. In this case we also have $\mathrm{Re}(\Gamma + \delta) = 1 - \rho$ and the ratio $(1 - \rho)/(1 + \rho)$ can thus be seen to correspond to the degree of polarisation of the transmitted light for incident linearly polarised light. If, in addition we have $\delta = 0$, then it follows that the transmitted field for all incident polarisation states have equal degrees of polarisation. If this is not the case, then incident circularly polarised light will depolarise at a different rate to incident linearly polarised light.

The reconstruction of the Stokes vector of a uniformly polarised object field consisting of a single mode using $\Delta\boldsymbol{\kappa} = 0$ correlations has been studied previously using reference speckles [314]. Conceptually, the use of reference speckles is informationally equivalent to determining the values of the parameters of $\mathbf{C}_s$ in Eq. (7.19), which, once known, can be used to invert the image Stokes vector, even in the multiple scattering regime. This is possible provided that the light has not fully depolarised, which corresponds to the case $\rho < 1$. In the limit $\rho = 1$, for which the Mueller matrix corresponds to a perfect depolariser, $\mathbf{C}_s$ becomes the singular

matrix

$$\mathbf{C}_s \sim \begin{pmatrix} 1 & 0 & 0 & 1 \\ 0 & 0 & 0 & 0 \\ 0 & 0 & 0 & 0 \\ 1 & 0 & 0 & 1 \end{pmatrix}. \tag{7.21}$$

In this case no information regarding $\bar{\mathcal{H}}^O_{xy}(\mathbf{0})$ or $\bar{\mathcal{H}}^O_{yx}(\mathbf{0})$ is present within $\bar{\mathcal{H}}^I(\mathbf{0})$ and it would thus only be possible to recover $\bar{\mathcal{H}}^O_{xx}(\mathbf{0})$ and $\bar{\mathcal{H}}^O_{yy}(\mathbf{0})$. While $\bar{\mathcal{H}}^O_{xx}(\mathbf{0})$ and $\bar{\mathcal{H}}^O_{yy}(\mathbf{0})$ describe the relative amplitudes of the x and y components of the incident polarisation state, the relative phase between these components, which is contained within $\bar{\mathcal{H}}^O_{\theta\phi}(\mathbf{0})$ and $\bar{\mathcal{H}}^O_{\phi\theta}(\mathbf{0})$, would be lost, and the incident polarisation state would hence be unrecoverable.

For non-uniformly polarised, multi-mode object fields, it is also necessary to consider correlations for which $\Delta\boldsymbol{\kappa} \neq \mathbf{0}$. In the case $\Delta\boldsymbol{\kappa} \neq \mathbf{0}$, the form of the correlation matrix in Eq. (7.19) no longer applies and, due to the lack of symmetry, it is difficult to make general comments on the form of $\mathbf{C}_s$. We may appeal, however, to Eqs. (5.56) or (5.84) to gain some physical insight, remembering of course that these results were derived for relatively thin scattering media. Focusing on Eq. (5.84) in particular, which incorporates to some degree the effects of multiple scattering, for paraxial modes, the factor that varies most dramatically as a function of the four wavevectors is $\mathrm{sinc}([\gamma_i - \gamma_j - \gamma_p + \gamma_q]L/2)$. As was discussed in Section 5.3.2, when two of the four wavevectors are fixed and the third is left to vary (the fourth then automatically determined by the memory effect condition), this function is only non-zero on a sharp, elliptical band in k-space whose width decreases with increasing medium thickness.

Consider again the second term of the right hand side of Eq. (7.17). Let $\Delta\boldsymbol{\kappa} \neq 0$ be fixed and suppose that $\boldsymbol{\kappa}_i$ is some arbitrary wavevector such that $\mathcal{H}^O(\boldsymbol{\kappa}_i, \boldsymbol{\kappa}_i + \Delta\boldsymbol{\kappa})$ is non-zero. As argued, the value of $\mathbf{C}_s(\boldsymbol{\kappa}_j, \boldsymbol{\kappa}_i; \boldsymbol{\kappa}_j + \Delta\boldsymbol{\kappa}, \boldsymbol{\kappa}_i + \Delta\boldsymbol{\kappa})$, thought of as a function of $\boldsymbol{\kappa}_j$, will be zero everywhere apart from on an elliptical band in k-space that passes through $\boldsymbol{\kappa}_i$ and is oriented orthogonally to $\Delta\boldsymbol{\kappa}$. The integral over $\boldsymbol{\kappa}_j$ can therefore be restricted to $\mathcal{B}(\boldsymbol{\kappa}_i, \Delta\boldsymbol{\kappa})$, which we define as the intersection of $\mathcal{S}_a$ and the aforementioned band. The effect of changing $\Delta\boldsymbol{\kappa}$ to $\Delta\boldsymbol{\kappa}'$ is to rotate the

orientation of the band so that it is effectively orthogonal to $\Delta\boldsymbol{\kappa}'$ at the point $\boldsymbol{\kappa}_i$. The effect of changing $\boldsymbol{\kappa}_i$ to $\boldsymbol{\kappa}_i'$, on the other hand, is to translate the band by the vector $\boldsymbol{\kappa}_i' - \boldsymbol{\kappa}_i$. We remind the reader of Figure 5.1 for pictorial examples.

Since, by definition, $\mathcal{B}(\boldsymbol{\kappa}_i, \Delta\boldsymbol{\kappa}) \subset \mathcal{S}_a$, we may assume that $\mathbf{C}_s$ does not depend strongly on $\boldsymbol{\kappa}_i$, as $\boldsymbol{\kappa}_i$ is assumed to lie close to the optical axis, which allows us to drop the $\boldsymbol{\kappa}_i$ dependence of $\mathcal{B}$. The second term on the right hand side of Eq. (7.17) can therefore be simplified, since

$$\begin{aligned}
&\int_{\mathcal{S}_a}\left[\int_{\mathcal{S}_a}\mathbf{C}_s(\boldsymbol{\kappa}_j,\boldsymbol{\kappa}_i;\boldsymbol{\kappa}_j+\Delta\boldsymbol{\kappa},\boldsymbol{\kappa}_i+\Delta\boldsymbol{\kappa})\mathrm{d}\boldsymbol{\kappa}_j\right]\mathcal{H}^O(\boldsymbol{\kappa}_i,\boldsymbol{\kappa}_i+\Delta\boldsymbol{\kappa})\mathrm{d}\boldsymbol{\kappa}_i \\
&\quad\approx\int_{\mathcal{S}_a}\left[\int_{\mathcal{B}(\Delta\boldsymbol{\kappa})}\mathbf{C}_s(\boldsymbol{\kappa}_j,\boldsymbol{\kappa}_i;\boldsymbol{\kappa}_j+\Delta\boldsymbol{\kappa},\boldsymbol{\kappa}_i+\Delta\boldsymbol{\kappa})\mathrm{d}\boldsymbol{\kappa}_j\right]\mathcal{H}^O(\boldsymbol{\kappa}_i,\boldsymbol{\kappa}_i+\Delta\boldsymbol{\kappa})\mathrm{d}\boldsymbol{\kappa}_i \\
&\quad\approx\mathbf{C}_s(\Delta\boldsymbol{\kappa})\bar{\mathcal{H}}^O(\Delta\boldsymbol{\kappa}),
\end{aligned} \tag{7.22}$$

where $\mathbf{C}_s(\Delta\boldsymbol{\kappa})$ is the internal integral of $\mathbf{C}_s(\boldsymbol{\kappa}_j,\boldsymbol{\kappa}_i;\boldsymbol{\kappa}_j+\Delta\boldsymbol{\kappa},\boldsymbol{\kappa}_i+\Delta\boldsymbol{\kappa})$ over $\mathcal{B}(\Delta\boldsymbol{\kappa})$ in Eq. (7.22). Inserting Eq. (7.22) into Eq. (7.17) yields

$$\bar{\mathcal{H}}^I(\Delta\boldsymbol{\kappa}) \sim \Big(\mathbf{C}_b + \mathbf{C}_s(\Delta\boldsymbol{\kappa})\Big)\bar{\mathcal{H}}^O(\Delta\boldsymbol{\kappa}), \tag{7.23}$$

which gives a linear relation between $\bar{\mathcal{H}}^O$ and $\bar{\mathcal{H}}^I$. We emphasise that it is not possible to drop the $\Delta\boldsymbol{\kappa}$ dependence of $\mathbf{C}_s$. Although the area of $\mathcal{B}(\Delta\boldsymbol{\kappa})$ is invariant under rotations caused by changes in $\Delta\boldsymbol{\kappa}$, the orientation of $\mathcal{B}(\Delta\boldsymbol{\kappa})$ leads to an important asymmetry between the elements of the $\mathbf{A}$ matrix terms appearing in Eq. (5.84). If, for example, $\mathcal{B}(\Delta\boldsymbol{\kappa})$ is oriented in the k_x direction, then there will be a numerical difference between the elements of $\mathbf{A}$ that describe the scattering of incident x and y polarisation states. This difference will be inverted if $\mathcal{B}(\Delta\boldsymbol{\kappa})$ is instead oriented in the k_y direction. Behaviour of this kind demonstrates that the memory effect is sensitive to polarisation.

7.2.2 Recovering the field components

Suppose that an estimate of $\bar{\mathcal{H}}^O(\Delta\boldsymbol{\kappa})$ is known for all $\Delta\boldsymbol{\kappa}$. We turn now to the question of how the complex object field $\mathbf{a}(\boldsymbol{\kappa})$ can be subsequently determined for

all $\boldsymbol{\kappa} \in \mathcal{S}_a$. This is a problem of phase retrieval and can be tackled in several ways, such as using the z transform [315] or semidefinite programming [316]. Here we present the z transform approach, for which phase ambiguities in the recovery procedure become readily apparent. It is worth noting from the outset that $\mathbf{a}(\boldsymbol{\kappa})$ and its associated correlation function $\bar{\mathcal{H}}^O(\Delta\boldsymbol{\kappa})$ will in general be two dimensional discrete signals, since they take two dimensional vector arguments. Nevertheless, it is always possible to construct corresponding one dimensional signals, which reduces the problem to a one dimensional phase retrieval. For more details, see Ref. [316].

The method presented in this section aims to reconstruct the complex field components and is based on Refs. [316, 317, 318]. If only the incident polarisation states are of interest, one may instead wish to reconstruct the object Stokes vectors, which would forgo the need to determine the global phase factors associated with each polarisation state. Such a method is beyond the scope of this thesis and will be pursued in future work.

For the purposes of this section we suppose that there are N plane wave components contained within $\mathcal{S}_a$. Suppose that, for some discrete set of paraxial modes, the x and y components of the unknown object field can be expressed as the pair of discrete signals

$$\mathbf{a}_x = (a_x[0], a_x[1], \ldots, a_x[N-1]), \tag{7.24}$$

$$\mathbf{a}_y = (a_y[0], a_y[1], \ldots, a_y[N-1]), \tag{7.25}$$

where each element corresponds to one of the N different plane wave components present in the incident field. The z transforms of these signals are given by

$$\mathcal{Z}_x(z) = \sum_{n=0}^{N-1} a_x(n) z^{-n} = a_x[0] + \frac{a_x[1]}{z} + \frac{a_x[2]}{z^2} + \ldots + \frac{a_x[N-1]}{z^{N-1}} \tag{7.26}$$

and similarly for $\mathcal{Z}_y$. Multiplying through by z^{N-1} gives

$$\begin{aligned} z^{N-1}\mathcal{Z}_x(z) &= a_x[0]z^{N-1} + a_x[1]z^{N-2} + \ldots + a_x[N-2]z + a_x[N-1], \\ &= a_x[0]\Big(z^{N-1} + \frac{a_x[1]}{a_x[0]}z^{N-2} + \ldots + \frac{a_x[N-2]}{a_x[0]}z + \frac{a_x[N-1]}{a_x[0]}\Big), \\ &= a_x[0]\prod_{n=1}^{N-1}(z - z_n), \end{aligned} \tag{7.27}$$

where z_n are the $N-1$ complex roots of the polynomial.

What is actually known is not $\mathbf{a}_x$, $\mathbf{a}_y$ or their associated z transforms, but instead a collection of discrete autocorrelation functions $\mathcal{H}_{xx}$, $\mathcal{H}_{xy}$, $\mathcal{H}_{yx}$ and $\mathcal{H}_{yy}$, whose elements come from the different components of $\bar{\mathcal{H}}^O(\Delta\boldsymbol{\kappa})$. The autocorrelation function $\mathcal{H}_{xx}$, for example, is given by the length $2N-1$ signal

$$\mathcal{H}_{xx} = (\mathcal{H}_{xx}[-(N-1)], \ldots, \mathcal{H}_{xx}[0], \ldots, \mathcal{H}_{xx}[N-1]), \tag{7.28}$$

where

$$\mathcal{H}_{xx}(m) = \sum_{n=0}^{N-1} a_x[n]a_x^*[n-m]. \tag{7.29}$$

The other correlation functions are defined similarly by taking the appropriate product of object signals in Eq. (7.29). The z transforms of these signals, namely $\mathcal{Z}_{xx}, \mathcal{Z}_{xy}, \mathcal{Z}_{yx}$ and $\mathcal{Z}_{yy}$ can be computed in an analogous manner to Eq. (7.26). It can be shown from the definition of the z transform that

$$\mathcal{Z}_{xx}(z) = \mathcal{Z}_x(z)\mathcal{Z}_x^*\Big(\frac{1}{z^*}\Big). \tag{7.30}$$

Note that for $|z| = 1$ we have $1/z^* = z$ and hence $\mathcal{Z}_{xx} = |\mathcal{Z}_x|^2$. Thus, by taking absolute values of Eq. (7.27) for z lying on the unit circle we have

$$\begin{aligned} \mathcal{Z}_{xx}(z) = |\mathcal{Z}_x(z)|^2 &= |a_x[0]|^2 \prod_{n=1}^{N-1} |z - z_n|^2 \\ &= (-1)^{N-1}|a_x[0]|^2 \prod_{n=1}^{N-1} z_n^* \prod_{n=1}^{N-1}(z - z_n)\Big(z - \frac{1}{z_n^*}\Big), \end{aligned} \tag{7.31}$$

where the final equality makes use of the fact that for $|z| = 1$ we have

$$z^* - z_n^* = -\frac{z_n^*}{z}\Big(z - \frac{1}{z_n^*}\Big). \tag{7.32}$$

Comparing the polynomial factorisations of Eqs. (7.27) and (7.31), we see that z_n are commons roots to both $\mathcal{Z}_x$ and $\mathcal{Z}_{xx}$. In order to recover $\mathcal{Z}_x$ from $\mathcal{Z}_{xx}$, it is thus sufficient to pick the correct $N-1$ roots from the polynomial factorisation of $\mathcal{Z}_{xx}$ that are also roots of $\mathcal{Z}_x$. Once these roots have been determined, by expanding the corresponding polynomial, $\mathcal{Z}_x$ will have been recovered up to a constant factor. Without any additional information however, this is impossible, as there is no way to know which roots to pick. Each choice of $N-1$ roots will lead to a different reconstruction of $\mathcal{Z}_x$, and thus $\mathbf{a}_x$, and the problem is therefore ambiguous.

The ambiguity can be resolved by making use of information contained within the other correlation functions. A similar calculation to Eq. (7.31) shows that, for $|z| = 1$,

$$\mathcal{Z}_{xy}(z) = (-1)^{N-1} a_x[0] a_y^*[0] \prod_{n=1}^{N-1} w_n^* \prod_{n=1}^{N-1} (z - z_n)(z - \frac{1}{w_n^*}), \tag{7.33}$$

where w_n are the roots of the corresponding polynomial for $\mathcal{Z}_y$. Since z_n are also roots of $\mathcal{Z}_{xy}$, the complex roots necessary to reconstruct $\mathcal{Z}_x$ are therefore those that are common to both $\mathcal{Z}_{xx}$ and $\mathcal{Z}_{xy}$. This method, of course, assumes that none of the other roots in $\mathcal{Z}_{xx}$ or $\mathcal{Z}_{xy}$ coincide with any of z_n, in which case the problem would be irresolvable. Such cases, however, are generally pathological in the absence of noise. Therefore, by factorising both $\mathcal{Z}_{xx}$ and $\mathcal{Z}_{xy}$, which are computable from $\mathcal{H}_{xx}$ and $\mathcal{H}_{xy}$, and identifying their common roots, $\mathcal{Z}_x$ can be reconstructed. Similarly, the roots necessary to recover $\mathcal{Z}_y$, namely w_n, are those that are common to both $\mathcal{Z}_{yy}$ and $\mathcal{Z}_{yx}$, which can be computed from $\mathcal{H}_{yx}$ and $\mathcal{H}_{yy}$. Once the roots have been determined, the elements of $\mathbf{a}_x$ and $\mathbf{a}_y$ can be read off as the coefficients of the polynomial expansions $\prod(z - z_n)$ and $\prod(z - w_n)$, as in Eq. (7.27).

By construction, the expanded polynomials will have unit coefficients in z^{N-1}, and it is therefore still necessary to determine, for example, $|a_x[0]|$ and $a_y[0]/a_x[0]$ in order to determine the object polarisation states. There are many ways to determine

these values, with potentially differing numerical stabilities and accuracies. Here we present a simple method for the purposes of illustrating the possibility of the reconstruction. Assuming that $z = 1$ is neither a root of $\mathcal{Z}_x$ nor $\mathcal{Z}_y$, evaluating Eqs. (7.31) and (7.35) at $z = 1$ yields the equations

$$Z_{xx}(1) = |a_x[0]|^2 \prod_{n=1}^{N-1} |1 - z_n|^2, \tag{7.34}$$

$$Z_{xy}(1) = a_x[0]a_y^*[0] \prod_{n=1}^{N-1} (1 - z_n)(1 - w_n^*), \tag{7.35}$$

$$Z_{yy}(1) = |a_y[0]|^2 \prod_{n=1}^{N-1} |1 - w_n|^2. \tag{7.36}$$

From Eq. (7.26) however, $\mathcal{Z}_{xx}(1)$ is simply the sum of the elements of autocorrelation function, i.e. $\sum_{n=-N+1}^{N-1} \mathcal{H}_{xx}[n]$. With this in mind, manipulating Eqs. (7.34)-(7.36) leads to

$$|a_x[0]| = \frac{\sqrt{\sum_{n=-N+1}^{N-1} \mathcal{H}_{xx}[n]}}{\prod_{n=1}^{N-1} |1 - z_n|}, \tag{7.37}$$

$$a_y[0] = a_x[0] \frac{\sum_{n=-N+1}^{N-1} \mathcal{H}_{yy}[n]}{\sum_{n=-N+1}^{N-1} \mathcal{H}_{xy}[n]} \prod_{n=1}^{N-1} \frac{1 - z_n}{1 - w_n}. \tag{7.38}$$

The incident field can only be recovered up to a global phase ambiguity, and we may therefore set $\arg\big(a_x[0]\big) = 0$ arbitrarily, after which $a_x[0]$ and $a_y[0]$ follow. If $z = 1$ were in fact a root of $\mathcal{Z}_x$ or $\mathcal{Z}_y$, one could instead select a different value lying on the unit circle $|z| = 1$.

7.3 Numerical example

In this section we present some preliminary numerical data, showing the existence of the correlations discussed in Section 7.2.1 as well as demonstrating the reconstruction process. Specifically, we perform numerical simulations of random media using the method described in Chapter 6, using the same parameter set as used previously for isotropic spheres of size $x = 2$. We suppose that the support of the object field is limited to a 3×3 grid of modes centred at the origin of k-space. Since

the mode spacing is $0.175k$, the greatest value of $|\boldsymbol{\kappa}|$ is equal to $\sim 0.25k$. While the assumption that the wavevectors associated with these modes lie close to the z axis may be questionable in this case, we are currently limited in available k-space resolution.

7.3.1 Correlations

Before examining the recovery algorithm, we first present numerical data that shows the different types of correlation functions discussed in Section 7.2.1. Figure 7.2 shows the Frobenius norm of 4×4 correlation matrices associated with different pairs of 2×2 blocks of the transmission matrix as a function of thickness. Each data point is averaged over 10^4 different realisations of the scattering matrix. The blue data correspond to the case $\boldsymbol{\kappa}_i = \boldsymbol{\kappa}_j = \boldsymbol{\kappa}_p = \boldsymbol{\kappa}_q = \mathbf{0}$, i.e. correlations between elements within a diagonal block of the transmission matrix. The orange data correspond to the case $\boldsymbol{\kappa}_i = \boldsymbol{\kappa}_p = \mathbf{0}$ and $\boldsymbol{\kappa}_j = \boldsymbol{\kappa}_q = 0.175k(1,0)^{\mathrm{T}}$, i.e. correlations between elements of a non-diagonal block of the transmission matrix. For both the blue and orange data we have $\Delta\boldsymbol{\kappa} = 0$ and their behaviour is thus essentially the same as the FT and OT curves in Figure 6.6.

The purple data in Figure 7.2 show the case $\boldsymbol{\kappa}_i = \boldsymbol{\kappa}_j = \mathbf{0}$ and $\boldsymbol{\kappa}_p = \boldsymbol{\kappa}_q = 0.175k(1,0)^{\mathrm{T}}$. Here, we have $\Delta\boldsymbol{\kappa} = 0.175k(1,0)^{\mathrm{T}}$ and the data correspond to correlations between two different diagonal blocks of the transmission matrix. For small thicknesses the purple data overlap with the blue data. For large thicknesses, however, the purple data continue to decay along an exponentially decaying curve. Returning to the integral over $\mathcal{B}(\Delta\boldsymbol{\kappa})$ in Eq. (7.22), these correlations correspond to the special case $\boldsymbol{\kappa}_j = \boldsymbol{\kappa}_i$, i.e. when the integration variable $\boldsymbol{\kappa}_j$ lies at the centre of the band. It is interesting to note that within our data, for $L/l < 4$, $\Delta\boldsymbol{\kappa} = 0$ and $\Delta\boldsymbol{\kappa} \neq 0$ correlations are transmitted effectively equally through the scattering medium. As shall be seen shortly, this corresponds to the regime where the imagine field has yet to depolarise and the object polarisation states can be inferred by direct Stokes imaging.

For the green and red data in Figure 7.2, we again fix $\boldsymbol{\kappa}_i = \mathbf{0}$ and $\boldsymbol{\kappa}_p = 0.175k(1,0)^{\mathrm{T}}$ and imagine $\boldsymbol{\kappa}_j$ as being able to vary. For any choice of $\boldsymbol{\kappa}_j$, $\boldsymbol{\kappa}_q$ is automatically required to be $\boldsymbol{\kappa}_q = \boldsymbol{\kappa}_j + 0.175k(1,0)^{\mathrm{T}}$ so as to satisfy the mem-

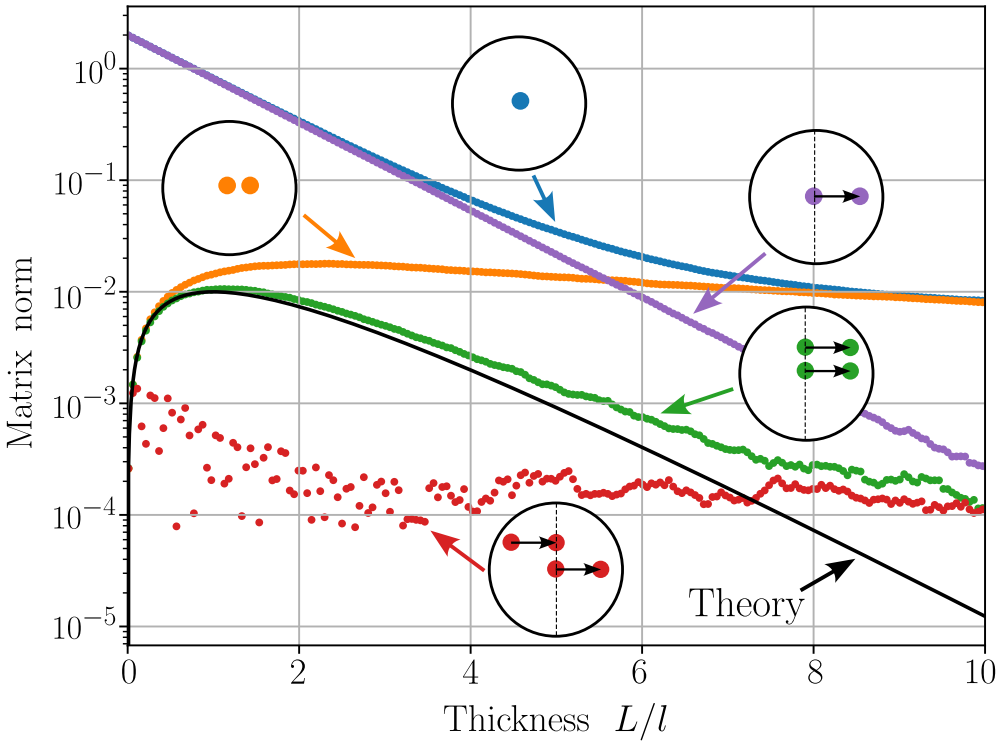

Figure 7.2: Frobenius norms of 4×4 correlation matrices associated with different pairs of blocks of the transmission matrix. The different coloured data are associated with correlations between (blue) the elements of a diagonal block of the transmission matrix, (orange) the elements of an off-diagonal block, (purple) different diagonal blocks (green) different non-diagonal blocks for which $\boldsymbol{\kappa}_j \in \mathcal{B}(\Delta\boldsymbol{\kappa})$ and (red) different non-diagonal blocks for which $\boldsymbol{\kappa}_j \notin \mathcal{B}(\Delta\boldsymbol{\kappa})$. The theory curve was calculated from Eq. (5.84).

ory effect conditions. For this choice of $\boldsymbol{\kappa}_i$ and $\boldsymbol{\kappa}_p$, $\mathcal{B}(\Delta\boldsymbol{\kappa})$ is essentially a vertical line through the origin of k-space, and we therefore expect large correlations for $\boldsymbol{\kappa}_j = 0.175k(0, \pm 1)^{\mathrm{T}}$. The green data correspond to the choice $\boldsymbol{\kappa}_j = 0.175k(0, 1)^{\mathrm{T}}$, whereas the red data correspond to $\boldsymbol{\kappa}_j = 0.175k(-1, 1)^{\mathrm{T}}$. For the red data, since $\boldsymbol{\kappa}_j \notin \mathcal{B}(\Delta\boldsymbol{\kappa})$, we expect the correlations to be weak. For small thicknesses, the behaviour of the red data is oscillatory with a weak, decaying amplitude, as is characteristic of a sinc function. For small thicknesses, we are unable to capture the functional form of these oscillations, as the oscillation rate is too high for the limited number of data points we have. It is also important to note that, in light of the discussion in Section 6.3.3, the precision of our data is limited to on the order of $\sim 10^{-4}$ due to the limited number of realisations used in performing averages. One can therefore think of 10^{-4} as essentially representing 'zero' in Figure 7.2, as we are unable to resolve smaller values.

For the green data in Figure 7.2, we also plotted a theoretical curve computed from Eq. (5.84). As can be seen, this curve fits very well for small thickness, but deviates from the numerical data for large thicknesses. It is difficult at present to assess whether this deviation is due to numerical inaccuracies inherent within the simulation or a physical phenomenon due to higher order scattering terms. If the latter case were true, it would suggest that such correlations decay more slowly than exponential, and thus polarisation information may be preserved over greater thicknesses than Eq. (5.84) would suggest. We also note that changing $\boldsymbol{\kappa}_i$ or $\Delta\boldsymbol{\kappa}$ had virtually no effect on the data. Although, as previously discussed, changing $\Delta\boldsymbol{\kappa}$ does in general alter the elements of the correlation matrix by introducing an asymmetry between the x and y directions, this effect is not observed when taking the norm of the correlation matrix. The data in Figure 7.2 are thus representative of all paraxial correlations that are of the same qualitative nature with regard to the position of $\boldsymbol{\kappa}_j$ in k-space relative to $\mathcal{B}(\Delta\boldsymbol{\kappa})$.

7.3.2 Recovery

In this section we turn to the problem of polarisation recovery. The object field was chosen to be a 3×3 grid of random polarisation states. For different scattering medium thicknesses, we calculate the image field by multiplying the object field by the full discrete transmission matrix. The image Stokes vectors for each mode in the 3×3 grid can be calculated numerically from the image field components using standard equations (see, for example, Ref. [12]). These quantities were calculated and averaged over 10^4 scattering realisations. From these Stokes vectors, estimates for the object polarisation states can be found by decomposing the Stokes vectors into fully polarised and fully depolarised components [12]. Figure 7.3 shows Lissajous diagrams that correspond to the fully polarised components of the image Stokes vectors for different modes in the support of the object field. The red and blue colours correspond to different handednesses of the polarisation states. For linear or near-linear states, the handedness becomes degenerate. The panel labelled 'Object' shows the object field polarisation states. For each thickness, a percentage error between the image Stokes vectors and the object Stokes vectors was computed by flattening the image Stokes vectors into a single array $\mathbf{s}^I$ and computing the statistic

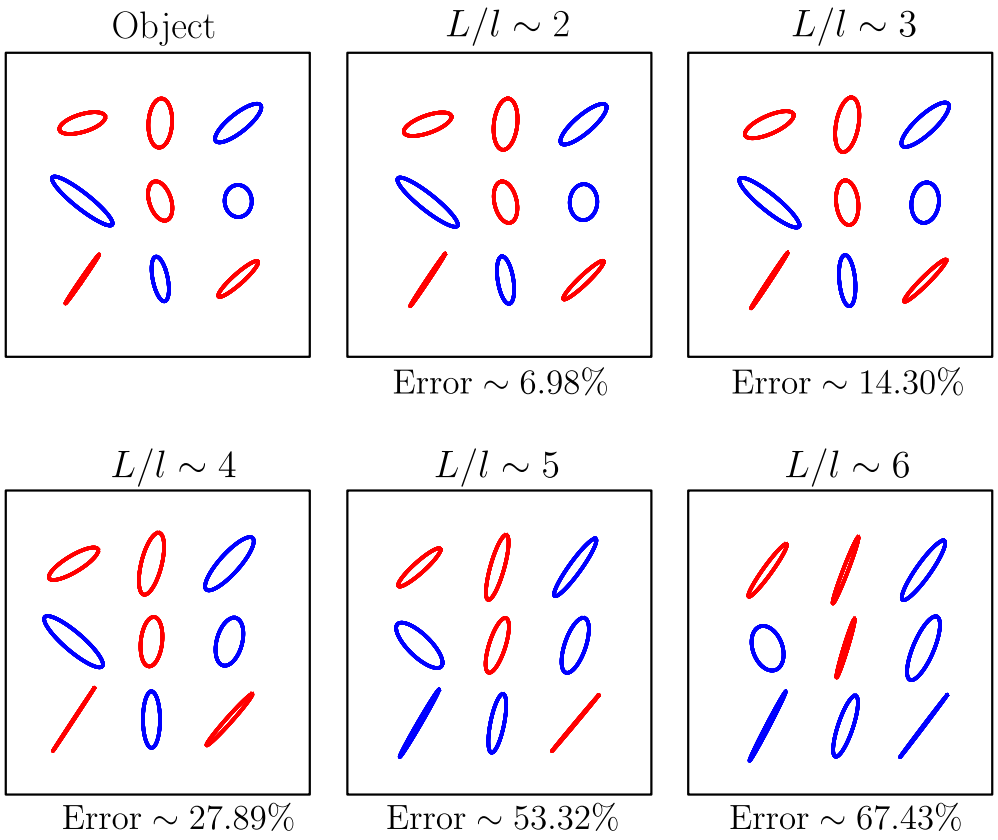

Figure 7.3: Lissajous diagrams showing the object polarisation states and image polarisation states at different medium thicknesses as determined by taking the fully polarised component of the mean image Stokes parameters.

Error $= 100||\mathbf{s}^I - \mathbf{s}^O||/||\mathbf{s}^O||$, where $\mathbf{s}^O$ is the corresponding flattened array of the object Stokes vectors and the norm is the Frobenius norm. Visually, we see that the image polarisation states begin to lose resemblance to the object polarisation states at around $L/l \sim 5$, which is consistent with our previous discussion regarding the separation of the blue and purple curves in Figure 7.2.

Stokes polarimetry is evidently unable to accurately recover the object polarisation states for thick scattering media, and more sophisticated methods are required. We next present data in which the reconstruction method outlined in Section 7.2.2 is applied to the same set of object polarisation states. As discussed in the text accompanying Eq. (7.23), an accurate estimate of $\bar{\mathcal{H}}^O(\Delta\boldsymbol{\kappa})$ requires careful consideration of how correlations corresponding to different choices of $\Delta\boldsymbol{\kappa}$ are transported through the medium. For simplicity, and to highlight other computational features of the reconstruction process, we shall only consider the simple case of thin scattering

media, for which we may instead use Eq. (7.18). In this case, only the correlations corresponding to the blue and purple curves in Figure 7.2 are important. Reconstructions at larger thicknesses that make use of the correlations corresponding to the orange and green curves in Figure 7.2 will be considered in future works.

We may calculate $\bar{\mathcal{H}}^I$ by taking discrete correlations of the image field components contained within $\mathcal{S}_a$, averaging over 10^4 different scattering matrix realisations. In light of Eq. (7.23), for isotropic spheres $\bar{\mathcal{H}}^O$ is a scaled version of $\bar{\mathcal{H}}^I$, and $\bar{\mathcal{H}}^I$ can thus be taken as an estimate for $\bar{\mathcal{H}}^O$. For each component of $\bar{\mathcal{H}}^O$, we form polynomials whose coefficients are given by the corresponding vector components. Since the object contains nine modes, the resulting polynomials are of degree eight. Following the algorithm outlined in Section 7.2.2, we then compare the roots of $\mathcal{Z}_{xx}$ and $\mathcal{Z}_{xy}$, as well as $\mathcal{Z}_{yx}$ and $\mathcal{Z}_{yy}$, all of which are degree sixteen polynomials. If we knew $\bar{\mathcal{H}}^O$ exactly, $\mathcal{Z}_{xx}$ and $\mathcal{Z}_{xy}$, for example, would have eight common roots. In our numerical data, however, these common roots will not perfectly align, but will instead be separated by some small, non-zero distance in the complex plane. In order to decide which roots are common to $\mathcal{Z}_{xx}$ and $\mathcal{Z}_{xy}$, we therefore compute the distances between all possible pairs of roots and take the eight pairs whose distances are shortest, ensuring that no roots are common to more than one pair. Suppose for example that z_1 and z_2 are sufficiently close so as to be deemed to be a common root of $\mathcal{Z}_{xx}$ and $\mathcal{Z}_{xy}$. There remains a choice as to what value should actually be taken as an estimate for a root of $\mathcal{Z}_x$. One may take for example z_1, z_2, $(z_1 + z_2)/2$, or some other function of the z_1 and z_2. We found from numerical testing that the roots from $\mathcal{Z}_{xy}$ and $\mathcal{Z}_{yx}$ tended to be closer to the true roots computed directly from the object field than those from $\mathcal{Z}_{xx}$ and $\mathcal{Z}_{yy}$, and so these values were chosen. Using these roots, we may then find polynomial expansions of $\mathcal{Z}_x$ and $\mathcal{Z}_y$. The coefficients of these polynomials can then be read off as the components of $\mathbf{a}_x$ and $\mathbf{a}_y$. Finally, using Eqs. (7.37) and (7.38), we may compute factors relating $\mathbf{a}_x$ and $\mathbf{a}_y$, which completes the reconstruction.

Similarly to Figure 7.3, Figure 7.4 shows Lissajous diagrams of the object polarisation states as well as reconstructions for different medium thicknesses. We calculated the same error statistic as before, but this time flattening the field component arrays, rather than the Stokes vectors. What is most striking about Figure

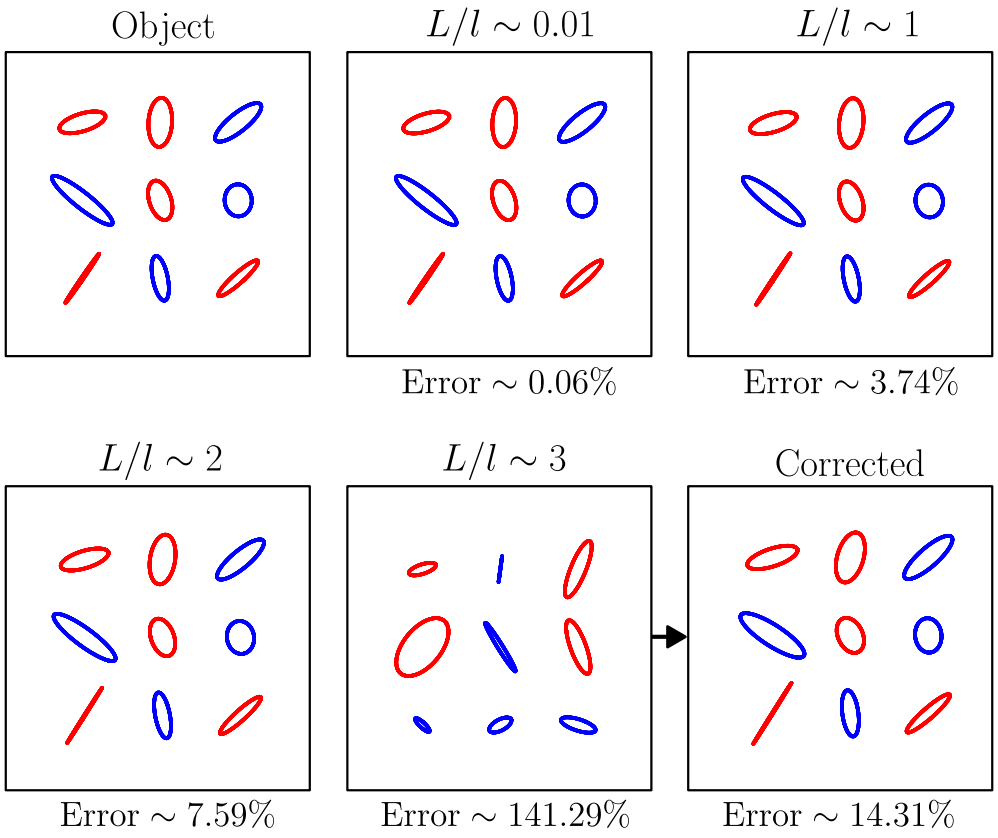

Figure 7.4: Lissajous diagrams showing the object polarisation states and the reconstructed polarisation states at different medium thicknesses. The 'corrected' panel is calculated from the data for $L/l \sim 3$ as discussed in the text.

7.4 is that, after $L/l \sim 3$, the error increases dramatically and the reconstructed field bears little resemblance to the object field. This in fact is a problem with our implementation of the second part of the algorithm described in Section 7.2.2. To understand better what is happening, consider Figure 7.5, which shows the distribution of the roots of $\mathcal{Z}_{xx}$ and $\mathcal{Z}_{xy}$ in the complex plane for the same data as in Figure 7.4 for thickness $L/l \sim 3$. Specifically, black circles show the roots of $\mathcal{Z}_{xx}$, red and green circles together show the roots of $\mathcal{Z}_{xy}$ and orange crosses show the true roots of $\mathcal{Z}_x$ computed directly from the object field. In finding the common roots of $\mathcal{Z}_{xx}$ and $\mathcal{Z}_{xy}$, it is necessary to find the eight pairs of black, and green or red circles that are closest together in the complex plane. The green circles represent the roots of $\mathcal{Z}_{xy}$ that were found to lie closest to a root of $\mathcal{Z}_{xx}$ and were thus chosen as an estimate for the roots of $\mathcal{Z}_x$. The red circles denote the remaining roots of $\mathcal{Z}_{xy}$ that were discarded. Ideally, every orange cross should be neighboured by a pair of

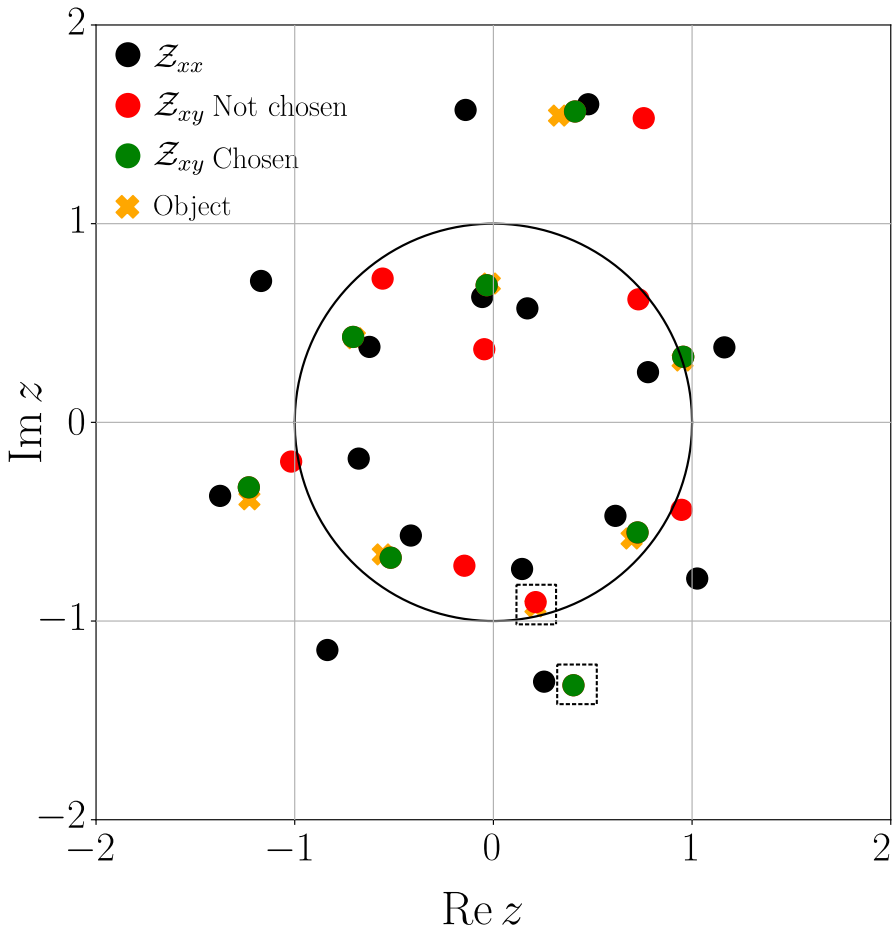

Figure 7.5: Distribution of roots of $\mathcal{Z}_{xx}$ and $\mathcal{Z}_{xy}$ in the complex plane. Black circles are roots of $\mathcal{Z}_{xx}$, red circles are roots of $\mathcal{Z}_{xy}$ that were not chosen, green circles are roots of $\mathcal{Z}_{xy}$ that were chosen, and orange crosses are the true roots of $\mathcal{Z}_x$ calculated directly from the object.

black and green circles, all of which lie close together in the complex plane.

As can be seen in Figure 7.5, most of the green circles lie close to an orange cross, indicating that the method is generally identifying good estimates for the roots of $\mathcal{Z}_x$. There is one green circle, however, encaged in dashed box, that does not lie close to an orange cross and does not therefore correspond to a true root of $\mathcal{Z}_x$. The reason this root was selected is that it happened to, by chance, lie close to another black circle to which it has no real relationship. The root that should have been chosen, but which was discarded, is the red circle encaged in a dashed box. Although this root does lie close to a black circle, it was not close enough to be accepted by our implementation of the algorithm. The final sub-figure in Figure 7.4 shows the resulting reconstruction if we manually select the aforementioned red circle instead

of the encaged green circle. As can be seen, this yields a far superior reconstruction, both visually and numerically. Of course, performing this step required knowledge of the object field, which would not be available in the ideal version of the problem. The purpose of this discussion, however, was to demonstrate that the polarimetric information required to reconstruct the object is indeed present within the measured z transforms. Selecting the correct roots to retrieve this information, however, can be a difficult task. It is clear that this problem will only worsen as the size of the support of the object field, and thus the number of complex roots, increases. In future works, we shall therefore consider alternative phase retrieval algorithms. It is also possible that reconstructing the object Stokes vectors, which are real quantities, rather than the complex field components, requires less information and may therefore scale better with object size than the method presented here.

As a final comment, we note that the distribution of roots in the complex plane depends strongly on the incident polarisation states in a non-trivial way. To illustrate this, Figure 7.6 shows a couple of examples of the roots of $\mathcal{Z}_x$ and $\mathcal{Z}_y$ for different randomly generated objects. Blue and orange crosses show the roots of $\mathcal{Z}_x$ and $\mathcal{Z}_y$, while the corresponding plus signs shown the inverse conjugates of these roots. These latter points are related to the roots by inversion about the circle $|z| = 1$. Lissajous diagrams corresponding to the polarisation states within the objects from which these roots were computed are shown in the top right corners. Ideally, we would not like crosses or plus signs of different colours to lie too close to each other, as these may interfere with the distance calculations discussed previously. The regions enclosed by dashed boxes show examples of where these roots do lie close together and would thus be problematic. Though only two examples are given here, pairs such as these can be observed commonly when randomly generating different object polarisation states.

7.4 Conclusion

In this chapter, we have given an introductory examination of the preservation of polarimetric information as light is transmitted through a random medium. In addition, we have outlined an algorithm for the potential recovery of the polarisation

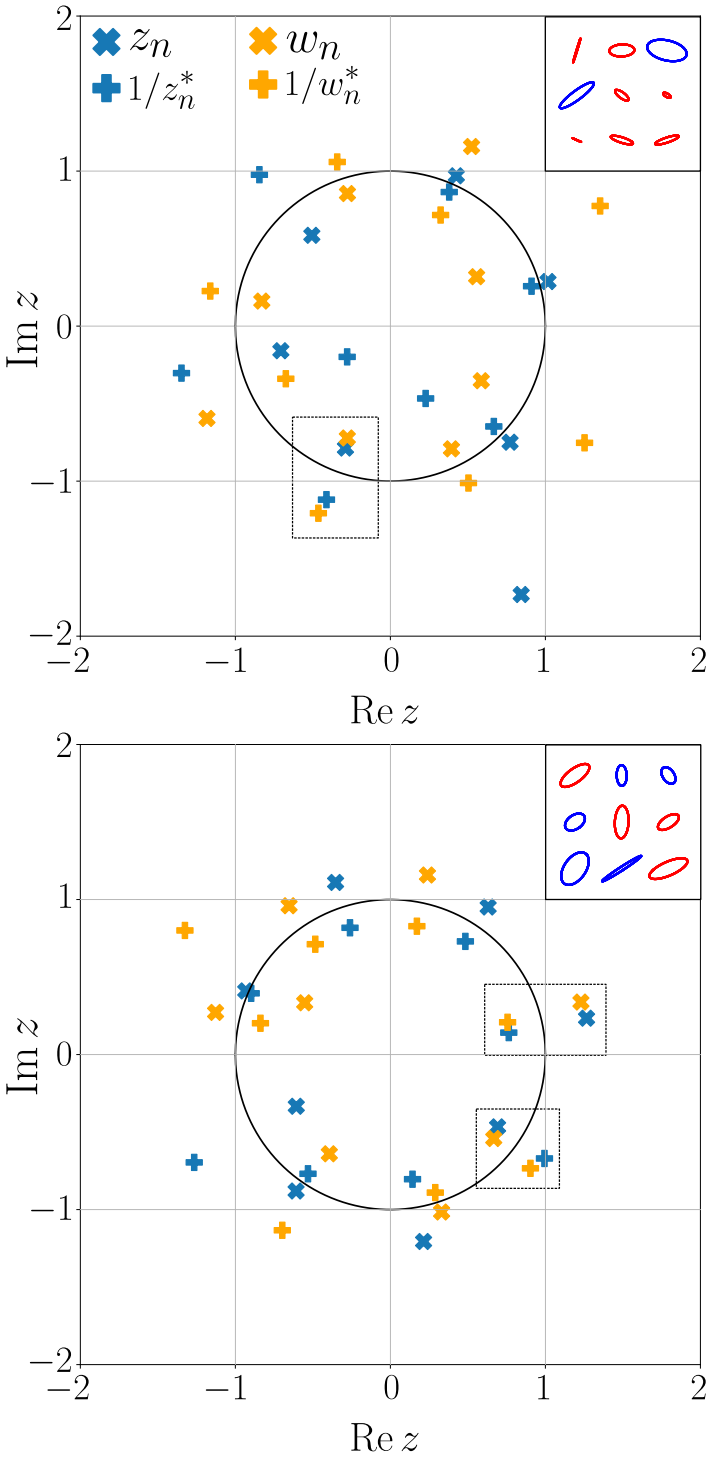

Figure 7.6: Complex roots associated with different object polarisation states. Lissajous diagrams of the polarisation states of the object fields are shown in the corners of the figures.

states contained within an object field hidden behind a random scattering medium. Using the simulation method of Chapter 6, we have demonstrated the algorithm nu-

merically for thin scattering media using the ballistic component of the correlation matrix $\mathbf{C}_b$. One of the primary challenges of the method at present is in selecting the correct complex roots to reconstruct the object, as some roots happen to be spuriously closer to other unrelated roots, which interferes with the common root finding algorithm. This problem may be ameliorated by using a more sophisticated root selection process, by using a greater number of samples to improve numerical convergence, by incorporating the effects of $\mathbf{C}_s$ to improve the accuracy of the estimation of $\bar{\mathcal{H}}^O$, or by using an alternative phase retrieval algorithm.

Extending the recovering procedure to thicker scattering media requires the use of the scattered field correlations encoded in $\mathbf{C}_s$, as described by Eq. (7.23). Of course, Eq. (7.23), the derivation of which rests on assumptions about the banded nature of $\mathbf{C}_s$ as motivated by partial theoretical results, may not necessarily hold in the multiple scattering regime. If this were the case, an alternative approach would be necessary to invert the integral in Eq. (7.17) to obtain an estimation of $\bar{\mathcal{H}}^O$. It is also not at present known to what extent $\Delta\boldsymbol{\kappa} \neq \mathbf{0}$ correlations are preserved in the deep multiple scattering regime. Though numerical data hints at the possibility of a sub-exponential decay of the magnitudes of the correlation functions, this is by no means conclusive. The question of how the specific set of polarisation states within the object influences the distribution of roots in the complex plane is also a difficult and open question. With the current phase retrieval algorithm, one could imagine, for example, designing a set of object polarisation states whose roots are maximally separated in the complex plane, so as to be more easily recoverable. While such a construction may be of theoretical interest, its practical utility is not immediately clear. As a final remark, it may also be interesting to extend the theory explored in this chapter to account for partially coherent objects, such as the light emitted by a hidden fluorophore. Problems such as this and others, however, require a large amount of additional work.

Chapter 8

Conclusion

The central aim of this thesis was to model the propagation and scattering of polarised light in random media using random matrices. Specifically, we have used random matrix techniques to analyse the scattering and transfer matrices associated with discrete, random scattering media. While random matrix theory has been extensively employed to study the scattering of electrons and scalar optical waves, this work constitutes the first theoretical investigation of using random matrices to model the statistical properties of scattered polarised light. The importance of incorporating the vectorial nature of light into theoretical models and simulation methods was highlighted in Chapter 2, where we reviewed a variety of fundamental concepts pertinent to the scattering of polarised light. For individual scatterers, the properties of the scattered field, such as its phase function and angular distribution of scattered polarisation state, depend non-trivially on the polarisation state of the incident electric field vector in conjunction with the geometric and morphological properties of the scatterer. The intricate details of these light-matter interactions can then have stark consequences when light is made to propagate through multiple scattering media composed of such scatterers. Most notably, details of this kind are crucial in understanding and determining the rate at which light depolarises as it travels through random media.

In Chapter 2, we also highlighted the limits of purely analytic approaches to theoretical modelling, as the complexity of the mathematics associated with multiple

scattering rebuffs attempts to derive general results. We then reviewed a selection of numerical techniques designed to overcome this limitation, from rigorous methods based on Maxwell's equations, such as the T-matrix approach, to approximate methods founded on heuristic arguments, such as the Monte Carlo approach. The discussion in this chapter built a picture of the landscape of extant methods, allowing us to identify a gap that our random matrix method was able to fill.

Chapter 3 concerned the constraints satisfied by the scattering and transfer matrices due to energy conservation, reciprocity and time reversal symmetry. These were derived in the general case of an arbitrary, non-magnetic, non-absorbing scattering medium confined within a slab, where the incident and scattered fields were decomposed into vectorial angular spectra containing both propagating and evanescent wave components. The symmetries for the discrete scattering and transfer matrices, defined with respect to discrete angular spectra are summarised in Eqs. (3.137), (3.142), (3.163) and (3.173), which are a set of novel results that extend those known previously for scalar waves. It was further shown that the corresponding results for scalar waves emerge from the vectorial laws as special cases. Finally, in Section 3.4 we explored the group structure of the transfer matrices and introduced the differential transfer matrix, whose algebraic properties ultimately allowed for a novel parametrisation of the scattering matrix for thin scattering media. The results of Chapter 3, in addition to having more general theoretical importance, allowed us to carefully define the appropriate set of scattering and transfer matrices that correspond to physically realisable systems. They therefore served as the foundation from which our subsequent theoretical and numerical investigations followed.

Having established the boundaries of allowable scattering and transfer matrices, in Chapter 4 we proceeded to assess their statistical properties using some basic results from random matrix theory. We began by analysing the joint statistics of 2×2 blocks of matrices drawn from the circular orthogonal ensemble, having deemed this ensemble to be appropriate for matrices satisfying our constraints. In doing so we found that no polarisation state was scattered preferentially over the ensemble, with the exception of the backscattering direction, for which it was more probable for the scattered field's polarisation state to be co-polarised to that of the incident field. The mean Mueller matrix for all blocks was found to be that of

a pure depolariser, perfectly depolarising for off-diagonal scattering matrix blocks and yielding a degree of polarisation of 1/3 for all incident polarisation states for scattering matrix blocks corresponding to direct backscattering. In addition, the diattenuation and retardance vectors were also found to be distributed isotropically over the Poincaré sphere, but diattenuation and retardance were shown to follow non-trivial probability distributions, for which we found exact analytic results given by Eqs. (4.23) and (4.26). Finally, we found that for large scattering matrices, the statistics of diattenuation and retardance were also derivable from the assumption that the scattering matrix elements are Gaussian.

The circular ensembles were patently limited in their ability to model realistic scattering media, and in Chapter 5 we thus presented a more general theory able to model discrete scattering media containing particulate scatterers of arbitrary shape a size, given knowledge of their single scattering properties. Our approach began with the far field Foldy Lax equations, from which one can derive a Born series for the scattered field, where each term incorporates scattering of different a order. By relating these expressions to the scattering matrix, we were then primed to study the statistical properties of the scattering matrix elements by performing analytic calculations on the resulting expressions. Assuming a uniform distribution for the distribution of the particle positions, we found the means, covariances and pseudo-covariances of the elements of the scattering matrix. For the mean, incorporating all scattering orders, we found in Eq. (5.44) that the forward scattering blocks of the transmission matrix followed an exponential law. We found expressions for the covariance and pseudo-covariance between different matrix elements in the single scattering and first order multiple scattering regimes, given by, for example, Eqs. (5.56) and (5.84). In both cases the correlations were seen to be non-zero for special combinations of wavevectors, namely those satisfying the memory effect and conjugate memory effect, and an extended analysis of the geometric nature of these correlations was given in Section 5.3.2. We ended the chapter by considering briefly how our results may be extended to the scattering of evanescent modes by deriving a near field extension to the amplitude matrix appearing in our far field theory. Using this, we showed that our previous results can be translated into corresponding near field results using a few transformations. As noted however, further work is required

to ensure that the assumptions made within our work, such as the uniform particle density and single scattering approximation, are still consistent in scattering regimes where near field modes are important.

Unable to provide a full, statistical multiple scattering theory of the scattering matrix elements, in Chapter 6 we developed a simulation technique able to generate scattering matrices for scattering media of arbitrary thickness. Conceptually, our method accepts as input parameters statistical quantities pertaining to the single scattering properties of the random medium, and is able to generate similar statistical data in the multiple scattering regime. These input parameters were precisely those derived in Chapter 5, and our method is not tied to any particular type of scatterer. In Chapter 6 we outlined in detail many of the mathematical intricacies associated with the model and, to validate the technique, in Section 6.2 we presented simulated data for isotropic and chiral spheres of different sizes exploring a wide range of polarimetric phenomena. These included the polarisation properties of the transmission scattering medium's eigenvalues and eigenvectors; the degree of polarisation as a function of medium thickness for different incident polarisation states, as well as the statistics of diattenuation and retardance in different scattering directions. For the last of these, we saw that in the limit of large medium thickness, the results of our simulations converged to those derived in Chapter 4 from the circular ensembles. In its present form, our simulation method is restricted to propagating plane wave components. It would be interesting, however, to generalise the method to incorporate evanescent waves, which would open up the possibility of simulating dense scattering media. Such a method may be realisable using the general form of the constraints from Chapter 3, along with the near-field scattering extensions to the results of Chapter 5. Careful consideration must be given, however, to the numerous assumptions made within our approach, and additional work is thus needed to develop the idea further.

In Section 6.3, we gave an quantitative assessment of the numerical performance of our simulation technique, so as to identify areas of weakness that may be improved in future works. In our analysis we focused particularly on computational speed and efficiency, numerical precision and convergence, and accuracy. Considering the range of operations necessary in running the simulation, we identified areas

that required the greatest computation time and determined numerically the computational complexity for each one. We found that the bottleneck of our code was in setting up the covariance and pseudo-covariance matrices before random matrix generation begins. This is largely a consequence of the size of the covariance matrices, which are on the order of $\sim N^4 \times N^4$ for N modes. Improving the algorithm that identifies which elements of the sparse covariances matrices are non-zero may help to reduce the computational burden to more reasonable levels. Being a Monte Carlo approach in nature, our method suffers from relatively poor scaling of numerical precision with number of realisations and a large amount of data is thus required to calculate statistical quantities to high precision. Perhaps the most pressing issue, however, as discussed in Section 6.3.4, is the poor integration accuracy when computing the cross section using a Cartesian cubature scheme. Before symmetrising the scattering matrices, we saw that this problem was resolvable by choosing a suitable k-space spacing that gives a zero mean error across all incident modes. After symmetrisation, however, we saw that the error was always non-zero, regardless of the choice of mode spacing. In theory, this problem is potentially surmountable by incorporating more general cubature schemes. At present, however, doing so leads to theoretical issues that require further research to resolve.

Finally, in Chapter 7, we applied our simulation technique to the problem of recovering a hidden incident field with a non-uniform distribution of polarisation states across different plane wave components. This problem, envisaged as a thought experiment, gives a concrete way of analysing the more general question of how well polarisation information is preserved on transmission through a scattering medium. In order to reconstructed the hidden field, we first derived the relationship between the correlation function of the incident field components, and that of the transmitted field, which was assumed to be measurable. The functions that maps these two quantities are the correlation functions of the transmission matrix elements derived in earlier chapters, which were seen to be invertible in the scattering regimes considered. The second part of the recovery process requires reconstructing the hidden field components from their correlation functions. A method for doing so was presented, and numerical data demonstrating the recovery process for relatively thin media was given. The core issue with the algorithm at present lies in selecting the

correct roots of the z transforms, as random numerical noise leads to roots being displaced from their correct positions in the complex plane. Our study was however preliminary, and an improvement to the method, or the adoption of alternative phase retrieval methods so as to extend the reconstruction process to thicker scattering media, presents itself naturally as a future extension.

In summary, we have successfully developed and realised random matrix methods for modelling the scattering of polarised light in random media. The framework within this thesis was built largely from the ground up, taking inspiration from various aspects of statistical optics and scattering theory. While the more foundational aspects of our work, such as the derivation of matrix symmetries, culminated in conclusive results, for the majority of the remainder of the thesis there remains a wealth of open questions and areas where further work is necessary. The conclusion of this thesis does therefore not signify the resolution of a specific problem, but rather the genesis of new tools and ideas that ultimately, we hope, will help researchers better understand the random scattering of polarised light.

Appendix A

Jones and Mueller calculi

In this section we give a brief review of the Jones and Mueller calculi, which are mathematical tools for describing how the polarisation state of light is transformed upon interaction with linear optical systems. We refer the reader to Refs. [12, 16, 17, 18] for further details.

The complex electric field vector $\mathbf{E}(\mathbf{r}, t)$ at position $\mathbf{r} = (x, y, z)^{\mathrm{T}}$ and time t associated with a fully polarised, monochromatic plane wave propagating along the z axis of a Cartesian coordinate system is given by

$$\mathbf{E}(\mathbf{r}, t) = \begin{pmatrix} E_x \\ E_y \\ 0 \end{pmatrix} e^{i(kz - \omega t)}, \tag{A.1}$$

where E_x and E_y are constant, complex factors, k is the wavenumber and ω is the optical frequency. Vibrations of the electric field vector are necessarily orthogonal to the direction of propagation, which is equivalent to the electric field having a vanishing z component. The constants E_x and E_y, on the other hand, are unconstrained, and different pairs of values correspond to different polarisation states. Since the complex exponential factor in Eq. (A.1) only imparts a global phase onto the electric field vector, the plane wave's polarisation state is fully described by the

truncated vector

$$\mathbf{J} = \begin{pmatrix} E_x \\ E_y \end{pmatrix}, \tag{A.2}$$

which is known as a Jones vector.

Suppose that the plane wave passes through some arbitrary non-depolarising optical element that does not alter its propagation direction. In general, the Jones vector of the field transmitted through the element $\mathbf{J}'$ may be different to that of the incident field $\mathbf{J}$. Provided that the element is linear, this transformation can be described by the matrix equation

$$\mathbf{J}' = \mathbf{T}\mathbf{J}, \tag{A.3}$$

where $\mathbf{T}$ is known as the Jones matrix. The transformation of Jones vectors using Jones matrices is known as the Jones calculus.

Parallel to the Jones calculus is the Mueller calculus, in which the transformation of Stokes vectors are described using Mueller matrices. The Mueller calculus can be thought of as a superset of the Jones calculus in the sense that Eq. (A.3) has an equivalent formulation in terms of Stokes vectors and Mueller matrices[1]. The use of Stokes vectors, however, also allows for the description of the transformation of partially polarised and unpolarised optical fields. Furthermore, the use of Mueller matrices allows for the description of depolarising optical systems.

For partially polarised light, the electric field vector cannot be expressed as in Eq. (A.1). Instead, the field components can be thought of as stochastic processes that fluctuate in space and time. The polarisation state, however, can still be described using a Stokes vector $\mathbf{S}$, which, in the same coordinate system as before, can be

[1] One caveat to this statement is that a Jones matrix may also incorporate a global phase factor, i.e. a complex exponential that can be factored out of the matrix. Depending on how one sets up the relevant propagation equations, this may, for example, be used to account for a phase change due to propagation through the optical element that is equal for both components of the electric field. Such factors do not appear in the Mueller calculus.

defined as

$$\mathbf{S} = \begin{pmatrix} S_0 \\ S_1 \\ S_2 \\ S_3 \end{pmatrix} = \begin{pmatrix} \langle |E_x|^2 \rangle + \langle |E_y|^2 \rangle \\ \langle |E_x|^2 \rangle - \langle |E_y|^2 \rangle \\ 2\langle \mathrm{Re}(E_x E_y^*) \rangle \\ 2\langle \mathrm{Im}(E_x E_y^*) \rangle \end{pmatrix}, \tag{A.4}$$

where $\langle \cdot \rangle$ denotes a statistical average over the ensemble of electric field realisations. The components S_0, S_1, S_2 and S_3 are collectively known as the Stokes parameters. The transformation of the Stokes vector through a linear optical system can be expressed using the Mueller matrix $\mathbf{M}$ through the equation

$$\mathbf{S}' = \mathbf{M}\mathbf{S}, \tag{A.5}$$

where $\mathbf{S}'$ and $\mathbf{S}$ are Stokes vectors analogous to $\mathbf{J}'$ and $\mathbf{J}$ in Eq. (A.3).

The Poincaré sphere is a geometric construction that serves as a useful graphical representation of the space of possible Stokes vectors. We define the normalised Stokes vector[2] $\mathbf{s} = (s_1, s_2, s_3)^{\mathrm{T}}$, composed of normalised Stokes parameters $s_i = S_i/S_0$ for $1 \leq i \leq 3$. It can be shown that for any arbitrary field the inequality

$$S_0^2 \geq S_1^2 + S_2^2 + S_3^2, \tag{A.6}$$

holds. It follows that $\mathbf{s}$ necessarily lies on or within the sphere of unit radius centred at the origin of three dimensional space. This sphere is the (normalised) Poincaré sphere, and each point on or within it corresponds to a different polarisation state. Eq. (A.6) achieves equality if and only if the field is fully polarised, meaning points on the surface of the Poincaré sphere correspond to fully polarised, elliptical polarisation states. In general, however, the magntiude of the vector $\mathbf{s}$, which is also known as the degree of polarisation, ranges from 0 to 1, taking the value 0 in the limiting case of fully unpolarised light, in which case $\mathbf{s}$ is the zero vector.

[2]Note carefully that the normalised Stokes vector has three components, while the regular Stokes vector has four.

Bibliography

[1] C. Bohren and D. Huffman, *Absorption and Scattering of Light by Small Particles*. Wiley, 1983.

[2] N. Byrnes and M. R. Foreman, "Universal bounds for imaging in scattering media," *New J. Phys.*, vol. 22, p. 083023, 2020.

[3] S. Rotter and S. Gigan, "Light fields in complex media: Mesoscopic scattering meets wave control," *Rev. Mod. Phys.*, vol. 89, p. 015005, 2017.

[4] J. Stetefeld, S. A. McKenna, and T. R. Patel, "Dynamic light scattering: a practical guide and applications in biomedical sciences," *Biophys. Rev.*, vol. 8, pp. 409–427, 2016.

[5] S. M. Popoff, G. Lerosey, R. Carminati, M. Fink, A. C. Boccara, and S. Gigan, "Measuring the transmission matrix in optics: An approach to the study and control of light propagation in disordered media," *Phys. Rev. Lett.*, vol. 104, p. 100601, 2010.

[6] A. P. Mosk, A. Lagendijk, G. Lerosey, and M. Fink, "Controlling waves in space and time for imaging and focusing in complex media," *Nat. Photon.*, vol. 6, pp. 283–292, 2012.

[7] C. W. J. Beenakker, "Random-matrix theory of quantum transport," *Rev. Mod. Phys.*, vol. 69, pp. 731–808, 1997.

[8] Y. Imry, "Active transmission channels and universal conductance fluctuations," *EPL*, vol. 1, pp. 249–256, 1986.

[9] D. Bicout, C. Brosseau, A. S. Martinez, and J. M. Schmitt, "Depolarization of multiply scattered waves by spherical diffusers: Influence of the size parameter," *Phys. Rev. E*, vol. 49, pp. 1767–1770, 1994.

[10] M. Mehta, *Random Matrices*. Elsevier Science, 2004.

[11] A. Chrysostomou, P. W. Lucas, and J. H. Hough, "Circular polarimetry reveals helical magnetic fields in the young stellar object HH 135–136," *Nature*, vol. 450, pp. 71–73, 2007.

[12] R. M. A. Azzam and N. Bashara, *Ellipsometry and Polarized Light*. North-Holland, 1987.

[13] M. Gu, Q. Zhang, and S. Lamon, "Nanomaterials for optical data storage," *Nat. Rev. Mater.*, vol. 1, p. 16070, 2016.

[14] S. L. Jacques, J. C. Ramella-Roman, and K. L. M.D., "Imaging skin pathology with polarized light," *J Biomed Opt .*, vol. 7, pp. 329 – 340, 2002.

[15] M. R. Foreman, C. M. Romero, and P. Török, "Determination of the three-dimensional orientation of single molecules," *Opt. Lett.*, vol. 33, pp. 1020–1022, 2008.

[16] E. Wolf, *Introduction to the Theory of Coherence and Polarization of Light*. Cambridge University Press, 2007.

[17] C. Brosseau, *Fundamentals of Polarized Light: A Statistical Optics Approach*. Wiley, 1998.

[18] M. R. Foreman, *Informational limits in optical polarimetry and vectorial imaging*. Phd, Imperial College London, 2010.

[19] M. Born and E. Wolf, *Principles of Optics: Electromagnetic Theory of Propagation, Interference and Diffraction of Light*. Elsevier Science, 2013.

[20] K. F. Warnick and W. C. Chew, "Numerical simulation methods for rough surface scattering," *Waves Random Complex Media*, vol. 11, p. R1, 2001.

[21] D. A. Long and D. Long, *The Raman effect: a unified treatment of the theory of Raman scattering by molecules*, vol. 8. Wiley Chichester, 2002.

[22] J. R. Lakowicz, "Introduction to fluorescence," in *Principles of Fluorescence Spectroscopy*, pp. 1–23, Springer, 1999.

[23] C. I. Valencia, E. R. Méndez, and B. S. Mendoza, "Second-harmonic generation in the scattering of light by two-dimensional particles," *J Opt Soc Am B*, vol. 20, pp. 2150–2161, 2003.

[24] A. V. Zayats, I. I. Smolyaninov, and A. A. Maradudin, "Nano-optics of surface plasmon polaritons," *Phys. Rep.*, vol. 408, pp. 131–314, 2005.

[25] R. J. Charlson, J. E. Lovelock, M. O. Andreae, and S. G. Warren, "Oceanic phytoplankton, atmospheric sulphur, cloud albedo and climate," *Nature*, vol. 326, pp. 655–661, 1987.

[26] M. I. Mishchenko, J. M. Dlugach, M. A. Yurkin, L. Bi, B. Cairns, L. Liu, R. L. Panetta, L. D. Travis, P. Yang, and N. T. Zakharova, "First-principles modeling of electromagnetic scattering by discrete and discretely heterogeneous random media," *Phys. Rep.*, vol. 632, pp. 1–75, 2016.

[27] M. Mishchenko, L. Travis, and A. Lacis, *Multiple Scattering of Light by Particles: Radiative Transfer and Coherent Backscattering*. Cambridge University Press, 2006.

[28] H. van de Hulst, *Light Scattering by Small Particles*. Dover Publications, 1981.

[29] R. J. Potton, "Reciprocity in optics," *Rep. Prog. Phys.*, vol. 67, pp. 717–754, 2004.

[30] D. Lacoste and B. van Tiggelen, "Stokes parameters for light scattering from a Faraday-active sphere," *J Quant Spectrosc Radiat Transf*, vol. 63, pp. 305–319, 1999.

[31] Y. Yu, Y. Chen, H. Hu, W. Xue, K. Yvind, and J. Mork, "Nonreciprocal transmission in a nonlinear photonic-crystal Fano structure with broken symmetry," *Laser Photonics Rev.*, vol. 9, pp. 241–247, 2015.

[32] L. Bi, J. Hu, P. Jiang, D. H. Kim, G. F. Dionne, L. C. Kimerling, and C. A. Ross, "On-chip optical isolation in monolithically integrated non-reciprocal optical resonators," *Nat. Photonics*, vol. 5, pp. 758–762, 2011.

[33] V. V. Tuchin, *Tissue Optics: Light Scattering Methods and Instruments for Medical Diagnosis*. SPIE, 2015.

[34] M. Mishchenko, J. Hovenier, and L. Travis, *Light Scattering by Nonspherical Particles: Theory, Measurements, and Applications*. Elsevier Science, 1999.

[35] G. Können, *Polarized Light in Nature*. Cambridge University Press, 1985.

[36] M. F. Hantke, J. Bielecki, O. Kulyk, D. Westphal, D. S. Larsson, M. Svenda, H. K. Reddy, R. A. Kirian, J. Andreasson, J. Hajdu, *et al.*, "Rayleigh-scattering microscopy for tracking and sizing nanoparticles in focused aerosol beams," *IUCr*, vol. 5, pp. 673–680, 2018.

[37] R. W. Taylor and V. Sandoghdar, "Interferometric Scattering Microscopy: Seeing Single Nanoparticles and Molecules via Rayleigh Scattering," *Nano Lett.*, vol. 19, pp. 4827–4835, 2019.

[38] A. V. Malinka, "Light scattering by optically soft large particles of arbitrary shape," *J. Opt. Soc. Am. A*, vol. 28, pp. 2086–2090, 2011.

[39] S. Wang, X. Pan, and L. Tong, "Modeling of nanoparticle-induced Rayleigh–Gans scattering for nanofiber optical sensing," *Opt. Commun.*, vol. 276, pp. 293–297, 2007.

[40] J. Tyynelä, J. Leinonen, C. D. Westbrook, D. Moisseev, and T. Nousiainen, "Applicability of the Rayleigh-Gans approximation for scattering by snowflakes at microwave frequencies in vertical incidence," *J. Geophys. Res. Atmos.*, vol. 118, pp. 1826–1839, 2013.

[41] H. R. Gordon, "Rayleigh-Gans scattering approximation: surprisingly useful for understanding backscattering from disk-like particles," *Opt. Express*, vol. 15, pp. 5572–5588, 2007.

[42] D. Toublanc, "Henyey–Greenstein and Mie phase functions in Monte Carlo radiative transfer computations," *Appl. Opt.*, vol. 35, pp. 3270–3274, 1996.

[43] T. Binzoni, T. S. Leung, A. H. Gandjbakhche, D. Rüfenacht, and D. T. Delpy, "The use of the Henyey–Greenstein phase function in Monte Carlo simulations in biomedical optics," *Phys. Med. Biol.*, vol. 51, pp. N313–N322, 2006.

[44] L. Tsang, J. Kong, and K. Ding, *Scattering of Electromagnetic Waves: Theories and Applications*. Wiley, 2000.

[45] N. Ghosh, A. Pradhan, P. K. Gupta, S. Gupta, V. Jaiswal, and R. P. Singh, "Depolarization of light in a multiply scattering medium: Effect of the refractive index of a scatterer," *Phys. Rev. E*, vol. 70, p. 066607, 2004.

[46] K.-n. Liou and J. E. Hansen, "Intensity and polarization for single scattering by polydisperse spheres: a comparison of ray optics and Mie theory," *J Atmos Sci*, vol. 28, pp. 995–1004, 1971.

[47] W. J. Glantschnig and S.-H. Chen, "Light scattering from water droplets in the geometrical optics approximation," *Appl. Opt.*, vol. 20, pp. 2499–2509, 1981.

[48] J. Goodman, *Speckle Phenomena in Optics: Theory and Applications*. Roberts & Company, 2007.

[49] J. Goodman, *Statistical Optics*. Wiley, 2015.

[50] G. Maret and P. E. Wolf, "Multiple light scattering from disordered media. The effect of brownian motion of scatterers," *Z. Phys. B*, vol. 65, pp. 409–413, 1987.

[51] D. J. Pine, D. A. Weitz, P. M. Chaikin, and E. Herbolzheimer, "Diffusing wave spectroscopy," *Phys. Rev. Lett.*, vol. 60, pp. 1134–1137, 1988.

[52] A. Dogariu and R. Carminati, "Electromagnetic field correlations in three-dimensional speckles," *Phys. Rep.*, vol. 559, pp. 1–29, 2015.

[53] J. Ellis and A. Dogariu, "Differentiation of globally unpolarized complex random fields," *J. Opt. Soc. Am. A*, vol. 21, pp. 988–993, 2004.

[54] B. Berne and R. Pecora, *Dynamic Light Scattering: With Applications to Chemistry, Biology, and Physics*. Dover Publications, 2013.

[55] E. Akkermans and G. Montambaux, *Mesoscopic Physics of Electrons and Photons*. Cambridge University Press, 2007.

[56] A. Zardecki and W. G. Tam, "Multiple scattering corrections to the Beer-Lambert law. 2: Detector with a variable field of view," *Appl. Opt.*, vol. 21, pp. 2413–2420, 1982.

[57] J. Berk and M. R. Foreman, "Role of multiple scattering in single particle perturbations in absorbing random media," *Phys. Rev. Research*, vol. 3, p. 033111, 2021.

[58] R. Lenke and G. Maret, "Multiple scattering of light: coherent backscattering and transmission," in *Scattering in polymeric and colloidal systems*, ch. 1, pp. 1–73, Taylor & Francis, 2000.

[59] J. Bertolotti, *Light transport beyond diffusion*. PhD thesis, Universita degli Studi di Firenze, 2007.

[60] Y. Kuga and A. Ishimaru, "Retroreflectance from a dense distribution of spherical particles," *J. Opt. Soc. Am. A*, vol. 1, pp. 831–835, 1984.

[61] M. P. V. Albada and A. Lagendijk, "Observation of Weak Localization of Light in a Random Medium," *Phys. Rev. Lett.*, vol. 55, pp. 2692–2695, 1985.

[62] P.-E. Wolf and G. Maret, "Weak localization and coherent backscattering of photons in disordered media," *Phys. Rev. Lett.*, vol. 55, pp. 2696–2699, 1985.

[63] M. Segev, Y. Silberberg, and D. N. Christodoulides, "Anderson localization of light," *Nat. Photon*, vol. 7, pp. 197–204, 2013.

[64] F. C. MacKintosh, J. X. Zhu, D. J. Pine, and D. A. Weitz, "Polarization memory of multiply scattered light," *Phys. Rev. B*, vol. 40, pp. 9342–9345, 1989.

[65] F. C. MacKintosh and S. John, "Diffusing-wave spectroscopy and multiple scattering of light in correlated random media," *Phys. Rev. B*, vol. 40, pp. 2383–2406, 1989.

[66] C. Macdonald and I. Meglinski, "Backscattering of circular polarized light from a disperse random medium influenced by optical clearing," *Laser Phys. Lett.*, vol. 8, pp. 324–328, 2011.

[67] A. Ishimaru, S. Jaruwatanadilok, and Y. Kuga, "Polarized pulse waves in random discrete scatterers," *Appl. Opt.*, vol. 40, pp. 5495–5502, 2001.

[68] G. Yao and L. V. Wang, "Propagation of polarized light in turbid media: simulated animation sequences," *Opt. Express*, vol. 7, pp. 198–203, 2000.

[69] J. P. Dark and A. D. Kim, "Asymptotic theory of circular polarization memory," *J Opt Soc Am A*, vol. 34, pp. 1642–1650, 2017.

[70] M. Xu and R. Alfano, "Circular polarization memory of light," *Phys. Rev. E*, vol. 72, p. 065601, 2005.

[71] M. Xu and R. R. Alfano, "Random walk of polarized light in turbid media," *Phys. Rev. Lett.*, vol. 95, p. 213901, 2005.

[72] L. F. Rojas-Ochoa, D. Lacoste, R. Lenke, P. Schurtenberger, and F. Scheffold, "Depolarization of backscattered linearly polarized light," *J. Opt. Soc. Am. A*, vol. 21, pp. 1799–1804, 2004.

[73] C. Zhang, S. Horder, T. K. Lee, and W. Wang, "Development of polarization speckle based on random polarization phasor sum," *J. Opt. Soc. Am. A*, vol. 36, pp. 277–282, 2019.

[74] N. Ghosh, P. K. Gupta, A. Pradhan, and S. K. Majumder, "Anomalous behavior of depolarization of light in a turbid medium," *Phys. Lett. A*, vol. 354, pp. 236–242, 2006.

[75] S. G. Demos and R. R. Alfano, "Temporal gating in highly scattering media by the degree of optical polarization," *Opt. Lett.*, vol. 21, pp. 161–163, 1996.

[76] K. Yoo and R. Alfano, "Time resolved depolarization of multiple backscattered light from random media," *Phys. Lett. A*, vol. 142, pp. 531–536, 1989.

[77] J. D. van der Laan, J. B. Wright, D. A. Scrymgeour, S. A. Kemme, and E. L. Dereniak, "Evolution of circular and linear polarization in scattering environments," *Opt. Express*, vol. 23, pp. 31874–31888, 2015.

[78] S. Sanyal, A. K. Sood, S. Ramkumar, S. Ramaswamy, and N. Kumar, "Novel polarization dependence in diffusing-wave spectroscopy of crystallizing colloidal suspensions," *Phys. Rev. Lett.*, vol. 72, pp. 2963–2966, 1994.

[79] V. Sankaran, J. T. Walsh, and D. J. Maitland, "Polarized light propagation through tissue phantoms containing densely packed scatterers," *Opt. Lett.*, vol. 25, pp. 239–241, 2000.

[80] A. Dogariu, C. Kutsche, P. Likamwa, G. Boreman, and B. Moudgil, "Time-domain depolarization of waves retroreflected from dense colloidal media," *Opt. Lett.*, vol. 22, pp. 585–587, 1997.

[81] N. Ghosh, H. S. Patel, and P. K. Gupta, "Depolarization of light in tissue phantoms - effect of a distribution in the size of scatterers," *Opt. Express*, vol. 11, pp. 2198–2205, 2003.

[82] C. M. Macdonald, S. L. Jacques, and I. V. Meglinski, "Circular polarization memory in polydisperse scattering media," *Phys. Rev. E*, vol. 91, p. 033204, 2015.

[83] J. R. Mourant, J. P. Freyer, A. H. Hielscher, A. A. Eick, D. Shen, and T. M. Johnson, "Mechanisms of light scattering from biological cells relevant to non-invasive optical-tissue diagnostics," *Appl. Opt.*, vol. 37, pp. 3586–3593, 1998.

[84] S. Otsuki, "Multiple scattering of polarized light in turbid birefringent media: a monte carlo simulation," *Appl. Opt.*, vol. 55, no. 21, pp. 5652–5664, 2016.

[85] V. V. Tuchin, "Polarized light interaction with tissues," *J. Biomed. Opt.*, vol. 21, p. 071114, 2016.

[86] S. G. Demos and R. R. Alfano, "Optical polarization imaging," *Appl. Opt.*, vol. 36, pp. 150–155, 1997.

[87] H. Tian, J. Zhu, S. Tan, Y. Zhang, and X. Hou, "Influence of the particle size on polarization-based range-gated imaging in turbid media," *AIP Adv.*, vol. 7, p. 095310, 2017.

[88] P. Shukla, R. Sumathi, S. Gupta, and A. Pradhan, "Influence of size parameter and refractive index of the scatterer on polarization-gated optical imaging through turbid media," *J. Opt. Soc. Am. A*, vol. 24, pp. 1704–1713, 2007.

[89] J. M. Schmitt and S. H. Xiang, "Cross-polarized backscatter in optical coherence tomography of biological tissue," *Opt. Lett.*, vol. 23, pp. 1060–1062, 1998.

[90] A. H. Hielscher, A. A. Eick, J. R. Mourant, D. Shen, J. P. Freyer, and I. J. Bigio, "Diffuse backscattering Mueller matrices of highly scattering media," *Opt. Express*, vol. 1, pp. 441–453, 1997.

[91] A. H. Hielscher, A. A. Eick, J. R. Mourant, J. P. Freyer, and I. J. Bigio, "Biomedical diagnostic with diffusely backscattered linearly and circularly polarized light," in *Biomedical Sensing, Imaging, and Tracking Technologies II*, vol. 2976, pp. 298 – 305, SPIE, 1997.

[92] S. Demos, H. Savage, A. S. Heerdt, S. Schantz, and R. Alfano, "Time resolved degree of polarization for human breast tissue," *Opt. Commun.*, vol. 124, pp. 439–442, 1996.

[93] T. Ma, X. Hu, L. Zhang, J. Lian, X. He, Y. Wang, and Z. Xian, "An Evaluation of Skylight Polarization Patterns for Navigation," *Sensors*, vol. 15, pp. 5895–5913, 2015.

[94] W. Jue, Q. Jianqiang, and G. Lei, "An equivalent incident light model for multiple scattering and polarization neutral point of skylight," *J Opt*, vol. 22, p. 075603, 2020.

[95] M. V. Berry, M. R. Dennis, and R. L. Lee, "Polarization singularities in the clear sky," *New J. Phys.*, vol. 6, p. 162, 2004.

[96] G. W. Kattawar and G. N. Plass, "Radiance and Polarization of Multiple Scattered Light from Haze and Clouds," *Appl. Opt.*, vol. 7, pp. 1519–1527, 1968.

[97] L. Landau, *The Classical Theory of Fields*. Elsevier Science, 2013.

[98] J. Jin, *The Finite Element Method in Electromagnetics*. IEEE Press, 2014.

[99] K. Yee, "Numerical solution of initial boundary value problems involving maxwell's equations in isotropic media," *IEEE Trans. Antennas Propag.*, vol. 14, pp. 302–307, 1966.

[100] R. White, *An Introduction to the Finite Element Method with Applications to Nonlinear Problems*. Wiley, 1985.

[101] C.-p. Yu and H.-c. Chang, "Compact finite-difference frequency-domain method for the analysis of two-dimensional photonic crystals," *Opt. Express*, vol. 12, pp. 1397–1408, 2004.

[102] J.-F. Lee, R. Lee, and A. Cangellaris, "Time-domain finite-element methods," *IEEE Trans. Antennas Propag.*, vol. 45, pp. 430–442, 1997.

[103] T. Rylander and A. Bondeson, "Stable FEM-FDTD hybrid method for Maxwell's equations," *Comput. Phys. Commun.*, vol. 125, pp. 75–82, 2000.

[104] A. Monorchio, A. R. Bretones, R. Mittra, G. Manara, and R. G. Martín, "A hybrid time-domain technique that combines the finite element, finite difference and method of moment techniques to solve complex electromagnetic problems," *IEEE Trans. Antennas Propag.*, vol. 52, pp. 2666–2674, 2004.

[105] J.-P. Berenger, "A perfectly matched layer for the absorption of electromagnetic waves," *J. Comput. Phys.*, vol. 114, pp. 185–200, 1994.

[106] M. Morgan and K. Mei, "Finite-element computation of scattering by inhomogeneous penetrable bodies of revolution," *IEEE Trans. Antennas Propag.*, vol. 27, pp. 202–214, 1979.

[107] A. Alexanian, N. Kolias, R. Compton, and R. York, "Three-dimensional FDTD analysis of quasi-optical arrays using Floquet boundary conditions and Berenger's PML," *IEEE Microw. Guided Wave Lett*, vol. 6, pp. 138–140, 1996.

[108] M. Fusco, "Fdtd algorithm in curvilinear coordinates (EM scattering)," *IEEE Trans. Antennas Propag.*, vol. 38, pp. 76–89, 1990.

[109] P. Yang and K. N. Liou, "Finite-difference time domain method for light scattering by small ice crystals in three-dimensional space," *J. Opt. Soc. Am. A*, vol. 13, pp. 2072–2085, 1996.

[110] S. H. Tseng, A. Taflove, D. Maitland, and V. Backman, "Pseudospectral time domain simulations of multiple light scattering in three-dimensional macroscopic random media," *Radio Sci.*, vol. 41, 2006.

[111] F. Kahnert, "Numerical methods in electromagnetic scattering theory," *J Quant Spectrosc Radiat Transf*, vol. 79-80, pp. 775–824, 2003.

[112] R. Harrington, I. Antennas, and P. Society, *Field Computation by Moment Methods*. Wiley, 1993.

[113] A. Lakhtakia and G. Mulholland, "On two numerical techniques for light scattering by dielectric agglomerated structures," *J. Res. Natl. Inst*, vol. 98, p. 699, 1993.

[114] D. Schaubert, D. Wilton, and A. Glisson, "A tetrahedral modeling method for electromagnetic scattering by arbitrarily shaped inhomogeneous dielectric bodies," *IEEE Trans. Antennas Propag.*, vol. 32, pp. 77–85, 1984.

[115] K. Sertel and J. L. Volakis, "Method of moments solution of volume integral equations using parametric geometry modeling," *Radio Sci.*, vol. 37, pp. 10–1–10–7, 2002.

[116] T. Sarkar and S. Rao, "The application of the conjugate gradient method for the solution of electromagnetic scattering from arbitrarily oriented wire antennas," *IEEE Trans. Antennas Propag.*, vol. 32, pp. 398–403, 1984.

[117] A. Zwanborn and P. van den Berg, "A weak form of the conjugate gradient FFT method for plate problems," *IEEE Trans. Antennas Propag.*, vol. 39, pp. 224–228, 1991.

[118] K. Sertel and J. Volakis, "Multilevel fast multipole method solution of volume integral equations using parametric geometry modeling," *IEEE Trans. Antennas Propag.*, vol. 52, pp. 1686–1692, 2004.

[119] A. Heldring, J. M. Tamayo, E. Ubeda, and J. M. Rius, "Accelerated direct solution of the method-of-moments linear system," *Proc. IEEE*, vol. 101, pp. 364–371, 2013.

[120] X. Millard and Q. H. Liu, "A fast volume integral equation solver for electromagnetic scattering from large inhomogeneous objects in planarly layered media," *IEEE Trans. Antennas Propag.*, vol. 51, pp. 2393–2401, 2003.

[121] M. Yurkin and A. Hoekstra, "The discrete dipole approximation: An overview and recent developments," *J Quant Spectrosc Radiat Transf*, vol. 106, pp. 558–589, 2007.

[122] A. Lakhtakia, "Macroscopic theory of the coupled dipole approximation method," *Opt. Commun.*, vol. 79, pp. 1–5, 1990.

[123] S. Sukhov, D. Haefner, and A. Dogariu, "Coupled dipole method for modeling optical properties of large-scale random media," *Phys. Rev. E*, vol. 77, p. 066709, 2008.

[124] J. J. Goodman, B. T. Draine, and P. J. Flatau, "Application of fast-Fourier-transform techniques to the discrete-dipole approximation," *Opt. Lett.*, vol. 16, pp. 1198–1200, 1991.

[125] E. M. Purcell and C. R. Pennypacker, "Scattering and Absorption of Light by Nonspherical Dielectric Grains," *ApJ*, vol. 186, pp. 705–714, 1973.

[126] B. T. Draine and P. J. Flatau, "Discrete-dipole approximation for scattering calculations," *J. Opt. Soc. Am. A*, vol. 11, pp. 1491–1499, 1994.

[127] C. E. Dungey and C. F. Bohren, "Light scattering by nonspherical particles: a refinement to the coupled-dipole method," *J. Opt. Soc. Am. A*, vol. 8, pp. 81–87, 1991.

[128] B. T. Draine and P. J. Flatau, "User Guide for the Discrete Dipole Approximation Code DDSCAT 7.3," *arXiv*, 2013.

[129] I. Stevanovic, P. Crespo-Valero, K. Blagovic, F. Bongard, and J. R. Mosig, "Integral-equation analysis of 3-D metallic objects arranged in 2-D lattices using the Ewald transformation," *IEEE Trans Microw Theory Tech*, vol. 54, pp. 3688–3697, 2006.

[130] P. C. Chaumet and A. Sentenac, "Numerical simulations of the electromagnetic field scattered by defects in a double-periodic structure," *Phys. Rev. B*, vol. 72, p. 205437, 2005.

[131] B. Gallinet, J. Butet, and O. J. F. Martin, "Numerical methods for nanophotonics: standard problems and future challenges," *Laser Photonics Rev.*, vol. 9, pp. 577–603, 2015.

[132] A. A. Shcherbakov and A. V. Tishchenko, "Light scattering in plane dielectric layers: Modeling in the 2d reciprocal space," *J Quant Spectrosc Radiat Transf*, vol. 113, pp. 2424–2430, 2012. Electromagnetic and Light Scattering by nonspherical particles XIII.

[133] D. Mackowski and B. Ramezanpour, "A plane wave model for direct simulation of reflection and transmission by discretely inhomogeneous plane parallel media," *J Quant Spectrosc Radiat Transf*, vol. 213, pp. 95–106, 2018.

[134] D. Mackowski, "Van de Hulst Essay: The DDA, the RTE, and the computation of scattering by plane parallel layers of particles," *J Quant Spectrosc Radiat Transf*, vol. 189, pp. 43–59, 2017.

[135] B. Ramezanpour and D. W. Mackowski, "Direct prediction of bidirectional reflectance by dense particulate deposits," *J Quant Spectrosc Radiat Transf*, vol. 224, pp. 537–549, 2019.

[136] M. I. Mishchenko, L. D. Travis, and D. W. Mackowski, "T-matrix computations of light scattering by nonspherical particles: A review," *J Quant Spectrosc Radiat Transf*, vol. 55, pp. 535–575, 1996.

[137] P. Waterman, "Matrix formulation of electromagnetic scattering," *Proc. IEEE*, vol. 53, pp. 805–812, 1965.

[138] L. Tsang, J. Kong, and R. Shin, *Theory of Microwave Remote Sensing*. Wiley, 1985.

[139] J. B. Schneider, *Electromagnetic detection of buried dielectric targets*. University of Washington, 1991.

[140] D.-S. Wang and P. W. Barber, "Scattering by inhomogeneous nonspherical objects," *Appl. Opt.*, vol. 18, pp. 1190–1197, 1979.

[141] A. Lakhtakia, V. K. Varadan, and V. V. Varadan, "Scattering and absorption characteristics of lossy dielectric, chiral, nonspherical objects," *Appl. Opt.*, vol. 24, pp. 4146–4154, 1985.

[142] J. J. Wang, Y. P. Han, Z. F. Wu, and L. Han, "T-matrix method for electromagnetic scattering by a general anisotropic particle," *J Quant Spectrosc Radiat Transf*, vol. 162, pp. 66–76, 2015.

[143] B. Peterson and S. Ström, "T Matrix for Electromagnetic Scattering from an Arbitrary Number of Scatterers and Representations of E(3)," *Phys. Rev. D*, vol. 8, pp. 3661–3678, 1973.

[144] Y. lin Xu, "Electromagnetic scattering by an aggregate of spheres," *Appl. Opt.*, vol. 34, pp. 4573–4588, 1995.

[145] M. I. Mishchenko and L. D. Travis, "Light scattering by polydisperse, rotationally symmetric nonspherical particles: Linear polarization," *J Quant Spectrosc Radiat Transf*, vol. 51, pp. 759–778, 1994.

[146] M. I. Mishchenko, L. Liu, D. W. Mackowski, B. Cairns, and G. Videen, "Multiple scattering by random particulate media: exact 3D results," *Opt. Express*, vol. 15, pp. 2822–2836, 2007.

[147] D. W. Mackowski and M. I. Mishchenko, "Calculation of the T matrix and the scattering matrix for ensembles of spheres," *J. Opt. Soc. Am. A*, vol. 13, pp. 2266–2278, 1996.

[148] J. Uozumi and T. Asakura, "First-order intensity and phase statistics of Gaussian speckle produced in the diffraction region," *Appl. Opt.*, vol. 20, pp. 1454–1466, 1981.

[149] K. O'Donnell, "Speckle statistics of doubly scattered light," *J. Opt. Soc. Am. A*, vol. 72, pp. 1459–1463, 1982.

[150] J. C. Dainty, "I the statistics of speckle patterns," in *Progress in optics*, vol. 14, pp. 1–46, Elsevier, 1977.

[151] W. Wang, S. Zhang, and J. Grimble, "Statistics of polarization speckle produced by a constant polarization phasor plus a random polarization phasor sum," *J. Opt. Soc. Am. A*, vol. 37, pp. 1888–1894, 2020.

[152] C. Brosseau, R. Barakat, and E. Rockower, "Statistics of the Stokes parameters for gaussian distributed fields," *Opt. Commun.*, vol. 82, pp. 204–208, 1991.

[153] R. Barakat, "The Statistical Properties of Partially Polarized Light," *Optica Acta*, vol. 32, pp. 295–312, 1985.

[154] O. Korotkova and E. Wolf, "Generalized Stokes parameters of random electromagnetic beams," *Opt. Lett.*, vol. 30, pp. 198–200, 2005.

[155] D. Eliyahu, "Vector statistics of correlated Gaussian fields," *Phys. Rev. E*, vol. 47, pp. 2881–2892, 1993.

[156] D. Eliyahu, "Statistics of Stokes variables for correlated Gaussian fields," *Phys. Rev. E*, vol. 50, pp. 2381–2384, 1994.

[157] B. Zhang, X. Wen, J. Dai, Y. Wang, and W. Wang, "Development of polarization speckle with a finite number of k-distribution-amplitude steps," *Opt. Commun.*, vol. 520, p. 128546, 2022.

[158] N. Bender, H. Yilmaz, Y. Bromberg, and H. Cao, "Customizing speckle intensity statistics," *Optica*, vol. 5, pp. 595–600, 2018.

[159] M. Nieto-Vesperinas and N. García, "Non-circular gaussian speckle contrast in the exact theory of multiple scattering of waves from random rough surfaces," *Opt. Commun.*, vol. 35, pp. 25–30, 1980.

[160] M. El-Nicklawy, A. Abd-Rabou, A. Elmahdy, R. El-Agmy, and N. Mansour, "Autocorrelation of non-Circular Statistical Gaussian Speckle Field," *Int. J. New. Hor. Phys*, vol. 7, pp. 25–30, 2020.

[161] S. Chandrasekhar, *Radiative Transfer*. Dover Publications, 1960.

[162] M. v. van Rossum and T. M. Nieuwenhuizen, "Multiple scattering of classical waves: microscopy, mesoscopy, and diffusion," *Rev. Mod. Phys.*, vol. 71, p. 313, 1999.

[163] A. Ishimaru, *Wave propagation and scattering in random media*, vol. 2. Academic press New York, 1978.

[164] M. I. Mishchenko, "Vector radiative transfer equation for arbitrarily shaped and arbitrarily oriented particles: a microphysical derivation from statistical electromagnetics," *Appl. Opt.*, vol. 41, pp. 7114–7134, 2002.

[165] P. Liu, "A new phase function approximating to Mie scattering for radiative transport equations," *Phys. Med. Biol.*, vol. 39, p. 1025, 1994.

[166] M. Hammer, A. N. Yaroslavsky, and D. Schweitzer, "A scattering phase function for blood with physiological haematocrit," *Phys. Med. Biol.*, vol. 46, p. N65, 2001.

[167] J. C. del Toro Iniesta and B. Ruiz Cobo, "Inversion of the radiative transfer equation for polarized light," *Living Rev. Sol. Phys.*, vol. 13, p. 4, 2016.

[168] R. J. Rutten *et al.*, *Radiative transfer in stellar atmospheres*. Citeseer, 1995.

[169] A. Rozanov, V. Rozanov, M. Buchwitz, A. Kokhanovsky, and J. Burrows, "SCIATRAN 2.0–A new radiative transfer model for geophysical applications in the 175–2400 nm spectral region," *ASR*, vol. 36, pp. 1015–1019, 2005.

[170] M. S. Patterson, B. C. Wilson, and D. R. Wyman, "The propagation of optical radiation in tissue I. Models of radiation transport and their application," *Lasers Med Sci*, vol. 6, pp. 155–168, 1991.

[171] S. Jaruwatanadilok, "Underwater wireless optical communication channel modeling and performance evaluation using vector radiative transfer theory," *J-SAC*, vol. 26, pp. 1620–1627, 2008.

[172] A. Ishimaru, Y. Kuga, R. L.-T. Cheung, and K. Shimizu, "Scattering and diffusion of a beam wave in randomly distributed scatterers," *J. Opt. Soc. Am.*, vol. 73, pp. 131–136, 1983.

[173] A. Ishimaru, "Diffusion of light in turbid material," *Appl. Opt.*, vol. 28, pp. 2210–2215, 1989.

[174] K. M. Yoo, F. Liu, and R. R. Alfano, "When does the diffusion approximation fail to describe photon transport in random media?," *Phys. Rev. Lett.*, vol. 64, pp. 2647–2650, 1990.

[175] D. Balsara, "Fast and accurate discrete ordinates methods for multidimensional radiative transfer. Part I, basic methods," *J Quant Spectrosc Radiat Transf*, vol. 69, pp. 671–707, 2001.

[176] V. Rozanov and A. Kokhanovsky, "The solution of the vector radiative transfer equation using the discrete ordinates technique: Selected applications," *Atmos. Res.*, vol. 79, pp. 241–265, 2006.

[177] C. Siewert, "A discrete-ordinates solution for radiative-transfer models that include polarization effects," *J Quant Spectrosc Radiat Transf*, vol. 64, pp. 227–254, 2000.

[178] S. A. Prahl, M. J. van Gemert, and A. J. Welch, "Determining the optical properties of turbid media by using the adding–doubling method," *Appl. Opt.*, vol. 32, pp. 559–568, 1993.

[179] R. Garcia and C. Siewert, "A generalized spherical harmonics solution for radiative transfer models that include polarization effects," *J Quant Spectrosc Radiat Transf*, vol. 36, pp. 401–423, 1986.

[180] E. Abulwafa, "Galerkin technique for radiative transfer in a plane-parallel medium," *J Quant Spectrosc Radiat Transf*, vol. 61, pp. 287–298, 1999.

[181] S. T. Thynell and M. N. Özişik, "Use of eigenfunctions for solving radiation transfer in anisotropically scattering, plane-parallel media," *J. Appl. Phys.*, vol. 60, pp. 541–551, 1986.

[182] C. Siewert, J. Maiorino, and M. Özişik, "The use of the itFN method for radiative transfer problems with reflective boundary conditions," *J Quant Spectrosc Radiat Transf*, vol. 23, pp. 565–573, 1980.

[183] M. Benassi, R. Cotta, and C. Siewert, "The PN method for radiative transfer problems with reflective boundary conditions," *J Quant Spectrosc Radiat Transf*, vol. 30, pp. 547–553, 1983.

[184] E. Zege and L. Chaikovskaya, "New approach to the polarized radiative transfer problem," *J Quant Spectrosc Radiat Transf*, vol. 55, pp. 19–31, 1996.

[185] V. P. Tishkovets and K. Jockers, "Multiple scattering of light by densely packed random media of spherical particles: Dense media vector radiative transfer equation," *J Quant Spectrosc Radiat Transf*, vol. 101, pp. 54–72, 2006.

[186] M. I. Mishchenko, "Maxwell's equations, radiative transfer, and coherent backscattering: A general perspective," *Quant Spectrosc Radiat Transf*, vol. 101, pp. 540–555, 2006.

[187] L. Wang, S. L. Jacques, and L. Zheng, "MCML—Monte Carlo modeling of light transport in multi-layered tissues," *Comput Methods Programs Biomed*, vol. 47, pp. 131–146, 1995.

[188] R. Yuan, J. Ma, P. Su, Y. Dong, and J. Cheng, "Monte-Carlo integration models for multiple scattering based optical wireless communication," *IEEE Trans Commun*, vol. 68, pp. 334–348, 2019.

[189] S. T. Flock, M. S. Patterson, B. C. Wilson, and D. R. Wyman, "Monte Carlo modeling of light propagation in highly scattering tissues. I. Model predictions

and comparison with diffusion theory," *IEEE. Trans. Biomed. Eng.*, vol. 36, pp. 1162–1168, 1989.

[190] L. M. Zurk, L. Tsang, and D. P. Winebrenner, "Scattering properties of dense media from Monte Carlo simulations with application to active remote sensing of snow," *Radio Sci.*, vol. 31, pp. 803–819, 1996.

[191] S. Audic and H. Frisch, "Monte-Carlo simulation of a radiative transfer problem in a random medium: Application to a binary mixture," *J Quant Spectrosc Radiat Transf*, vol. 50, pp. 127–147, 1993.

[192] B. C. Wilson and G. Adam, "A Monte Carlo model for the absorption and flux distributions of light in tissue," *Med Phys*, vol. 10, pp. 824–830, 1983.

[193] T. Yun, N. Zeng, W. Li, D. Li, X. Jiang, and H. Ma, "Monte Carlo simulation of polarized photon scattering in anisotropic media," *Opt. Express*, vol. 17, pp. 16590–16602, 2009.

[194] J. C. Ramella-Roman, S. A. Prahl, and S. L. Jacques, "Three Monte Carlo programs of polarized light transport into scattering media: part I," *Opt. Express*, vol. 13, pp. 4420–4438, 2005.

[195] A. N. Witt, "Multiple scattering in reflection nebulae. I-A Monte Carlo approach.," *Astrophys. J., Suppl. Ser.*, vol. 35, pp. 1–6, 1977.

[196] S. Bartel and A. H. Hielscher, "Monte Carlo simulations of the diffuse backscattering Mueller matrix for highly scattering media," *Appl. Opt.*, vol. 39, pp. 1580–1588, 2000.

[197] D. M. Benoit and D. C. Clary, "Quaternion formulation of diffusion quantum Monte Carlo for the rotation of rigid molecules in clusters," *Chem. Phys.*, vol. 113, pp. 5193–5202, 2000.

[198] M. J. Raković, G. W. Kattawar, M. Mehrűbeoğlu, B. D. Cameron, L. V. Wang, S. Rastegar, and G. L. Coté, "Light backscattering polarization patterns from turbid media: theory and experiment," *Appl. Opt.*, vol. 38, pp. 3399–3408, 1999.

[199] M. Xu, "Electric field Monte Carlo simulation of polarized light propagation in turbid media," *Opt. Express*, vol. 12, pp. 6530–6539, 2004.

[200] R. Graaff, M. H. Koelink, F. F. M. de Mul, W. G. Zijlstra, A. C. M. Dassel, and J. G. Aarnoudse, "Condensed Monte Carlo simulations for the description of light transport," *Appl. Opt.*, vol. 32, pp. 426–434, 1993.

[201] L. Wang and S. L. Jacques, "Hybrid model of Monte Carlo simulation and diffusion theory for light reflectance by turbid media," *J. Opt. Soc. Am. A*, vol. 10, pp. 1746–1752, 1993.

[202] B. Hecht, B. Sick, U. P. Wild, V. Deckert, R. Zenobi, O. J. Martin, and D. W. Pohl, "Scanning near-field optical microscopy with aperture probes: Fundamentals and applications," *Chem. Phys.*, vol. 112, pp. 7761–7774, 2000.

[203] N. Byrnes and M. R. Foreman, "Symmetry constraints for vector scattering and transfer matrices containing evanescent components: Energy conservation, reciprocity, and time reversal," *Phys. Rev. Res.*, vol. 3, p. 013129, 2021.

[204] F. J. Dyson, "The S matrix in quantum electrodynamics," *Phys. Rev.*, vol. 75, p. 1736, 1949.

[205] P. Yu, Q. Zhao, X. Hu, Y. Li, and L. Gong, "Tailoring arbitrary polarization states of light through scattering media," *Appl. Phys. Lett.*, vol. 113, p. 121102, 2018.

[206] B. Zhuang, C. Xu, Y. Geng, G. Zhao, H. Chen, Z. He, Z. Wu, and L. Ren, "Round-trip imaging through scattering media based on opticaltransmission matrix," *Chin. Opt. Lett.*, vol. 16, p. 041102, 2018.

[207] J. Xu, H. Ruan, Y. Liu, H. Zhou, and C. Yang, "Focusing light through scattering media by transmission matrix inversion," *Opt. Express*, vol. 25, pp. 27234–27246, 2017.

[208] J. Hüpfl, N. Bachelard, M. Kaczvinszki, M. Horodynski, M. Kühmayer, and S. Rotter, "Optimal cooling of multiple levitated particles through far-field wavefront-shaping," *arXiv*, 2021.

[209] P. Praveenkumar, R. Amirtharajan, K. Thenmozhi, and J. B. B. Rayappan, "Pixel scattering matrix formalism for image encryption—a key scheduled substitution and diffusion approach," *Int J Electron Commun*, vol. 69, pp. 562–572, 2015.

[210] L. Gong, Q. Zhao, H. Zhang, X.-Y. Hu, K. Huang, J.-M. Yang, and Y.-M. Li, "Optical orbital-angular-momentum-multiplexed data transmission under high scattering," *Light Sci. Appl.*, vol. 8, p. 27, 2019.

[211] A. I. Rahachou and I. V. Zozoulenko, "Scattering matrix approach to the resonant states and Q values of microdisk lasing cavities," *Appl. Opt.*, vol. 43, pp. 1761–1772, 2004.

[212] H. Yu, J.-H. Park, and Y. Park, "Measuring large optical reflection matrices of turbid media," *Opt. Commun.*, vol. 352, pp. 33–38, 2015.

[213] H. Gao, H. Hu, Q. Zhan, Y. Zhang, and W. Zhang, "Efficient Switchable Common Path Interferometer for Transmission Matrix Characterization of Scattering Medium," *IEEE Photonics J.*, vol. 14, pp. 1–5, 2022.

[214] S. Tripathi, R. Paxman, T. Bifano, and K. C. Toussaint, "Vector transmission matrix for the polarization behavior of light propagation in highly scattering media," *Opt. Express*, vol. 20, pp. 16067–16076, 2012.

[215] Y.-Y. Xie, B.-Y. Wang, Z.-J. Cheng, Q.-Y. Yue, and C.-S. Guo, "Measurement of vector transmission matrix and control of beam focusing through a multiple-scattering medium based on a vector spatial light modulator and two-channel polarization holography," *Appl. Phys. Lett.*, vol. 110, p. 221105, 2017.

[216] B. Judkewitz, R. Horstmeyer, I. M. Vellekoop, I. N. Papadopoulos, and C. Yang, "Translation correlations in anisotropically scattering media," *Nat. Phys.*, vol. 11, pp. 684–689, 2015.

[217] A. Goetschy and A. Stone, "Filtering random matrices: The effect of incomplete channel control in multiple scattering," *PRL*, vol. 111, p. 063901, 2013.

[218] H. Kajioka, "Transmission theory of mode-coupled multimode fiber based on scattering matrix," *IEICE TRANSACTIONS (1976-1990)*, vol. 62, pp. 546–547, 1979.

[219] S. F. Mingaleev and K. Busch, "Scattering matrix approach to large-scale photonic crystal circuits," *Opt. Lett.*, vol. 28, pp. 619–621, 2003.

[220] M. McCall, "On the application of coupled mode theory for modeling fiber bragg gratings," *J. Light. Technol.*, vol. 18, p. 236, 2000.

[221] S. Mizuno and S.-i. Tamura, "Theory of acoustic-phonon transmission in finite-size superlattice systems," *Phys. Rev. B*, vol. 45, p. 734, 1992.

[222] R. Bracewell and R. Bracewell, *The Fourier Transform and Its Applications*. McGraw-Hill, 1986.

[223] A. Borisenko, I. Tarapov, and R. Silverman, *Vector and Tensor Analysis with Applications*. Dover Publications, 2012.

[224] R. Carminati, J. J. Sáenz, J.-J. Greffet, and M. Nieto-Vesperinas, "Reciprocity, unitarity, and time-reversal symmetry of the s matrix of fields containing evanescent components," *Phys. Rev. A*, vol. 62, p. 012712, 2000.

[225] J. A. Stratton and L. J. Chu, "Diffraction theory of electromagnetic waves," *Phys. Rev.*, vol. 56, pp. 99–107, 1939.

[226] R. Carminati, M. Nieto-Vesperinas, and J.-J. Greffet, "Reciprocity of evanescent electromagnetic waves," *J. Opt. Soc. Am. A*, pp. 706–712, 1998.

[227] D. A. B. Miller, "Waves, modes, communications, and optics: a tutorial," *Adv. Opt. Photon.*, vol. 11, pp. 679–825, 2019.

[228] S. K. Selvaraja and P. Sethi, "Review on optical waveguides," in *Emerging Waveguide Technology* (K. Y. You, ed.), ch. 6, Rijeka: IntechOpen, 2018.

[229] R. Carminati and J. Schotland, *Principles of Scattering and Transport of Light*. Cambridge University Press, 2021.

[230] A. W. Lohmann, R. G. Dorsch, D. Mendlovic, Z. Zalevsky, and C. Ferreira, "Space–bandwidth product of optical signals and systems," *J. Opt. Soc. Am. A*, vol. 13, pp. 470–473, 1996.

[231] P. Pai, J. Bosch, and A. P. Mosk, "Optical transmission matrix measurement sampled on a dense hexagonal lattice," *OSA Contin.*, vol. 3, pp. 637–648, 2020.

[232] P. Mello, P. Mello, and N. Kumar, *Quantum Transport in Mesoscopic Systems: Complexity and Statistical Fluctuations, a Maximum-entropy Viewpoint*. Oxford University Press, 2004.

[233] I. Lindell, *Multiforms, Dyadics, and Electromagnetic Media*. Wiley, 2015.

[234] Y. V. Gulyaev, Y. N. Barabanenkov, M. Y. Barabanenkov, and S. A. Nikitov, "Optical theorem for electromagnetic field scattering by dielectric structures and energy emission from the evanescent wave," *Phys. Rev. E*, vol. 72, p. 026602, 2005.

[235] R. Bhandari, "Transpose symmetry of the Jones matrix and topological phases," *Opt. Lett.*, vol. 33, pp. 854–856, 2008.

[236] P. Mello, P. Pereyra, and N. Kumar, "Macroscopic approach to multichannel disordered conductors," *Ann Phys*, vol. 181, pp. 290–317, 1988.

[237] P. Pereyra, "Symmetries, parametrization, and group structure of transfer matrices in quantum scattering theory," *J. Math. Phys.*, vol. 36, pp. 1166–1176, 1995.

[238] B. Hall, *Lie Groups, Lie Algebras, and Representations: An Elementary Introduction*. Springer, 2003.

[239] A. T. Fomenko, *Symplectic geometry*. CRC Press, 1995.

[240] J. J. Gil and R. Ossikovski, *Polarized Light and the Mueller Matrix Approach*. CRC Press, 2022.

[241] L. Tsang and J. Kong, *Scattering of Electromagnetic Waves: Advanced Topics*. Wiley, 2004.

[242] M. Simon, *Probability Distributions Involving Gaussian Random Variables: A Handbook for Engineers and Scientists*. Springer US, 2008.

[243] U. Frisch, *Wave Propagation in Random Media: A Theory of Multiple Scattering*. Institut d'Astrophysique de Paris, 1965.

[244] S. Mudaliar and J. Lee, "Wave propagation and scattering from a random medium with a random interface," . *Electromagn. Waves Appl.*, vol. 9, pp. 925–951, 1995.

[245] A. Doicu and M. I. Mishchenko, "An overview of methods for deriving the radiative transfer theory from the Maxwell equations. II: Approach based on the Dyson and Bethe–Salpeter equations," *J Quant Spectrosc Radiat Transf*, vol. 224, pp. 25–36, 2019.

[246] N. Byrnes and M. R. Foreman, "Polarisation statistics of vector scattering matrices from the circular orthogonal ensemble," *Opt. Commun.*, vol. 503, p. 127462, 2022.

[247] E. P. Wigner, "Random matrices in physics," *SIAM Rev*, vol. 9, pp. 1–23, 1967.

[248] G. Akemann, J. Baik, and P. Di Francesco, *The Oxford Handbook of Random Matrix Theory*. Oxford University Press, 2015.

[249] A. R. Feier, *Methods of proof in random matrix theory*. PhD thesis, Harvard University, 2012.

[250] I. Garg and N. Deo, "A random matrix approach to RNA folding with interaction," *Pramana*, vol. 73, pp. 533–541, 2009.

[251] J. N. Bandyopadhyay and S. Jalan, "Universality in complex networks: Random matrix analysis," *Phys. Rev. E*, vol. 76, p. 026109, 2007.

[252] C. P. Hughes, J. P. Keating, and N. 'Connell, "Random matrix theory and the derivative of the Riemann zeta function," *Proc. R. Soc. A: Math. Phys. Eng. Sci.*, vol. 456, pp. 2611–2627, 2000.

[253] F. J. Dyson, "Statistical Theory of the Energy Levels of Complex Systems. I," *J. Math. Phys.*, vol. 3, no. 1, pp. 140–156, 1962.

[254] F. J. Dyson, "Statistical Theory of the Energy Levels of Complex Systems. II," *J. Math. Phys.*, vol. 3, no. 1, pp. 157–165, 1962.

[255] F. J. Dyson, "Statistical Theory of the Energy Levels of Complex Systems. III," *J. Math. Phys.*, vol. 3, no. 1, pp. 166–175, 1962.

[256] P. Forrester, *Log-Gases and Random Matrices (LMS-34)*. Princeton University Press, 2010.

[257] J. Sakurai and J. Napolitano, *Modern Quantum Mechanics*. Cambridge University Press, 2020.

[258] S. MATSUMOTO, "General moments of matrix elements from circular orthogonal ensembles," *Random Matrices: Theory Appl.*, vol. 01, p. 1250005, 2012.

[259] S.-Y. Lu and R. A. Chipman, "Homogeneous and inhomogeneous Jones matrices," *J. Opt. Soc. Am. A*, vol. 11, pp. 766–773, 1994.

[260] S.-Y. Lu and R. A. Chipman, "Interpretation of Mueller matrices based on polar decomposition," *J. Opt. Soc. Am. A*, vol. 13, pp. 1106–1113, 1996.

[261] W. A. Friedman and P. A. Mello, "Marginal distribution of an arbitrary square submatrix of the s-matrix for dyson's measure," *J. Phys. A Math. Theor.*, vol. 18, p. 425, 1985.

[262] P. Pereyra and P. A. Mello, "Marginal distribution of the S-matrix elements for Dyson's measure and some applications," *J. Phys. A Math. Theor.*, vol. 16, p. 237, 1983.

[263] R. A. Horn and C. R. Johnson, *Matrix Analysis*. Cambridge University Press, 2012.

[264] S. R. Garcia, E. Prodan, and M. Putinar, "Mathematical and physical aspects of complex symmetric operators," *J. Phys. A Math. Theor.*, vol. 47, p. 353001, 2014.

[265] J. A. Dı´az-García and R. Gutiérrez-Jáimez, "On Wishart distribution: Some extensions," *Linear Algebra Appl.*, vol. 435, pp. 1296–1310, 2011.

[266] A. Mathai, *Jacobians Of Matrix Transformation And Functions Of Matrix Arguments*. World Scientific Publishing Company, 1997.

[267] A. Vannucci and A. Bononi, "Statistical Characterization of the Jones Matrix of Long Fibers Affected by Polarization Mode Dispersion (PMD)," *J. Lightwave Technol.*, vol. 20, p. 783, 2002.

[268] D. Zwillinger and A. Jeffrey, *Table of Integrals, Series, and Products*. Elsevier Science, 2007.

[269] M. Cvitković, A.-S. Smith, and J. Pande, "Asymptotic expansions of the hypergeometric function with two large parameters—application to the partition function of a lattice gas in a field of traps," *J. Phys. A Math. Theor.*, vol. 50, p. 265206, 2017.

[270] W. Friedman and P. Mello, "Information theory and statistical nuclear reactions II. Many-channel case and Hauser-Feshbach formula," *Ann Phys*, vol. 161, pp. 276–302, 1985.

[271] S. M. Popoff, G. Lerosey, M. Fink, A. C. Boccara, and S. Gigan, "Controlling light through optical disordered media: transmission matrix approach," *New J. Phys.*, vol. 13, p. 123021, 2011.

[272] V. A. Marchenko and L. A. Pastur, "Distribution of eigenvalues for some sets of random matrices," *Mat. Sb.*, vol. 114, pp. 507–536, 1967.

[273] A. Aubry and A. Derode, "Singular value distribution of the propagation matrix in random scattering media," *Waves Random Complex Media*, vol. 20, pp. 333–363, 2010.

[274] S. Feng, C. Kane, P. A. Lee, and A. D. Stone, "Correlations and fluctuations of coherent wave transmission through disordered media," *Phys. Rev. Lett.*, vol. 61, pp. 834–837, 1988.

[275] F. Scheffold and G. Maret, "Universal conductance fluctuations of light," *Phys. Rev. Lett.*, vol. 81, pp. 5800–5803, 1998.

[276] P. W. Brouwer, "Generalized circular ensemble of scattering matrices for a chaotic cavity with nonideal leads," *Phys. Rev. B*, vol. 51, p. 16878, 1995.

[277] V. Twersky, "On propagation in random media of discrete scatterers," in *Proc. Symp. Appl. Math*, vol. 16, pp. 84–116, 1964.

[278] L. Mandel, E. Wolf, and C. U. Press, *Optical Coherence and Quantum Optics*. Cambridge University Press, 1995.

[279] P. Schreier and L. Scharf, *Statistical Signal Processing of Complex-Valued Data: The Theory of Improper and Noncircular Signals*. Cambridge University Press, 2010.

[280] Rubén G. Barrera and Augusto Garcia-Valenzuela, "Coherent reflectance in a system of random mie scatterers and its relation to the effective-medium approach," *J. Opt. Soc. Am. A*, vol. 20, pp. 296–311, 2003.

[281] R. West, D. Gibbs, L. Tsang, and A. Fung, "Comparison of optical scattering experiments and the quasi-crystalline approximation for dense media," *J. Opt. Soc. Am. A*, vol. 11, pp. 1854–1858, 1994.

[282] P. Matthews, *Vector Calculus*. Springer London, 2012.

[283] J. Dainty, *Laser Speckle and Related Phenomena*. Springer Berlin Heidelberg, 2013.

[284] P. J. Schreier and L. L. Scharf, "Second-order analysis of improper complex random vectors and processes," *IEEE Trans. Signal Process.*, vol. 51, pp. 714–725, 2003.

[285] R. Berkovits and S. Feng, "Correlations in coherent multiple scattering," *Phys. Rep.*, vol. 238, pp. 135–172, 1994.

[286] V. Malyshkin, A. McGurn, T. Leskova, A. Maradudin, and M. Nieto-Vesperinas, "Speckle correlations in the light scattered from a weakly rough one-dimensional random metal surface," *Opt. Lett.*, vol. 22, pp. 946–948, 1997.

[287] T. Kawanishi, Z. L. Wang, M. Izutsu, and H. Ogura, "Conjugate memory effect of random scattered waves," *J. Opt. Soc. Am. A*, vol. 16, pp. 1342–1349, 1999.

[288] R. Berkovits and M. Kaveh, "Time-reversed memory effects," *Phys. Rev. B*, vol. 41, p. 2635, 1990.

[289] A. Doicu and M. I. Mishchenko, "Overview of methods for deriving the radiative transfer theory from the Maxwell equations. I: Approach based on the far-field Foldy equations," *J Quant Spectrosc Radiat Transf*, vol. 220, pp. 123–139, 2018.

[290] P. N. den Outer, T. M. Nieuwenhuizen, and A. Lagendijk, "Location of objects in multiple-scattering media," *J. Opt. Soc. Am. A*, vol. 10, pp. 1209–1218, 1993.

[291] L. Tsang and J. A. Kong, "Multiple scattering of electromagnetic waves by random distributions of discrete scatterers with coherent potential and quantum mechanical formalism," *J. Appl. Phys.*, vol. 51, pp. 3465–3485, 1980.

[292] M. I. Mishchenko and M. A. Yurkin, "Impressed sources and fields in the volume-integral-equation formulation of electromagnetic scattering by a finite object: A tutorial," *J Quant Spectrosc Radiat Transf*, vol. 214, pp. 158–167, 2018.

[293] A. J. Devaney and E. Wolf, "Multipole expansions and plane wave representations of the electromagnetic field," *J. Math. Phys.*, vol. 15, pp. 234–244, 1974.

[294] M. Mishchenko, M. Andrew A. Lacis, L. Travis, and A. Lacis, *Scattering, Absorption, and Emission of Light by Small Particles*. Cambridge University Press, 2002.

[295] M. I. Mishchenko, "Multiple scattering, radiative transfer, and weak localization in discrete random media: unified microphysical approach," *Rev. Geophys.*, vol. 46, 2008.

[296] N. Byrnes and M. R. Foreman, "Random matrix theory of polarized light scattering in disordered media," *Waves Random Complex Media*, vol. 0, no. 0, pp. 1–29, 2022.

[297] A. Stroud, *Approximate Calculation of Multiple Integrals*. Prentice-Hall, 1971.

[298] J. B. Keller, "Closest unitary, orthogonal and hermitian operators to a given operator," *Math. Mag.*, vol. 48, pp. 192–197, 1975.

[299] L. S. Froufe-Pérez, M. Yépez, P. A. Mello, and J. J. Sáenz, "Statistical scattering of waves in disordered waveguides: From microscopic potentials to limiting macroscopic statistics," *Phys. Rev. E*, vol. 75, p. 031113, 2007.

[300] P. A. Mello and A. D. Stone, "Maximum-entropy model for quantum-mechanical interference effects in metallic conductors," *Phys. Rev. B*, vol. 44, pp. 3559–3576, 1991.

[301] D. A. Zimnyakov, Y. P. Sinichkin, P. V. Zakharov, and D. N. Agafonov, "Residual polarization of non-coherently backscattered linearly polarized light: the influence of the anisotropy parameter of the scattering medium," *Waves Random Complex Media*, vol. 11, pp. 395–412, 2001.

[302] P. Sun, Y. Ma, W. Liu, C. Xu, and X. Sun, "Experimentally determined characteristics of the degree of polarization of backscattered light from polystyrene sphere suspensions," *J Opt*, vol. 15, p. 055708, 2013.

[303] D. Wackerly, W. Mendenhall, and R. Scheaffer, *Mathematical Statistics with Applications*. Cengage Learning, 2014.

[304] O. Katz, P. Heidmann, M. Fink, and S. Gigan, "Non-invasive single-shot imaging through scattering layers and around corners via speckle correlations," *Nat. Photon*, vol. 8, pp. 784–790, 2014.

[305] J. Bertolotti, E. G. van Putten, C. Blum, A. Lagendijk, W. L. Vos, and A. P. Mosk, "Non-invasive imaging through opaque scattering layers," *Nature*, vol. 491, pp. 232–234, 2012.

[306] J. Bertolotti and O. Katz, "Imaging in complex media," *Nat. Phys.*, vol. 18, pp. 1008–1017, 2022.

[307] J. R. Fienup, "Phase retrieval algorithms: a comparison," *Appl. Opt.*, vol. 21, pp. 2758–2769, 1982.

[308] R. Berkovits and M. Kaveh, "The Vector Memory Effect for Waves," *EPL*, vol. 13, p. 97, 1990.

[309] R. V. Vinu and R. K. Singh, "Experimental determination of generalized stokes parameters," *Opt. Lett.*, vol. 40, pp. 1227–1230, 2015.

[310] D. Eliyahu, M. Rosenbluh, and I. Freund, "Angular intensity and polarization dependence of diffuse transmission through random media," *J. Opt. Soc. Am. A*, vol. 10, pp. 477–491, 1993.

[311] I. Freund, "Optical intensity fluctuations in multiply scattering media," *Opt. Commun.*, vol. 81, pp. 251–258, 1991.

[312] I. Freund, M. Kaveh, R. Berkovits, and M. Rosenbluh, "Universal polarization correlations and microstatistics of optical waves random complex media," *Phys. Rev. B*, vol. 42, pp. 2613–2616, 1990.

[313] I. Freund and E. Barkai, "Third-order polarization correlations in highly random media," *J. Opt. Soc. Am. A*, vol. 8, pp. 1559–1567, 1991.

[314] I. Freund, "Stokes-vector reconstruction," *Opt. Lett.*, vol. 15, pp. 1425–1427, 1990.

[315] L. Tong, G. Xu, B. Hassibi, and T. Kailath, "Blind channel identification based on second-order statistics: A frequency-domain approach," *IEEE Trans. Inf. Theory*, vol. 41, pp. 329–334, 1995.

[316] K. Jaganathan and B. Hassibi, "Reconstruction of Signals From Their Autocorrelation and Cross-Correlation Vectors, With Applications to Phase Retrieval and Blind Channel Estimation," *IEEE Trans. Signal Process.*, vol. 67, pp. 2937–2946, 2019.

[317] O. Raz, N. Dudovich, and B. Nadler, "Vectorial Phase Retrieval of 1-D Signals," *IEEE Trans. Signal Process.*, vol. 61, pp. 1632–1643, 2013.

[318] O. Raz, O. Schwartz, D. Austin, A. S. Wyatt, A. Schiavi, O. Smirnova, B. Nadler, I. A. Walmsley, D. Oron, and N. Dudovich, "Vectorial Phase Retrieval for Linear Characterization of Attosecond Pulses," in *Research in Optical Sciences*, p. HW2C.5, Optica Publishing Group, 2012.